

การเปลี่ยนเชิงเร่งปฏิกิริยาแบบใช้แสงของกลีเซอรอลเป็นไดไฮดรอกซีแอซีโตน



นายตฤณ เจตสุคนธร

จุฬาลงกรณ์มหาวิทยาลัย

บทคัดย่อและแฟ้มข้อมูลฉบับเต็มของวิทยานิพนธ์ตั้งแต่ปีการศึกษา 2554 ที่ให้บริการในคลังปัญญาจุฬาฯ (CUIR)
เป็นแฟ้มข้อมูลของนิสิตเจ้าของวิทยานิพนธ์ ที่ส่งผ่านทางบัณฑิตวิทยาลัย

The abstract and full text of theses from the academic year 2011 in Chulalongkorn University Intellectual Repository (CUIR)
are the thesis authors' files submitted through the University Graduate School.

วิทยานิพนธ์นี้เป็นส่วนหนึ่งของการศึกษาตามหลักสูตรปริญญาวิทยาศาสตรดุษฎีบัณฑิต

สาขาวิชาเคมีเทคนิค ภาควิชาเคมีเทคนิค

คณะวิทยาศาสตร์ จุฬาลงกรณ์มหาวิทยาลัย

ปีการศึกษา 2560

ลิขสิทธิ์ของจุฬาลงกรณ์มหาวิทยาลัย

PHOTOCATALYTIC CONVERSION OF GLYCEROL TO DIHYDROXYACETONE



A Dissertation Submitted in Partial Fulfillment of the Requirements
for the Degree of Doctor of Philosophy Program in Chemical Technology

Department of Chemical Technology

Faculty of Science

Chulalongkorn University

Academic Year 2017

Copyright of Chulalongkorn University

ตฤณ เจตสุคนธร : การเปลี่ยนเชิงเร่งปฏิกิริยาแบบใช้แสงของกลีเซอรอลเป็นไดไฮดรอกซีแอสีโทน (PHOTOCATALYTIC CONVERSION OF GLYCEROL TO DIHYDROXYACETONE) อ.ที่ปริกษาวิทยานิพนธ์หลัก: ศ. ดร.มะลิ หุ่นสม, อ.ที่ปริกษาวิทยานิพนธ์ร่วม: ศ. ดร.นากาฮิโระ ไชโตะ, 264 หน้า.

งานวิจัยนี้ศึกษาการเปลี่ยนกลีเซอรอลเป็นสารเพิ่มมูลค่าในวัฏภาคของเหลวด้วยตัวเร่งปฏิกิริยาเชิงแสงไทเทเนียมไดออกไซด์ ตัวแปรที่ศึกษา ได้แก่ สัดส่วนของตัวเร่งปฏิกิริยา (1-3 กรัมต่อลิตร) ความเข้มข้นของตัวรับอิเล็กตรอนชนิดไฮโดรเจนเปอร์ออกไซด์ (0.3-1.5 โมลต่อลิตร) ความเข้มของแสงยูวี (1.1-4.7 มิลลิวัตต์ต่อตารางเซนติเมตร) ระยะเวลาในการทำปฏิกิริยา (4-8 ชั่วโมง) และชนิดของตัวรับอิเล็กตรอน (ออกซิเจนและไฮโดรเจนเปอร์ออกไซด์) พบว่าตัวเร่งปฏิกิริยาไทเทเนียมไดออกไซด์วัฏภาคอนาเทส สามารถเปลี่ยนกลีเซอรอลได้ร้อยละ 71.42 ที่สัดส่วนของตัวเร่งปฏิกิริยา 3 กรัมต่อลิตร ความเข้มข้นของไฮโดรเจนเปอร์ออกไซด์เท่ากับ 1.5 โมลต่อลิตร ความเข้มของแสงยูวี 4.7 มิลลิวัตต์ต่อตารางเซนติเมตร และระยะเวลาในการทำปฏิกิริยา 8 ชั่วโมง การเติมโลหะเดี่ยว ได้แก่ บิสมัท แพลทินัม แพลเลเดียม และทอง และโลหะคู่ ได้แก่ ทอง-บิสมัท ทอง-แพลทินัม และทอง-แพลเลเดียม บนตัวเร่งปฏิกิริยาเชิงแสงไทเทเนียมไดออกไซด์สามารถปรับปรุงกัมมันตภาพเชิงแสงในการเปลี่ยนรูปของกลีเซอรอลเป็นสารเพิ่มมูลค่า โดยพบว่าการเติมโลหะคู่ ทอง-แพลเลเดียม ร้อยละ 3 โดยน้ำหนักของแต่ละโลหะ สามารถเปลี่ยนกลีเซอรอลได้สูงสุดถึงร้อยละ 98.75 ที่ระยะเวลาในการทำปฏิกิริยา 24 ชั่วโมงเมื่อใช้ออกซิเจนเป็นตัวรับอิเล็กตรอน และให้ร้อยละผลได้ของกลีเซอรอลดีไฮด์ ไดไฮดรอกซีแอสีโทน กรดไฮดรอกซีไพรูวิก กรดกลีเซอริก กรดไกลโคลิก พอร์มัลดีไฮด์ และไกลคอลแอลดีไฮด์ ร้อยละ 16.35 7.47 8.45 1.69 21.92 22.94 และ 6.03 ตามลำดับ นอกจากนี้ยังพบว่าตัวเร่งปฏิกิริยาเชิงแสงไทเทเนียมไดออกไซด์ที่มีตำหนิในโครงสร้างซึ่งถูกสังเคราะห์ด้วยกระบวนการพลาสมาในของเหลว สามารถเปลี่ยนกลีเซอรอลได้ร้อยละ 58.49 ที่ระยะเวลาในการทำปฏิกิริยา 24 ชั่วโมงเมื่อใช้ออกซิเจนเป็นตัวรับอิเล็กตรอน และให้ร้อยละผลได้ของกลีเซอรอลดีไฮด์ ไดไฮดรอกซีแอสีโทน กรดไฮดรอกซีไพรูวิก กรดไกลโคลิก พอร์มัลดีไฮด์ และไกลคอลแอลดีไฮด์ ร้อยละ 4.85 3.32 2.11 2.15 26.61 และ 39.15 ตามลำดับ

| | | |
|------------|------------|----------------------------------|
| ภาควิชา | เคมีเทคนิค | ลายมือชื่อนิสิต |
| สาขาวิชา | เคมีเทคนิค | ลายมือชื่อ อ.ที่ปริกษาหลัก |
| ปีการศึกษา | 2560 | ลายมือชื่อ อ.ที่ปริกษาร่วม |

5672813723 : MAJOR CHEMICAL TECHNOLOGY

KEYWORDS: GLYCEROL CONVERSION / PHOTOCATALYTIC OXIDATION PROCESS (PCO) / SOLUTION PLASMA / TITANIUM DIOXIDE

TRIN JEDSUKONTORN: PHOTOCATALYTIC CONVERSION OF GLYCEROL TO DIHYDROXYACETONE. ADVISOR: PROF. MALI HUNSOM, Ph.D., Dr. de L'INPT, CO-ADVISOR: PROF. NAGAIRO SAITO, Ph.D., 264 pp.

This work was carried out to convert glycerol to value-added compounds in liquid phase over TiO₂-based photocatalyst. The investigated parameters were catalyst dosage (1-3 g/L), H₂O₂ concentration (0.3-1.5 mol/L), UV light intensity (1.1-4.7 mW/cm²), reaction time (4-8 h) and electron acceptor types (O₂ and H₂O₂). It was found that TiO₂ in anatase phase can achieved the glycerol conversion of around 71.42% at catalyst dosage of 3 g/L, H₂O₂ concentration of 1.5 mol/L, UV light intensity 4.7 mW/cm² and reaction time 8 h. The addition of monometallic (bismuth, platinum, palladium, and gold) and bimetallic (gold-bismuth, gold-platinum, and gold-palladium) on TiO₂ can enhance the photocatalytic activity for glycerol conversion to value-added compounds. Among all studied photocatalysts, the AuPd/TiO₂ with 3 wt.% of each metal promoted the highest glycerol conversion up to 98.75% at 24 h of reaction time and using O₂ as electron acceptor and provided the yield of glyceraldehyde, dihydroxyacetone, hydroxypyruvic acid, glyceric acid, glycolic acid, formaldehyde and glycolaldehyde of 16.35, 7.47, 8.45, 1.69, 21.92, 22.94 and 6.03%, respectively. In addition, it was found that the defective TiO₂ photocatalyst, which was successfully synthesized through solution plasma process can promote the glycerol conversion to value-added compounds. It gave the glycerol conversion of around 58.49% at 24 h of reaction time and using O₂ as electron acceptor and provided the yield of glyceraldehyde, dihydroxyacetone, hydroxypyruvic acid, glycolic acid, formaldehyde and glycolaldehyde of 4.85, 3.32, 2.11, 2.15, 26.61 and 39.15%, respectively.

Department: Chemical Technology Student's Signature

Field of Study: Chemical Technology Advisor's Signature

Academic Year: 2017 Co-Advisor's Signature

ACKNOWLEDGEMENTS

After an intensive period of five years, today is the day: writing this note of thanks is the finishing touch on my dissertation. It has been a period of intense learning for me, not only in the scientific area, but also on a personal level. Doing this dissertation has had a big impact on me. I would like to reflect on the people who have supported and helped me so much throughout this period.

I would first like to express my deepest gratitude and sincere appreciation to my supervisor, Prof. Dr. Mali Hunsom and co-supervisor, Prof. Dr. Nagahiro Saito for encouraging guidance, provision and support throughout this research. It is impossible to thank them enough for their time and effort. They always raise me up and respect me more than I respected myself. Without their trust, valuable advice, never-ending patience and seemingly inexhaustible knowledge of scientific research, this dissertation would not have been successfully completed.

I would also especially extend my appreciation to Assoc. Prof. Dr. Prasert Reubroycharoen, Prof. Dr. Pattarapan Prasassarakich, Dr. Nuttapol Pootrakulchote and Asst. Prof. Dr. Soipatta Soisuwan for serving as the chairman and members of the dissertation committee, respectively, and for their worthy comments and suggestions. And I am also thankful to Asst. Prof. Dr. Tomonaga Ueno for his suggestion and persevering help during 1 year of my research experience in Nagoya University, Japan.

I gratefully acknowledged the funding support from Chulalongkorn University through Dutsadi Phiphat Scholarship. Many thanks also go to the Department of Chemical Technology, Faculty of Science, Chulalongkorn University, Thailand and Green Mobility Collaborative Research Center, Graduate School of Engineering, Nagoya University, Japan for providing research facilities throughout this research work.

Finally, I would like to express my million thanks to my cherished family for their love, endless support, wise counsel and sympathetic ear. They are always there for me. Special thanks are also extended to all members of MHS's and Saito's Laboratory Group for their cheerful moral support and great friendships. We were not only able to support each other by deliberating over our problems and findings, but also happily by talking about things other than just our researches.

CONTENTS

| | Page |
|--|------|
| THAI ABSTRACT | iv |
| ENGLISH ABSTRACT | v |
| ACKNOWLEDGEMENTS | vi |
| CONTENTS | vii |
| LIST OF TABLES | xiii |
| LIST OF FIGURES | xv |
| CHAPTER I..... | 1 |
| 1.1 Rationales and theories | 1 |
| 1.2 Objectives of dissertation | 3 |
| 1.3 Research methodology and Experimental procedures..... | 3 |
| CHAPTER II..... | 6 |
| 2.1 Background | 6 |
| 2.2 Glycerol | 8 |
| 2.3 Sustainable use of glycerol surplus..... | 8 |
| 2.4 Oxidation of glycerol | 13 |
| 2.5 Photocatalytic process | 16 |
| Table 2.3 Overview of glycerol conversion over Pt, Pd and Au metal based catalysts in water solute via oxidation reactions [3, 13, 15, 24] (Cont.)..... | 18 |
| 2.6 Semiconductor material | 20 |
| 2.7 Titanium dioxide..... | 23 |
| 2.8 Doping TiO ₂ | 26 |
| 2.8.1 Doping with transition metals | 27 |
| 2.8.2 Doping with noble metals..... | 30 |

| | Page |
|--|------|
| 2.8.3 Non-metal modification | 31 |
| 2.9 Defective TiO ₂ | 34 |
| 2.9.1 Synthesis of defective TiO ₂ | 39 |
| 2.10 Solution plasma process (SPP) | 41 |
| 2.10.1 Solution plasma application | 44 |
| 2.10.1.1 Nanomaterial synthesis | 44 |
| 2.10.1.2 Wastewater treatment | 47 |
| 2.11 Key species in photocatalytic reactions | 48 |
| 2.11.1 Superoxide radical (O ₂ ^{•-}) | 50 |
| 2.11.2 Hydroxyl radical (OH [•]) | 52 |
| 2.11.3 Singlet molecular oxygen (¹ O ₂) | 53 |
| 2.12 Literature reviews | 54 |
| CHAPTER III | 62 |
| 3.1 Chemical substances and materials | 62 |
| 3.2 Laboratory instruments | 63 |
| 3.3 Synthesis of monometallic decorated on TiO ₂ | 64 |
| 3.4 Synthesis of Au-based bimetallic nanoparticles decorated on TiO ₂ | 66 |
| 3.5 Synthesis of black TiO ₂ through solution plasma process | 68 |
| 3.6 Photocatalytic activity test | 69 |
| 3.7 Detection of the generated reactive oxygen species (ROS) in photocatalytic system | 71 |
| 3.8 Catalyst characterizations | 72 |
| 3.8.1 X-ray Diffraction (XRD) | 72 |

| | Page |
|--|------|
| 3.8.2 X-ray Photoelectron Spectroscopy (XPS)..... | 73 |
| 3.8.3 Scanning Electron Microscopy with Energy Dispersive X-ray Spectroscopy (SEM/EDS) | 73 |
| 3.8.4 Transmission Electron Spectroscopy with Energy Dispersive X-ray Spectroscopy (TEM/EDS)..... | 73 |
| 3.8.5 Brunauer-Emmett-Teller method (BET)..... | 74 |
| 3.8.6 Fourier Transform Infrared Spectroscopy (FTIR)..... | 74 |
| 3.8.7 Electron Spin Resonance Spectroscopy (ESR/EPR)..... | 74 |
| 3.8.8 Dynamic Light Scattering (DLS)..... | 75 |
| 3.8.9 Ultra-Violet Spectroscopy (UV-Vis)..... | 75 |
| 3.9 Plasma characterizations | 76 |
| 3.9.1 Current and Voltage waveform..... | 76 |
| 3.9.2 Optical Emission Spectra (OES)..... | 76 |
| CHAPTER IV | 77 |
| 4.1 Effect of TiO ₂ phase on photocatalytic oxidation of glycerol | 77 |
| 4.2 Effect of operating parameters on photocatalytic oxidation of glycerol | 83 |
| 4.3 Evaluation of influence factors on photocatalytic oxidation of glycerol and product generation by 2 ^k factorial design | 88 |
| 4.3.1 Influence factors on glycerol conversion | 89 |
| 4.3.2 Influence factors on DHA selectivity..... | 94 |
| 4.3.3 Influence factors on GCD selectivity..... | 96 |
| 4.3.4 Influence factors on GCA selectivity..... | 98 |
| 4.3.5 Influence factors on glycolic acid (GCOA) selectivity | 100 |
| 4.4 Effect of electron acceptor types on photocatalytic oxidation of glycerol | 103 |

| | Page |
|--|------|
| 4.5 Mechanism of commercial TiO ₂ -induced photocatalytic oxidation of glycerol | 109 |
| CHAPTER V | 117 |
| 5.1 Monometallic NPs decorated on TiO ₂ | 117 |
| 5.1.1 Effect of decorated metal types | 117 |
| 5.1.1.1 Crystallite structure analysis | 118 |
| 5.1.1.2 Morphology analysis | 119 |
| 5.1.1.3 Chemical structure analysis..... | 120 |
| 5.1.1.4 Optical property analysis | 127 |
| 5.1.1.5 Photocatalytic activity test for glycerol conversion | 130 |
| 5.1.1.6 Mechanism of charge transfer in monometallic NPs decorated on TiO ₂ | 136 |
| 5.1.2 Effect of Au metal content..... | 140 |
| 5.1.2.1 Crystallite structure analysis | 140 |
| 5.1.2.2 Morphology analysis | 141 |
| 5.1.2.3 Chemical structure analysis..... | 142 |
| 5.1.2.4 Optical property analysis | 146 |
| 5.1.2.5 Photocatalytic activity test for glycerol conversion | 148 |
| 5.2 Bimetallic NPs decorated on TiO ₂ | 153 |
| 5.2.1 Crystallite structure analysis..... | 153 |
| 5.2.2 Morphology analysis..... | 155 |
| 5.2.3 Chemical structure analysis..... | 156 |
| 5.2.4 Optical property analysis | 161 |
| 5.2.5 Photocatalytic activity test for glycerol conversion | 163 |

| | Page |
|---|------|
| CHAPTER VI | 171 |
| 6.1 Formation of black TiO ₂ NPs through solution plasma process..... | 171 |
| 6.2 Characterization of the as-synthesized black TiO ₂ NPs..... | 173 |
| 6.2.1 Effect of HNO ₃ concentration, pulse width and repetition frequency | 173 |
| 6.2.1.1 Crystallite structure analysis | 174 |
| 6.2.1.2 Morphology analysis | 179 |
| 6.2.1.3 Chemical structure analysis..... | 181 |
| 6.2.1.4 Optical property analysis..... | 190 |
| 6.2.2 Effect of plasma discharge time | 194 |
| 6.2.2.1 Crystallite structure analysis | 194 |
| 6.2.2.2 Morphology analysis | 195 |
| 6.2.2.3 Chemical structure analysis..... | 198 |
| 6.2.2.4 Optical property analysis..... | 198 |
| 6.3 Photocatalytic activity of as-synthesized black TiO ₂ NPs | 202 |
| 6.4 Mechanism and role of generated ROS in the photooxidation of glycerol by using black TiO ₂ | 207 |
| CHAPTER VII..... | 218 |
| 7.1 Conclusions | 218 |
| 7.1.1 Commercial TiO ₂ -induced photocatalytic oxidation of glycerol to value-added compounds | 218 |
| 7.1.2 Metal-decorated TiO ₂ -induced photocatalytic oxidation of glycerol to value-added compounds | 219 |
| 7.1.3 Preparation of black TiO ₂ via solution plasma process and its photocatalytic oxidation of glycerol to value-added compounds..... | 220 |

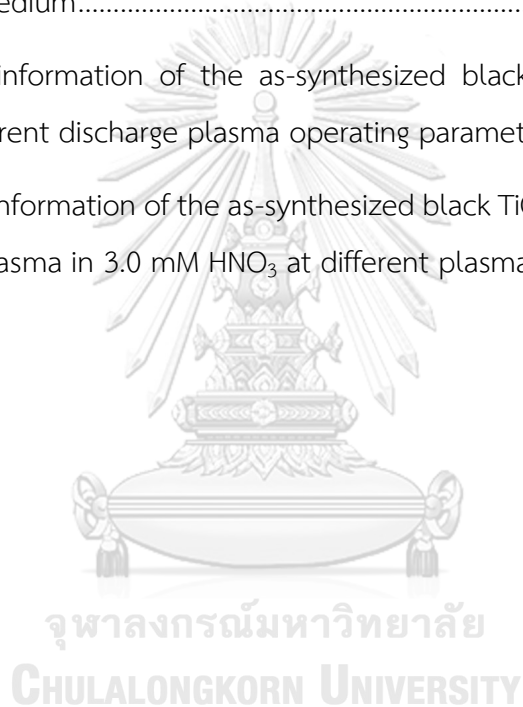
| | Page |
|---------------------------|------|
| 7.2 Recommendations | 221 |
| REFERENCES | 222 |
| APPENDICES..... | 248 |
| APPENDIX A | 249 |
| APPENDIX B | 255 |
| APPENDIX C | 262 |
| VITA..... | 264 |



LIST OF TABLES

| Table | Page |
|-------|--|
| 2.1 | Physicochemical properties of glycerol at 20 °C..... 9 |
| 2.2 | List of value-added compounds derived from glycerol..... 11 |
| 2.3 | Overview of glycerol conversion over Pt,Pd and Au metal based catalysts in water solute via oxidation reactions. 17 |
| 2.4 | Structural data of crystalline structure of TiO ₂ 24 |
| 2.5 | Work function and redox potential of some noble metals..... 32 |
| 4.1 | Glycerol conversion (X) and product selectivity (S) in the presence of different types TiO ₂ phase structure..... 78 |
| 4.2 | Photocatalytic- and catalytic conversions (X) of 0.3 M glycerol (GLY) and selectivity (S) towards the known products for 8 h..... 84 |
| 4.3 | Photocatalytic- and catalytic conversions (X) of 0.3 M DHA and selectivity (S) towards the known products for 8 h. 86 |
| 4.4 | Factor and levels used in the 2 ⁴ full factorial design. 89 |
| 4.5 | Experimental factorial matrix in 2 ⁴ factorial design and experimental results of TiO ₂ -induced photocatalytic oxidation of glycerol..... 91 |
| 4.6 | ANOVA results for analysis of glycerol conversion. 92 |
| 4.7 | ANOVA results for analysis of DHA selectivity..... 95 |
| 4.8 | ANOVA results for analysis of GCD selectivity..... 97 |
| 4.9 | ANOVA results for analysis of GCA selectivity..... 99 |
| 4.10 | ANOVA results for analysis of glycolic acid selectivity..... 101 |
| 5.1 | Properties of metal-decorated TiO ₂ photocatalysts..... 121 |

| Table | Page |
|--|------|
| 5.2 Glycerol conversions and product selectivity in the presence of TiO ₂ and metal-decorated TiO ₂ photocatalysts under the irradiated UV light in the presence of O ₂ as electron acceptor..... | 133 |
| 5.3 Properties of Au/TiO ₂ photocatalysts with different Au contents..... | 142 |
| 5.4 Properties of bimetallic Au ₃ M ₃ /TiO ₂ photocatalysts..... | 154 |
| 6.1 Plasma operating parameters for the synthesis of black TiO ₂ NPs in HNO ₃ solution medium..... | 175 |
| 6.2 Structural information of the as-synthesized black TiO ₂ NPs prepared under different discharge plasma operating parameters..... | 178 |
| 6.3 Structural information of the as-synthesized black TiO ₂ NPs prepared with solution plasma in 3.0 mM HNO ₃ at different plasma discharge times..... | 197 |



LIST OF FIGURES

| Figure | Page |
|---|------|
| 2.1 Biofuels consumption in the U.S. transportation sector..... | 7 |
| 2.2 Transesterification of triglycerides with alcohol | 7 |
| 2.3 Distribution of glycerol usage by market volume | 10 |
| 2.4 Market price of general glycerol oxidation products..... | 15 |
| 2.5 Main fields of applications for photocatalysis | 16 |
| 2.6 Schematic illustration of photocatalytic process on a semiconductor following electronic excitation..... | 20 |
| 2.7 Band gaps at (a) n-type semiconductor and (b) p-type semiconductor | 22 |
| 2.8 Band gap energies of various semiconductor photocatalysts with respect to the redox potentials of different chemical species at pH 7..... | 23 |
| 2.9 Crystal structures of TiO ₂ | 25 |
| 2.10 Schematic diagram showing the potentials for various redox processes occurring on the TiO ₂ surface at pH 7 | 26 |
| 2.11 Band structure of TiO ₂ (a) before contact (b) after contact with metal, where the Schottky barrier is designed. (Φ_m and E_f^{int} denoted the metal work function and fermi level if TiO ₂ is an intrinsic semiconductor respectively)..... | 29 |
| 2.12 Metal doped on semiconductor photocatalyst | 30 |
| 2.13 Schematic of the establishment of (a) oxygen vacancy (b) titanium vacancy and (c) titanium interstitial..... | 35 |
| 2.14 Effect of oxygen activity on the band gap of pure TiO ₂ | 36 |
| 2.15 A proposed band structure model for TiO ₂ with oxygen vacancies | 37 |

| Figure | Page |
|--|------|
| 2.16 Three categories of plasma phase corresponding to the relationship between pressure and temperature..... | 42 |
| 2.17 Schematic of plasma generation model in liquid: (a) direct discharge between two electrodes using AC (pulse) power supply; (b) contact discharge between an electrode and the surface of surrounding electrolyte using a DC power supply; (c) radio frequency (RF) and microwave (MW) generation for plasma discharge; (d) laser ablation technique assisted plasma generation..... | 45 |
| 2.18 Schematic of the experimental setup for solution plasma experiments and synthesis flow for nanocarbon production | 46 |
| 2.19 Schematic of the pulsed plasma discharge in a liquid method | 47 |
| 2.20 Reactive oxygen species generated in the photocatalytic reduction and oxidation steps of oxygen and water | 49 |
| 2.21 pH dependence of one-electron redox of H ₂ O, H ₂ O ₂ , and O ₂ . Dotted line shows two-electron (2e ⁻) process..... | 50 |
| 2.22 Reaction pathway for O ₂ reduction on surface of TiO ₂ | 51 |
| 2.23 A proposed reaction scheme of OH [•] formation on TiO ₂ surface | 52 |
| 2.24 The pathway and spin states of singlet molecular oxygen formation | 54 |
| 3.1 Preparation procedure of monometallic-decorated TiO ₂ photocatalyst..... | 65 |
| 3.2 Preparation procedure of Au-based bimetallic-decorated TiO ₂ photocatalyst..... | 67 |
| 3.3 Schematic diagram of the experimental set up of solution plasma process..... | 68 |
| 3.4 Light distribution spectra of 120 W UV high pressure mercury lamp | 70 |
| 3.5 Schematic diagram of photoreactor with external light source..... | 70 |

| Figure | Page |
|--|------|
| 4.1 (a) N ₂ adsorption-desorption isotherms and (b) pore size distribution of the utilized commercial anatase TiO ₂ powder..... | 80 |
| 4.2 (a) UV-Vis spectra and (b) the dependent of ($\alpha h\nu^{1/2}$) on photon energy of the utilized commercial anatase TiO ₂ powder..... | 81 |
| 4.3 Representative high resolution XPS spectra of (a) Ti2p and (b) O1s of utilized commercial TiO ₂ powder..... | 82 |
| 4.4 Catalytic- and photocatalytic conversions of 0.3 M glycerol and selectivity towards the known products at particular times of experiment of (a) batch no. 5, (b) batch no. 6 and (c) batch no. 7 of Table 4.2..... | 85 |
| 4.5 Half-normal probability plot of glycerol conversion..... | 90 |
| 4.6 Plot of (a) predicted value and residual, and (b) Pareto analysis of glycerol conversion..... | 93 |
| 4.7 Plot of (a) predicted value and residual, and (b) Pareto analysis of DHA selectivity..... | 95 |
| 4.8 Plot of (a) predicted value and residual, and (b) Pareto analysis of GCD selectivity..... | 97 |
| 4.9 Plot of (a) predicted value and residual, and (b) Pareto analysis of GCA selectivity..... | 100 |
| 4.10 Plot of (a) predicted value and residual, and (b) Pareto analysis of GCOA selectivity..... | 102 |
| 4.11 Variation of glycerol conversion and selected product yields at different experimental conditions of (a) UV light/TiO ₂ , (b) UV light/TiO ₂ /H ₂ O ₂ (0.3 M) and (c) UV light/TiO ₂ /O ₂ | 104 |
| 4.12 Variation of (a) pCBA and (b) FFA as a function of time in irradiated-UV light and TiO ₂ system in the presence of H ₂ O ₂ and O ₂ as electron acceptors..... | 106 |

| Figure | Page |
|--------|--|
| 4.13 | Variation of pCBA and FFA as a function of time in the presence of H ₂ O ₂ at different concentrations 108 |
| 4.14 | Variation of glycerol conversion and selected product yields at different experimental conditions of (a) UV light/TiO ₂ /0.075 M H ₂ O ₂ and (b) UV light/TiO ₂ /0.3 M H ₂ O ₂ 110 |
| 5.1 | Representative XRD patterns of the TiO ₂ and metal-decorated TiO ₂ photocatalysts 119 |
| 5.2 | (Left) Representative TEM images of the TiO ₂ and metal-decorated TiO ₂ photocatalysts with (Right) respective decorated-metal particle size distribution. 122 |
| 5.3 | Representative of SEM-EDX of the metal-decorated TiO ₂ photocatalyst..... 123 |
| 5.4 | Representative XPS spectra of (a) TiO ₂ , (b) Bi ₃ /TiO ₂ , (c) Pd ₃ /TiO ₂ , (d) Pt ₃ /TiO ₂ and (e) Au ₃ /TiO ₂ 126 |
| 5.5 | Valence band spectra of TiO ₂ and metal-decorated TiO ₂ photocatalysts 128 |
| 5.6 | Representative (a) UV-visible spectra and the depended of $(\alpha h\nu)^{1/2}$ on photon energy of TiO ₂ and metal-decorated TiO ₂ photocatalysts..... 129 |
| 5.7 | Variation of glycerol as a function of time in the presence of TiO ₂ and metal-decorated TiO ₂ under the irradiated UV light in the presence of O ₂ as electron acceptor, a light intensity of 4.68 mW/cm ² , photocatalyst loading of 3 g/L 131 |
| 5.8 | Variation of (a) pCBA and (b) FFA as a function of time in the irradiated UV light in the presence of different metal-decorated TiO ₂ photocatalysts using O ₂ as electron acceptors 132 |

| Figure | Page |
|--|------|
| 5.9 Yield of selected products obtained from glycerol photocatalytic conversion via TiO_2 and metal-decorated TiO_2 at loading of 3.0 g/L with an average light intensity of 4.7 mW/cm^2 and using O_2 as the electron acceptor | 134 |
| 5.10 Mechanism of the charge transfer in (a) TiO_2 , (b) Bi_3/TiO_2 , (c) Pd_3/TiO_2 | 138 |
| 5.11 Representative XRD of monometallic Au_x/TiO_2 photocatalyst with different Au contents | 141 |
| 5.12 Representative SEM-EDX images of Au_x/TiO_2 photocatalyst with different Au contents | 143 |
| 5.13 (Left) Representative TEM images of Au_x/TiO_2 photocatalyst with different Au contents and (Right) Au particle size distribution on the surface of TiO_2 | 144 |
| 5.14 Representative HR-XPS spectra of Ti2p of Au_x/TiO_2 photocatalyst with different Au contents | 145 |
| 5.15 Representative HR-XPS spectra of Au4f of Au_x/TiO_2 photocatalyst with different Au contents | 146 |
| 5.16 Representative UV-Vis spectra of Au_x/TiO_2 photocatalyst with different Au contents | 148 |
| 5.17 Representative (a) glycerol conversion and (b) plot of $\ln(C_t/C_0)$ as a function of time in the presence of Au_x/TiO_2 ($x = 1$ to 7) at photocatalyst loading of 3.0 g/L, light intensity of 4.7 mW/cm^2 and using O_2 as the electron acceptor | 150 |
| 5.18 Yield of selected products obtained from glycerol photocatalytic conversion via Au_x/TiO_2 photocatalysts at loading of 3.0 g/L, light intensity of 4.7 mW/cm^2 and using O_2 as the electron acceptor..... | 151 |

| Figure | Page |
|--|------|
| 5.19 Representative XRD of Au ₃ M ₃ /TiO ₂ photocatalysts compare with Au ₃ /TiO ₂ photocatalyst..... | 154 |
| 5.20 Representative SEM-EDX analysis of Au ₃ M ₃ /TiO ₂ photocatalysts | 155 |
| 5.21 (Left) Representative TEM images of Au ₃ M ₃ /TiO ₂ photocatalysts and (Right) respective decorated-metal particle size distribution..... | 157 |
| 5.22 Representative TEM-EDX mapping images and line-scan profile of Au ₃ M ₃ /TiO ₂ photocatalysts..... | 158 |
| 5.23 Representative HR-XPS spectra of Ti2p of Au ₃ M ₃ /TiO ₂ photocatalysts | 159 |
| 5.24 Representative HR-XPS spectra of Au4f of Au ₃ M ₃ /TiO ₂ photocatalysts..... | 160 |
| 5.25 Representative HR-XPS spectra of Bi 4f, Pt 4f and Pd 3d in Au ₃ M ₃ /TiO ₂ photocatalysts | 162 |
| 5.26 Representative UV-Vis spectra of Au ₃ M ₃ /TiO ₂ photocatalysts..... | 163 |
| 5.27 Representative (a) glycerol conversion and (b) plot of ln (C _t /C ₀) as a function of time in the presence of Au ₃ M ₃ /TiO ₂ compared with Au ₃ /TiO ₂ at photocatalyst loading of 3.0 g/L, light intensity of 4.7 mW/cm ² and using O ₂ as the electron acceptor..... | 165 |
| 5.28 Schematic profiles of contact metal (a) AuBi, (b) AuPt and (c) AuPd with corresponding work-function in bimetallic NPs system..... | 166 |
| 5.29 Yield of selected products obtained from glycerol photocatalytic conversion via Au ₃ M ₃ /TiO ₂ at photocatalyst loading of 3.0 g/L, light intensity of 4.7 mW/cm ² and using O ₂ as the electron acceptor | 169 |
| 6.1 Model of the plasma generation..... | 172 |
| 6.2 Representative OES of plasma discharge through a Ti electrode in HNO ₃ solution..... | 173 |

| Figure | Page |
|--|------|
| 6.3 Representative XRD patterns of the as-synthesized black TiO ₂ NPs formed from discharge plasma conditions of (a) 20 kHz and 0.5 μs, (b) 50 kHz and 0.5 μs, (c) 80 kHz and 0.5 μs, (d) 20 kHz and 1.0 μs and (e) 20 kHz and 2.0 μs in (I) 0.3 mM or (II) 3.0 mM HNO ₃ as the discharge medium electrolyte solution..... | 177 |
| 6.4 Representative (a) SEM, (b) TEM and (c) high-resolution TEM images of the as-synthesized black TiO ₂ NPs formed with a 20 kHz, 2.0 μs discharge plasma in 3.0 mM HNO ₃ | 180 |
| 6.5 Representative EPR spectra of the as-synthesized black TiO ₂ NPs formed from different discharge plasma conditions in (a) 0.3 mM and (b) 3.0 mM HNO ₃ | 182 |
| 6.6 Representative XPS survey spectra of the as-synthesized black TiO ₂ NPs formed in (a) 0.3 mM and (b) 3.0 mM HNO ₃ under different discharge plasma conditions..... | 184 |
| 6.7 Representative deconvoluted peak area of high resolution Ti 2p XPS spectra of the reference TiO ₂ and the as-synthesized black TiO ₂ NPs formed in (a) 0.3 mM or (b) 3.0 mM HNO ₃ under different discharge plasma conditions..... | 186 |
| 6.8 Representative deconvoluted peak area O1s XPS spectra of the reference TiO ₂ and the as-synthesized black TiO ₂ NPs formed in (a) 0.3 mM or (b) 3.0 mM HNO ₃ under different discharge plasma conditions..... | 187 |
| 6.9 Representative FTIR spectra of the as-synthesized black TiO ₂ NPs formed in (a) 0.3 mM or (b) 3.0 mM HNO ₃ under different discharge plasma conditions..... | 189 |
| 6.10 Representative UV-Vis spectra and Tauc's plot (inset) of the as-synthesized black TiO ₂ NPs formed in (a) 0.3 mM and (b) 3.0 mM HNO ₃ under different discharge plasma conditions..... | 191 |

| Figure | Page |
|--|------|
| 6.11 Alternation of the band gap energy of the as-prepared black TiO ₂ NPs via (a) the Ti ³⁺ /Ti ⁴⁺ and (b) Ti-OH/TiO ratios | 193 |
| 6.12 Representative XRD patterns of the as-synthesized black TiO ₂ NPs through the solution plasma process at frequency of 20 kHz and pulse width of 2.0 μs at different plasma discharge times..... | 195 |
| 6.13 Representative TEM images of the as-synthesized black TiO ₂ NPs through the solution plasma process at the frequency of 20 kHz and the pulse width of 2.0 μs at different plasma discharge times | 196 |
| 6.14 Particle size distribution from DLS technique of the as-synthesized black TiO ₂ NPs through the solution plasma process at the frequency of 20 kHz and the pulse width of 2.0 μs at different plasma discharge times. | 197 |
| 6.15 Representative deconvoluted peak area Ti2p XPS spectra of the as-synthesized black TiO ₂ NPs through the solution plasma process at the frequency of 20 kHz and the pulse width of 2.0 μs at different plasma discharge times..... | 199 |
| 6.16 Representative UV-Vis spectra of the as-synthesized black TiO ₂ NPs through the solution plasma process at the frequency of 20 kHz and the pulse width of 2.0 μs at different plasma discharge times..... | 200 |
| 6.17 Representative valence band spectra of the as-synthesized black TiO ₂ NPs through the solution plasma process at the frequency of 20 kHz and the pulse width of 2.0 μs at different plasma discharge times..... | 201 |
| 6.18 Schematic diagram of DOS of the as-synthesized black TiO ₂ NPs through the solution plasma process at the frequency of 20 kHz and the pulse width of 2.0 μs at different plasma discharge times | 202 |

| Figure | Page |
|---|------|
| 6.19 Variation of glycerol conversion as a function of time via as-synthesized black TiO ₂ NPs under the irradiated UV light at catalyst loading of 3.0 g/L with an average light intensity of 4.7 mW/cm ² and using O ₂ as the electron acceptor | 204 |
| 6.20 Yield of selected products obtained from glycerol photocatalytic conversion via as-synthesized black TiO ₂ NPs at catalyst loading of 3.0 g/L with an average light intensity of 4.7 mW/cm ² and using O ₂ as the electron acceptor | 205 |
| 6.21 Variation conversion levels of (a) GCD and (b) DHA and selected product yield obtained with the black TiO ₂ photocatalyst at 3.0 g/L, a light intensity of 4.7 mW/cm ² using O ₂ as the electron acceptor. | 208 |
| 6.22 Representative conversion levels of (a) glycerol, (b) GCD and (c) DHA in the presence of various scavenger species (10 mM) with the black TiO ₂ photocatalyst at 3.0 g/L, light intensity of 4.7 mW/cm ² , and using O ₂ as the electron acceptor | 210 |
| 6.23 Yield of selected products obtained from glycerol photocatalytic conversion in the presence of various scavengers via black TiO ₂ NPs at loading of 3.0 g/L with light intensity of 4.7 mW/cm ² and using O ₂ as the electron acceptor | 214 |
| 6.24 Yield of selected products obtained from GCD photocatalytic conversion in the presence of various scavengers via black TiO ₂ NPs at loading of 3.0 g/L with light intensity of 4.7 mW/cm ² and using O ₂ as the electron acceptor | 215 |
| 6.25 Yield of selected products obtained from DHA photocatalytic conversion in the presence of various scavengers via black TiO ₂ NPs at loading of 3.0 g/L with light intensity of 4.7 mW/cm ² and using O ₂ as the electron acceptor | 216 |

CHAPTER I

INTRODUCTION

1.1 Rationales and theories

Glycerol (1,2,3-propanetriol) is an important by-product of transesterification process. In this process, production of 1000 kg of biodiesel usually generates about 100 kg of crude glycerol, or 10% production. Due to the enormous growth of the biodiesel industry during the recent years, the glycerol market is experiencing a surplus, which makes aqueous glycerol as an attractive compound for synthesizing other value-added chemical substances [1] because the three-hydroxyl groups of glycerol molecule are susceptible to many reactions ranging from biological to chemical catalytic routes such as fermentation, dehydration, hydrogenation, oxidation, polymerization and oligomerization. Among the variety of effective catalytic routes, the oxidation of glycerol plays a special attention due to the practical valuable compounds that are formed. Glyceraldehyde (GCD), dihydroxyacetone (DHA), glycolic acid (GCOA), glyceric acid (GCA), and hydroxypyruvic acid (HPA), which are commonly oxidative products of glycerol, are of commercial value. However, several glycerol oxidative products are formed simultaneously, due to the reactivity of primary and secondary hydroxyl groups. In order to control the selectivity, a careful design of the catalyst is required. Chemoselective catalytic oxidation of glycerol over metallic catalysts such as platinum, silver, palladium and gold has been shown to be a good technique for obtaining selective oxidation products from glycerol [2-4].

Nevertheless, glycerol oxidation process at a commercial scale still faced the major hindrance because its requirement for an alkaline condition, high operating temperature and pressure and the deactivation of the utilized catalyst. Thus, it is

important and in urgent need to find new green processes to address the increasing demands of sustainable and clean energy technologies.

In the last two decades, photocatalytic technology has been regarded as one of the most attractive processes due to its superior features, such as being environmentally benign, economical cost, high efficiency and the room temperature and atmospheric pressure operation. Thus, many researches have focused on this process, with versatile applications ranging from the field of wastewater and air remediation [8,9], carbon dioxide (CO₂) reduction [10], clean hydrogen (H₂) production [11] and the synthesis of high value organic compounds [12], towards developing an efficient solar-to-energy conversion [13].

Currently, the semiconductor metal oxides are usually used in photocatalytic reaction including TiO₂, ZnO, Al₂O₃, SiO₂, ZrO₂, CeO₂, SnO₂, Fe₂O₃, SrTiO₃ and BaTiO₃, but specie that is effective and widely used is titanium dioxide (TiO₂) because of its high photocatalytic activity, stability, and suitable band-gap energy [5]. Actually, TiO₂ has four crystalline phases: anatase, rutile, brookite and titania B [6]. Anatase phase is generally more chemically and optically active compared with other phases. Crystalline structures of TiO₂ can be controlled by heat treatment and sometimes by addition of dopants [7]. There are always structural defects on the surface and inside the TiO₂ particles [8]. These defects are related with the amount of the photoexcited electrons. Surface defects are advantageous for high photoactivity because they are used as active sites on which the electron donors or acceptors are adsorbed. In contrary, the bulk defects exhibited lower the photoactivity because they provide sites for the recombination of the photogenerated electrons. According to the electron spin resonance (EPR) spectroscopic study, the photoexcited electrons are trapped at the Ti³⁺ sites on the surface or Ti⁴⁺ sites within the bulk and the holes are trapped at lattice oxygen ions [9, 10]. Therefore, the bulk defects should be reduced to yield high

photoactivity. The reduction of bulk defects can be achieved by high temperature calcination, however the anatase phase is metastable and transforms to rutile phase when the temperature is over about 500 °C. Moreover, the surface area is reduced dramatically during the high temperature calcinations.

Thus, the photocatalytic processes including the modification of TiO₂ photocatalyst for selective oxidation is seeming to be interested. Up to now, only titanium dioxide (TiO₂) and sodium decatungstate (Na₄W₁₀O₃₂) have been studied in photocatalytic oxidation of glycerol. An interested issue is the need to control the oxidation power of photoexcited semiconductor, which induces to get the desired product and the design of high performance photocatalyst. Therefore, this research aims to synthesize the highly efficient TiO₂-based photocatalysts and study the transformation of glycerol to high value chemical substances through the environmental friendly photocatalytic process.

1.2 Objectives of dissertation

1. To investigate the effect of reaction parameters on photocatalytic conversion of glycerol to value-added compounds by using TiO₂-based photocatalyst
2. To study the role and mechanism of TiO₂-based photocatalyst on photocatalytic conversion of glycerol to value-added compounds

1.3 Research methodology and Experimental procedures

1. Literature review for involved publications from both national and international journals
2. Prepare all tools, equipment and chemical reagents required for the experiment

3. Study the effect of reaction parameters on glycerol conversion and product selectivities by using commercial TiO_2 . The investigated reaction parameters are
 - Catalyst dosage (1.0-3.0 g/L)
 - Oxidizing agent (H_2O_2) concentration (0.3-1.5 mol/L)
 - Light intensity (1.1-4.7 mW/cm²)
 - Irradiation time (4-8 h)
 - Type of oxidizing agent (H_2O_2 and O_2)
4. Feasibility and activity tests for glycerol conversion by using as-prepared metal-decorated TiO_2 photocatalysts
 - 4.1 Prepare monometallic-decorated TiO_2 by sol-immobilization method. The investigated parameters are
 - Types of transition metals (Au, Pt, Pd and Bi)
 - Loadings of transition metals (1-7 wt.%)
 - 4.2 Characterize the morphology and properties of as-prepared TiO_2 by SEM-EDX, TEM, XRD, UV-Vis and XPS
 - 4.3 Study glycerol conversion and product yields by using as-prepared metal-decorated TiO_2 photocatalysts
 - 4.4 Study the role of reactive oxygen species generated in glycerol photooxidation catalyzed via metal-decorated TiO_2 system by using radical scavenger technique
5. Feasibility and activity tests for glycerol conversion by using as-prepared bimetallic decorated on TiO_2 photocatalysts
 - 5.1 Prepare bimetallic-decorated TiO_2 by sol-immobilization method. The investigated parameters are
 - Types of couple transition metals (Au-Pt, Au-Pd and Au-Bi)

- 5.2 Characterize the morphology and properties of as-prepared TiO_2 by SEM-EDX, TEM-EDX, XRD, UV-Vis and XPS
- 5.3 Study glycerol conversion and product yields by using as-prepared bimetallic decorated on TiO_2 photocatalysts
6. Feasibility and activity tests for glycerol conversion by using as-prepared black TiO_2 photocatalysts
 - 6.1 Prepare black TiO_2 by solution plasma technique. The investigated parameters for discharge plasma are
 - HNO_3 solution medium concentration (0.3 and 3.0 mM)
 - Repetition frequency (20-80 kHz)
 - Pulse Width (1-2 μs)
 - Plasma discharge time (1-4 h)
 - 6.2 Characterize the generated plasma properties by Oscilloscope and OES
 - 6.3 Characterize the morphology and properties of as-prepared defective black TiO_2 by SEM-EDX, TEM, XRD, UV-Vis, FTIR, DLS, EPR and XPS
 - 6.4 Study glycerol conversion and product yields by using as-prepared defective black TiO_2 photocatalysts
 - 6.5 Study the role of reactive oxygen species generated in glycerol photooxidation catalyzed via black TiO_2 system by using radical scavenger technique
7. Write up manuscripts and dissertation

CHAPTER II

THEORY AND LITERATURE REVIEWS

This chapter provides a general overview of the current sources for production of energy, fuels and chemicals. The use of glycerol as an alternative resource concept is introduced. The potential of glycerol for the production of high value-added products using catalytic methodology is discussed with an emphasis on photo-catalytic oxidation reaction. Moreover, the several approaches for synthesis and modification of titanium dioxide are enumerated. Finally, several literature reviews related to this dissertation is provided.

2.1 Background

Alternative fuels and chemical compounds, produced from renewable biomass resources, have become a high attraction due to the increasing in environmental consciousness throughout the world. The Energy Information Administration (EIA) reveals that consumption of marketed renewable energy will grow by about 3.5 quadrillion Btu, from 9.0 quadrillion Btu in 2013 to 12.5 quadrillion Btu in 2040[11]. In many years ago, biofuels have been the high priority alternative fuel because it can be used instead of petroleum-derived diesel and much lower levels of harmful emission (eg. carbon monoxide, CO). As for biodiesel, the most commonly used biofuel, it can be used in conventional diesel engines.

The Renewable Fuel Standard (RFS) reported that biodiesel consumption in the U.S. transportation sector has been increasing rapidly every year through 2022 as shown in Figure 2.1. Currently, the RFS requires 24 billion gallons of biofuels to be used in 2017 and it has recorded an average annual growth rate of 10%, expanding from 24 billion gallons in 2015 to 36 billion gallons in 2022.

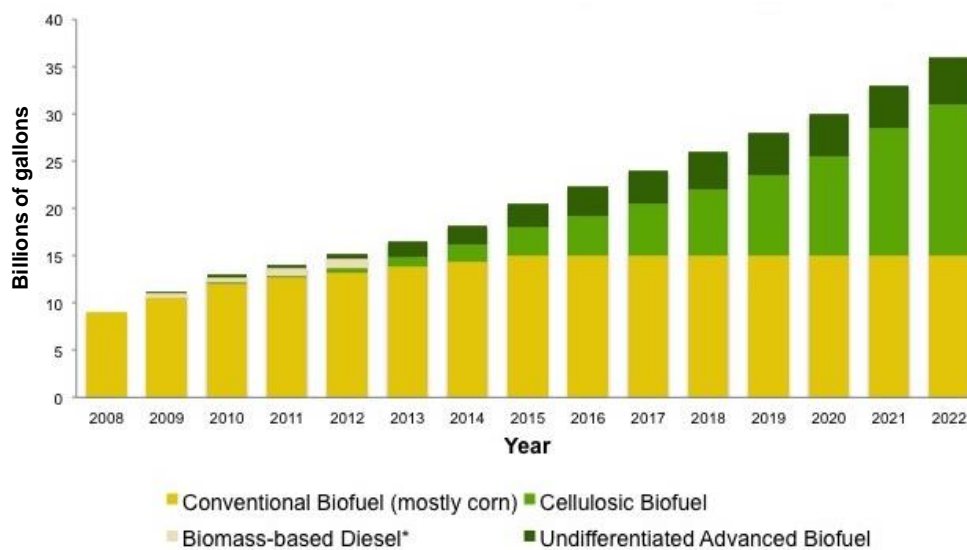


Figure 2.1 Biofuels consumption in the U.S. transportation sector [12].

Biodiesels is typically derived from the transesterification (also called alcoholysis) of triglycerides in fat or oil with methanol to form ester and glycerol (Figure 2.2) [13]. This reaction typically requires a catalyst to improve the reaction rate and yield. After transesterification of triglycerides, the products are a mixture of esters, glycerol, alcohol, catalyst and tri-, di- and monoglycerides. In this process, 1000 kg of produced biodiesel usually generates about 100 kg of crude glycerol, or 10 wt.% production as a by-product. Due to the enormous growth of the biodiesel industry during the recent years, the glycerol market is experiencing a surplus, which results in painfully low price of aqueous glycerol [14].

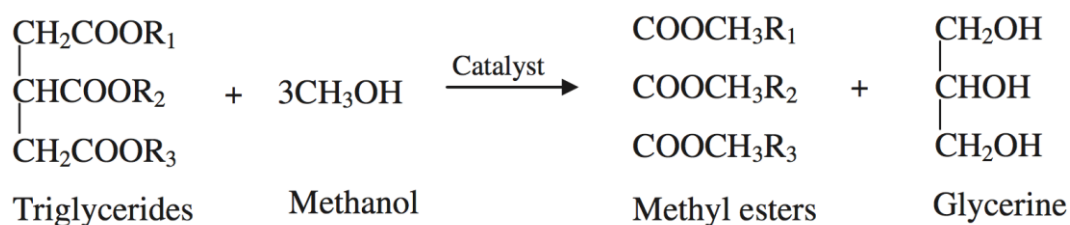


Figure 2.2 Transesterification of triglycerides with alcohol [13].

2.2 Glycerol

Glycerol ($C_3H_8O_3$), also known as glycerine, glycylic alcohol, glyceritol, 1,2,3-trihydroxypropane, and 1,2,3 propanetriol) is an organic chemical that is widely used in pharmaceutical, cosmetic, and food industries. Glycerol is odorless, colorless, viscous, and less toxic alcohol that consists of a three-carbon chain with a hydrophilic alcoholic hydroxyl group (-OH) attached to each carbon. To indicate this arrangement, the chemical formula of glycerol may be written as $HO-CH_2-CH(OH)-CH_2-OH$. Glycerol is entirely soluble in alcohols, water, and a hygroscopic substance but insoluble in hydrocarbons. It has only slight solubility in such organic solvents (e.g. ethyl acetate and diethyl ether). It is also a high-quality solvent for many chemical compounds such as phenol, bromine and iodine due to the presence of the hydroxyl group. The unique physical and chemical properties of glycerol are illustrated in Table 2.1

Glycerol is a highly flexible and reactive molecule forming both intra- and intermolecular hydrogen bonds. It possesses a large quantity of reactions owing to the existence of primary and secondary alcoholic groups that can be substituted with further chemical groups. Thus, the multi-functional structure of glycerol can be converted by several different reaction pathways such as dehydration, hydrogenation, oxidation and reforming. Utilizing the surplus of glycerol would render the biodiesel life cycle more environmentally friendly and heighten the economic viability of the biodiesel supply chain.

2.3 Sustainable use of glycerol surplus

Due to the enormous growth of the biodiesel industry during the recent years, the glycerol market is experiencing a surplus, which makes aqueous glycerol an attractive compound for using its original form as a raw material in a broad range of

Table 2.1 Physicochemical properties of glycerol at 20 °C [15].

| Properties | Values |
|---------------------------------|----------------|
| Chemical formula | $C_3H_5(OH)_3$ |
| Molecular mass (g/mol) | 92.09382 |
| Viscosity (Pa.s) | 1.5 |
| Density (g/cm ³) | 1.261 |
| Solubility in 100 parts | |
| Water or alcohol | Infinitely |
| Ether | Insoluble |
| Boiling point (°C) | 290 |
| Melting point (°C) | 18.2 |
| Flash Point (°C, closed cup) | 160 |
| Food energy (kcal/g) | 4.32 |
| Surface tension (mN/m) | 64.00 |
| Temperature coefficient (mN/mK) | -0.0598 |

industries such as drugs, medicals, pharmaceuticals, polymer, and foods as displayed in Figure 2.3. However, the glycerol from biodiesel industry contains various impurities, and is therefore not fit for such applications without the purification process. In addition, the capacity of the existing market is not adequate to utilize the large amount of glycerol currently produced, and the gap between the utilization capacity of the market and the amount of glycerol produced will multiply in the near future if no new applications are found. Besides, the price of glycerol from biodiesel process has been rapidly declined until the present.

Alternatively, glycerol also attracted for converting to other value-added chemical products. The valorization of glycerol for value-added chemicals is became

one manner of relieving the glycerol oversupply in recent decade. Some significant products from glycerol are including liquid fuels (e.g. methanol, ethanol), synthetic gas (e.g. H_2 , CO) and commodity chemicals (e.g. propylene glycol, dihydroxyacetone). The production of hydrogen or syngas is one promising use of glycerol. Converting glycerol to hydrogen is considered a renewable alternative because hydrogen is widely used to power fuel cell systems. Because of hydrogen deficiency, an integrated process in which hydrogen can be supplied from glycerol is considered the only economically viable approach to operate a biorefinery.

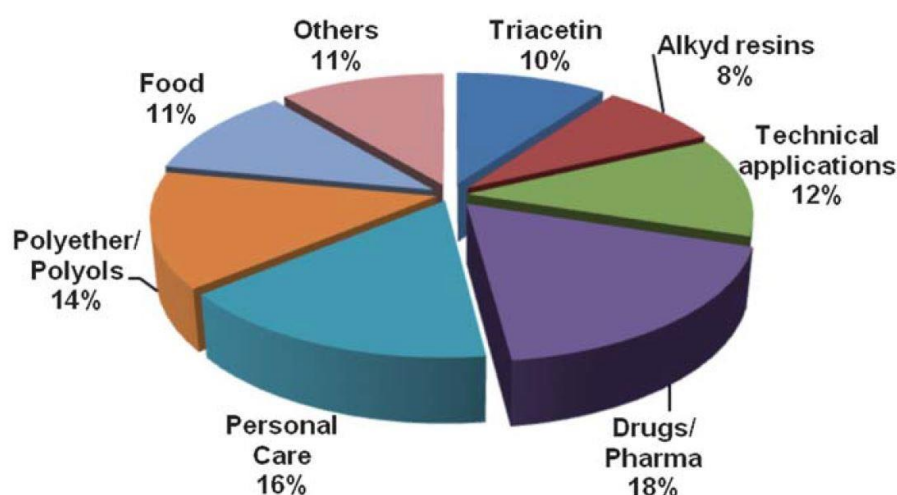


Figure 2.3 Distribution of glycerol usage by market volume [16].

When glycerol is gasified at high temperature, the syngas including H_2 and CO will be obtained. This gas is a vital building block for the petrochemical industry, and is used to prepare various chemicals (e.g. methanol, ethanol). The syngas with hydrogen and carbon monoxide molar ratio of 2:1 is a suitable feedstock for Fischer-Tropsch synthesis to produce green diesel (long chain hydrocarbons) with high cetane number [17, 18]. Alternatively, gases that are produced from thermal cracking of glycerol would have medium heating value and can be used as a fuel gas to produce electricity.

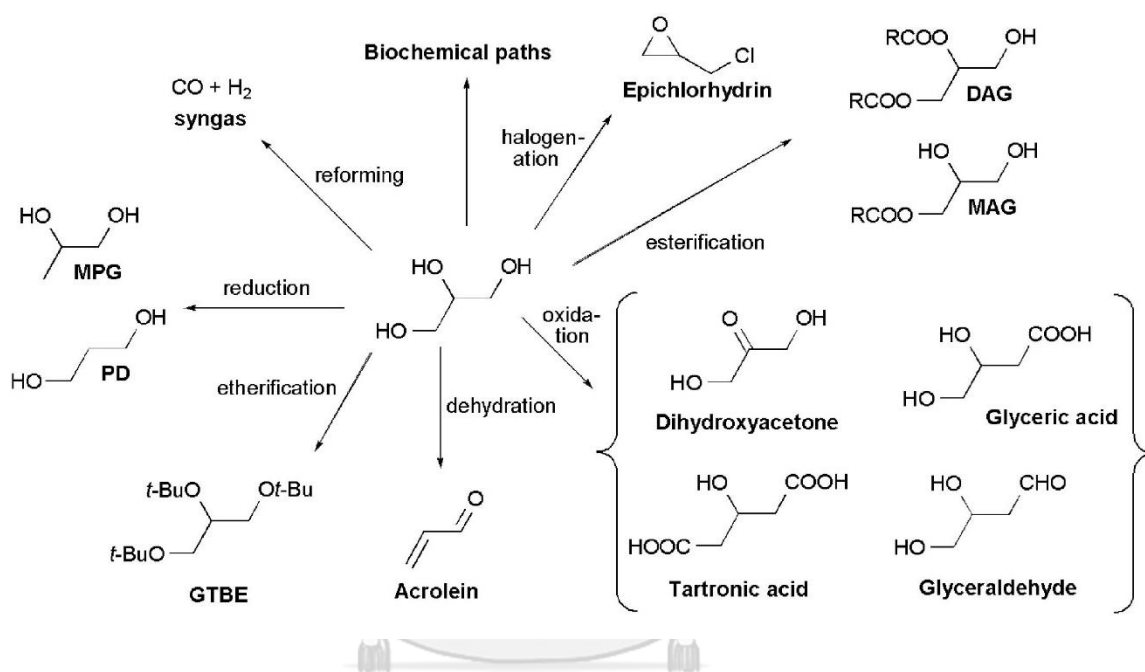
Table 2.2 List of value-added compounds derived from glycerol.

| | Name | Molecular structure | Applications |
|-----------|---------------------------|---------------------|---|
| Oxidation | Glyceraldehyde (GCD) | | - Precursor of cosmetics |
| | Dihydroxyacetone (DHA) | | - Artificial tanning agent - Feedstock for the synthesis of fine chemicals |
| | Glycolic acid (GCOA) | | - Dyeing agent in textile industry - Skin care agent |
| | Glyceric acid (GCA) | | - Base material for functional surfactant - Monomer for oligoesters or polymer |
| | Oxalic acid | | - Cleaning or bleaching agent - Stain and rust remover - Grinding agent |
| | Tartronic acid | | - Raw materials in pharmacy - Additive in candy, drink, wine - Antiseptic |
| Reduction | 1,2 Propanediol | | - Functional fluids (antifreeze, deicing, cosmetics, liquid detergent etc.) |
| | 1,3 Propanediol | | - Copolymer to produce polyester (textile fibers exhibiting chemical resistance) |
| | Ethylene glycol | | - Coolant and heat-transfer agent - Antifreeze - Precursor to polymer |

Moreover, glycerol is recognized as a top-twelve building block that can be converted to numerous chemicals like aldehydes, acids, or alcohol. Selective oxidation and reduction are major routes for glycerol valorization. As listed in Table 2.2, glycerol can be oxidized to DHA, which is used in cosmetic industries as well as in pharmacy and medicine, or glyceraldehyde, which is a precursor of cosmetics. Besides, it also can be reduced to compounds like diols, which are used in cosmetics, detergent, or in the manufacture of textile fiber.

Due to glycerol contained the large number of functional groups, namely two primary and one secondary hydroxyl groups, a variety of reaction configurations can be employed by various catalytic solutions in order to convert glycerol into numerous value-added products (Scheme 1). There have been numerous reports about the feasibility of converting glycerol into chemical and gases. For instance, some reaction pathways were proceed through dehydration via protonation of the secondary group of glycerol and transform to acrolein by release of hydronium ion and water molecule [19]. Glycerol can be catalytically reduced to ethylene glycol or propanediols in the presence of hydrogen at specified temperature and suitable catalysts [20]. Etherification of glycerol with isobutene to produce glycerol tertiary butyl ether (GTBE) is most attractive, serving as antiknock additive for petrol [21]. Esterification of glycerol with carboxylic acid leads to mono-acyl and di-acyl glycerol (MAG/DAG) which can be used as emulsifiers in food, detergents and cosmetic industries [22]. Polyglycerols has been known as non-ionic surfactants in food products, was typically synthesized in the presence of an acid or base catalyst through oligomerization of glycerol [23]. The halogenation reaction of glycerol with gaseous HCl leads to dichloropropane mixtures which upon treated with NaOH to yield epichlorohydrin (ECH). ECH is an important precursor for epoxy resins which can be applied in paints and construction materials [24]. Steam reforming of glycerol in the presence of catalyst leads to syngas that can

be converted to hydrogen or used for the synthesis of methanol [25]. The dehydration of glycerol can yield acrolein as a major product, which is an important intermediate for the agro- and chemical industries. Due to its toxicity, acrolein is usually directly converted to the desired high value-added derivatives such as acrylic acid or sodium polyacrylate [26].

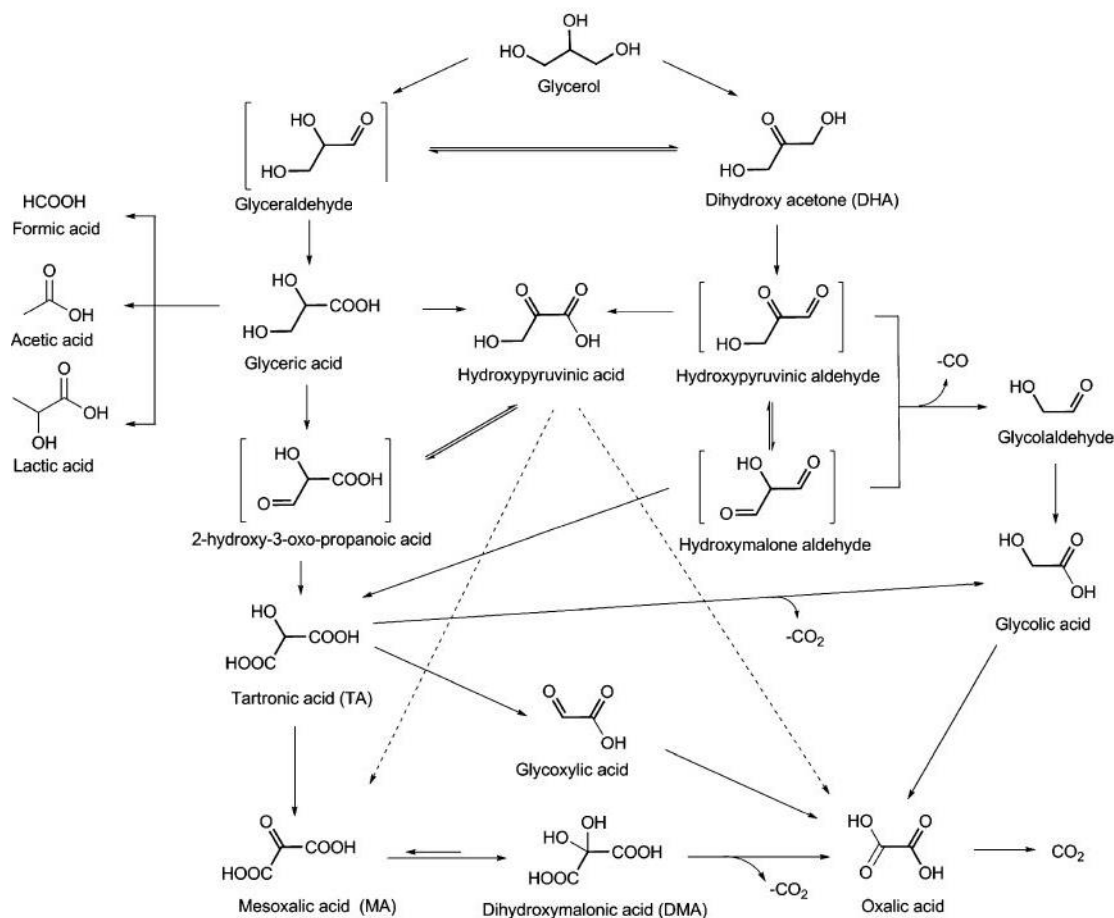


Scheme 1. Some possible valorization reactions from glycerol [26].

2.4 Oxidation of glycerol

One of the most attention routes for glycerol transformation to value added compounds lies in its catalytic oxidation reaction. Glycerol oxidations are currently received significantly attention because glycerol's structure lends itself well to catalytic oxidative process using inexpensive oxidizing agents such as hydrogen peroxide, oxygen, air, or bleach. A combination of these inexpensive oxidizing agents with an surplus of glycerol will allow the production of various new derivatives. Due to the multitude of possible pathways for glycerol oxidation, multiple products that

can be obtained from glycerol oxidation are GCD, DHA, GCA, HPA, tartronic acid (TART) and mesoxalic (MOXA) like C_3 oxygenates in association with C_2 oxygenates such as glycolic acid (GCOA), oxalic acid (OXAL) and C_1 products like formic acid (FMA) as displayed in Scheme 2.



Scheme 2. Possible intermediates and products obtained from the oxidation of glycerol [27].

To gain insight into the market potential, the price ranks of selected glycerol oxidation derivatives catalogue are provided in Figure 2.4. Apparently, there is an economic stimulus to model process to produce these value-added products by

starting from glycerol. However, the market for glycerol oxidation products are not yet commercially developed due to the current catalytic processes provided too slightly small yields and selectivities. Therefore, there is significantly driven to develop new catalytic process that involves with environmental benign and promoting high yield and selectivity for glycerol transformation.

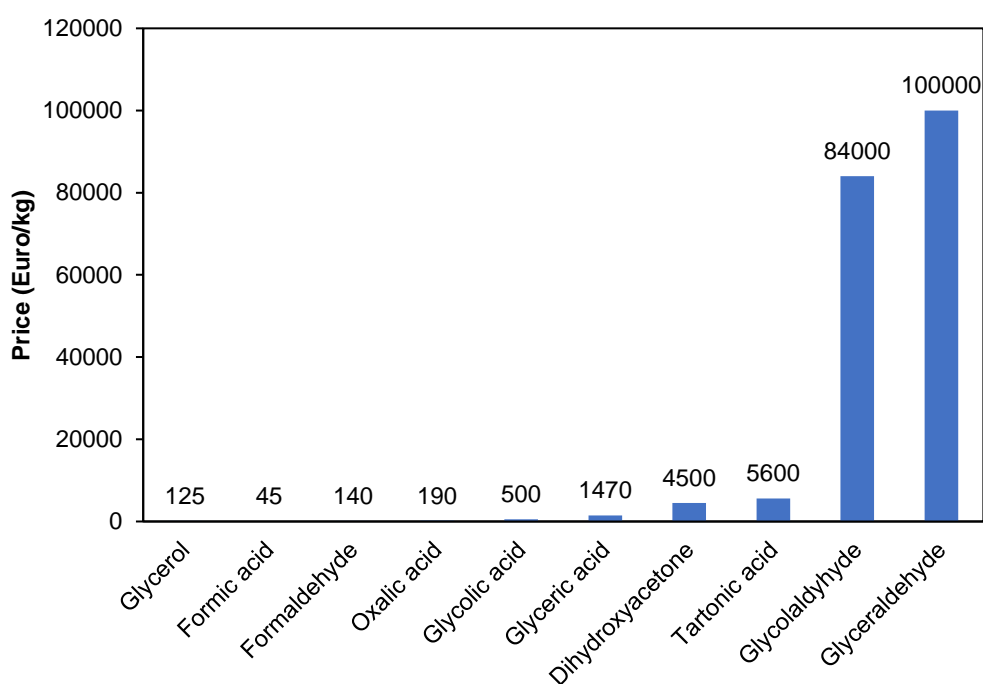


Figure 2.4 Market price of general glycerol oxidation products.

The major challenges associated with the selective oxidation of glycerol are (i) the control of reaction pathway approached to a desired product, (ii) high catalytic activity and resistance to poisoning, and (iii) maximizing the yield of desired products. To address these challenges, the most common catalysts used for the oxidation of glycerol are based on supported metal nanoparticles. To date, a prosperity of modified catalysts for glycerol oxidations have been studied. Well known modified

catalysts are altered with various transition metal such as Au, Pt, Pd and Bi. In fact, the nature of the metal, as well as the pH, widely controls the selectivity for converting either type of alcohol. An overview of Pt, Pd and Au based catalyst is given in Table 2.3. Typically, the reactions are carried out between 303-398 K, with air and oxygen as the oxidant (1-10 bar) and in either acidic or basic conditions

2.5 Photocatalytic process

Photocatalytic process has received much attention during the last three decades for various promising environmental applications ranging from production of hydrogen and high valuable substances to disinfection of water as shown in Figure 2.5.

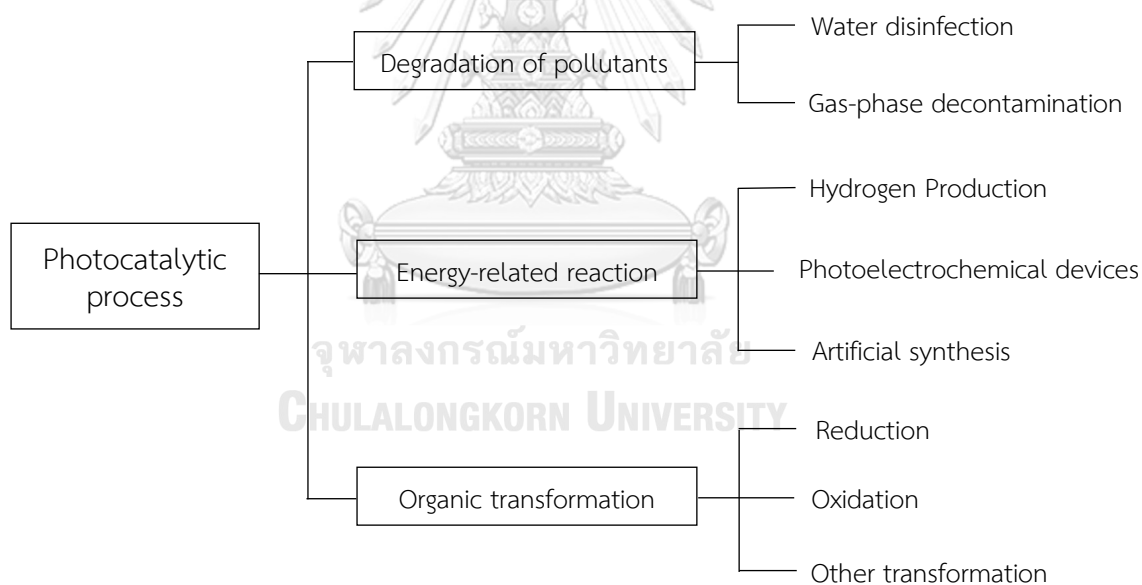


Figure 2.5 Main fields of applications for photocatalysis [28].

Table 2.3 Overview of glycerol conversion over Pt,Pd and Au metal based catalysts in water solute via oxidation reactions [3, 13, 15, 24].

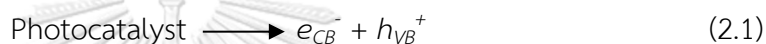
| No | Catalyst | Oxidant | Reaction conditions | Glycerol conversion (%) | Selectivity (%) |
|----|---------------------------|--------------------------|--------------------------------------|-------------------------|-------------------------|
| 1 | 0.5% Au/C | O ₂ (9.8 bar) | 333 K, NaOH/GLY = 2 (mol/mol), 0.5 h | 50 | 65 (S _{GCA}) |
| 2 | 2.9% Pd/C | O ₂ (9.8 bar) | 333 K, NaOH/GLY = 2 (mol/mol), 5 h | 30 | 82 (S _{GCA}) |
| 3 | 0.8% Au/C | O ₂ (11 bar) | 333 K, NaOH/GLY = 2 (mol/mol), 0.5 h | 6.8 | 67 (S _{GCA}) |
| 4 | 1% Au/C | O ₂ (1 bar) | 333 K, pH=12, 2 h | 50 | 44 (S _{GCA}) |
| 5 | 1.8% Au/TiO ₂ | O ₂ (11 bar) | 333 K, NaOH/GLY = 2 (mol/mol), 0.5 h | 33 | 64 (S _{GCA}) |
| 6 | 1% Au/C | O ₂ (10 bar) | 333 K, NaOH/GLY = 2 (mol/mol), 3 h | 90 | 60 (S _{GCA}) |
| 7 | 1.47% Au/TiO ₂ | O ₂ (10 bar) | 333 K, NaOH/GLY = 2 (mol/mol), 5 h | 80 | 63 (S _{GCA}) |
| 8 | 0.75% Au/C | O ₂ (10 bar) | 333 K, NaOH/GLY = 2 (mol/mol), 3 h | 100 | N/A |
| 9 | 0.59% Au/C | O ₂ (10 bar) | 333 K, NaOH/GLY = 2 (mol/mol), 2 h | 100 | 63 (S _{GCA}) |
| 10 | 0.6% Au/C | O ₂ (8 bar) | 333 K, NaOH/GLY = 2 (mol/mol), 1 h | 35 | 64 (S _{GCA}) |
| 11 | 0.99% Au/C | O ₂ (10 bar) | 333 K, NaOH/GLY = 2 (mol/mol), 5 h | 50 | 83 (S _{GCA}) |
| 12 | 0.74% Au/MMWCNT | O ₂ (3 bar) | 333 K, NaOH/GLY = 2 (mol/mol), 4 h | 50 | 56 (S _{DHA}) |
| 13 | 1% Au/C | O ₂ (3 bar) | 323 K, NaOH/GLY = 4 (mol/mol) | 100 | 45 (S _{GCA}) |
| 14 | 1% Au/TiO ₂ | O ₂ (1 bar) | 363 K, NaOH/GLY = 4 (mol/mol) | 30 | 21 (S _{GCA}) |
| 15 | 1% Pt/TiO ₂ | O ₂ (1 bar) | 363 K, NaOH/GLY = 4 (mol/mol) | 30 | 9.5 (S _{GCA}) |
| 16 | 1% Au/C | O ₂ (3 bar) | 323 K, NaOH/GLY = 4 (mol/mol), 1 h | 73 | 68 (S _{GCA}) |
| 17 | 1.5% Au/TiO ₂ | O ₂ (3 bar) | 323 K, NaOH/GLY = 4 (mol/mol), 3 h | 90 | 60 (S _{GCA}) |
| 18 | 3% Pd/C | O ₂ (11 bar) | 333 K, NaOH/GLY = 2 (mol/mol), 0.5 h | 29 | 83 (S _{GCA}) |

Table 2.3 Overview of glycerol conversion over Pt, Pd and Au metal based catalysts in water solute via oxidation reactions [3, 13, 15, 24] (Cont.).

| No | Catalyst | Oxidant | Reaction conditions | Glycerol conversion (%) | Selectivity (%) |
|----|------------------------|----------------------------------|--------------------------------------|-------------------------|------------------------|
| 19 | 3% Pt/C | O ₂ (11 bar) | 333 K, NaOH/GLY = 2 (mol/mol), 0.5 h | 16 | 70 (S _{GCA}) |
| 20 | 3% Pt/C | O ₂ (11 bar) | 333 K, NaOH/GLY = 0 (mol/mol), 5 h | 9 | 25 (S _{GCA}) |
| 21 | 3% Pd/C | O ₂ (11 bar) | 333 K, NaOH/GLY = 0 (mol/mol), 5 h | 1.3 | 25 (S _{GCA}) |
| 22 | 0.5% Pt/CS | O ₂ (10 bar) | 343 K, NaOH/GLY = 0.8 (mol/mol), 2 h | 87.3 | 93 (S _{LA} *) |
| 23 | 1% Pd/C | O ₂ (3 bar) | 323 K, NaOH/GLY = 4 (mol/mol) | 90 | 80 (S _{GCA}) |
| 24 | 0.5% Pt/C | O ₂ (3 bar) | 333 K, NaOH/GLY = 2 (mol/mol), 3 h | 20 | 60 (S _{GCA}) |
| 25 | 0.65% Pd/C | O ₂ (3 bar) | 333 K, NaOH/GLY = 2 (mol/mol), 3 h | 95 | 64 (S _{GCA}) |
| 26 | 0.32% Au/C | O ₂ (3 bar) | 333 K, NaOH/GLY = 2 (mol/mol), 3 h | 100 | 60 (S _{GCA}) |
| 27 | 1% Pt/C | O ₂ (3 bar) | 323 K, NaOH/GLY = 4 (mol/mol), 4 h | 81.6 | 50 (S _{GCA}) |
| 28 | 5% Pt/C | O ₂ (3 bar) | 333 K, NaOH/GLY = 1 (mol/mol), 3 h | 63.1 | 75 (S _{GCA}) |
| 29 | 5% Pd/C | O ₂ (3 bar) | 333 K, NaOH/GLY = 1 (mol/mol), 3 h | 57.2 | 78 (S _{GCA}) |
| 30 | 1% Pd/TiO ₂ | O ₂ (1 bar) | 363 K, NaOH/GLY = 4 (mol/mol) | 30 | 64 (S _{GCA}) |
| 31 | 5% Pt/MWCNT | O ₂ Flow (150 mL/min) | 333 K, NaOH/GLY = 0 (mol/mol), 6 h | 70.1 | 70 (S _{GCA}) |
| 32 | 5% Pt/MWCNT | O ₂ Flow (150 mL/min) | 333 K, NaOH/GLY = 0 (mol/mol), 6 h | 48.2 | 66 (S _{GCA}) |
| 33 | 5% Pt/C | O ₂ Flow (300 mL/min) | 393 K, pH=4, 7 h | 19.2 | N/A |
| 34 | 5% Pt-Bi/C | O ₂ Flow (300 mL/min) | 393 K, pH=4 | 20 | 51 (S _{DHA}) |
| 35 | 5% Pt/C | O ₂ Flow (150 mL/min) | 333 K, NaOH/GLY = 0 (mol/mol), 6 h | 50 | 47 (S _{GCA}) |
| 38 | 3%Pt-0.6%Bi/C | O ₂ (5 bar) | 343 K, pH=7 | N/A | 48 (S _{DHA}) |

*LA is Lactic acid

The photocatalytic process can be described as the light-induced excitation of semiconductor, which has an electronic band structure, separated by a band gap between the highest occupied energy band (valence band) and the lowest empty band (conduction band). Photocatalytic reaction is a process in which highly reactive species are formed when photo-excitation takes place in the catalyst substrate. When photocatalyst exposes the light of energies equal to or greater than the band gap of material, the electron can be excited from the valence band to the conduction band, within a femtosecond timescale, and simultaneously generating the electronic vacancy or a positive hole in the valence band.



As a result, the negative electron (e_{CB}^-) and positive hole (h_{VB}^+) are created as reducing and oxidizing agents. The e_{CB}^- and h_{VB}^+ can recombine on the bulk or surface of semiconductor particle (pathway 3,4 in Figure 2.6), releasing the accompanying energy as heat, and is detrimental for the photocatalytic activity as the redox properties of semiconductor are quenched. However, if the e^- and h^+ migrate to the surface of the semiconductor without recombination, they can react with electron acceptor or donor of adsorbed species such as water, oxygen, and other organic or inorganic species. Subsequently, oxidation and reduction reaction can be initiated (pathway 1,2 in Figure 2.6). These charges transfer processes are dependent on the position of conduction and valence band edges and also the redox potential of the adsorb species [5]. These oxidation and reduction reactions are the basic mechanisms of photocatalytic reaction. A simplified mechanism for photocatalytic process on a semiconductor is illustrated in Figure 2.6.

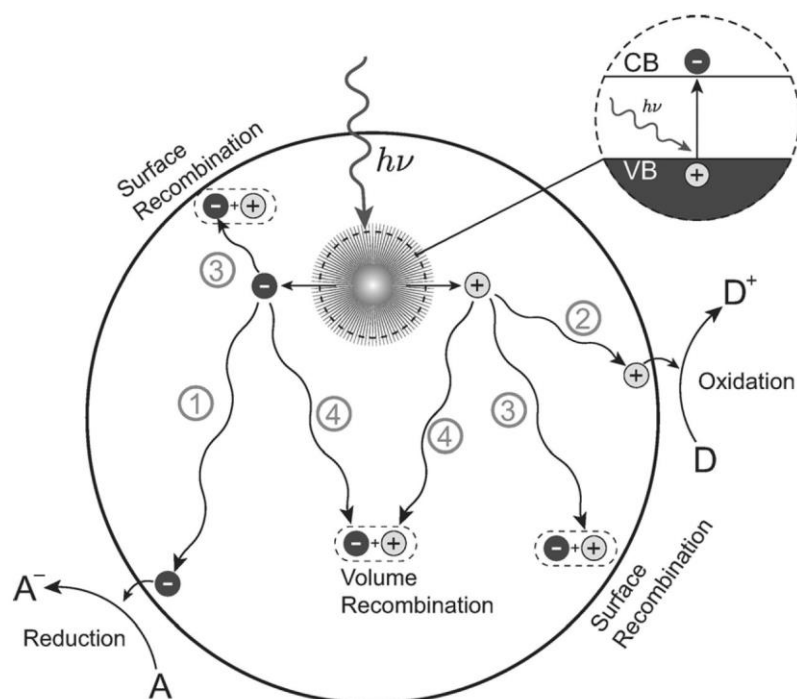


Figure 2.6 Schematic illustration of photocatalytic process on a semiconductor following electronic excitation. A=electron acceptor, D=electron donor. Pathway 1 and 2 are desired redox reaction, pathway 3 is surface recombination and pathway 4 is bulk of semiconductor recombination [29].

2.6 Semiconductor material

Semiconductors can be divided into two types; including intrinsic and extrinsic semiconductors [30]. Intrinsic semiconductors are pure material and do not contain any defects or impurities. The activation of an electron from the valence band to the conduction band gives a free electron in the conduction band and a free h^+ in the valence band. There are no energy levels present within the band gap. Consequently, activation of electrons by light can occur only when light has an energy level exceeding the band gap energy. However, mostly the energy of light in the visible range appears to be insufficient to activate electrons; the band gap is too high. Impurities (or dopant)

might introduce another band between the valence and conduction band resulting in a lower band gap for activation of electrons. With these impurities visible light might activate electrons at lower energy levels. Semiconductors with these dopants or impurities are called extrinsic semiconductors. Extrinsic semiconductors contain impurities which are brought into the lattice during preparation of the semiconductor, e.g. by decorating noble metal on the surface of semiconductor TiO_2 . Impurities provide free carriers by accepting or donating an electron. Such a process of introducing into the lattice is called doping, and those impurities that contribute donate electrons to the conduction band are called donor and those that accept electron from the valence band (or supply h^+ to the valence band) are called acceptor. Donors are impurities which have more electrons than the host material. Most electrons of the impurity located in the valence band, but the remaining electrons has no valence band to occupy. Therefore, the electrons are situated in the so-called donor band, which is higher than the valence band. Due to the attraction of the electrons by the high positive charged impurity atom, this band is situated just below the conduction band minimum (Figure 2.7(a)). Such material is called an n-type semiconductor (n corresponds with negative).

When the dopant has fewer electrons than its host material, it is called an acceptor and can trap electrons. The acceptor band (Figure 2.7(b)) is situated just above the valence band maximum and can withdraw electrons from this filled band. This will leave holes, which allow the remaining electrons to move creating mobile holes. This semiconductor is identified as a p-type semiconductor (p stands for positive).

So, doping of impurities into the lattice of a semiconductor makes it possible for electrons with less energy to jump to a higher band. This makes the semiconductor more sensitive for visible light.

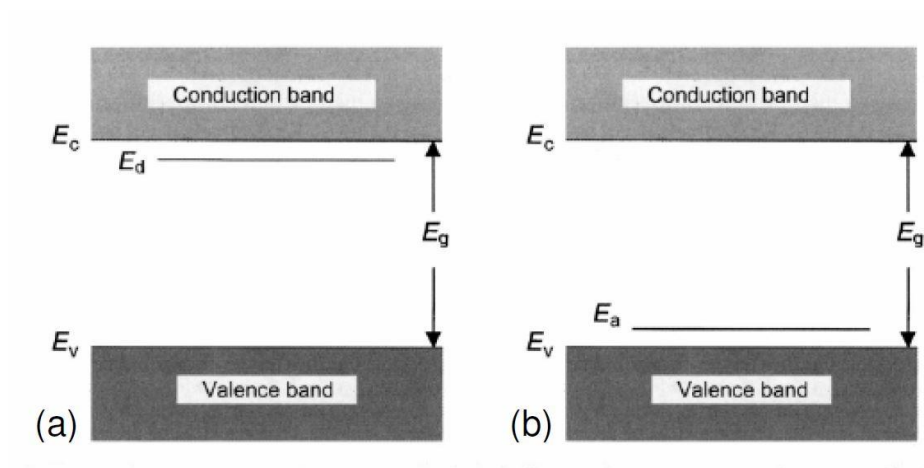


Figure 2.7 Band gaps at (a) n-type semiconductor and (b) p-type semiconductor.

Semiconductors as TiO_2 , Fe_2O_3 , ZnO , Cu_2O , WO_3 , CdS , BiWO_6 , etc., are widely used as photocatalysts. The band gaps of these semiconductor photocatalysts are displayed in Figure 2.8. Among all widely used photocatalysts, TiO_2 is the most popular photocatalyst because of its relatively high activity, chemical and biological stability, availability with low production costs, and non-toxicity. Thus, it has been widely studied and proven to have a potential to completely oxidize a variety of organic compounds, including persistent organic pollutants.

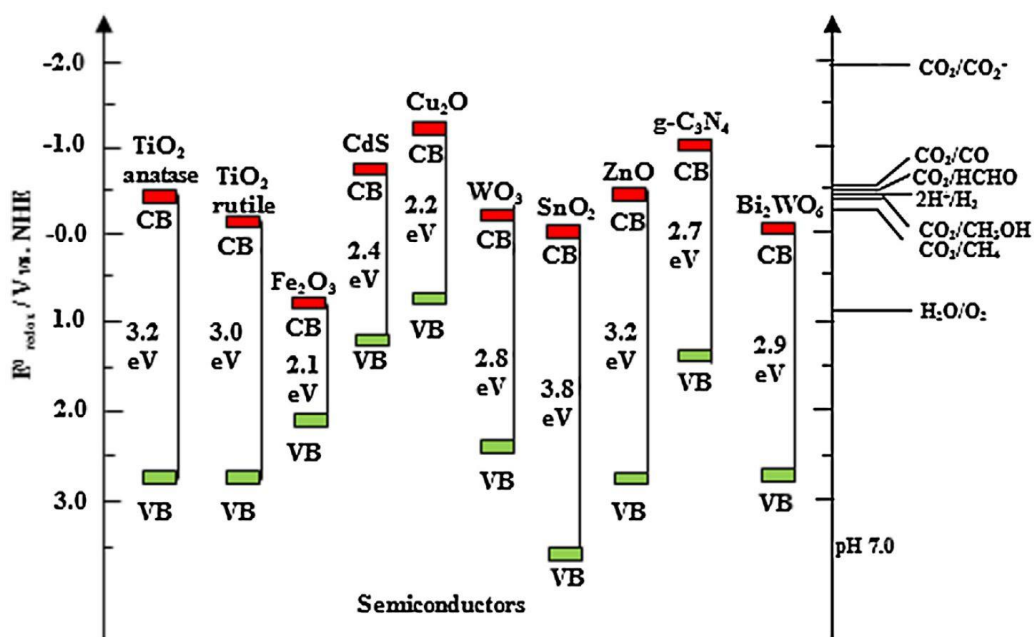


Figure 2.8 Band gap energies of various semiconductor photocatalysts with respect to the redox potentials of different chemical species at pH 7 [31].

2.7 Titanium dioxide

Titanium dioxide belongs to the family of transition metal oxides. It can be divided into three major crystallographic phases; brookite, rutile, and anatase. In each type, the titanium ion coordinates with six oxygen atoms, which in turn are linked to three titanium atoms and so on. Anatase and rutile structures are tetragonal, whereas brookite is orthorhombic. Brookite is not economically significant since it is not commonly accessible and difficult to synthesize, whereas rutile and anatase play the most important role in applications of TiO_2 . The bulk properties of anatase, rutile, and brookite crystalline forms are demonstrated in Table 2.4. The structures of anatase and rutile are both given in Figure 2.9. Anatase TiO_2 is considered to be the active photocatalytic module based on charge carrier dynamics, chemical properties, and the activity of photocatalytic degradation of organic compounds. While TiO_2 in

rutile phase is less effective than the anatase phase caused by the rapid recombination of photogenerated e^-h^+ pairs on the surface of the rutile phase and the smaller attachment of reactant and hydroxides ions on the surface of rutile phase than those of anatase phase [32].

Table 2.4 Structural data of crystalline structure of TiO_2 [31, 33, 34]

| Properties | Anatase | Rutile | Brookite |
|-----------------------------------|----------------------------|------------------------------|-------------------------------------|
| Crystal structure | Tetragonal | Tetragonal | Orthorhombic |
| Lattice constant (Å) | a = b = 3.784 c = 9.515 | a = b = 4.5936 c = 2.9587 | a = 9.184 b = 5.447 c = 5.154 |
| Molecule (cell) | 2 | 2 | 4 |
| Volume/molecule (Å ³) | 34.061 | 31.216 | 32.172 |
| Density (g/cm ³) | 3.79 | 4.13 | 3.99 |
| Melting point (°C) | Turning into rutile | 1870 | Turning into rutile |
| Boiling point (°C) | 2927* | - | - |
| Band gap (eV) | 3.2 | 3.0 | 3.3 |
| Refractive index (n_g) | 2.5688 | 2.9467 | 2.8090 |
| Dielectric constant | 55 | 110-117 | 78 |
| Ti-O bond length (Å) | 1.937 (4) 1.965 (2) | 1.949 (4) 1.980 (2) | 1.87-2.04 |
| O-Ti-O bond angle | 81.2° 90.0° | 77.7° 92.6° | 77.0°-105° |

* Pressure at pO_2 is 101.325 kPa

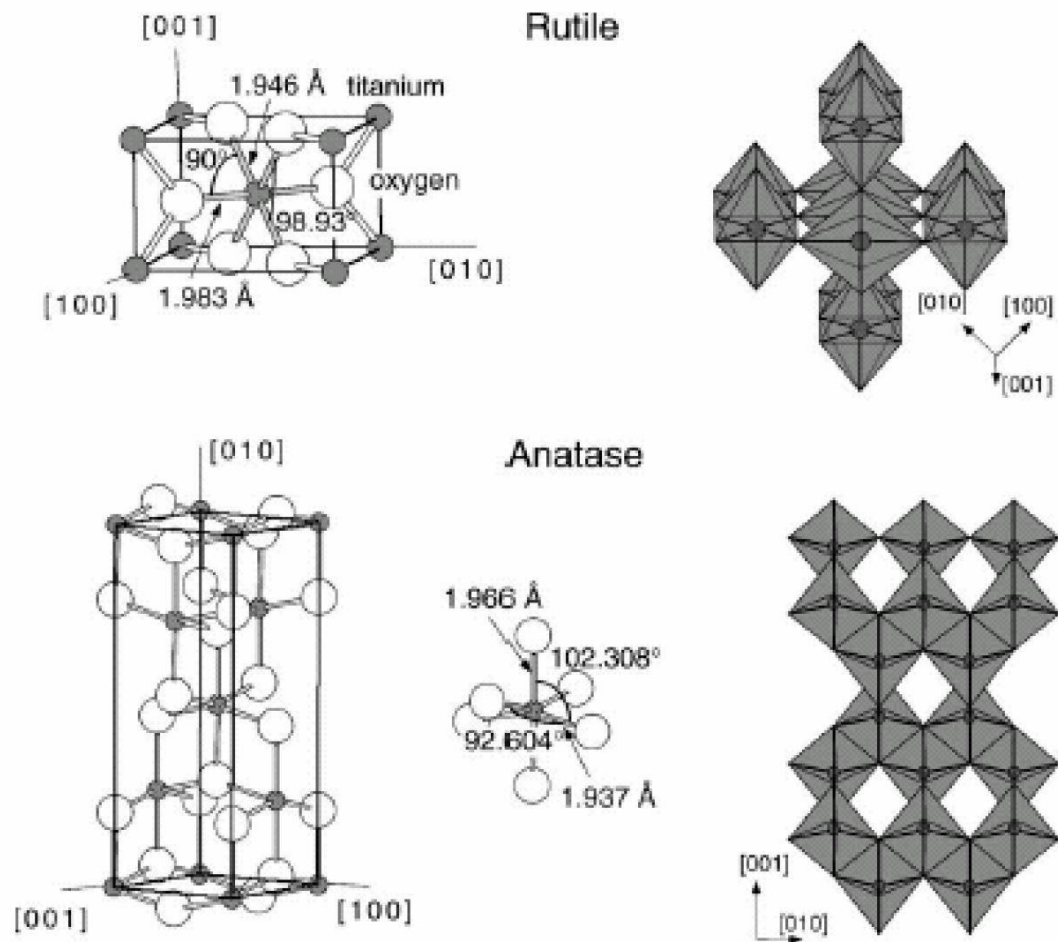


Figure 2.9 Crystal structures of TiO_2 [35].

TiO_2 exhibits a characteristic band gap energy between the valence band and the conduction band about 3.23 eV for anatase form and 3.06 eV for rutile form, which enable the formation of excited e^- and photogenerated h^+ by the light wavelength shorter than 390 nm for anatase and 405 nm for rutile. The conduction band of TiO_2 is composed of only the 3d orbitals of titanium, while the valence band is combined of the 2p orbitals of oxygen hybridized with the 3d orbitals of titanium [36]. The diagram of TiO_2 energy band in pH 7 solution is revealed in Figure 2.10. As demonstrated, the redox potential of photogenerated h^+ is about +2.53 eV versus the standard hydrogen electrode (SHE). After reacted with water, these photogenerated h^+

can produce hydroxyl radicals (OH^\bullet), whose redox potential is a little decreased. The redox potential of e^- in conduction is about -0.52 eV, which is in rule negative enough to evolve hydrogen from water, while the e^- can be entrapped and lose some of their reducing power, as shown. However, even after trapped, a weighty number are still able to reduce oxygen molecule to superoxide radical ($\text{O}_2^{\bullet-}$), or to hydrogen peroxide (H_2O_2). The photogenerated h^+ , OH^\bullet , $\text{O}_2^{\bullet-}$ can all play important roles as key species in the photocatalytic reaction, as discussed in the later section.

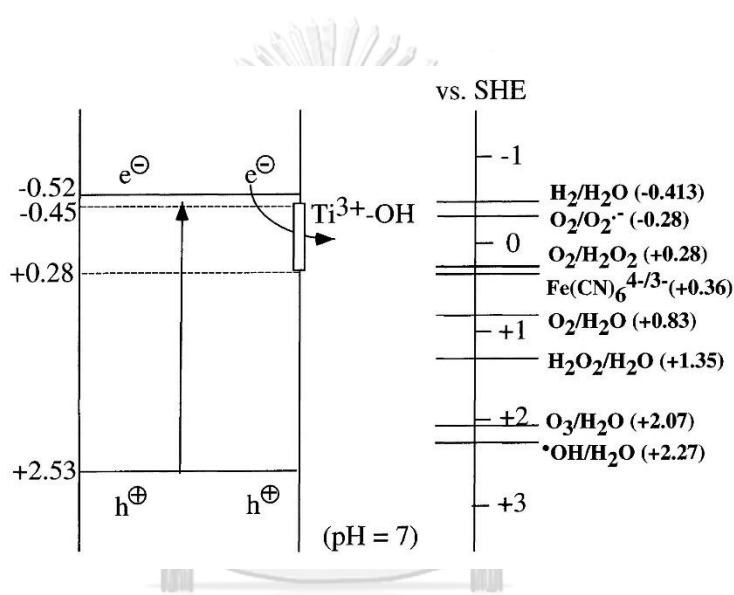


Figure 2.10 Schematic diagram showing the potentials for various redox processes occurring on the TiO_2 surface at pH 7 [37].

2.8 Doping TiO_2

Even though TiO_2 has several outstanding features, its practical usage is restricted due to its wide band gap; as it can only be stimulated by ultraviolet light which harvests 2–5% of sunlight [38]. Since visible light accounts for 45% of the solar spectrum, there is a challenge to create a new prospect of titania based photocatalysts which are effective under the visible light region. In addition, proper modification of the electronic and optical features of TiO_2 results in not only the narrowing of its band

gap but also increased lifetime of photogenerated h^+ and e^- by efficient charge carrier separation and retardation of $e^- - h^+$ recombination.

Doping or decorating of TiO_2 has been an attractive strategy in band gap engineering to change the optical properties and charge-transfer mechanism of photocatalysts, that lead to enhance efficiency of photocatalytic system. The introduction of additional energy level or reduction of band gap energy, which results in more absorption of visible light region and suppression of $e^- - h^+$ recombination are the main purpose of doping TiO_2 .

2.8.1 Doping with transition metals

The surplus energy levels within the band gap of semiconductor can be delivered by doping with transition metal. It results in lower photon energy requirement for e^- transfer from one of these additional levels to the conduction band, compared with the state of an unmodified TiO_2 . Apart from the doping transition metal possessing its own catalytic activity, it also served as a source of charge-carriers entrapment which can increase the life span of separated $e^- - h^+$ pairs, and thus enhance the photocatalytic reaction rate. TiO_2 has been modified with various transition metals such as Fe, V, Mn, Ni, Cd and Co. The overall efficiency and surface characteristics of a semiconductor photocatalyst will be altered by the addition of metal which is not chemically bonded to TiO_2 [39]. Figure 2.11 shows the band structure of TiO_2 before and after modified with a metal. The work function of metal (Φ_m) is higher than of semiconductor (Φ_s) which results in higher Fermi level of the semiconductor (E_{F_s}) than Fermi level of metal (E_{F_m}). When the metal is got in contact with TiO_2 (Figure 2.11(b)), e^- will flow from semiconductor to metal until the two Fermi levels achieve an equilibrium. This results in the generation of upshift band bending due to an excess of positive charges in TiO_2 , which generated from the transferring e^- [40]. Consequently,

this upshift band bending at the semiconductor-metal interface create a small barrier known as Schottky barrier, which serves as an e^- entrapment by preventing the migration of e^- turning back to the semiconductor and thus reducing the e^-h^+ recombination [41]. Figure 2.12 demonstrates the mechanism of metal doped on semiconductor photocatalyst where Schottky barrier of metal in contact with surface of semiconductor can suppress the e^-h^+ recombination. Umebayashi et al. [42] carried out Ab initio band gap calculations based on density functional theory (DFT) in order to examine the electronic structure of various transition metal (Cr, Fe, Co, V, Ni and Mn) doped on TiO_2 . They found that the localized level was shifted toward a lower energy based on the increasing of atomic number of the doped metal. Choi et al. [43] systematically investigated the photocatalytic activity of TiO_2 modified with 21 different metal, such as Fe^{2+} , Mo^{5+} , Os^{3+} , Re^{5+} and V^{5+} . These modified metals can be markedly improved the photocatalytic oxidation of CHCl_3 and reduction of CCl_4 .

Doping transition metal ions on TiO_2 can enhance the rate of photocatalytic activity with an improvement of trapping to recombination rate ratio. Nevertheless, the impurity energy levels are formed in the band gap of TiO_2 when metal oxides or ions are incorporated into TiO_2 , which also led to an increment of photogenerated h^+ and e^- recombination rate. Only trapped h^+ and e^- that conveyed to the surface of photocatalyst can participate the photocatalytic reaction. This means that doping transition metal ions should be existed near the surface to allow effective charge transfer. Joshi et al. [44] reported the detrimental effect of transition metal ions doped TiO_2 on photocatalytic activity due to the formation of localized d -states, which acted as a trapping site that capture photogenerated h^+ from valence band or excited e^- from conduction band. In case of modified with high concentration of metal ions, it can be acted as recombination centers. Gupta et al. [45] further reported that raising metal doped concentration affected in a shorten space charge layer where

photogenerated h^+ and excited e^- within this region can be effectively separated by the electric field before recombination. However, surpassing the optimal metal doped concentration results in an extremely shortened space charge layer such that light penetrated depth exceeds the width of this space charge layer. Consequently, recombination rate enlarges due to the deficiency of a driving force to separate them.

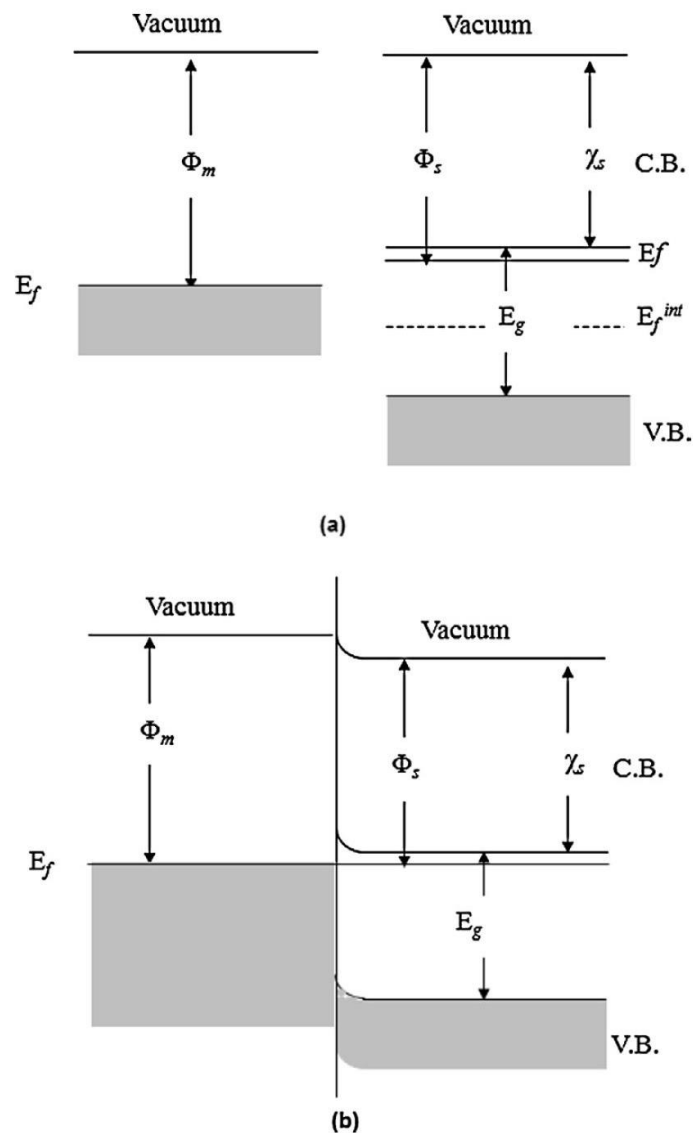


Figure 2.11 Band structure of TiO_2 (a) before contact (b) after contact with metal, where the Schottky barrier is designed. (Φ_m and E_f^{int} denoted the metal work function and fermi level if TiO_2 is an intrinsic semiconductor respectively) [39].

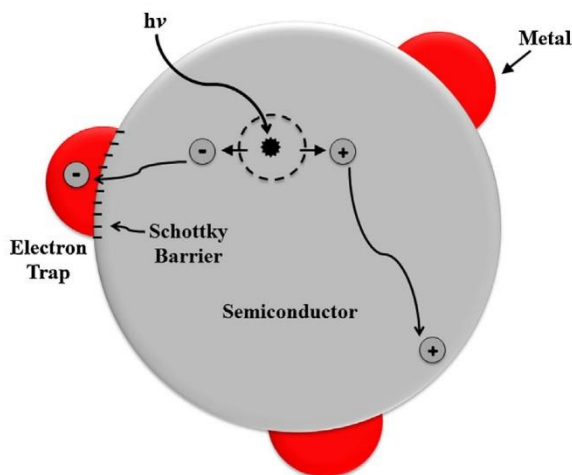


Figure 2.12 Metal doped on semiconductor photocatalyst [31].

2.8.2 Doping with noble metals

Addition of noble metal such as Au, Ag, Pt, Pd and Cu have been promised as another approach for modification of TiO_2 photocatalyst, which are very efficient for promoting photocatalytic activity. Because the Fermi level of these noble metals are lower than that of unmodified TiO_2 , excited e^- can migrate from the conduction band of TiO_2 to noble metal particles decorated on surface of TiO_2 . While the photogenerated h^+ is still carried through in the valence band of TiO_2 , which greatly reduces the possibility of e^-h^+ recombination and increases the photocatalytic activity. The work function of several transition metals and their reduction potential are concluded in Table 2.5. The noble metal ion with larger work function promotes the Schottky barrier effect which can reduce the e^-h^+ recombination. Therefore, the noble metals with appropriate work function can benefit e^- transfer, leading to higher photocatalytic activity, and overwhelmed the Schottky energy barrier. Other than Schottky barrier, doping of noble metals can improve the visible light absorption ability through localized surface plasmon resonance effect (LSPR), which occur either by collective polarization or oscillation of valence electrons in plasmonic metal

nanostructures or noble metal element creating trap sites that broadcasts light within semiconductor photocatalyst [46]. Moreover, the metallic size and morphology also effect on LSPR characteristics as well as the resonance wavelength.

Rupa et al. [47] prepared 1 wt.% of noble metal, including Ag, Au and Pt, doped on TiO₂ by photo-deposition technique. These metals doped on TiO₂ exhibited outstanding photocatalytic activity, compared with undoped TiO₂, towards the decolorization of tartrazine even under visible light irradiation. Krejcikova et al. [48] synthesized the different Ag metal loading onto TiO₂ and conducted the CO₂ reduction from these prepared material series. They found that the methane yield in gas phase and methanol yield in liquid phase were significantly increased with increasing of Ag concentration, which attributed to the facile transfer of e^- from conduction band of TiO₂ to doped Ag nanoparticles due to higher Fermi level of TiO₂ and the formation of Schottky barrier. Nosaka et al. [49] reported the hydrogen production via photocatalytic reaction of aqueous alcohol over the various noble metals (Pt, Rh, Pd, Au, Cu and Ag) doped TiO₂. The exponential increase of photocatalytic activity was observed and in accordance with the increasing of work function of metal co-catalyst. Thus, they suggested that the function of noble metal nanoparticles would be to create an electric field gradient, causing a proficient e^-h^+ separation.

2.8.3 Non-metal modification

Since the cost of metal is much higher than those of non-metals, the doping with non-metal into TiO₂ structure has been also extensively investigated. Many studies have been devoted to the development of TiO₂ performance by doping it with various anions as a replacement for oxygen in the TiO₂ lattice. These non-metals created heteroatomic surface structure and modified the physicochemical properties and photocatalytic activity of TiO₂ toward visible light response. Some of the non-

Table 2.5 Work function and redox potential of some noble metals [50].

| | Work Function | Reaction | E^0_{redox} at pH=0 / V vs. NHE |
|----|---------------|---|---|
| Ag | 4.26 | $\text{Ag}^+ + e^- \rightarrow \text{Ag}$ | 0.799 |
| Cu | 4.65 | $\text{Cu}^{2+} + 2e^- \rightarrow \text{Cu}$ | 0.337 |
| Ru | 4.71 | $\text{Ru}^{2+} + 2e^- \rightarrow \text{Ru}$ | 0.460 |
| Rh | 4.98 | $\text{Ru}^{3+} + 3e^- \rightarrow \text{Rh}$ | 0.758 |
| Au | 5.10 | $\text{Au}^{3+} + 3e^- \rightarrow \text{Au}$ | 1.500 |
| Pd | 5.12 | $\text{Pd}^{2+} + 2e^- \rightarrow \text{Pd}$ | 0.915 |
| Ir | 5.27 | $\text{Ir}^{3+} + 3e^- \rightarrow \text{Ir}$ | 1.160 |
| Pt | 5.65 | $\text{Pt}^{2+} + 2e^- \rightarrow \text{Pt}$ | 1.190 |

metals such as carbon (C), nitrogen (N), sulfur (S) and fluorine (F) have been widely used [51-55]. The mixture of the p states of these non-metal anions dopant with $O2p$ states of TiO_2 via interstitial or substitutional doping was shifted the valance band edge upwards leading to narrowing band gap energy of TiO_2 [51]. The effective narrowing band gap energy can only take place by anions doping if the non-metal has a lower electronegativities than O and comparable radius with O atoms, with the aim of homogeneous distribution and uplifting the valence band [56]. In addition, the doped non-metal anions are less likely to generate recombination centers caused by the presence of d states deep in the band gap of TiO_2 which results in being more effective for photocatalytic activity compared to cations doping [51, 57].

Asahi et al. [51] firstly conducted the calculation of electronic band structure of TiO_2 doped with non-metal anions including F, N, P, S and C. The result indicated that the superior activity of N owing to its p state combined with O $2p$ states influencing

band gap narrowing. Irie et al. [58] fabricated $\text{TiO}_{2-x}\text{N}_x$ powders by heating TiO_2 under NH_3 atmosphere and used for the decomposition of 2-propanol. They confirmed the formation of isolated N 2p states above the valence band, which are responsible for the responsive visible-light region. In addition, the multiply of the nitrogen concentration depressed the quantum yield under UV irradiation, demonstrating that surplus doping ions could also work as recombination sites. Valentin et al. [59] examined the role of interstitial and substitutional C dopant on the alteration of the TiO_2 band structures. They revealed that carbon doping induces the formation of several localized occupied states between the gap of TiO_2 depending upon the dopant type, and the presence or absence of oxygen vacancies. The presence of these states is supposed to cause the narrowed band gap energy and significant red shift of the absorption band edge toward the visible region. Vohra et al. [60] synthesized fluorinated- TiO_2 (F- TiO_2) for Photocatalytic degradation of tetramethylammonium (TMA). It was found that the F doping was improved the photocatalytic activity due to the enhancement of surface acidity, formation of oxygen vacancies or Ti^{3+} , and creation of surface hydroxyl radicals, therefore altering the interfacial e^-/h^+ transfer, surface charge allocation, and substrate-surface interaction.

Despite the numerous research deal with non-metal modification on TiO_2 , its quantum efficiency of anions doping is still low. This is due to the fact that it is difficult to introduce high doping concentration on TiO_2 . Therefore, the modification of the TiO_2 band structure can only achieve to a small level. In addition, the doping of foreign elements in the lattice of TiO_2 will lead to the formation of defects due to the incompatible atom size or unbalanced charge. These defect sites may act as recombination centers for photogenerated charges and therefore will diminish the photocatalytic activity [61].

2.9 Defective TiO₂

In the past few decades, many research reported that the introduction of defect disorder into TiO₂ structure can modulate some physical and chemical properties of TiO₂. It has been documented that the properties of TiO₂ are closely related to defect disorder, rather than structure and composition [62]. Therefore, defect engineering seems to be the most capable approach in synthesizing of TiO₂ with boosted performance in solar energy conversion and alternative applications. The most common defects in the lattice of non-stoichiometric materials are point defects, which have size in atomic range. The point defects in non-stoichiometric oxide materials are mainly involved oxygen vacancies, cation vacancies and cation interstitials. These defects result in the creation of either acceptor- or donor-type centers within band gap of semiconductor materials. For a long time, defect disorder of TiO₂ has been explained as the presence of three types of ionic defects including oxygen vacancies ($V_o^{\bullet\bullet}$), titanium vacancies (V_{Ti}'''), and titanium interstitials ($Ti_i^{\bullet\bullet\bullet}$). Figure 2.13 was schematically illustrated the formation of three types of point defects during the interaction of oxygen with TiO₂ surface [63].

As displayed in Figure 2.13(a), subtraction of one oxygen ion from the TiO₂ lattice leads to the formation of oxygen vacancy. If deduction of two lattice oxygen ions occurs as displayed in Figure 2.13(b), it leads to the establishment of either a tri- or tetra-titanium interstitial. The formation of these two defect types is preferred under reducing condition. Figure 2.13(c) demonstrates the building-up new oxides layer containing titanium vacancy through oxygen adsorption on the surface. The titanium vacancies are usually formed under oxidizing conditions when oxygen is adsorbed and occupied in building-up new lattice layer and it exhibited an extremely slow diffusion rate and have been regularly considered as extrinsic defects. Thenceforth, it is

prominently noted that the defect disorder of surface layer, which has been reported so far, include both oxygen vacancies and titanium interstitials.

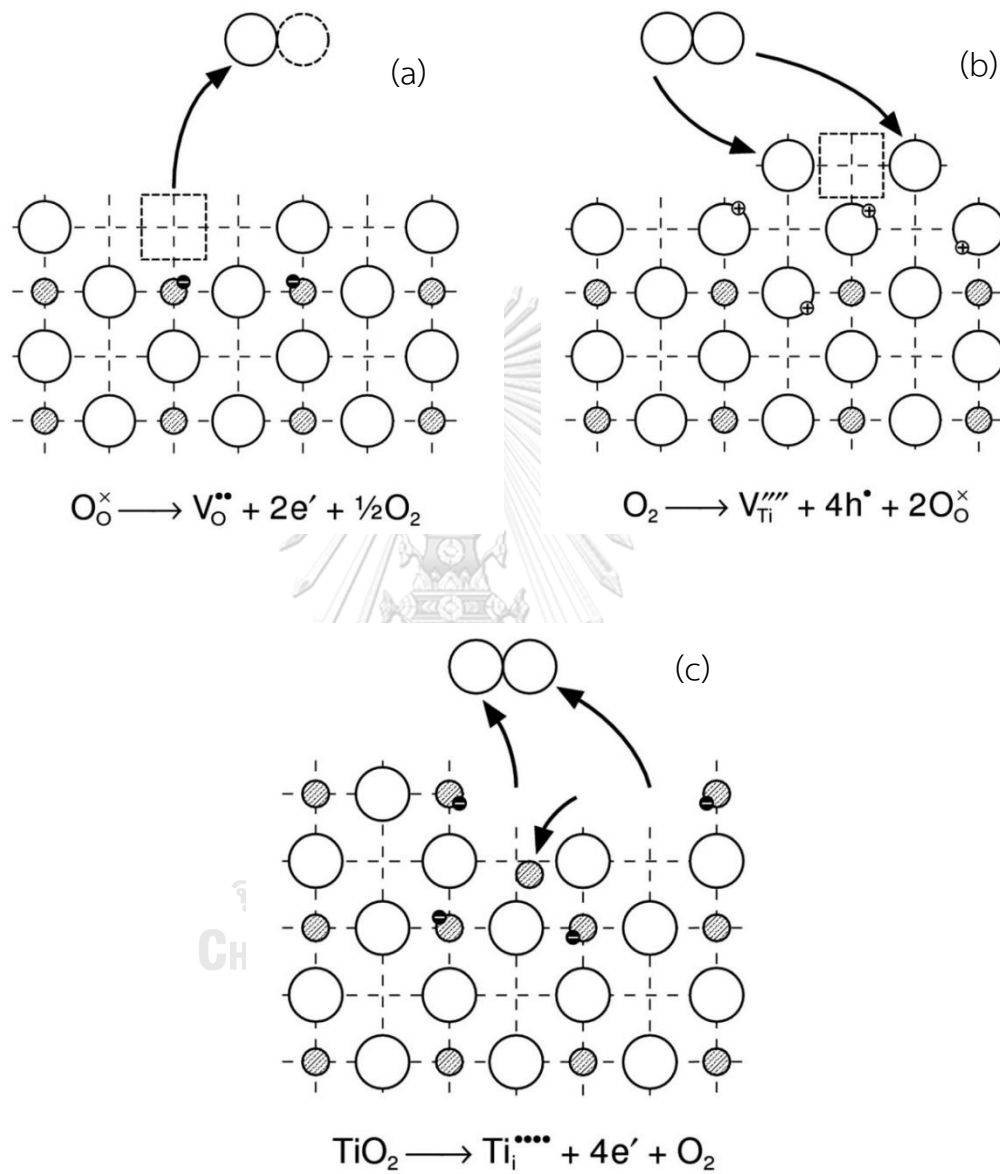


Figure 2.13 Schematic of the establishment of (a) oxygen vacancy (b) titanium vacancy and (c) titanium interstitial (small and large circles denote titanium ions and lattice oxygen, respectively, and the square denotes an empty lattice site) [62].

Nowotny et al. [64] reported that the change of oxygen activity and the associated defect lattice reduced the optical band gap of TiO_2 as shown in Figure 2.14. Strongly reducing environment led to the reduction of band gap energy of TiO_2 to the level of 2.4 eV and 2.9 eV for the indirect and direct transitions, respectively. These phenomena seem to be related to structural relaxations that are made by oxygen vacancies and the associated generation of superior defect lattices.

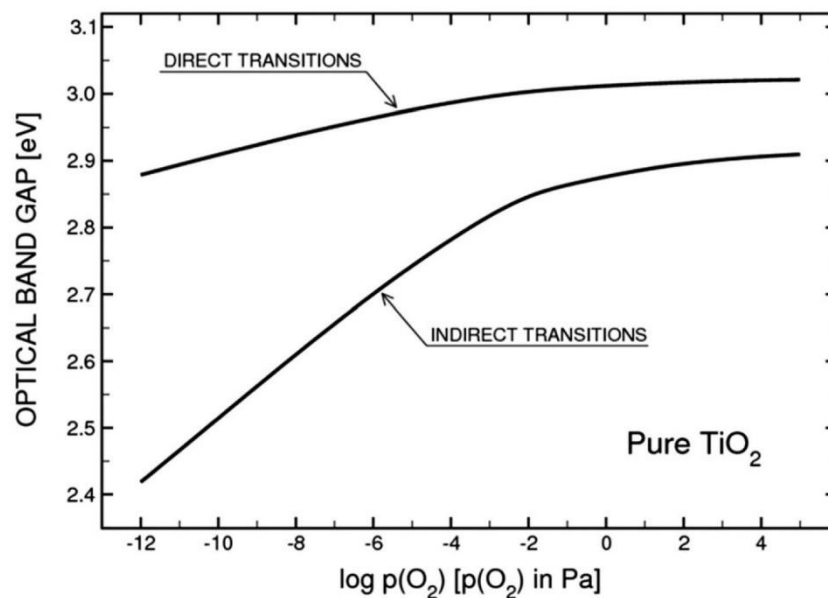


Figure 2.14 Effect of oxygen activity on the band gap of pure TiO_2 [64].

A missing of oxygen atom from the bulk or surface of TiO_2 photocatalyst results in one or two e^- lefting over at the oxygen vacancy site, which have a direct effect on the electronic structure of TiO_2 by forming a donor level below the conduction band as depicted in Figure 2.15 [65]. The energy level creating from oxygen vacancies is located at 0.75-1.18 eV below the conduction band. In addition, the removal of oxygen atom to form oxygen vacancies can also redistributed the excess e^- among the nearest neighboring Ti atoms around the oxygen vacancies site, and form shallow donor states

below the conduction band originating from Ti 3d states [66]. Oertzen et al. [67] has also been confirmed that these shallow donor states were increased as increasing an amount of oxygen vacancies, and can even overlap the conduction band in the case of highly oxygen deficient non-stoichiometric TiO_2 . These can be postulated that the presence of oxygen vacancies can greatly shift the Fermi level of TiO_2 toward high energy.

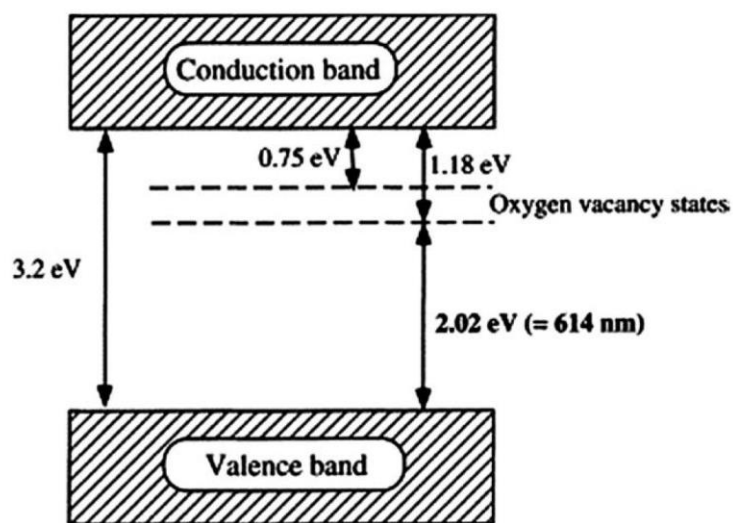
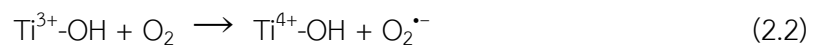


Figure 2.15 A proposed band structure model for TiO_2 with oxygen vacancies [65].

In addition, the introduction of oxygen vacancies in TiO_2 lattice are not only modified the electronic structure but also the optical properties of TiO_2 . That is, the extension of light absorption spectra of TiO_2 from UV to visible light region is occurred because of the presence of oxygen vacancy states below the conduction band. The as-formed oxygen vacancy states can take part in a new photo-excitation process. Namely, the e^- can be directly excited from the valence band to the oxygen vacancy states with photon flux energy of visible light spectrum. Moreover, the leftover e^- in oxygen vacancies can also interacted with adjacent atomic Ti^{4+} to form the Ti^{3+} species

[68]. These Ti^{3+} defect species can also create a shallow donor states just below the conduction band, which could conduce to the visible light response.

Apart from the oxygen vacancies, Ti^{3+} defect species are received much attention as the dominant defect in TiO_2 , which also responsible for the improvement of TiO_2 photocatalytic efficiency. Liu et al. [69] reported that both Ti^{3+} defects and oxygen vacancies were major defects in surface TiO_2 . Sirisuk et al. [70] have shown that Ti^{3+} defects in TiO_2 photocatalyst played an important role in photocatalytic process. Basically, Ti^{3+} defect species can be produced by the reduction of Ti^{4+} ions via two typic methods. One is that a Ti^{4+} takes an electron. The e^- can be trapped and led to reduce Ti^{4+} cations to Ti^{3+} states. Another process for Ti^{4+} reduction to Ti^{3+} is performed by a loss of oxygen from the lattice of TiO_2 . So, the generation of Ti^{3+} usually coincided with the formation of oxygen vacancies. That is, when the Ti^{4+} ion is transformed to Ti^{3+} , the local static balance is broken down, and the oxygen vacancies should be introduced due to charge recompense. Park et al. [71] proposed the mechanism of Ti^{3+} defect species contributing in photocatalytic reaction. That is, the presence of Ti^{3+} defect sites were acted as trap of e^- and h^+ results in the prevention of e^- - h^+ recombination, and the consequent reactions involved with e^- and h^+ were markedly improved. Furthermore, in the presence of O_2 , the Ti^{3+} defect sites simply reacted with O_2 molecule, leading to the formation of radical such as $O_2^{\bullet-}$, OH^{\bullet} , and HO_2^{\bullet} as following equation;



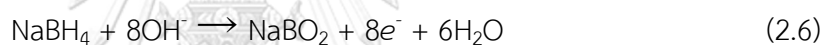
2.9.1 Synthesis of defective TiO₂

Since the oxygen vacancies and Ti³⁺ defect sites strongly influence on the surface chemistry and photocatalytic performance of TiO₂, numerous research efforts have been devoted to synthesizing the new kind of this material via several approaches which are roughly categorized into two main groups including partial reduction method and partial oxidation method.

The partial reduction method is frequently used to prepare the defective TiO₂ by using suitable reductant under certain condition. Typically, TiO₂ parent materials are reduced by H₂ environment at elevated temperature. During the hydrothermal process, hydrogen atoms react with lattice oxygen of TiO₂, which results in the generation of oxygen vacancies and concurrently leaves two excess e⁻ behind one oxygen vacancy site. These excess e⁻ can delocalize to neighboring titanium atom to form Ti³⁺ defect species or can also remain at the position of oxygen vacancies to form e⁻-containing oxygen vacancies. The types of defect species are very sensitive to their treating conditions. For example, Liu et al. [69] reported that under hydrogen treatment at temperature below 450 °C, the synthesized sample possessed only e⁻-trapped oxygen vacancies, whereas the sample contained both of oxygen vacancies and Ti³⁺ defect species in case of hydrogen treatment at temperature higher than 450 °C. Yu et al. [72] also demonstrated that the defective types were strongly depended on the hydrothermal temperature and time. Longer hydrogenation time at 600-700 °C induced the formation of Ti³⁺ defect species and also increased the presence of O⁻ species, which might be caused by the diffusion of Ti³⁺ defects from the bulk of TiO₂ lattice to the surface and then reacted with surface absorbed oxygen molecules and/or surface oxygen vacancies during longer hydrogenation, finally resulting in the formation of O⁻ species. In comparison, Ti³⁺ defect species are easily formed in rutile than anatase structure, while oxygen vacancies are more favorable generated in anatase than rutile,

as reported by Morgan et al. [73]. Under oxygen-deficient condition, both of defect species were stabilized, with Ti^{3+} species predicted to become the favored defect, especially at high temperature. It could be pointed out that the Ti^{3+} defect species were most probably formed under more severe condition than oxygen vacancies.

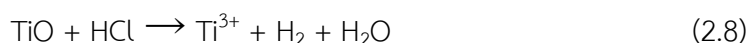
In addition to H_2 , other reductants such as sodium borohydride ($NaBH_4$), diethylene glycol (DEG), metallic zinc (Zn), aluminum (Al) and carbon monoxide (CO) were also utilized to produce defective TiO_2 under reduction method. Zheng et al. [74] synthesized stable Ti^{3+} self-doped TiO_2 by using the redox reaction between Zn and Ti^{4+} ($Zn + Ti^{4+} \rightarrow Zn^{2+} + Ti^{3+}$). Sayed et al. [75] refluxed TiO_2 at 220 °C in DEG (a reducing agent and solvent) to fabricate Ti^{3+} -containing in TiO_2 matrix. Kang et al. [76] also reduced TiO_2 nanotubes with strong reducing agent as $NaBH_4$ as proposed following;



In another study, the combination of electrolysis and plasma has been performed to synthesize the oxygen-deficient TiO_2 microsphere [77]. Due to the generation of highly energetic species such as e^- , atoms and radicals during this process that are available to reduce the surface of TiO_2 , leading to formation defected TiO_2 materials. Moreover, the electron beam irradiation was also conveyed to reduce Ti^{4+} to Ti^{3+} - TiO_2 because of the surface reduction by bombarded e^- [78].

Although Ti^{4+} was a major chemical state of stable titanium chemistry, the +2 and +3 of chemical oxidation states of Ti-based compounds are also usual such as TiO , Ti_2O_3 , $TiCl_3$ and TiH_2 . Considering that the partial oxidation of these compounds is enabled to the formation of Ti^{3+} defective of TiO_2 materials under proper condition. Grabstanowicz et al. [79] were firstly used H_2O_2 aqueous solution to oxidize TiH_2 powder and then thermally treated under argon atmosphere at 630 °C to form Ti^{3+}

self-doped rutile TiO₂. Liu et al. also used the same TiH₂ as precursor and H₂O₂ as oxidizing agent under different thermal treatment conditions to produce Ti³⁺ defected anatase TiO₂. Besides, the presence of Ti³⁺ defect species in TiO₂ can be alternatively generated by the oxidative reaction between TiO and HCl which proposed by Pie et al. as following [80];



Zu et al. [81] also successfully synthesized Ti³⁺-doped TiO₂ with dominant [110] rutile facets by using HCl in hydrothermal system of titanium powder.

2.10 Solution plasma process (SPP)

Plasma is a state of matter generated by a destabilizing gas. It is one of the four fundamental states of matter, and was first described by chemist Irving Langmuir in the 1920s. Unlike the other three states of solid, liquid, and gas, plasma does not independently exist on the earth under normal surface conditions, and can only be artificially generated by heating neutral gases or by subjecting that gas to a strong electromagnetic field [82]. Plasma has no fixed volume or shape, and are less dense than solid or liquid. But unlike ordinary gases, plasmas are made up of atoms in which some or all of the electrons have been stripped away and positively charged nuclei, called ions, move freely. Normally, plasma can be classified into 2 types including (i) high-temperature plasma or thermal equilibrium plasma and (ii) low-temperature plasma or non-thermal equilibrium plasma.

Solution plasma process (SPP) is relatively new techniques for plasma generation in liquid phase. It is one type in three categories plasma phase which corresponding to the relationship between pressure and temperature as shown in Figure 2.16.

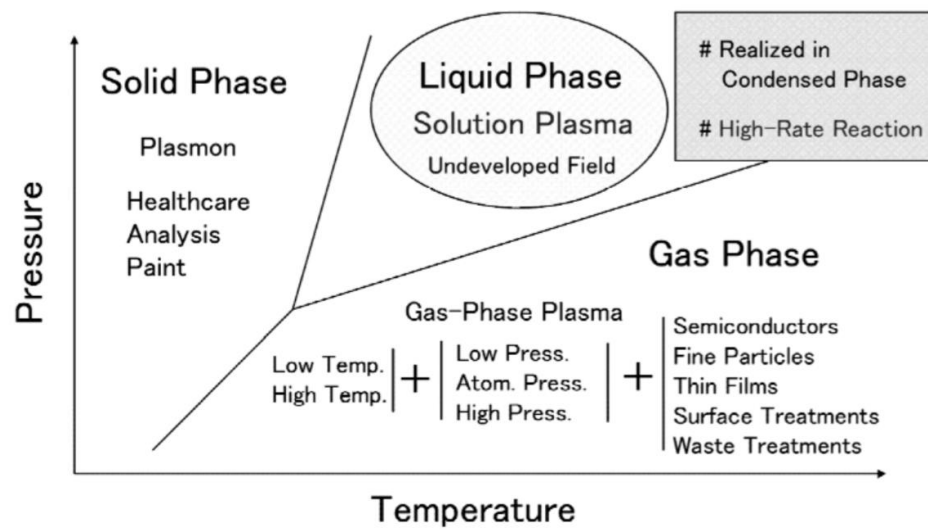


Figure 2.16 Three categories of plasma phase corresponding to the relationship between pressure and temperature [83].

The solution plasma has more attractive available in variety application fields such as analytical optical emission spectrometry, nanomaterial synthesis, surface functionalization, hydrogen production, water treatment, decomposition of toxic compounds and polymerization.

In general, it has many experimental set up of plasma in liquid generation, which including solution medium, electrode materials, electrode configurations, current-voltage power supply, etc. By examining electrode configurations and power sources, the plasma generation in liquid phase can be broadly subdivided into four categories:

1. Direct discharge between two electrodes

Figure 2.17(a) displayed the scheme of direct discharge between 2 electrodes, which usually comes in such forms as plasma discharge in liquid, solution plasma, electric spark discharge, streamer discharge, arc discharge, and capillary discharge. Two

identical size and shape electrodes are submerged in the liquid solution at a short gap distance. Plasma is generated between two electrodes under liquid solution after passing electric current through the solution. Hence, the liquid medium must be conductive electrolytes. For nanomaterial fabrication, both ion in liquid medium and electrode serve as a raw material for nanoparticle formation.

2. Contact discharge between an electrode and the surface of surrounding electrolyte

In 1963, Hickling and Ingram stated a contact glow discharge electrolysis (CDGE) [84], whereby a high-temperature plasma sheath was formed between an electrode and the surface of surrounding electrolyte because of a high electric field, which consequently accompanied by a glow discharge photoemission. This model of plasma generation using CDGE was schemed as Figure 2.17(b) and it was also supported by Azumi et al. [85], Sengupta et al. [86], and Campbell et al. [87]. In this model, two electrodes are submerged in electrolyte solution with their gap distance about 5-100 mm. The distance between two electrodes did not affect the plasma formation intensely for this case and the shape and size of electrode can be modified. The surface area of both electrodes is normally different between cathode and anode. One of electrode has a larger surface area than another one, which is covered with a thin film of water vapor and plasma discharge was occurred inside this thin film. The direct current power supply was passed the electric current through the electrolyte solution medium and then bubbles were generated due to Joule-heating. Subsequently, plasma was generated at the cathode side. In most case, the anode was a metal wire, while the cathode was composed of a metal plate with a large surface area such as Pt mesh.

3. Radio frequency (RF) and microwave (MW) generation for plasma discharge

Plasma generation by irradiation with radio frequency (RF) and microwave (MW) was demonstrated in Figure 2.17(c). This technique is considered to be effective to generate plasma in solution at low electrical power. When plasma is generated in solution using RF or MW, a lower pressure is often applied because energy is absorbed in water as it possesses a dielectric constant and dielectric loss. The dielectric constant and dielectric loss of the liquid media are vital factors in this plasma generation process. Unlike other techniques, nevertheless, it is not required to use an electrolyte solution. RF or MW generated plasma can be maintained in water over the wide range of water conductivity (0.2-7000 mS/m). Because plasma can be generated even in pure water, it is very advantage of this technique and so various applications can be expected.

4. Laser ablation technique assisted plasma generation

The plasma generation in liquid by using laser ablation techniques is illustrated in Figure 2.17(d). The laser beam irradiated to a solid substrate which submerged in the liquid led to a plasma ball generation on the surface of solid. This technology is applied in such research as nanomaterial synthesis [88, 89] and deep-sea mass spectrometry [90].

จุฬาลงกรณ์มหาวิทยาลัย
CHULALONGKORN UNIVERSITY

2.10.1 Solution plasma application

2.10.1.1 Nanomaterial synthesis

The several types of plasma mentioned previously have been applied for fabrication of various nanomaterials. The numerous researches in nanomaterial synthesis field through solution plasma have been devoted to the synthesis of noble metal nanoparticles such as Au, Pt, Pd and Ag because noble metal ions are more facilely reduced. However, nanoparticles comprised other metals such as Cu, Fe, Sn, and Ni which have been also fabricated. The direct discharge between two electrodes

has been mostly used for producing metal nanomaterials and composite or alloy materials of metal, in which the metal wire electrode and/or ions in liquid were served as a source material for nanoparticle formation.

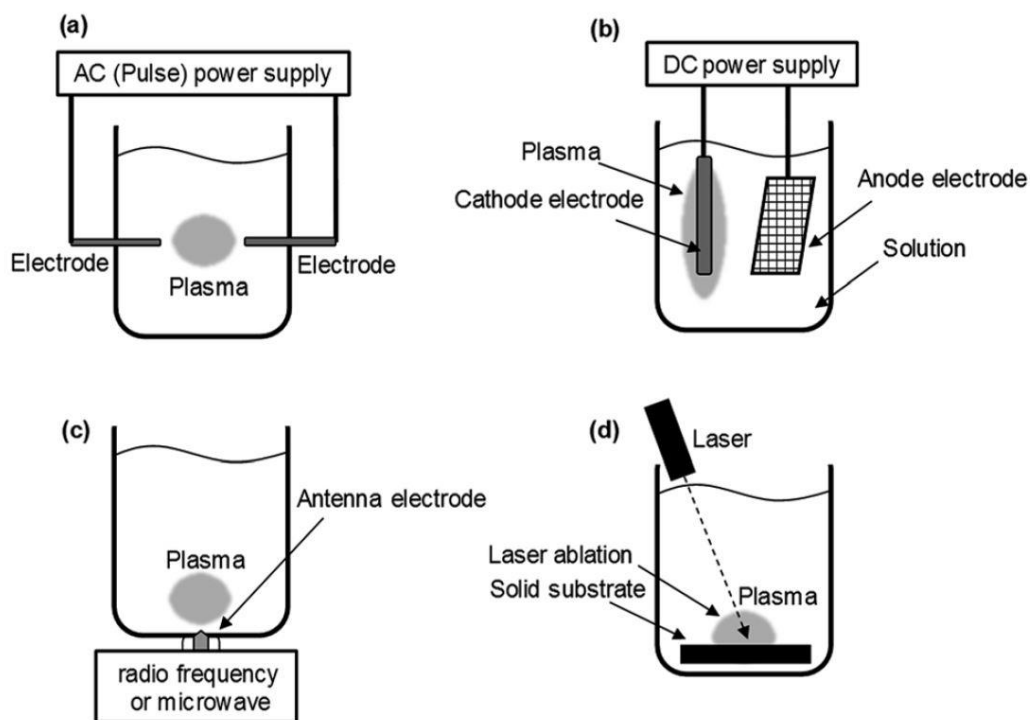


Figure 2.17 Schematic of plasma generation model in liquid: (a) direct discharge between two electrodes using AC (pulse) power supply; (b) contact discharge between an electrode and the surface of surrounding electrolyte using a DC power supply; (c) radio frequency (RF) and microwave (MW) generation for plasma discharge; (d) laser ablation technique assisted plasma generation [91].

Saito et al. synthesized various nanomaterials such as Pt [92], Au [93-96], Cu [97], C [98, 99], CuO [100], ZnO [100], Pt-Au alloy [101], Ag-Pt bimetallic nanocomposites [102], Ag incorporated mesoporous silica [103, 104] and also functionalized surface of material [105] by using solution plasma process. A typical setup for solution plasma process is shown in Figure 2.18. The applied voltages were

around 1.6-2.4 kV with pulse width at 2 μ s. Tarasenko et al. also reported the ZnO nanoparticle synthesis using electrical discharge techniques in water, in which the current was 60 A, and alternating/direct current, pulsed power supply were utilized [106-108]. Tube-like nanocarbons or carbon nanotubes (CNTs) was also synthesized by arc discharge in liquid toluene as reported by Hatakeyama et al. [109]. Abdullaeva et al. also reported the synthesis of spherical ferromagnetic Fe_3O_4 nanoparticles [110], onion-like carbon-encapsulated Ni, Co, and Fe magnetic nanoparticles [111], Ni and Fe coated graphitic carbon [112] by pulsed plasma discharge in a liquid technique, in which the schematic process was displayed in Figure 2.19. In this technique, one of electrode must kept vibrating in order to stabilize the discharge process.

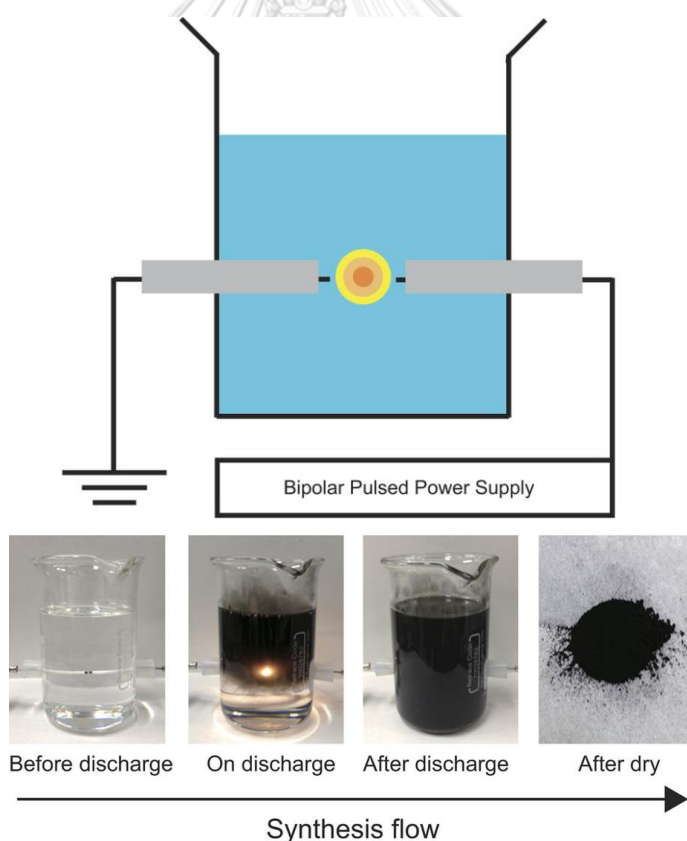


Figure 2.18 Schematic of the experimental setup for solution plasma experiments and synthesis flow for nanocarbon production[99] .

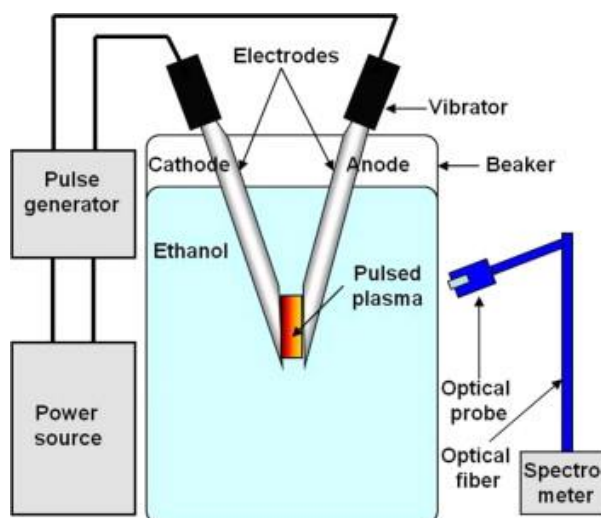
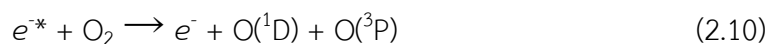
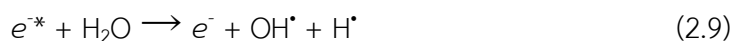


Figure 2.19 Schematic of the pulsed plasma discharge in a liquid method [111].

2.10.1.2 Wastewater treatment

In recent year, discharge plasma in liquid phase has been received interest as a tool for generating a large quantity of heat and a high yield of various oxidative active species, which are benefited for wastewater treatment. Among various oxidative active species, hydroxyl radicals (OH^\bullet) is the most forceful oxidizing species. Thus, the generation of OH^\bullet radicals by solution plasma in water and the decomposition of contaminants have been undertaken. The mechanism for the formation of OH^\bullet radicals by the solution plasma is concluded in Eqs. (2.9) - (2.12). Electrons is generated by dissociation of water molecules during discharge plasma in liquid phase and lead to the generation of OH^\bullet radicals (Eq. (2.9)). On the other side, highly energetic electrons (e^{-*}) can be interacted with dissolved oxygen and consequently formed the excited $\text{O}^{\text{(1D)}}$ and ground $\text{O}^{\text{(3P)}}$ states of oxygen atoms (Eq. (2.10)), which eventually produced OH^\bullet radicals from water (Eq. (2.11) and (2.12)) [113]. However, Due to the large amount of OH^\bullet radicals can be produced through solution plasma process; their subsequent recombination may be facilitated. Thus, it is disadvantageous to produce large amount

such species and the recombination process was depended on the diffusion condition of OH[•] radicals.



Horikoshi et al. [114] was successfully decomposed perfluorooctanoic acid (PFOA) in ion-exchange water using discharge plasma in liquid phase. After 90 second of discharge plasma in 0.01 mM PFOA aqueous media led to 59% defluorination accompanying the decomposition of PFOA. Hao et al. [115] reported the degradation of parachlorophenol (4-CP) by the pulsed discharge plasma process in aqueous solution combined with activated carbon. Qu et al. [116] also utilized hybrid system between pulsed corona discharge plasma combined and activated carbon for simultaneous removal of cadmium ions and phenol from water solution.

2.11 Key species in photocatalytic reactions

The photocatalytic reactions proceed via redox reactions caused by photogenerated h^+ and e^- created on the surface of photocatalysts. These generated h^+ and e^- can produce several reactive species, which are considered to be involved in actual oxidation and reduction reactions in photocatalytic process. Since photocatalyst are practically used with oxygen and water, both stepwise reduction and oxidation of adsorbed oxygen and water molecules take place concurrently in photocatalysis as shown in Figure 2.20. The species to which water or oxygen converts with high reactivity are generally called reactive oxygen species (ROS). Four major ROS are recognized, including superoxide radical ($\text{O}_2^{\bullet-}$), hydrogen peroxide (H_2O_2), singlet

oxygen ($^1\text{O}_2$), and hydroxyl radical (OH^\bullet). The efficiency of these generated ROS varies over a wide range relying on the kind of utilized photocatalysts and the nature of solution conditions. The standard potential for the one-electron redox of active species as a function of pH solution illustrated in Figure 2.21 [117]. The two-electron ($2e^-$) redox potential corresponds to the average of redox potential at each step. As commonly known, the potential of the valence band of TiO_2 about +2.14 to + 3.03 eV, depended on the pH solution, is low enough to oxidize H_2O , suggesting the possibility of the formation of OH^\bullet . As shown in Figure 2.21, at acidic condition, the reduction potential of $\text{O}_2^{\bullet-}$ ($\text{O}_2^{\bullet-}, 2\text{H}^+/\text{H}_2\text{O}_2$) is higher than that of H_2O_2 ($\text{H}_2\text{O}_2, \text{H}^+/\text{OH}^\bullet$). That is, the reduction of $\text{O}_2^{\bullet-}$ to H_2O_2 is thermodynamically more desirable than the reduction of H_2O_2 to OH^\bullet , though the difference is very trivial. As the actual reduction and oxidation take place at adsorption site on the surface of photocatalyst, the redox properties may significantly change depending on the degree of the stabilization energy by the adsorption [118].

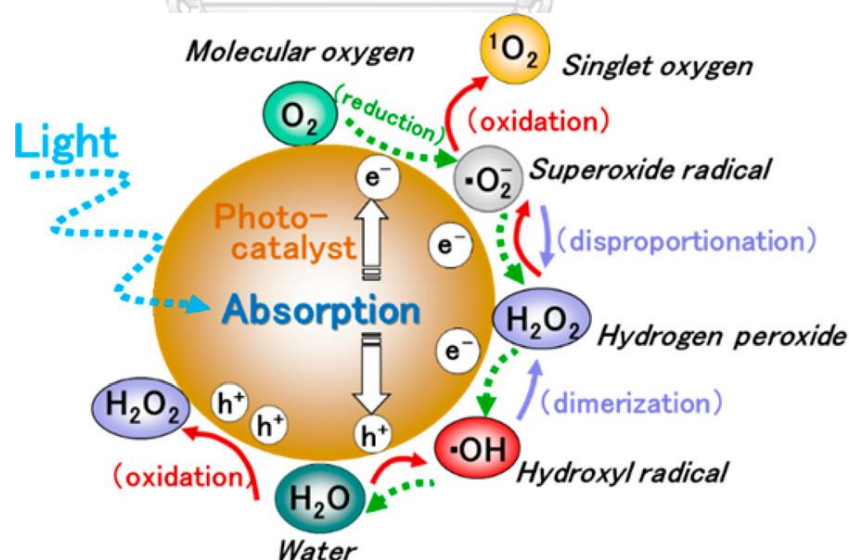


Figure 2.20 Reactive oxygen species generated in the photocatalytic reduction and oxidation steps of oxygen and water [118].

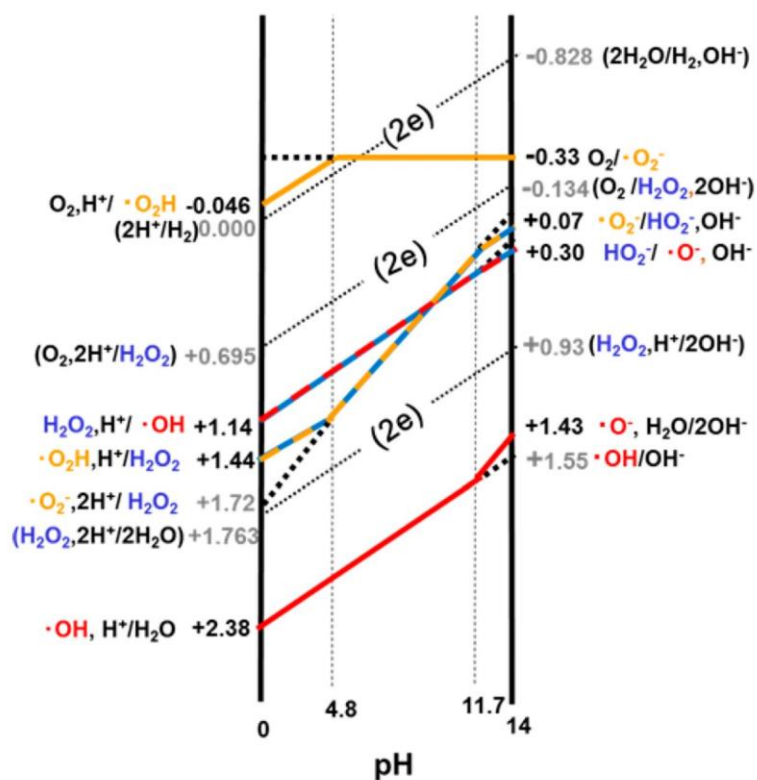
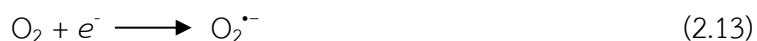


Figure 2.21 pH dependence of one-electron redox of H_2O , H_2O_2 , and O_2 . Dotted line shows two-electron ($2e^-$) process [117].

2.11.1 Superoxide radical ($\text{O}_2^{\cdot-}$)

A superoxide, also known as hyperoxide, is a compound that particularly important as the product of the one-electron reduction of dioxygen (O_2), which occurs widely in nature. Superoxide radical ($\text{O}_2^{\cdot-}$) are generally reacted towards a variety of organic and inorganic targets. Whereas molecular O_2 is a diradical containing two unpaired electrons, the addition of a second electron fills one of its two degenerate molecular orbitals, leaving a charged ionic species with single unpaired electron and a net negative charge of -1 . The reduction of oxygen with photoexcited e^- in conduction band could generated $\text{O}_2^{\cdot-}$ as depicted in Eq. (2.13).



The proposed mechanism of the reduction of O_2 on the surface of TiO_2 are illustrated in Figure 2.22. The surface Ti^{4+} of TiO_2 that adsorbs water molecule can be reduced with photoexcited e^- and then O_2 strikes it instantly to form superperoxo species ($TiOO^{\bullet}$). These superperoxo species are reduced to peroxo species ($Ti(O_2)$) and consequently protonated to form hydroperoxo ($TiOOH$) at the surface as displayed in Path A in Figure 2.22. On the other side, the adsorbed oxygen molecule on surface of TiO_2 can take photoexcited e^- to generate $O_2^{\bullet-}$. If $O_2^{\bullet-}$ does not participate in the reaction, the generated $O_2^{\bullet-}$ is transformed to H_2O_2 via disproportionation with proton (H^+). Due to the low reactivity of $O_2^{\bullet-}$, it generally converts to hydroperoxo radical (HO_2^{\bullet}) by the protonation, whose lifetime is not long because of the rapid reaction with $O_2^{\bullet-}$ or HO_2^{\bullet} to form H_2O_2 [119]. Moreover, as implied in Figure 2.22, $O_2^{\bullet-}$ can be generated via the photocatalytic oxidation of H_2O_2 with photogenerated h^+ (Eq. (2.14)).

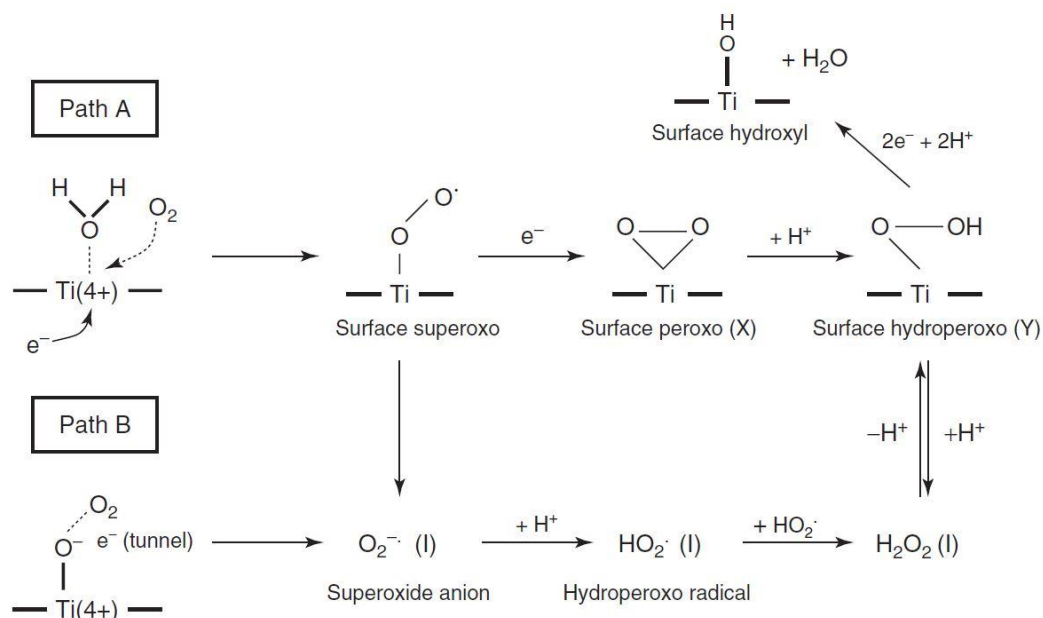


Figure 2.22 Reaction pathway for O_2 reduction on surface of TiO_2 [120].

2.11.2 Hydroxyl radical (OH[•])

Hydroxyl radical (OH[•]) is the neutral structure of hydroxide ion (OH⁻). It is one of the most highly reactive oxidizing agents that is able to react rapidly and unselectively with the chemical molecules and consequently short-lived. The lifetime of OH[•] radicals ranges between 0.001 and 1 second. Generally, OH[•] radicals are generated usually by coupled physical and/or chemical systems such as H₂O₂/Fe³⁺ or H₂O₂/Fe²⁺ (Fenton), H₂O₂/catalyst or peroxide/catalyst (Fenton-like), O₃ (ozonation), and H₂O₂/O₃ (peroxone) that are often associated with light irradiation. The plausible mechanism of OH[•] formation on the surface of TiO₂ in the presence of O₂ molecules under aquatic phase is proposed in Figure 2.23. OH[•] radicals are principally generated by the reduction of H₂O₂, which is created by the two-electron oxidation of H₂O and/or two-electron reduction of O₂ molecules.

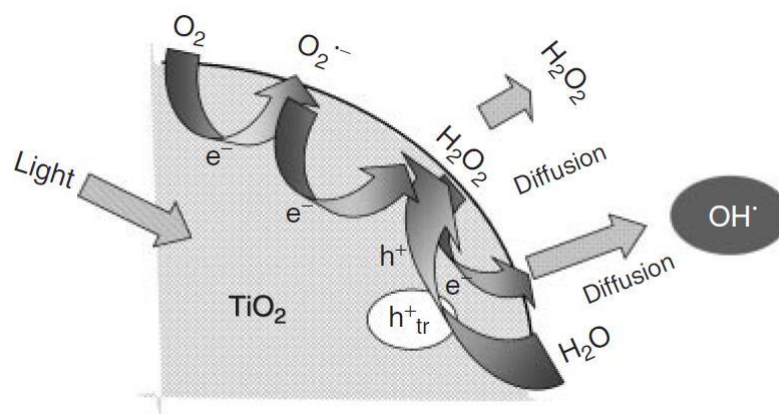
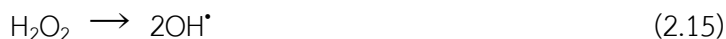


Figure 2.23 A proposed reaction scheme of OH[•] formation on irradiated TiO₂ surface [121].

In the system with H₂O₂, it mainly absorbs UV irradiation in the range of UV-C spectrum (100–280 nm) leading to yield two molecules of OH[•] radical via photolysis reaction as shown in Eq. (2.15) [122]. However, a potential drawback of these generated

OH[•] radicals is scavenged by H₂O₂ itself led to the formation of hydroperoxo radical (HO₂[•]) and water (Eq. (2.16)).



The later reaction has been stated to have a quite low rate constant ($k = 2.7 \times 10^7 \text{ M}^{-1}\text{s}^{-1}$) [123]. Thus, to maximize the effectiveness of OH[•] radicals in photocatalytic activity, the concentration of added H₂O₂ should be maintained at values where its ability to scavenge OH[•] radicals is limited compared to the other water constituents and/ or organic molecules. Moreover, the quantum yield of OH[•] radicals (Φ_{OH}) in the photolysis of H₂O₂ (Eq. (2.15)) is reported to be $\Phi_{\text{OH}} = 2.09 \pm 0.36$ in the gas phase and $\Phi_{\text{OH}} \sim 1$ in an aqueous solution [124]. The H₂O₂ photolysis yields two OH[•] radicals, which are unrestricted in the gas phase but are bounded with the solvent molecules in an aqueous solution. This solvent cage favors recombination as followed Eq. (2.17), which competes with OH[•] diffusion into the solution bulk for participation photocatalytic reaction.



2.11.3 Singlet molecular oxygen (¹O₂)

Singlet oxygen (¹O₂) is a high-energy form of oxygen, which is more chemical reactivity toward organic molecules than triplet ground state of oxygen (³O₂). Figure 2.24 demonstrated the formation pathway of singlet oxygen via the consecutive reduction and oxidation of O₂ molecule. The generated O₂^{•-} via reduction of O₂ with photoexcited e⁻ can be consecutively reduced with photogenerated h⁺ to form singlet oxygen as indicated by Eq. (2.18).



Since three electrons in the π^* state of $O_2^{\bullet -}$ cannot be discriminated from one another, three electronic state forms could be produced hinging on the relocated electron, which including $^3\Sigma_g^-$, $^1\Delta_g$, and $^1\Sigma_g^+$ states. The latter of two electronic states are named as “singlet oxygen”, which have energies of 94.3 kJ/mol and 156.9 kJ/mol above the first triplet ground state, respectively. The lifetime of $^1\Sigma_g^+$ state is extremely short in H_2O ($\sim 10^{-11}$ s) and straightaway changed to the $^1\Delta_g$ state of singlet oxygen, which is considered the chemically relevant form of 1O_2 . The lifetimes of 1O_2 greatly relied on its surrounding environment. It was reported to be about 2 μs for TiO_2 powder suspensions in water [125].

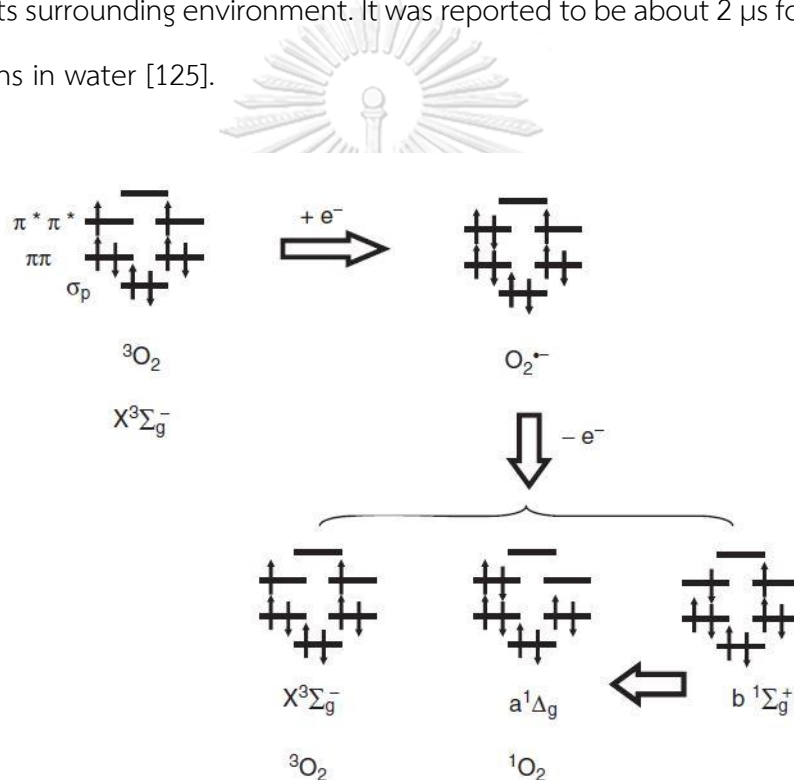


Figure 2.24 The pathway and spin states of singlet molecular oxygen formation.

2.12 Literature reviews

Photocatalytic oxidation over suspended solid photocatalysts (e.g. TiO_2 , ZnO) has been proposed as a sustainable process for treatment and purification of water and wastewater as well as the process for photoconversion of waste organic compound (e.g. glycerol) to hydrogen, methane, alcohols (e.g. ethanol) and other

hydrocarbons, which have high value-added substance. TiO_2 exhibits relatively high stability and activity under ultraviolet light, whose energy outdoes its band gap. The improvement of TiO_2 photocatalysts unveiling high reactivity under visible light should be addressed to not only proceed reaction using the solar spectrum but also suppress the recombination effect of e^- and h^+ in reaction process. Up to preceding few decades, various research works for TiO_2 modification and its applications for organic molecule transformation or degradation have been continuously proposed.

Augugliaro et al. [126] studied photocatalytic oxidation of glycerol by using home-prepared TiO_2 in rutile, anatase, and mixed anatase-rutile crystalline phase structure compared with those of commercial rutile and Degussa P25 in two different batch photoreactors, a cylindrical photoreactor and an annular photoreactor. The detected aqueous phase glycerol oxidation products in all system were GCD, DHA, FMA and CO_2 . Cylindrical photoreactor showed higher reaction rate and selectivity for all samples than annular photoreactor, due to the different reactor geometries and irradiation fields. Commercial Degussa P25 exhibited the highest photocatalytic activity among all samples with 25% glycerol conversion at catalyst amount 0.1 g/L and 5.2 h of irradiation time under incident photon flux of 1.2 mW/cm^2 . The selectivity of GCD, DHA, FMA, and CO_2 was found around 12%, 7.5%, 6.5%, and 20.6%, respectively.

The photocatalytic mechanism on the catalyst surface of Degussa P25 TiO_2 and Merck TiO_2 was investigated by Minero et al. [127] with using glycerol as a probe molecule. GCD and DHA are mainly observed as main products over Merck TiO_2 , while the major products catalyzed by Degussa P25 were glycolaldehyde (GCAD) and FMD. The dissimilar of major product between different TiO_2 specimens was principally due to the different surface morphology. Merck TiO_2 has a lower density and more uniform surface hydroxyl sites than Degussa P25 TiO_2 , which are more defect on the surface particle. The different surface characteristics of TiO_2 results in the unlike mechanism

of glycerol transformation. When glycerol molecules are weakly adsorbed on the surface of TiO_2 , the OH^\bullet radical mediated mechanism are undergone with H-abstraction to form C3 oxidation products (GCD and DHA). On the contrary, if chemisorption of glycerol was occurred on the surface of TiO_2 , the C2 (GCAD) and C1 (FMD) product were generated through β -fragmentation via direct e^- transfer mechanism.

Chong et al. [128] performed the photocatalytic reaction of aqueous glycerol on different facet of TiO_2 loaded with various metal nanoparticles including Rh, Ru, Cu, Ni, Pt, Pd, and Au. Glycerol can be converted with highly selective to hydroxyacetaldehyde (HAA) about 90% on the rutile TiO_2 , which have a high percentage of (110) facets, while anatase TiO_2 with dominant (101) or (001) facets can only provide a selectivity of HAA less than 50% and 20%, respectively. In addition, when metal co-catalyst was loaded on rutile TiO_2 with dominant (110) facet, the conversion of glycerol was significantly enhanced, and the yield of hydrogen production was also greatly increased. The selectivities of HAA were over 90% for all of the photocatalysts deposited with different metals. Thus, this can be implied that the major role of the metal co-catalyst are to improve the photogenerated h^+ and e^- charge separation, and catalyze H_2 production, while the selectivity of HAA was mainly depended on the facets of TiO_2 , not on the loaded metal co-catalysts.

The mechanism and kinetics of photocatalytic oxidation and reforming reaction of glycerol over TiO_2 and Pt/TiO_2 suspensions have been proposed by Panagiotopoulou et al. [129]. The general reaction pathways of photo-oxidation and photo-reforming are similarly. That is, the initial transformation steps of glycerol were proceeded involving either dehydrogenation reaction to form GCD or hydrogenolysis reaction to form propylene glycol. Afterwards, the several intermediates, including acetaldehyde, 2-oxopropanol, glycolaldehyde, ethanol, methanol and acetone can be continually progressed through decarbonylation, dehydrogenation and dehydration reactions.

Eventually, these intermediates are converted to gas phase, including CO_2 and H_2 . The rate of photo-oxidation and reforming of glycerol was quite low over bare TiO_2 and considerably improves over the presence of Pt on TiO_2 . The existence of Pt co-catalyst can efficiently separate the photogenerated h^+ and e^- , lead to suppress the e^-h^+ recombination as well as enhance the interfacial e^- transfer to electron acceptors. It was mainly due to the formation of Schottky barrier at TiO_2 and Pt metal interface. which resulted in efficient trapping of photogenerated e^- .

López-Tenllado et al. [130] prepared M/ TiO_2 photocatalyst (M=Au, Pt, Pd) by deposition-precipitation, impregnation, and photo-deposition method with different amounts of metal loading (0.5 – 3.0 wt.%) and employed toward hydrogen photocatalytic production from C3-chain alcohols (glycerol and isopropyl alcohol). The deposition of metal led to the formation of metal-titania interaction, resulting in the enhancement of e^- transfer from semiconductor to deposited metal, which promoted the photocatalytic activity. The 0.5%wt. Pt deposited on TiO_2 made by photo-deposition method was found to be superior in photocatalytic activity toward hydrogen production than deposited Pd and Au in both case of using glycerol and isopropyl alcohol as substrates. Both substrates are followed a dissociative adsorption Langmuir-Hinshelwood mechanism, but glycerol molecules are stronger adsorbed on TiO_2 surface than isopropyl alcohol.

Zhao et al. [131] also investigated the hydrogen production from glycerol-water mixtures by using Bi-doped TiO_2 nanotubes, which prepared through hydrothermal method with variable Bi/Ti molar ratios (0-5 %). The results showed that doped Bi can extend the adsorption wavelength toward visible light region, which should be related to the formation of Ti-O-Bi in the network of TiO_2 nanotubes. Moreover, Bi doping was created the new energy level of Bi ion below the conduction band of TiO_2 , which resulted in a reduction of band gap energy as well as a diminution of e^-h^+

recombination rate. The Bi doping with 2% of Bi/Ti molar ratio on TiO₂ nanotubes exhibited the highest hydrogen production rate under both solar and UV light spectrum. The hydrogen production rates decreased with excessive doping content of Bi due to the transformation of nanotubes with anatase phase to nanobelts with entire titanate phase (H₂Ti₂O₅·H₂O) structure.

The role of Bi for the enhancement of visible light adsorption property of TiO₂ photocatalyst was also pronounced by Bagwasi et al. [132]. They prepared Bi modified nitrogen doped TiO₂ (N-TiO₂) in the range of 1-13 mol.% Bi content via two steps of hydrothermal and impregnation hydrolysis method. The results revealed that all Bi modified N-TiO₂ photocatalysts showed the higher photocatalytic activity for the degradation of 2,4-Dichlorophenol under visible-light irradiation due to the presence of metastable bismuth titanate (Bi₂₀TiO₃₂) species in as-prepared photocatalyst which can enhance the light adsorption property toward the visible region together with effective photogenerated h^+ and e^- charge separation.

Tsukamoto et al. [133] stated that the photocatalytic activity of metal doped TiO₂ strongly relied on the catalyst architecture by studied the effect of Au metal deposited size and location on TiO₂ support for aerobic oxidation reaction. The results clarified that Au nanoparticles with diameter lower than 5 nm can promote the visible light adsorption due to the resonance oscillation of free e^- on Au, known as surface plasmon resonance (SPR). The location of Au nanoparticles at the interface of anatase and rutile crystal structure efficiently promotes aerobic oxidation owing to appropriated e^- transfer in Au-rutile-anatase contact site. That is, the activated e^- via SPR by visible light irradiation were transferred to rutile and then to adjacent anatase TiO₂ and consequently reacted with O₂ to form reactive oxygen species which can catalyzes the oxidation of substrates.

Bashir et al. [134] investigated the effect of metal loading in both mono- and bimetallic (Au, Pd and AuPd) on the photo-oxidation and photo-reforming of ethanol. The bimetallic AuPd containing 1.2 wt.% Au and 2.0 wt.% Pd decorated on TiO₂ exhibited the highest activity for both photo-oxidation and photo-reforming reaction mainly due to the synergistic effect between two metals. The presence of Au in bimetallic AuPd can keep the decorated Pd in its metallic states, which facilitated the charge transfer from Au to Pd resulting in the prolongation of photogenerated h^+ - e^- lifetime.

In 2011, Chen et al. [135] firstly developed an alternative approach to enhance the visible light and infrared adsorption of TiO₂ by introducing defect disorders in the structure of TiO₂ through the hydrogenation process at 20 bar and 200 °C for 5 days. Large amount of introduced defect disorder at the surface layer of TiO₂ was substantially shifted valance band position about 2.18 eV and also created the mid-gap state energy levels below the conduction band. These generated mid gap states can extend to and overlap with the conduction band edge to form band tail structure, which resulted in decreasing of band gap energy. Moreover, these generated mid gap states also acted as trapping sites of photo-excited e^- and prevent them to recombine with photogenerated h^+ . This finding is open up a new tactic for designing solar-driven photocatalyst.

Sinhamahapatra et al. [136] synthesized the black (defective) TiO₂ NPs through the two-step method of magnesiothermic reduction under 5% H₂-Ar atmosphere followed by acid treatment. All as-synthesized black TiO₂ NPs were deposited with Pt metal by photo-reduction and applied toward photocatalytic hydrogen production in water-methanol mixture. All prepared sample possessed the lower band gap energy than commercial anatase TiO₂ and the existence of band tail structure in both conduction band and valence band side, which could be attributed to the presence

of Ti^{3+} defects and/or oxygen vacancies in TiO_2 structure. In the presence of 1% Pt as co-catalyst with black TiO_2 provided highest hydrogen production rate about $43 \text{ mmol h}^{-1} \text{ g}^{-1}$ from the water and methanol mixture under the full light spectrum of solar range irradiation. However, in the absence of methanol, only small amount of hydrogen was produced. This is because methanol acted as sacrificial reagent for capturing photogenerated h^+ , which diminished the photogenerated h^+ and e^- recombination.

Apart from TiO_2 photocatalyst, Bi_2WO_6 was reported as efficient photocatalyst toward selective transformation of glycerol to dihydroxyacetone using oxygen as oxidant in water by Zhang et al. [137]. The glycerol was selectively oxidized to dihydroxyacetone with 91% selectivity at 96% conversion under visible light irradiation. In addition, they also performed the reaction test under N_2 atmosphere and the results showed trace conversion of glycerol, approving that oxygen was the prime oxidant in selective oxidation of glycerol. Besides, the series of control experiment with various radical scavenger, including ammonium oxalate (AO) for trapping photogenerated h^+ , benzoquinone (BQ) for scavenging $\text{O}_2^{\bullet-}$ radicals, and tert-butyl alcohol for OH^{\bullet} radicals trapping, were also parallel performed in order to better understanding the mechanism for selective photooxidation of glycerol. The observation provided that OH^{\bullet} radicals did not generate over Bi_2WO_6 and the main reactive oxygen species for selective oxidation of glycerol to dihydroxyacetone is photogenerated h^+ and $\text{O}_2^{\bullet-}$ radicals, which generated from the band gap excitation upon visible light irradiation. They proposed that the glycerol molecules, which adsorbed on the surface of catalyst, are primarily oxidized with photogenerated h^+ to form some intermediates and subsequently reacted with $\text{O}_2^{\bullet-}$ radicals to form dihydroxyacetone.

The various reactive oxygen species (ROS) generated under irradiation of TiO_2 photocatalyst was also promised as a vital factor to understand the involving

mechanism for organic molecules transformation or degradation. Up to date, there is still contradictory about the roles and contributions of which ROS deserves for transformation of organic compounds. Guo et al. [138] inspected the formation of various ROSs through the photooxidation of 1,5-diphenyl carbazide (DPCI) over TiO₂ with pure anatase phase, pure rutile phase. The quantity of ROS increased with the increasing of TiO₂ catalyst loading and irradiation time. The DPCI was mainly oxidized with radical species (e.g. ¹O₂, O₂^{•-}, and OH[•] radicals) over irradiated rutile TiO₂, while the photogenerated *h*⁺ are mainly involve for DPCI photooxidation over anatase TiO₂. It seems that the different phase structure of TiO₂ has affected on the type of ROS generation.

Kuang et al. [139] also studied the role of reactive oxygen species and photogenerated *h*⁺ in the photodegradation of anionic dye orange II (OII) and cationic dye methylene blue (MB) by TiO₂ under UV illumination using radical scavenger. The photogenerated *h*⁺ and surface-OH[•] radicals were main contributor for photodegradation of both dyes, giving an account of 60% of the total degradation and remaining 40% of total degradation could be contributed to ¹O₂, O₂^{•-} radicals. O₂^{•-} played a more important role in the degradation of OII, while ¹O₂ provided the similar contribution in both photodegradation of OII and MB. The contribution of radicals at the surface of catalyst was intensely significant to the photodegradation of organic dyes compared with the radicals in bulk solution. However, some results still intrigue mysteries because the generation of ROS in dyes system is complex due to the nature of photosensitizer dye molecules which could both quench and generate some ROSs at the same time. But at least, it can be suggested that the mechanism for photocatalytic degradation of organic dyes may vary with the concentration and type of ROSs produced in the system.

CHAPTER III

RESEARCH METHODOLOGY

This chapter provided the information about chemical substances and materials as well as experimental procedures for preparing the TiO₂-based photocatalyst and studying the photocatalytic conversion of glycerol over TiO₂-based photocatalyst. The catalyst preparation techniques were described. Also, the relevant characterization techniques were presented.

3.1 Chemical substances and materials

1. Glycerol (C₃H₈O₃), 99.5% purity, QReC
2. Hydrogen peroxide (H₂O₂), 30%wt, Merck
3. Oxygen gas (O₂), 95% purity, Praxair
4. Nitrogen gas (N₂), 99.99% purity, Praxair
5. Hydrogen gas (H₂), 99.999% purity, Praxair
6. Titanium (IV) dioxide (TiO₂), Pure anatase, Sigma Aldrich
7. Titanium (IV) dioxide (TiO₂), Pure rutile, Sigma Aldrich
8. Titanium (IV) dioxide (TiO₂), P25 Degussa, Sigma Aldrich
9. DL-Glyceraldehyde (C₃H₆O₃), ≥90% (GC), Sigma Aldrich
10. Dihydroxyacetone (C₃H₆O₃), ≥94%, Merck
11. Formaldehyde (HCHO), 37% w/w solution, Merck
12. Glycolaldehyde dimer (C₄H₈O₄), Sigma Aldrich
13. Glycolic acid (C₂H₄O₃), 70% w/w solution, Ajax Finechem
14. Glyceric acid (C₃H₆O₄), 20% w/w solution, TCI
15. β-Hydroxypyruvic acid (C₃H₄O₄), ≥95.0% (dry substance), Sigma Aldrich
16. Sulfuric acid (H₂SO₄), 98% purity, QReC

17. Nitric acid (HNO_3), 65% purity, QReC
18. Hydrochloric acid (HCl), 37% purity, Sigma Aldrich
19. Acetonitrile (CH_3CN), HPLC grade 99.9% purity, Merck
20. Poly(vinyl alcohol) ($[-\text{CH}_2\text{CHOH}-]_n$), 99+% hydrolyzed, Sigma Aldrich
21. Isopropyl alcohol ($\text{C}_3\text{H}_7\text{OH}$), $\geq 99.7\%$ purity, QReC
22. Furfuryl alcohol ($\text{C}_5\text{H}_6\text{O}_2$), 98.0% purity, Sigma Aldrich
23. 4-Chlorobenzoic acid ($\text{ClC}_6\text{H}_4\text{CO}_2\text{H}$), 99.0% purity, Sigma Aldrich
24. *p*-Benzoquinone ($\text{C}_6\text{H}_4(=\text{O})_2$), $\geq 98.0\%$ purity, Sigma Aldrich
25. Ammonium oxalate monohydrate ($(\text{NH}_4)_2\text{C}_2\text{O}_4 \cdot \text{H}_2\text{O}$), $\geq 99.5\%$, Sigma Aldrich
26. Potassium Iodide (KI), 99.0% purity, Ajax Finechem
27. Potassium Chloride (KCl), $\geq 99.0\%$ purity, Sigma Aldrich
28. Silver nitrate (AgNO_3), $\geq 99.0\%$ purity, Sigma Aldrich
29. Chloroplatinic acid hexahydrate ($\text{H}_2\text{PtCl}_6 \cdot 6\text{H}_2\text{O}$), Sigma Aldrich
30. Gold (III) chloride trihydrate ($\text{HAuCl}_4 \cdot 3\text{H}_2\text{O}$), Sigma Aldrich
31. Palladium (II) chloride (PdCl_2), Sigma Aldrich
32. Bismuth (III) chloride (BiCl_3), Sigma Aldrich
33. Titanium wire (99.99 wt.%, Nilaco Co.Ltd., Japan)
34. Ultrapure water
35. Deionized water

3.2 Laboratory instruments

1. Nylon Syringe filter, 0.1 μm pore size (CHROMAFIL[®] Xtra PA-45/13)
2. Polytetrafluoroethylene Membrane Filter, 0.1 μm pore size (Merck Millipore)
3. Oven (Model ED 115; WTB binder)
4. Hotplate and stirrer
5. Centrifuge (KUBOTA KC-25)

6. Ultrasonic water bath (NXPC-1505P, Koda)
7. High voltage bipolar pulse power supply (Kurita Co. Ltd, Japan)
8. High pressure mercury lamp (RUV 533 BC, Holland)

3.3 Synthesis of monometallic decorated on TiO₂

Four types of monometallic-decorated TiO₂ photocatalysts were prepared through sol-immobilization technique including Au/TiO₂, Pt/TiO₂, Pd/TiO₂ and Bi/TiO₂ by following steps. Firstly, 12 mL of 1 wt.% of HAuCl₄ solution (Au metal precursor) was dissolved in 38 mL of deionized water. Then, 2 wt.% of polyvinyl alcohol (PVA) was added to the precursor solution as protective agent under stirring at constant 300 rpm in order to stabilize the metal dispersion on the support and prevent agglomeration. Approximately 1.94 g of TiO₂ was added to the prepared solution and then excess NaBH₄ was slowly added to the colloid solution. The reaction was held for 24 h at atmospheric pressure and temperature to obtain complete sol immobilization. The obtained mixture was filtered and washed thoroughly several times with deionized water until no chloride ions were detected in the filtrate solution by the AgNO₃ test. Finally, the obtained solid was dried at 110 °C in hot air oven overnight and subsequently removed the organic scaffold residue and activated by heat and chemical treatments under a N₂ flow at 350 °C for 3 h followed by a H₂ flow at 350 °C for 3 h, respectively. At this stage, the ready-to-use Au₃/TiO₂ at 3 wt% Au content will be obtained.

The similar procedures were repeated but using 7.98 mL of 2 wt.% of H₂PtCl₆ solution dissolved in 42.02 mL of deionized water, 5.00 mL of 2 wt.% of PdCl₂ solution dissolved in 45.00 mL of 0.2M HCl and 9.09 mL of 1 wt.% of BiCl₃ solution dissolved in 40.91 mL of 0.2M HCl for synthesized Pt₃/TiO₂, Pd₃/TiO₂ and Bi₃/TiO₂, respectively.

The step-by-step preparation of monometallic decorated on TiO₂ was illustrated in Figure 3.1.

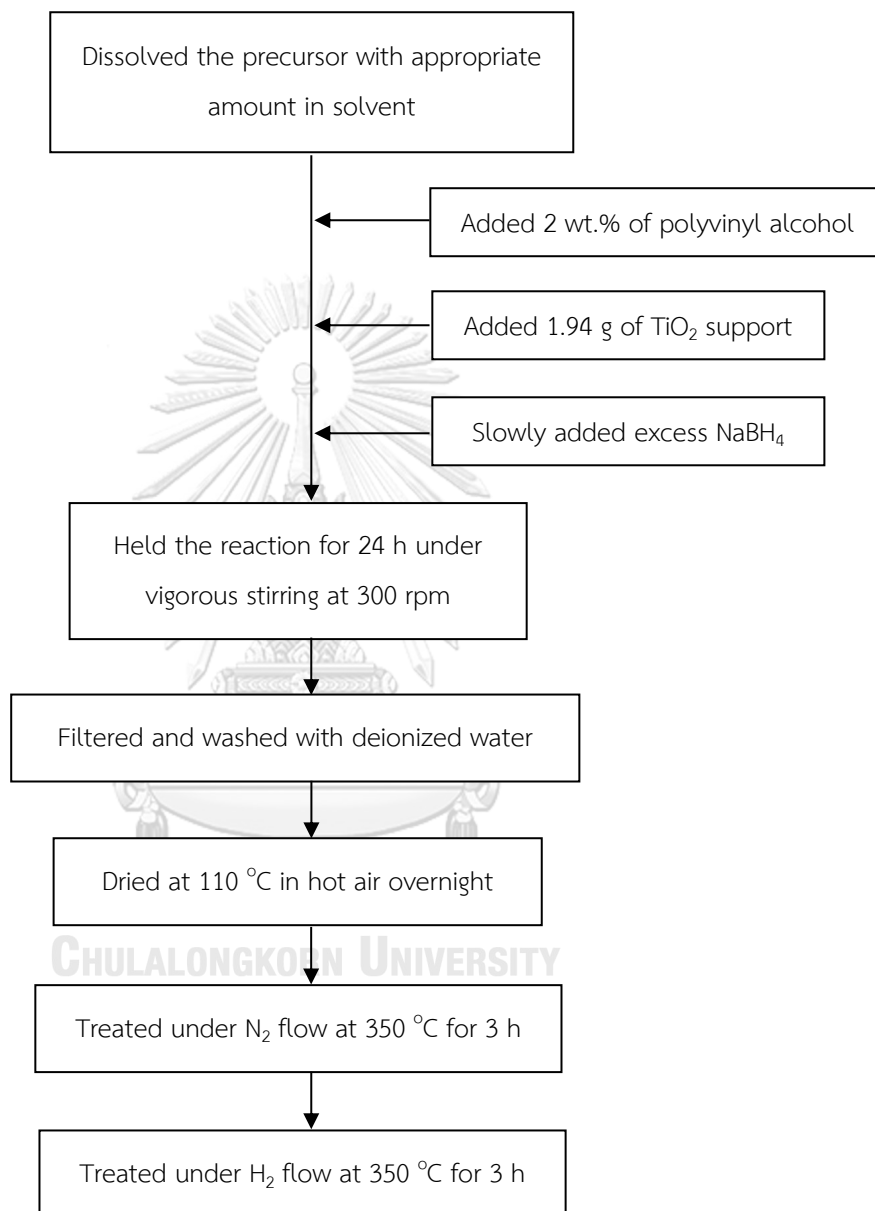


Figure 3.1 Preparation procedure of monometallic-decorated TiO₂ photocatalyst.

3.4 Synthesis of Au-based bimetallic nanoparticles decorated on TiO₂

Three types of Au-based bimetallic-decorated TiO₂ photocatalyst were prepared through sol-immobilization technique including AuPt/TiO₂, AuPd/TiO₂ and AuBi/TiO₂ by following steps. Firstly, 12 mL of 1 wt.% of HAuCl₄ solution was mixed with 16 mL of 1 wt.% of H₂PtCl₆ solution and dissolved in 22 mL of deionized water. Then, 2 wt.% of polyvinyl alcohol (protective agent) was added to the mixture precursor solution under stirring at constant 300 rpm in order to stabilize the metal dispersion on the support and prevent agglomeration. Approximately 1.88 g of TiO₂ was added to the prepared solution and then excess NaBH₄ was slowly added to the colloid solution. The reaction was held for 24 h at atmospheric pressure and temperature to obtain complete sol immobilization. The obtained mixture was filtered and washed thoroughly several times with deionized water until no chloride ions were detected in the filtrate solution by the AgNO₃ test. Finally, the obtained solid was dried at 110 °C in hot air oven overnight and subsequently removed the organic scaffold residue and activated by heat and chemical treatments under a N₂ flow at 350 °C for 3 h followed by a H₂ flow at 350 °C for 3 h, respectively. At this stage, the ready-to-use bimetallic Au₃Pt₃/TiO₂ at 3 wt.% Au and 3 wt.% Pt content will be obtained.

The similar procedures were repeated but using 5 mL of 2 wt.% of PdCl₂ solution, which dissolved in 0.2 M HCl, mixed with 12 mL of 1 wt.% of HAuCl₄ solution and 9.09 mL of 1 wt.% of BiCl₃ solution, which dissolved in 0.2 M HCl, mixed with 12 mL of 1 wt.% of HAuCl₄ solution for synthesized Au₃Pd₃/TiO₂ and Au₃Bi₃/TiO₂, respectively. The step-by-step preparation of Au-based bimetallic decorated on TiO₂ was illustrated in Figure 3.2.

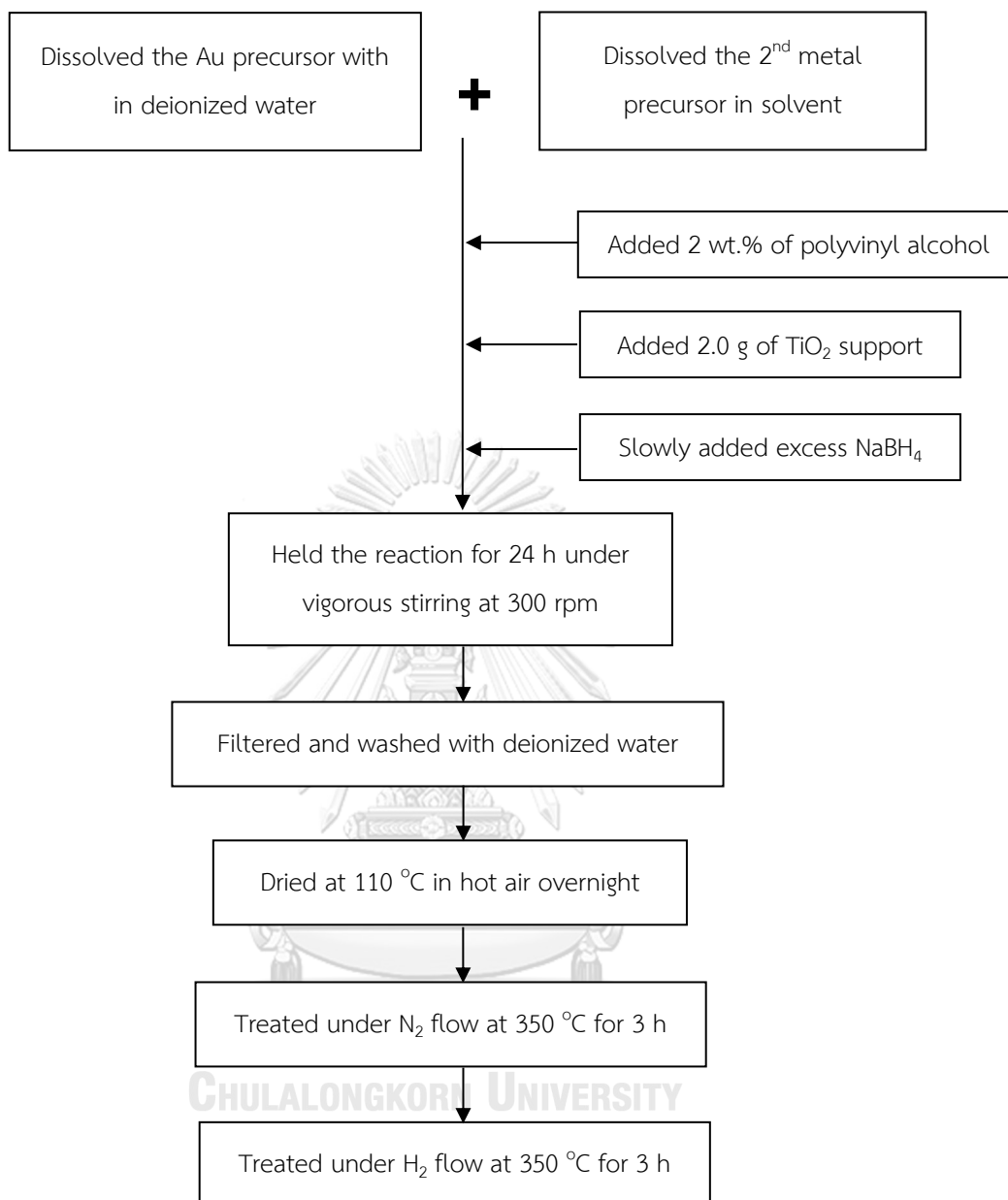


Figure 3.2 Preparation procedure of Au-based bimetallic-decorated TiO₂ photocatalyst.

3.5 Synthesis of black TiO₂ through solution plasma process

In this part, the defective black TiO₂ nanoparticles (NPs) was synthesized through the solution plasma process in a glass vessel having a capacity of 200 mL under atmospheric pressure as displayed in Figure 3.3.

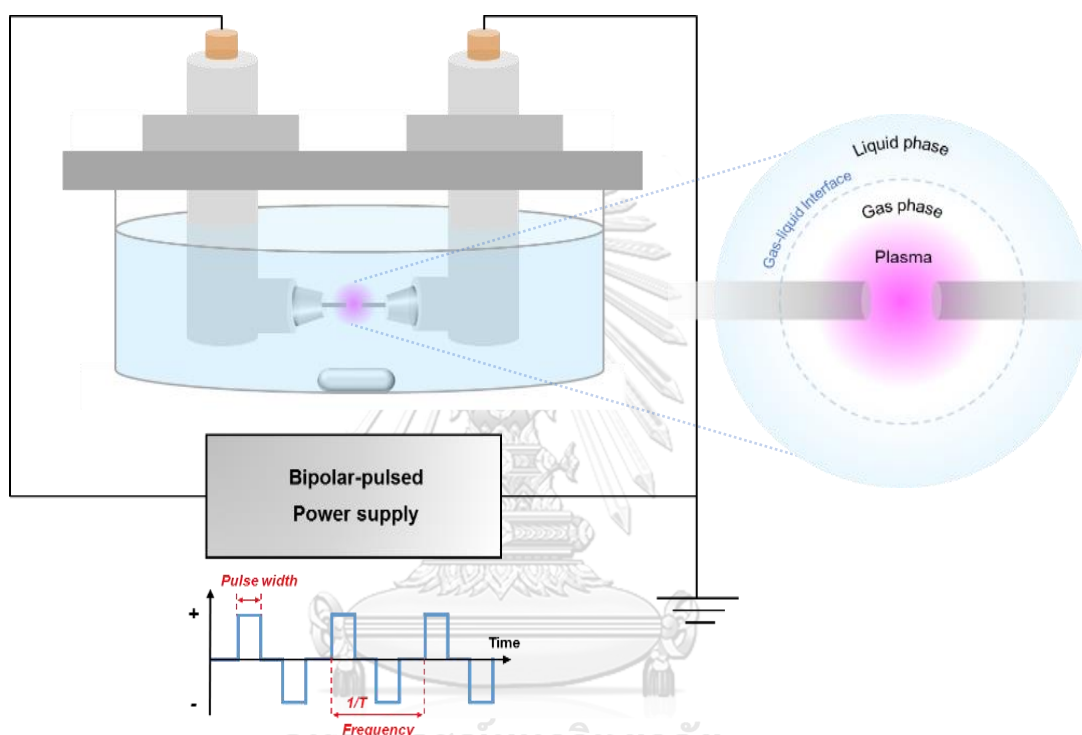


Figure 3.3 Schematic diagram of the experimental set up of solution plasma process.

Two of 1-mm diameter Ti wires (99.99 wt.%, Nilaco Co.Ltd., Japan) were used as the symmetric electrodes for the Ti precursor. Prior to use, the electrode tips were carefully polished with abrasive paper in order to obtain a confined smooth surface area. Both electrodes were equipped with a Teflon holder and submersed inside the electrolyte solution at the center of the reactor vessel, and connected with a high voltage bipolar pulsed power supply, which can strictly control the repetition frequency and pulse width. The plasma was generated around the tips of both

electrodes within the range of the applied frequency and pulse width of 20-80 kHz and 0.5-2.0 μ s, respectively. To control the reaction temperature at under 60 °C, the reactor vessel was immersed in a cooling bath with continuous stirring at 250 rpm. When the synthesis time was achieved (4 h), the obtained defective black TiO₂ NPs were collected by filtration a polytetrafluoroethylene membrane with an average pore size of 0.1 μ m (JWVP04700, Merck Millipore) and washed repeatedly with ultrapure water and then dried at 100 °C overnight.

3.6 Photocatalytic activity test

The photocatalytic conversion of glycerol to value-added compounds was carried out in liquid phase system. The photoreactor was a hollow cylindrical glass with a diameter of 10 cm which was placed in middle of a UV-protected box with dimensions of 0.68m \times 0.68 m \times 0.78 m. A 120 W UV high pressure mercury lamp (RUV 533 BC, Holland) with light spectral distribution as shown in Figure 3.4 was used as a light intensity generator. The UV lamp was constructed on the roof of the UV-protected box as displayed in Figure 3.5. In each experiment, 100 mL of 0.3 M glycerol solution was agitated at 300 rpm to achieve complete mixing. Oxygen was supplied continuously into the reactor at a constant feed rate of 200 mL/min. Prior to light illumination, the selected photocatalyst was suspended in a glycerol solution in the dark room for 30 min to reach an adsorption equilibrium. As the experiment progressed, the reaction was monitored by taking the liquid sample of around 2 mL at regular time intervals during reaction period. Then all collected liquid products were centrifuged on a KUBOTA KC-25 digital laboratory centrifuge to separate the solid catalyst from the aqueous product.

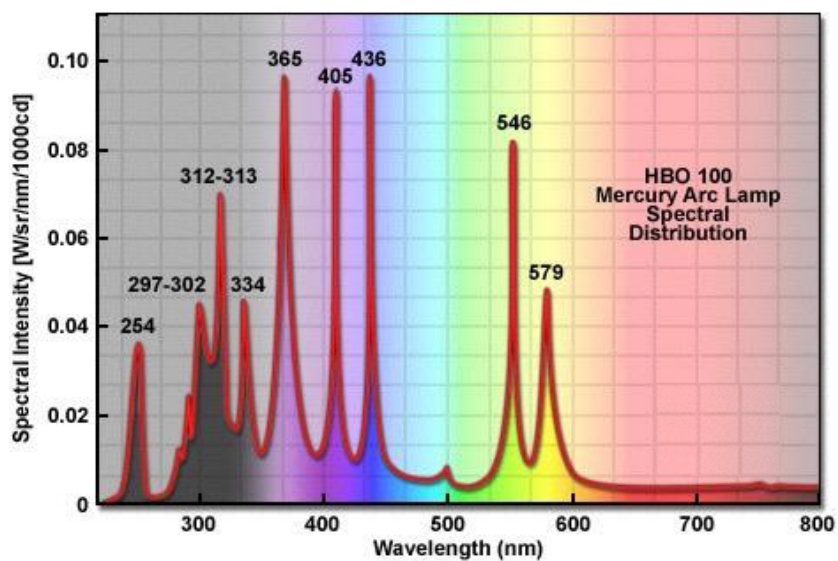


Figure 3.4 Light distribution spectra of 120 W UV high pressure mercury lamp.

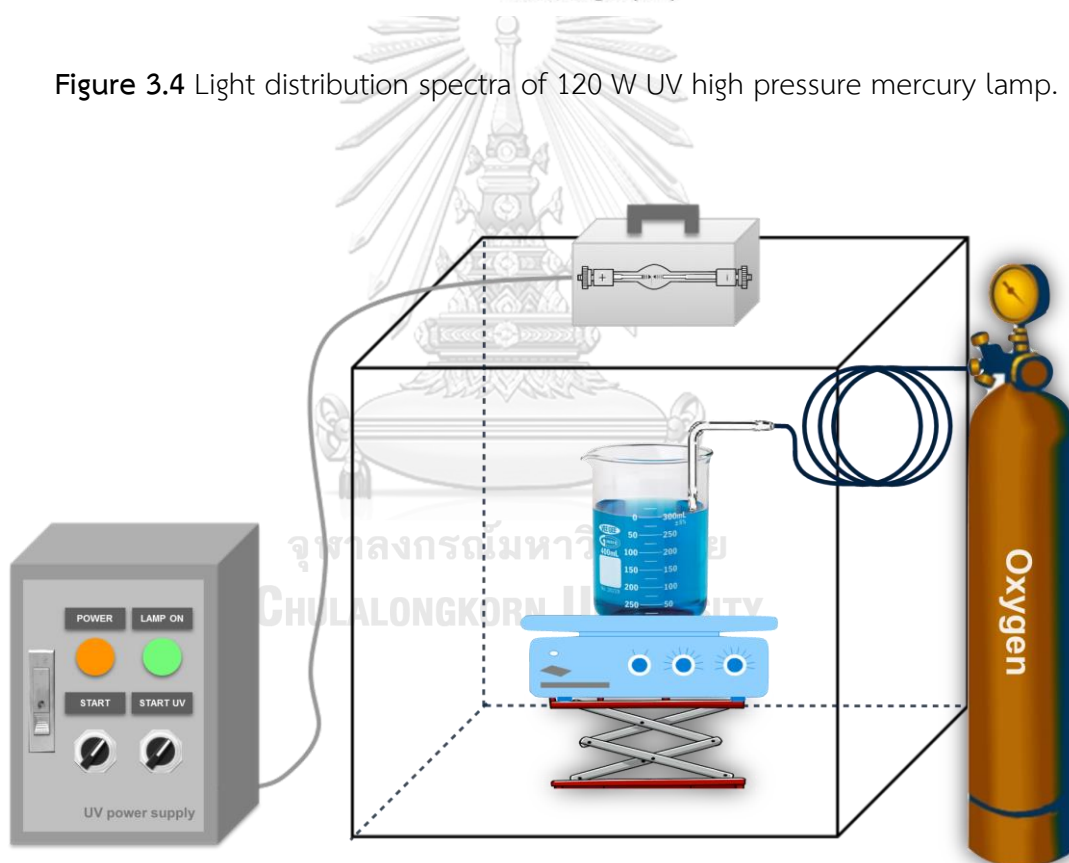


Figure 3.5 Schematic diagram of photoreactor with external light source.

The quantities of glycerol and all generated products in liquid phase were quantitatively analyzed by a high performance liquid chromatography (HPLC, Shimadzu

LC-10 ADVP) with a RID-10A refractive index detector. The stationary phase was an Aminex HPX-87H ion-exclusion (300 x 7.8 mm), and the mobile phase was a water-acetonitrile solution 65:35 (volume/volume) ratio with 0.5 mM H₂SO₄ at constant flow rate of 0.7 mL/min. The column temperature was controlled at 60 °C. The injection volume was 10 µL. The conversion of glycerol (*X*), yield (*Y*) and selectivity (*S*) of each selected product of the photocatalytic oxidation was calculated according to Eqs. (3.1) to (3.3), respectively:

$$X(\%) = \frac{\text{Amount of glycerol converted (C-based mole)}}{\text{Total amount of glycerol in reactant (C-based mole)}} \times 100 \quad (3.1)$$

$$Y(\%) = \frac{\text{Amount of glycerol converted to product } j \text{ (C-based mole)}}{\text{Total amount of glycerol in reactant (C-based mole)}} \times 100 \quad (3.2)$$

$$S(\%) = \frac{\text{Amount of product } j \text{ generated (C-based mole)}}{\text{Total amount of generated products (C-based mole)}} \times 100 \quad (3.3)$$

3.7 Detection of the generated reactive oxygen species (ROS) in photocatalytic system

In this part, two techniques of ROS measurement were employed. For the first technique, the generation of reactive oxygen species (ROSs) including the OH[•] radical and singlet oxygen (¹O₂) were detected via the loss of specific scavengers including para-chlorobenzoic acid (*p*CBA) and furfuryl alcohol (FFA), respectively. The photocatalytic reaction was performed at identical condition of catalyst dosage, light intensity, and irradiation time with the presence of specific scavengers and the absence of glycerol. The variation of *p*CBA and FFA concentration was also quantitatively analyzed by HPLC equipped with Pinnacle II C18 column (240 x 4.6 mm). The mobile phase was a methanol-water-acetonitrile 55:35:10 (volume/volume) ratio with 10 mM H₂SO₄ for *p*CBA detection, and 50:50 (volume/volume) ratio of water-ethanol mixture

was used as a mobile phase for FFA determination. All of 10 μL sample injection passed through the column with a constant flow rate of 0.4 mL/min and the column temperature was fixed at 40 $^{\circ}\text{C}$.

For the second technique, the capture of ROSs was simultaneously performed with the glycerol conversion. In order to trap ROSs during the photocatalytic reaction, 10 mM of various scavengers, including potassium iodide (KI, a quencher of h^+ and OH^{\bullet} at surface), iso-propyl alcohol (IPA, a quencher of bulk OH^{\bullet}), benzoquinone (BQ, a quencher of $\text{O}_2^{\bullet-}$), ammonium oxalate (AO, a quencher of h^+), furfuryl alcohol (FFA, a quencher of $^1\text{O}_2$) were added to the glycerol solution containing photocatalyst, for the elucidation of the role of different ROSs associated with glycerol conversion and product distributions. The quantities of glycerol and all generated products in the presence of scavengers were also quantitatively analyzed by a HPLC equipped with Aminex HPX-87H ion-exclusion (300 x 7.8 mm). The mobile phase was a water-acetonitrile solution 65:35 (volume/volume) ratio with 0.5 mM H_2SO_4 at constant flow rate of 0.7 mL/min.

3.8 Catalyst characterizations

3.8.1 X-ray Diffraction (XRD)

The crystal and phase structures of as-prepared photocatalyst were analyzed by using D8 Discover-Bruker AXS X-ray diffractometer equipped with $\text{Cu K}\alpha$ irradiation ($\lambda = 1.54056 \text{ \AA}$). The tube voltage and current of XRD system was operated at 45 kV and 200 mA, respectively. For data acquisition, the 2θ angle was acquired from the range of 10 to 90° with a step size of 0.02° and a scan speed of 3.0 degree/min. The diffractogram peaks were identified using the JCPDS database, together with the crystal phase and the lattice constant of the compounds found in the as-prepared material composition.

3.8.2 X-ray Photoelectron Spectroscopy (XPS)

The elemental oxidation states of as-synthesized photocatalyst were assessed by X-ray photoelectron spectroscopy (XPS; Ulvac-PHI 5000 VersaProbe II) with a monochromatized Al $K\alpha$ X-ray source ($h\nu = 1486.6$ eV). Survey-scan XPS spectra were recorded from the range of 0 to 1100 eV at a pass energy of 47 eV with an acquisition step of 0.5 eV. Narrow-scan spectra for the high resolution of elemental analysis were recorded at a pass energy of 12 eV and an acquisition step of 0.1 eV. The compensation of the charge-up was performed using a neutralization gun. The values of the binding energies were calibrated with respect to the C1s peak at 284.5 eV (adventitious hydrocarbon). After subtraction of the Shirley-type background, the core-level spectra were decomposed into their components with mixed Gaussian–Lorentzian lines by a non-linear least squares curve-fitting procedure, using the public software package XPSPEAK 4.1. The binding energies (EB) and FWHM of the peaks were determined from the fitting results.

3.8.3 Scanning Electron Microscopy with Energy Dispersive X-ray Spectroscopy (SEM/EDS)

Morphologies and structures of as-prepared photocatalyst were examined by scanning electron microscope (SEM; JSM-6610LV) at an electron accelerating voltage of 0.3 to 30 kV and it was operated in a vacuum mode. Energy dispersive X-ray spectroscopy (EDS) were attached to SEM instrument to perform the chemical element analysis at atomic resolution.

3.8.4 Transmission Electron Spectroscopy with Energy Dispersive X-ray Spectroscopy (TEM/EDS)

Morphologies and particle sizes were evaluated by Transmission Electron Spectroscopy (TEM; JEM-2500SE) with an accelerating voltage of 200 kV. The samples

for TEM analysis were prepared by dispersion of as-synthesized photocatalyst in ethanol under ultrasonication for 15 min. Then, the suspension was dropped onto a 150 mesh Cu TEM grid and the solvent left to evaporate for overnight prior to the investigation. The average metal particle sizes and their distribution were calculated by averaging of not less than 100 particles randomly distributed in TEM images.

The elemental line scan and mapping of decorated metal were also observed on a JEOL 2100 Plus that was equipped with a Bruker EDS. The EDS analysis was analyzed by using a nominal electron beam size of 1 nm.

3.8.5 Brunauer-Emmett-Teller method (BET)

N₂ adsorption-desorption isotherms were carried out at -196 °C using a Quantachrome Autosorb-1 MP instrument to identify the BET surface area, pore size, and pore volume of as-prepared photocatalyst. The average pore diameter was calculated based on BJH method. Prior to performing the measurement, all samples were degassed at 300 °C for at least 6 h under vacuum. The analysis time was 5 h.

3.8.6 Fourier Transform Infrared Spectroscopy (FTIR)

The functional groups of as-prepared sample were analyzed using Fourier transform infrared spectroscopy (FTIR) (Nicolet-8700; Thermo Scientific) over the wave number between 500-4,000 cm⁻¹ with resolution of 0.5 cm⁻¹ at room temperature. Before analysis, the as-prepared samples were ground with potassium bromide (KBr) powder and compressed to form pellet for FTIR analysis.

3.8.7 Electron Spin Resonance Spectroscopy (ESR/EPR)

The unpaired spin electron and magnetism were examined from the electron spin resonance (EPR) spectra, recorded at room temperature on a JES-FA200 ESR

spectrometer (JEOL) under a microwave power of 1 mW with a frequency of 9.44 GHz. The magnetic field was calibrated using the g-value of the Mn^{2+} signal from a manganese (Mn) marker as the standards.

3.8.8 Dynamic Light Scattering (DLS)

The particle size, in term of volume-based particle size diameter, of as-prepared material was determined by dynamic light-scattering (DLS) technique using an ELS-7300K (Otsuka electronics) photometer with a nominal measurable range of 0.5-5,000 nm.

3.8.9 Ultra-Violet Spectroscopy (UV-Vis)

The mixture solution of as-prepared sample and deionized water were used for measuring the light adsorption spectra by UV-vis spectroscopy using a UV-3600 Spectrograph (Shimadzu, Japan) at room temperature in the spectral range from 200 to 800 nm, with a spectral resolution of 0.5 nm and an optical absorption path of 1 mm.

In addition, Diffuse Reflectance Ultraviolet-Visible-Near Infrared (UV-Vis-NIR) spectra were also used for measuring adsorption spectra of some prepared materials with a UV-Vis-NIR Spectrophotometer (Lambda 950, Perkin Elmer). Prior to UV-Vis-NIR measurements, the powdered sample was packed onto a 20 mm diameter sample holder using a flat grinder and placed on a $BaSO_4$ coated integrating sphere with $BaSO_4$ as the reference cell.

3.9 Plasma characterizations

3.9.1 Current and Voltage waveform

Fundamental characteristic of current and voltage waveform of the discharge plasma was measured using a digital oscilloscope (DS1202CA; RIGOL Technologies Inc.), equipped with a current probe (model 2100; Pearson electronics) and a voltage probe (P6015A; Tektronix).

3.9.2 Optical Emission Spectra (OES)

The time-averaged optical emission spectra (OES) of the generated plasma were observed with an optical spectrometer (USB2000+UV-NIR; Ocean Optics) through a 400 μm diameter of horizontal quartz lens window in the spectral range from 300 to 1000 nm and a spectral resolution of 0.38 nm. The quartz window was located less than 3.0 cm away from the generated plasma.

CHAPTER IV

COMMERCIAL TiO₂-INDUCED PHOTOCATALYTIC OXIDATION OF GLYCEROL TO VALUE-ADDED COMPOUNDS

In this chapter, the feasibility for producing some high value-added compounds via the commercial TiO₂-induced photocatalytic oxidation of glycerol was explored. Effects of parameters including TiO₂ dosage (1-3 g/L), H₂O₂ concentration (0.3-1.5 M), UV light intensity (1.1-4.7 mW/cm²) and irradiation time (4-8 h) on the level of glycerol conversion and product selectivity were systematically investigated by using a 2^k factorial design. Moreover, the effect of electron acceptor types (H₂O₂ and O₂) on glycerol conversion and product generation was also investigated. Finally, the glycerol oxidation reaction mechanism and pathway via the TiO₂-induced photocatalytic oxidation in the presence of H₂O₂ and O₂ as oxidizing agent has been proposed.

4.1 Effect of TiO₂ phase on photocatalytic oxidation of glycerol

The effect of TiO₂ phase on photocatalytic oxidation of glycerol was firstly investigated in order to evaluate the type of TiO₂ that will use for the further studies. Three different types of photocatalyst, including commercial TiO₂ in rutile phase (Sigma-Aldrich), commercial TiO₂ in anatase phase (Sigma-Aldrich) and commercial TiO₂ in mixed anatase and rutile phase (Degussa P25) were used.

As shown in Table 4.1, the preliminary results revealed that commercial anatase TiO₂ showed high performance for photocatalytic oxidation of glycerol via H₂O₂ as oxidant with 67.30% conversion and five generated products were detected in this system including DHA, GCD, glyceric acid (GCA), glycolic acid (GCOA) and formic acid (FMA). In contrast, commercial rutile TiO₂ and commercial mixed anatase-rutile TiO₂ (P25) provided low performance for photocatalytic oxidation of glycerol. The higher

activity of anatase structure than the others could be explained by two possible reasons. First, the anatase structure generally has a greater band gap than the rutile structure. Although this reduces the light that can be absorbed, it may raise the valence band maximum to higher energy levels relative to the redox potentials of adsorbed molecules. This results in the increment of the oxidation power of electrons which facilitates the electron transfer from the TiO₂ to adsorbed molecules [140]. The another possible reason is that the anatase structure usually exhibits an indirect band gap that is smaller than its direct band gap. Whilst the rutile structure and mixed anatase-rutile are very similar to direct band gap. Semiconductors with indirect band gap generally exhibit long charge carrier life times compared to direct band gap materials. A longer electron-hole pair life in anatase than in others would make it more likely for charge carriers to participate in the surface reactions [141]. Thus, the commercial TiO₂ in anatase phase was selected for further studies in order to investigate the effective condition for photocatalytic oxidation of glycerol.

Table 4.1 Glycerol conversion (X) and product selectivity (S) in the presence of different types TiO₂ phase structure.

| Batch No. | TiO ₂ Phase | X_{GLY}^* (%) | S (%)** | | | | |
|-----------|------------------------------|------------------------|-----------|-------|-------|-------|------|
| | | | DHA | GCD | GCA | GCOA | FMA |
| 1 | Anatase (Sigma-Aldrich) | 67.30 | 0.40 | 0.00 | 19.60 | 71.76 | 8.24 |
| 2 | Rutile (Sigma-Aldrich) | 18.72 | 27.95 | 30.46 | 19.01 | 22.58 | 0.00 |
| 3 | Anatase-Rutile (Degussa P25) | 50.27 | 0.87 | 0.60 | 18.44 | 72.51 | 7.58 |

* Glycerol conversion performed with 100 mL of 0.3 M glycerol, TiO₂ loading of 3 g/L, light intensity of 4.68 mW/cm² and H₂O₂ concentration of 1.5 mol/L in 8 h reaction time

** Selectivity defined as [amount of desired product formed (C-based mole) / amount of all products formed (C-based mol)] x 100

The morphology and property of selected commercial anatase TiO₂ was further characterized by miscellaneous techniques before utilized in the next part. The particle size of commercial anatase TiO₂ powder was less than 25 nm. The BET surface area, average pore size and pore volume of the utilized photocatalyst were 22.84 m²/g, 8.07 nm and 0.046 cm³/g, respectively. N₂ adsorption-desorption showed type IV isotherms with H4-shaped hysteresis loops with narrow pore size distributions (Figure 4.1), which were the characteristic of the mesoporous materials. Figure 4.2(a) exhibits the optical absorption spectra of TiO₂ recorded using a UV-Visible spectrophotometer in the wavelength range of 300-800 nm at room temperature. A decrease of absorbance to a zero value was observed under the visible light region at the wavelength greater than 450 nm, suggesting its UV light absorption ability. Taking into account the linear portion of the fundamental absorption edge of its spectra, plotting of $(\alpha h\nu)^{1/n}$ against $(h\nu)$ (Figure 4.2(b)). The band gap energy of TiO₂ was 3.2 eV, conformed to the theoretical band gap energy of anatase TiO₂.

With regard to the chemical bonding state of Ti, as shown in Figure 4.3(a), after subtraction of the Shirley-type background, the core-level spectra were decomposed into their components with mixed Gaussian–Lorentzian lines by a non-linear least squares curve-fitting procedure, using the public software package XPSPEAK 4.1. The high resolution (HR)-XPS spectra of the utilized TiO₂ showed two symmetric peak shape of Ti2p assigning to the component of Ti2p_{1/2} and Ti2p_{3/2} at binding energy of 465.2 and 459.4 eV, respectively, confirming the state of Ti as Ti⁴⁺ in TiO₂ structures. For the O1s XPS spectra (Figure 4.3(b)), the main O1s peak appeared at the binding energy between 530.2-530.6 eV, 531.8-532.0 eV and 533.0 eV, assigning to the O1s peaks characteristic of O₂⁻, OH⁻ and adsorbed H₂O, respectively.

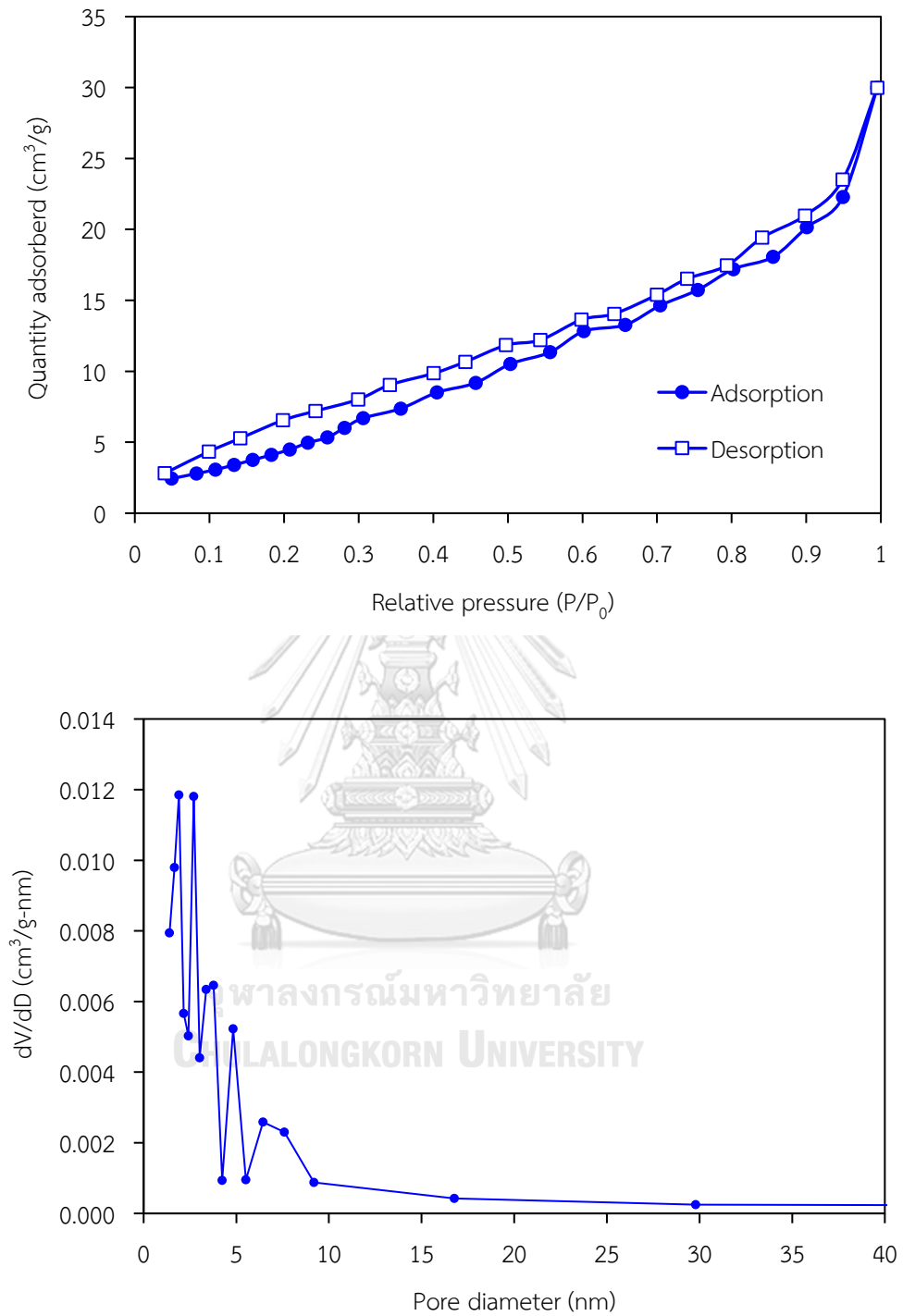


Figure 4.1 (a) N₂ adsorption-desorption isotherms and (b) pore size distribution of the utilized commercial anatase TiO₂ powder.

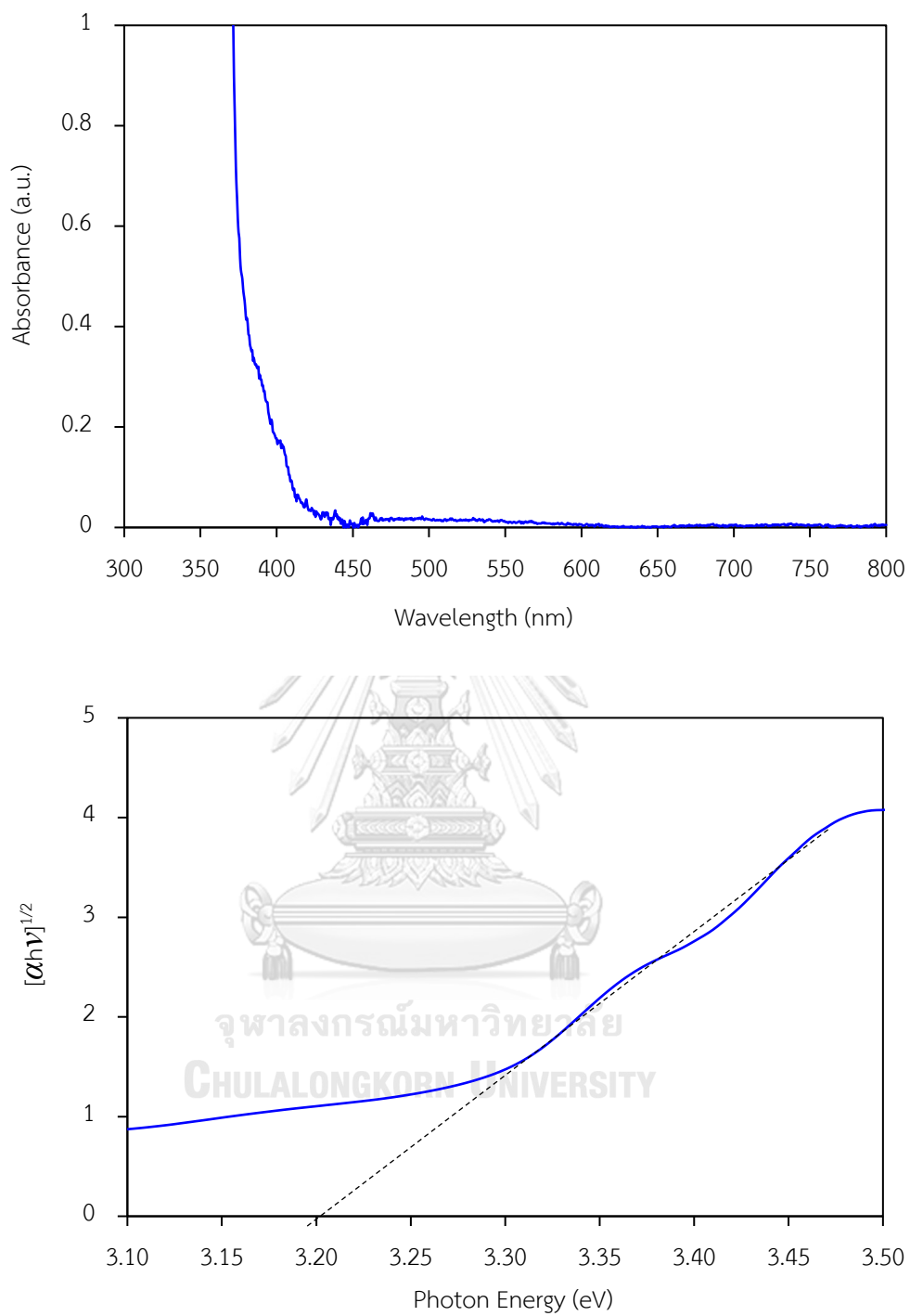


Figure 4.2 (a) UV-Vis spectra and (b) the dependent of $(\alpha h\nu)^{1/2}$ on photon energy of the utilized commercial anatase TiO₂ powder.

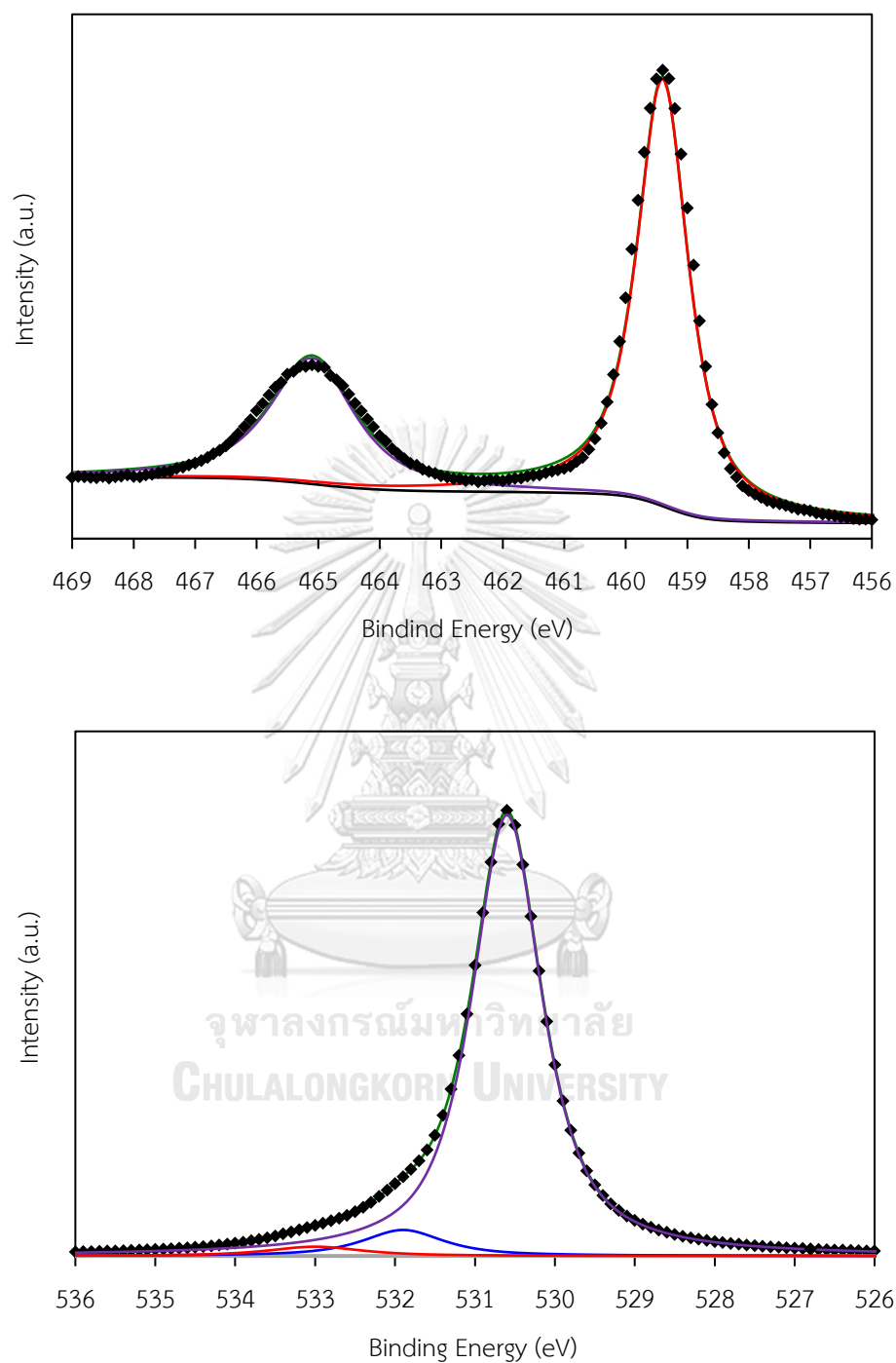
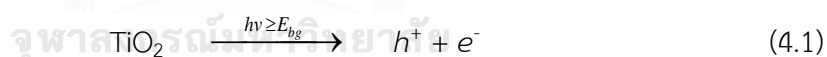


Figure 4.3 High resolution XPS spectra of (a) Ti2p and (b) O1s of utilized commercial TiO₂ powder.

4.2 Effect of operating parameters on photocatalytic oxidation of glycerol

Generally, oxidation of glycerol can be proceeded via the interaction with various oxidizing species, such as photogenerated h^+ [142], $O_2^{\bullet-}$ formed via reduction of O_2 [143], OH^{\bullet} radical [144] and H_2O_2 [145]. Therefore, to explore the route of glycerol conversion and product generation via the photocatalytic oxidation in the presence of H_2O_2 , the set of experiments with various conditions were carried out at light intensity of 4.68 mW/cm^2 , catalyst loading of 3 g/L , H_2O_2 concentration of 1.5 mol/L and irradiation time of 8 h . As demonstrated in Table 4.2, it was found that in the absence of light, the conversion of glycerol to other compounds was not achieved in the presence of TiO_2 or H_2O_2 separately or together (batch no. 1-3). Even though, the presence of only UV light cannot also promote conversion of glycerol to value-added compounds (batch no. 4). The glycerol conversion can be achieved in the presence of irradiated-UV light and TiO_2 (batch no.5), irradiated-UV light and H_2O_2 (batch no.6) and irradiated-UV light, H_2O_2 and TiO_2 (batch no.7).

Under irradiated-UV light and TiO_2 , photogenerated h^+ were produced as demonstrated in Eq. (4.1).



These generated h^+ can facilitate the glycerol conversion to three value added-compounds: DHA, GCD and GCA with product selectivity of 23.63, 68.21 and 8.16%, respectively at 8 h irradiation times (batch no. 5). Variation of glycerol conversion and product selectivity at a particular time for this condition was monitored and plotted in Figure 4.4(a). The results showed that the conversion of glycerol started after 1 h irradiation time, suggesting that a small number of photogenerated h^+ were generated during this time and cannot lead to the conversion of glycerol. As expected, the conversion of glycerol evidently increased along the irradiation time, while selectivity of DHA increased slightly and reached a plateau after 2 h . The selectivity of GCD

increased markedly within half an hour and remained constant until the 4th hour of irradiation time. Afterward, it slightly decreased, whereas GCA started to generate in the same manner, suggesting that GCD can be converted to GCA via the h^+ -mediated oxidation.

Table 4.2 Photocatalytic- and catalytic conversions (X) of 0.3 M glycerol (GLY) and selectivity (S) towards the known products for 8 h.

| Batch No. | Condition | | | | X_{GLY} (%) | S (%) | | | | |
|-----------|-----------|-----------------------|-------------------------------|--|----------------------|---------|-------|-------|-------|------|
| | GLY | UV light ^a | TiO ₂ ^b | H ₂ O ₂ ^c | | DHA | GCD | GCA | GCOA | FMA |
| 1 | ✓ | | ✓ | | - | - | - | - | - | - |
| 2 | ✓ | | | ✓ | - | - | - | - | - | - |
| 3 | ✓ | | ✓ | ✓ | - | - | - | - | - | - |
| 4 | ✓ | ✓ | | | - | - | - | - | - | - |
| 5 | ✓ | ✓ | ✓ | | 19.03 | 23.63 | 68.21 | 8.16 | - | - |
| 6 | ✓ | ✓ | | ✓ | 57.85 | 1.09 | 1.52 | 16.83 | 74.69 | 5.86 |
| 7 | ✓ | ✓ | ✓ | ✓ | 71.42 | 0.39 | 0.00 | 19.61 | 71.75 | 8.25 |

^a Light intensity of 4.68 mW/cm²; ^b TiO₂ loading of 3 g/L; ^c H₂O₂ concentration of 1.5 mol/L.

To prove the rearrangement and further oxidation of primary intermediated DHA, DHA was used as a reactant for photocatalytic activity test at light intensity of 4.68 mW/cm², catalyst loading of 3 g/L, H₂O₂ concentration of 1.5 mol/L and irradiation time of 8 h. The products which were found in the system using DHA as a reactant were GCD, GCA and GCOA as displayed in Table 4.3. At this stage, it might be implied that DHA can be also rearranged to form GCD or oxidized to GCA via h^+ -mediated oxidation with selectivity ratio ($S_{\text{GCD}}/S_{\text{DHA}}$) of 2.5:1.

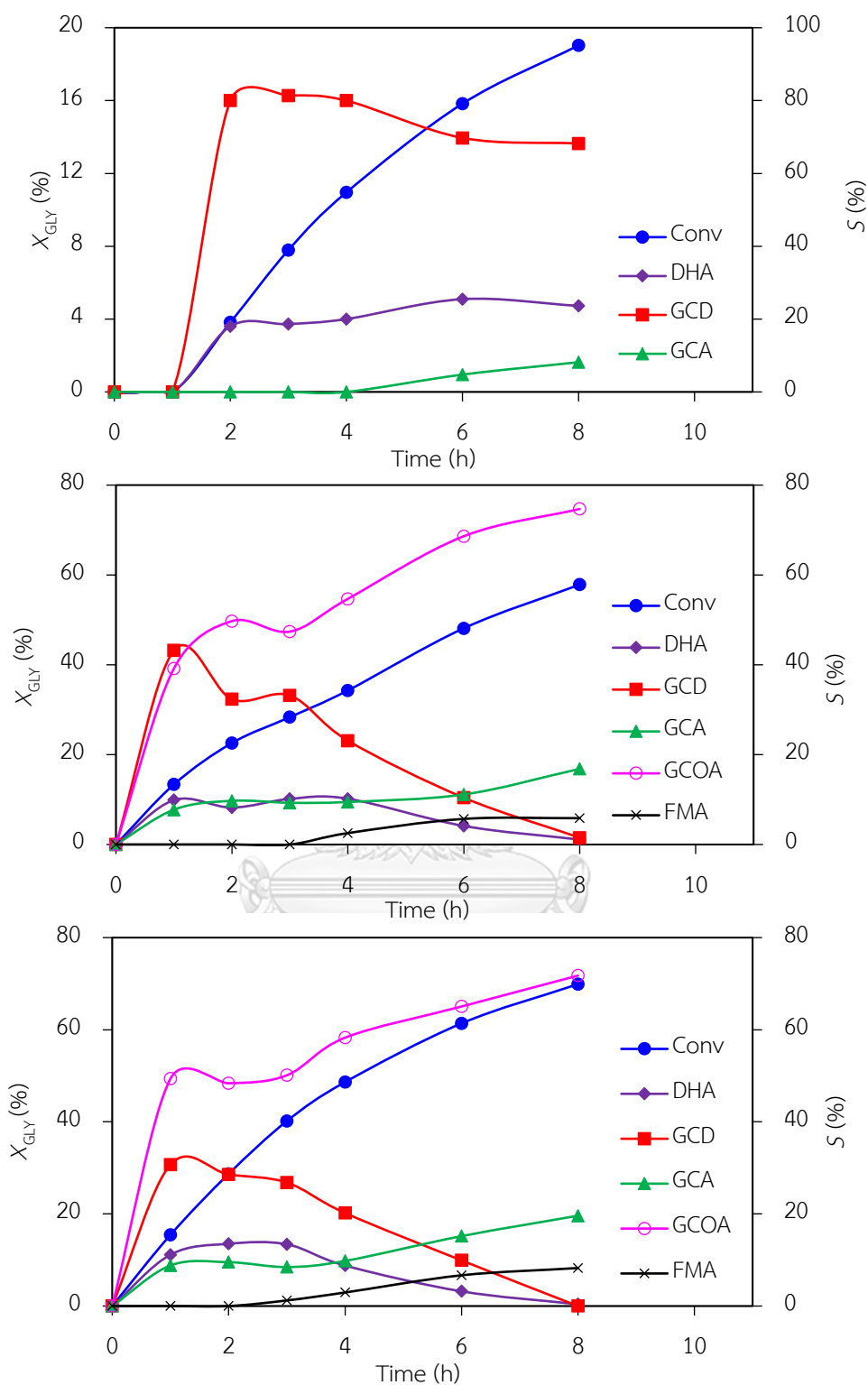


Figure 4.4 Catalytic- and photocatalytic conversions of 0.3 M glycerol and selectivity towards the known products at particular times of experiment of (a) batch no. 5, (b) batch no. 6 and (c) batch no. 7 of Table 4.2.

For the system with the UV light and H₂O₂ (batch no.6), five value-added compounds were generated via the radical-mediated oxidation route due to the presence of OH[•] radicals, which were produced by the splitting of H₂O₂ when it absorbed the UV light, as shown in Eq. (4.2) [146].



Table 4.3 Photocatalytic- and catalytic conversions (*X*) of 0.3 M DHA and selectivity (*S*) towards the known products for 8 h.

| Batch No. | Condition | | | | <i>X</i> _{DHA} (%) | <i>S</i> (%) | | |
|-----------|-----------|-----------------------|-------------------------------|--|-----------------------------|--------------|-------|-------|
| | DHA | UV light ^a | TiO ₂ ^b | H ₂ O ₂ ^c | | GCD | GCA | GCOA |
| 1 | ✓ | ✓ | ✓ | | 12.47 | 62.86 | 29.89 | 7.25 |
| 2 | ✓ | ✓ | | ✓ | 29.12 | 33.79 | 12.82 | 53.39 |
| 3 | ✓ | ✓ | ✓ | ✓ | 36.42 | 37.07 | 14.81 | 48.12 |

^a Light intensity of 4.68 mW/cm²; ^b TiO₂ loading of 3 g/L; ^c H₂O₂ concentration of 1.5 mol/L

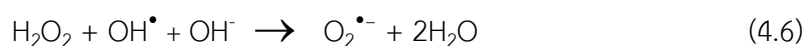
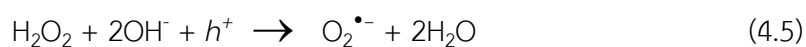
These generated OH[•] radicals can further react with glycerol to form GCD and DHA depending on the position of an attached C atom. That is, GCD and DHA are formed when the 1^o- and 2^o-C atoms are respectively attached and oxidized. As displayed in Figure 4.4(b), the conversion of glycerol has been started from the beginning of irradiation time. No induction period of glycerol conversion and product generation was observed in this system, suggesting that the generated OH[•] radicals had more oxidizing power than the photogenerated *h*⁺. With regard to product selectivity, the selectivity of DHA was observed at around 10% during the first 4 h of irradiation time and slightly decreased to 1.09% at 8 h. This might be attributed to the preferential attachment of the OH[•] radicals at the primary C atom of glycerol [147,

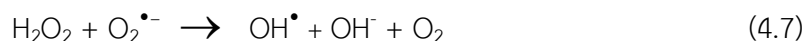
148] or the rearrangement of DHA to GCD, which was clearly shown by a high selectivity of GCD compared with that of DHA. Although a high selectivity of GCD was observed at the early period of experiment, a drastic drop occurred along the irradiation time. This is probably due to its further oxidation to GCA [149]. In case of generated DHA, it was also found that DHA can be rearranged to form GCD or further oxidized to GCA and GCOA at the selectivity ratio of around 2.6 : 1 : 4.2 (Table 4.3). Thus, it seems that a high selectivity of GCA should be observed at a particular time. Contradictory, the low selectivity of GCA of around 7.75-16.8% was observed during the experiment period. This might be due to the further oxidation of GCA to other compounds such as GCOA and FMA [150, 151]. Namely, excess OH^\bullet radicals can attach and cleave the C-C bond of GCA, resulting in the formation of GCOA and FMA. Higher selectivity of GCOA was observed compared to FMA, probably due to further rapid oxidation of FMA to other compounds in gas phase such as CO or CO_2 [152-154].

For the system with TiO_2 , H_2O_2 and UV light, the glycerol conversion and generation of products can proceed via either h^+ -mediated or radical-mediated routes. In addition to the generation of OH^\bullet radicals via the irradiated-UV light as Eq. (4.2), the OH^\bullet radicals can also be produced by the reduction of H_2O_2 with the conduction photogenerated electrons (e^-) (Eq.(4.3)) or by the photooxidation of H_2O_2 via the photogenerated h^+ (Eq.(4.4)) [155, 156].



The H_2O_2 can also be oxidized by the photogenerated h^+ (Eq.(4.5)) or OH^\bullet radicals (Eq.(4.6)) [157] to form $\text{O}_2^{\bullet-}$ radicals, which readily react with H_2O_2 to form OH^\bullet radicals (Eq.(4.7)) [158].





As illustrated in Table 4.2, approximately 71.42% of glycerol converted to other value-added compounds, close to the summation of glycerol conversion obtained from batches no.5 and no.6. The selectivity of all generated products was close to that of batch no.6. In addition, the product selectivity at particular time was revealed the similar trend to those in batch no. 6 (Figure 4.4(c)). At this stage, it can be said that the radical-mediated route was the dominant route for the formation of GCA, GCOA and FMA from the photocatalytic oxidation of glycerol induced by TiO₂ in the presence of H₂O₂. However, it is still difficult to conclude about the preferential route for glycerol conversion to DHA and GCD.

4.3 Evaluation of influence factors on photocatalytic oxidation of glycerol and product generation by 2^k factorial design

To gain more understanding about the effect of such parameters on glycerol conversion as well as product selectivity, a 2^k factorial design analysis was used to provide an empirical relation between the four independent variables related to the photocatalytic condition: *A*: TiO₂ dosage (1-3 g/L), *B*: H₂O₂ concentration (0.3-1.5 M), *C*: light intensity (1.1-4.7 mW/cm²) and *D*: irradiation time (4-8 h).

A full factorial design 2⁴ was done within the DESIGN EXPERT[®] software including ANOVA in order to evaluate the interactions between the process variables. The experiment region investigated for photocatalytic oxidation of glycerol and the code variables are shown in Table 4.4.

Table 4.4 Factor and levels used in the 2⁴ full factorial design.

| Code Variable | Description | Experimental field | | |
|------------------|---|--------------------|-----------|------------|
| | | Level (-1) | Level (0) | Level (+1) |
| <i>A</i> | TiO ₂ dosage (g/L) | 1 | 2 | 3 |
| <i>B</i> | H ₂ O ₂ concentration (mol/L) | 0.3 | 0.9 | 1.5 |
| <i>C</i> | Light intensity (mW/cm ²) | 1.11 | 2.90 | 4.68 |
| <i>D</i> | Irradiation time (h) | 4 | 6 | 8 |

The selected response factors of the glycerol conversion and product selectivity are listed in Table 4.5. All trials were performed with a completely randomized design to minimize errors due to possible systematic trends in the variables. Statistical analysis was then done for all the experimental values, and the effects of main factors and their interaction on the chosen responses were calculated with the main effects and interactions for the conversion of glycerol and product selectivity with a confidence level of 95%.

4.3.1 Influence factors on glycerol conversion

In the half-normal probability plot (Figure 4.5), the variables that deviated from straight line of the normal probability are considered to be the significant factor for this system. Thus, all the four evaluated variables including TiO₂ dosage (*A*), H₂O₂ concentration (*B*), light intensity (*C*), irradiation time (*D*) and interactions between the H₂O₂ concentration with light intensity (*BC*) had a considerable influence on the glycerol conversion.

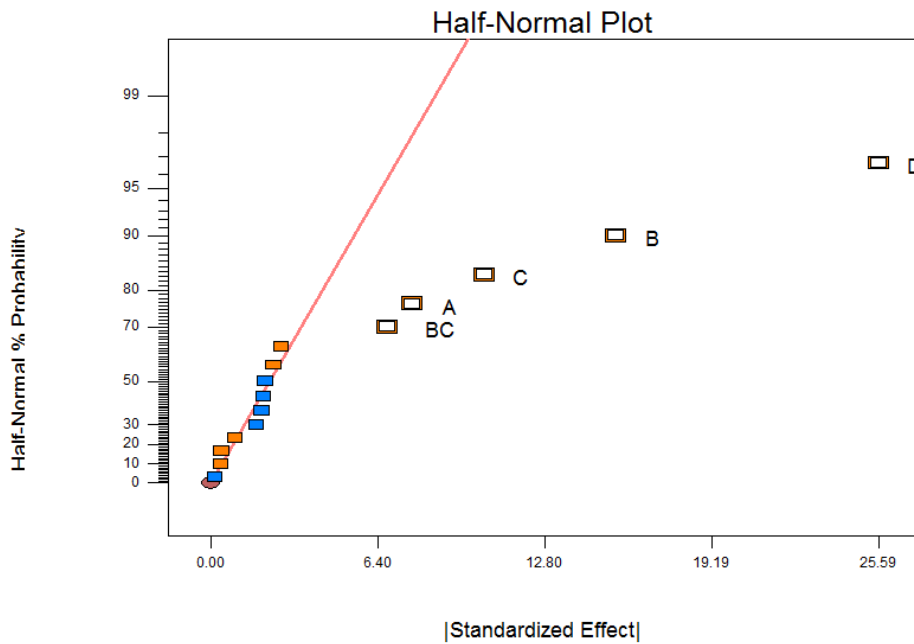


Figure 4.5 Half-normal probability plot of glycerol conversion.

As demonstrated in Table 4.6, the P value of TiO_2 dosage (A), H_2O_2 concentration (B), light intensity (C), irradiation time (D) and interaction between H_2O_2 concentration and light intensity (BC) were lower than the critical P value ($P_{\text{critical}} < 0.05$), confirming that all mentioned parameters had a significant effect on glycerol conversion. The experimental results were then fit with the linear first order regression model as expressed in Eq.(4.8).

$$X_{\text{GLY}}(\%) = 38.97 + 3.86A + 7.76B + 5.24C + 12.79D + 3.38BC \quad (4.8)$$

where A , B , C and D are TiO_2 dosage, H_2O_2 concentration, light intensity and irradiation time, respectively.

Table 4.5 Experimental factorial matrix in 2⁴ factorial design and experimental results of TiO₂-induced photocatalytic oxidation of glycerol.

| No. | Experimental design | | | | Experimental value | | | | X _{GLY} (%) | | | | S (%) | | | | |
|-----|---------------------|----|----|----|--------------------|-----|-----|---|----------------------|------|-------|-------|-------|-------|-------|-------|-------|
| | A | B | C | D | A | B | C | D | A | B | C | D | DHA | GCD | GCA | GCOA | FMA |
| 1 | -1 | -1 | -1 | -1 | 1 | 0.3 | 1.1 | 4 | 15.7 | 8.17 | 39.17 | 42.09 | 10.57 | 42.09 | 0.00 | 0.00 | 0.00 |
| 2 | +1 | -1 | -1 | -1 | 3 | 0.3 | 1.1 | 4 | 18.3 | 8.35 | 27.99 | 51.23 | 12.42 | 51.23 | 0.00 | 0.00 | 0.00 |
| 3 | -1 | +1 | -1 | -1 | 1 | 1.5 | 1.1 | 4 | 21.4 | 8.24 | 31.92 | 48.90 | 10.94 | 48.90 | 0.00 | 0.00 | 0.00 |
| 4 | +1 | +1 | -1 | -1 | 3 | 1.5 | 1.1 | 4 | 29.1 | 7.90 | 28.81 | 51.74 | 11.55 | 51.74 | 0.00 | 0.00 | 0.00 |
| 5 | -1 | -1 | +1 | -1 | 1 | 0.3 | 4.7 | 4 | 19.6 | 8.81 | 22.57 | 54.38 | 14.25 | 54.38 | 0.00 | 0.00 | 0.00 |
| 6 | +1 | -1 | +1 | -1 | 3 | 0.3 | 4.7 | 4 | 21.9 | 9.76 | 24.17 | 51.53 | 14.54 | 51.53 | 0.00 | 0.00 | 0.00 |
| 7 | -1 | +1 | +1 | -1 | 1 | 1.5 | 4.7 | 4 | 37.4 | 7.29 | 32.53 | 44.05 | 16.13 | 44.05 | 0.00 | 0.00 | 0.00 |
| 8 | +1 | +1 | +1 | -1 | 3 | 1.5 | 4.7 | 4 | 46.0 | 8.02 | 23.66 | 50.94 | 12.99 | 50.94 | 4.40 | 4.40 | 4.40 |
| 9 | -1 | -1 | -1 | +1 | 1 | 0.3 | 1.1 | 8 | 37.8 | 3.30 | 2.15 | 63.49 | 16.88 | 63.49 | 14.19 | 14.19 | 14.19 |
| 10 | +1 | -1 | -1 | +1 | 3 | 0.3 | 1.1 | 8 | 45.6 | 3.46 | 2.72 | 65.70 | 13.68 | 65.70 | 14.45 | 14.45 | 14.45 |
| 11 | -1 | +1 | -1 | +1 | 1 | 1.5 | 1.1 | 8 | 40.7 | 2.28 | 2.46 | 72.30 | 17.10 | 72.30 | 5.86 | 5.86 | 5.86 |
| 12 | +1 | +1 | -1 | +1 | 3 | 1.5 | 1.1 | 8 | 61.2 | 1.72 | 4.05 | 71.07 | 15.95 | 71.07 | 7.21 | 7.21 | 7.21 |
| 13 | -1 | -1 | +1 | +1 | 1 | 0.3 | 4.7 | 8 | 41.8 | 2.39 | 0.83 | 67.79 | 16.72 | 67.79 | 12.28 | 12.28 | 12.28 |
| 14 | +1 | -1 | +1 | +1 | 3 | 0.3 | 4.7 | 8 | 49.1 | 5.62 | 2.76 | 72.86 | 11.48 | 72.86 | 7.28 | 7.28 | 7.28 |
| 15 | -1 | +1 | +1 | +1 | 1 | 1.5 | 4.7 | 8 | 66.6 | 0.62 | 0.00 | 62.60 | 27.23 | 62.60 | 9.55 | 9.55 | 9.55 |
| 16 | +1 | +1 | +1 | +1 | 3 | 1.5 | 4.7 | 8 | 71.4 | 0.38 | 0.00 | 72.31 | 19.22 | 72.31 | 8.08 | 8.08 | 8.08 |

Table 4.6 ANOVA results for analysis of glycerol conversion.

| Sources of variation | Sum of squares | Degree of freedom | Mean squares | F_0 | P -value |
|---------------------------------------|----------------|-------------------|--------------|--------|------------|
| Model | 4443.08 | 5 | 888.62 | 74.90 | < 0.0001 |
| A-TiO ₂ Dosage | 238.24 | 1 | 238.24 | 20.08 | 0.0012 |
| B-H ₂ O ₂ conc. | 963.17 | 1 | 963.17 | 81.18 | < 0.0001 |
| C-Light intensity | 439.11 | 1 | 439.11 | 37.01 | 0.0001 |
| D-Irradiation Time | 2619.90 | 1 | 2619.90 | 220.82 | < 0.0001 |
| BC | 182.66 | 1 | 182.66 | 15.40 | 0.0028 |
| Residual | 118.65 | 10 | 11.86 | | |
| Total | 4561.73 | 15 | | | |

A high coefficient of determination (R^2) between the experimental data and calculated values was determined to be 0.9740 which did not follow any trend of residuals with regard to the predicted value (Figure 4.6(a)). This indicates that the developed linear polynomial model is satisfactory and can be used to represent the data over the experimental range. From the developed model equation, the constant 38.97 represented the average value of the response of the 16 assays. All investigated parameters had a positive effect on the glycerol conversion in the order of irradiation time > H₂O₂ concentration > light intensity > TiO₂ dosage. To confirm the importance of the factors and their interactions, Pareto analysis was used to calculate the effect percentages of each factor on the response:

$$P_i = \left(\frac{b_i^2}{\sum b_i^2} \right) \times 100 \quad (i \neq 0) \quad (4.9)$$

where b_i represents the estimation of the principal effect of the factor.

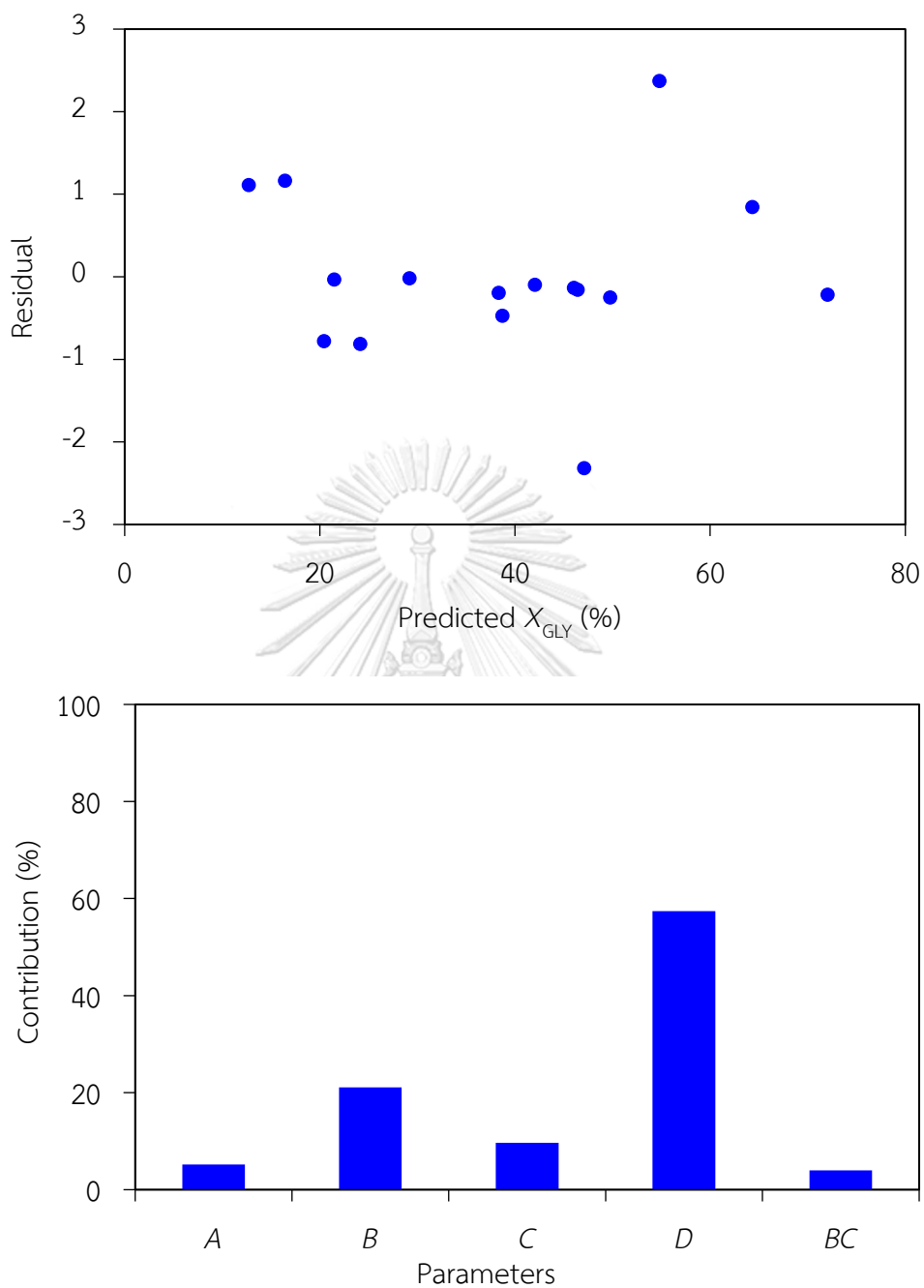


Figure 4.6 Plot of (a) predicted value and residual, and (b) Pareto analysis of glycerol conversion.

The contributions of the principal variables (A , B , C and D) on the percentage of glycerol conversion and their interaction are shown in Figure 4.6(b). This confirms

that the glycerol conversion was affected by all investigated parameters ranked as the order of irradiation time > H₂O₂ concentration > light intensity > TiO₂ dosage, which is consistent with the results obtained from the model equation. Irradiation time appeared to be the most important factor for the glycerol conversion due to the fact that long irradiation time can promote more generation of a e^-h^+ in valence and conduction band of the photocatalyst as well as OH[•] radicals from the dissociation of H₂O₂, which readily oxidizes glycerol. A greater impact of H₂O₂ concentration on glycerol conversion than TiO₂ dosage suggested that the conversion of glycerol prefers to proceed via the radical-mediated route. In the presence of H₂O₂ and UV light, some generated OH[•] radicals preferred to oxidize the glycerol at the primary C atom, resulting in other compounds (ex. GCD) or excess OH[•] radicals further oxidizing DHA to other smaller organic species as mentioned previously.

4.3.2 Influence factors on DHA selectivity

With regard to product selectivity of DHA, the ANOVA analysis result was shown in Table 4.7. It demonstrated that H₂O₂ concentration and irradiation time significantly affected DHA selectivity, while TiO₂ dosage and light intensity had an insignificant effect. The experimental results were fit with the linear first order regression model as expressed in Eq.(4.10) with R^2 greater than 0.9293. No structural distribution of the predicted values was observed (Figure 4.7(a)). This suggested that the developed regression model can be used to represent the data over the experimental range.

$$S_{\text{DHA}}(\%) = 5.39 + 0.26A - 0.846B - 0.03C - 2.92D \quad (4.10)$$

where A , B , C and D are TiO₂ dosage, H₂O₂ concentration, light intensity and irradiation time, respectively.

According to the Pareto analysis (Figure 4.7(b)), both H₂O₂ concentration and irradiation time had a negative effect on DHA selectivity. This suggested that the

conversion of DHA can be dominantly carried out by the radical-mediated route, and a long irradiation time can induce more conversion of DHA.

Table 4.7 ANOVA results for analysis of DHA selectivity.

| Sources of variation | Sum of squares | Degree of freedom | Mean squares | F_0 | P -value |
|---------------------------------------|----------------|-------------------|--------------|--------|------------|
| Model | 149.03 | 4 | 37.26 | 36.12 | < 0.0001 |
| A-TiO ₂ Dosage | 1.06 | 1 | 1.06 | 1.02 | 0.3334 |
| B-H ₂ O ₂ conc. | 11.24 | 1 | 11.24 | 10.90 | 0.0071 |
| C-Light intensity | 0.018 | 1 | 0.018 | 0.017 | 0.8986 |
| D-Irradiation Time | 136.71 | 1 | 136.71 | 132.55 | < 0.0001 |
| Residual | 11.35 | 11 | 1.03 | | |
| Total | 160.37 | 15 | | | |

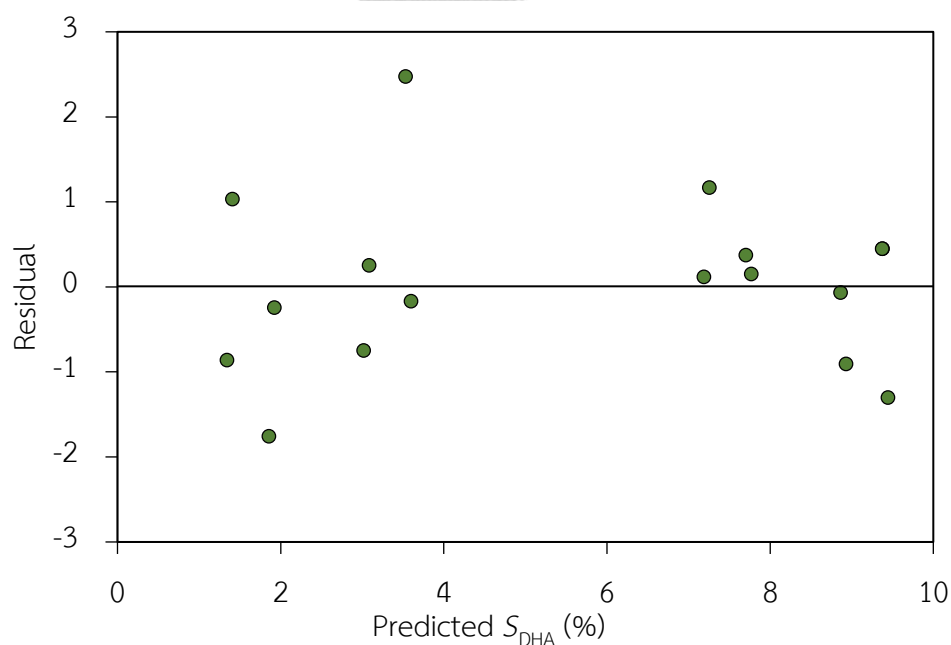


Figure 4.7 Plot of (a) predicted value and residual, and (b) Pareto analysis of DHA selectivity.

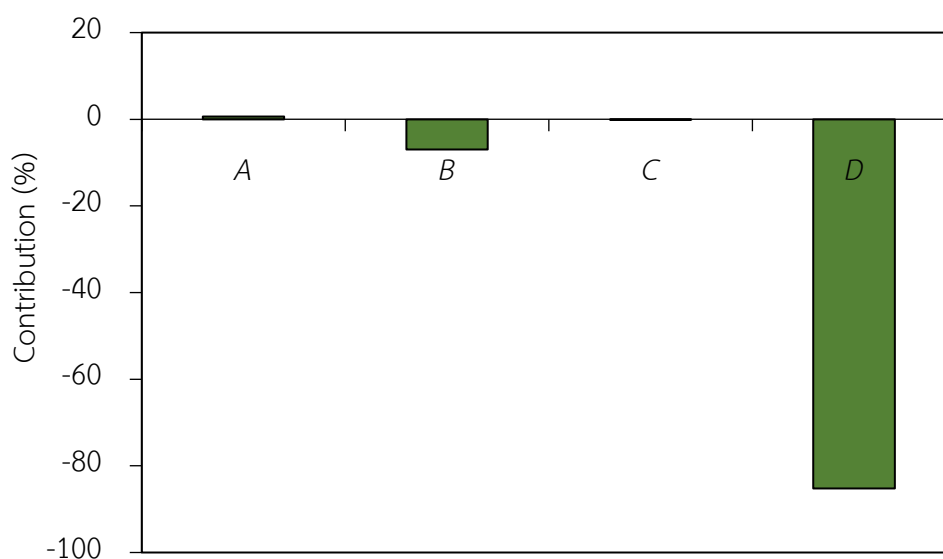


Figure 4.7 Plot of (a) predicted value and residual, and (b) Pareto analysis of DHA selectivity (Cont.).

4.3.3 Influence factors on GCD selectivity

For GCD selectivity, the ANOVA analysis showed that the parameters that affected GCD selectivity can be ranked as irradiation time > light intensity > TiO₂ dosage > H₂O₂ concentration (Table 4.8). The experimental results were fit with the linear first order regression model as expressed in Eq. (4.11). A high R^2 of greater than 0.9523 was obtained in this case with a random distribution of residual as shown in Figure 4.8(a), emphasizing that the regression model can be used to represent the data in the experimental range.

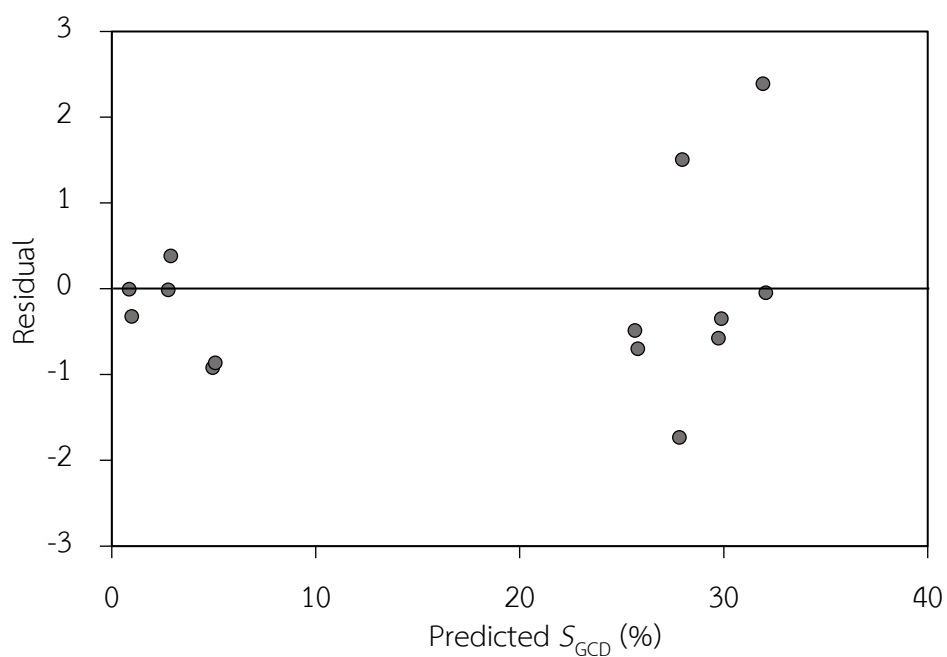
$$S_{\text{GCD}}(\%) = 15.36 - 1.09A + 0.07B - 2.05C - 13.49D \quad (4.11)$$

where A , B , C and D are TiO₂ dosage, H₂O₂ concentration, light intensity and irradiation time, respectively.

From the Pareto plot (Figure 4.8(b)), irradiation time affected principally GCD selectivity, but with a negative trend. This emphasizes that GCD can be further converted to other compounds.

Table 4.8 ANOVA results for analysis of GCD selectivity.

| Sources of variation | Sum of squares | Degree of freedom | Mean squares | F_0 | P -value |
|---------------------------------------|----------------|-------------------|--------------|----------|------------|
| Model | 2998.13 | 4 | 749.53 | 56.06 | < 0.0001 |
| A-TiO ₂ Dosage | 19.08 | 1 | 19.08 | 1.43 | 0.2574 |
| B-H ₂ O ₂ conc. | 0.072 | 1 | 0.072 | 5.352E-3 | 0.9430 |
| C-Light intensity | 67.04 | 1 | 67.04 | 5.01 | 0.0468 |
| D-Irradiation Time | 2911.95 | 1 | 2911.95 | 217.79 | < 0.0001 |
| Residual | 147.07 | 11 | 13.37 | | |
| Total | 3145.21 | 15 | | | |

**Figure 4.8** Plot of (a) predicted value and residual, and (b) Pareto analysis of GCD selectivity.

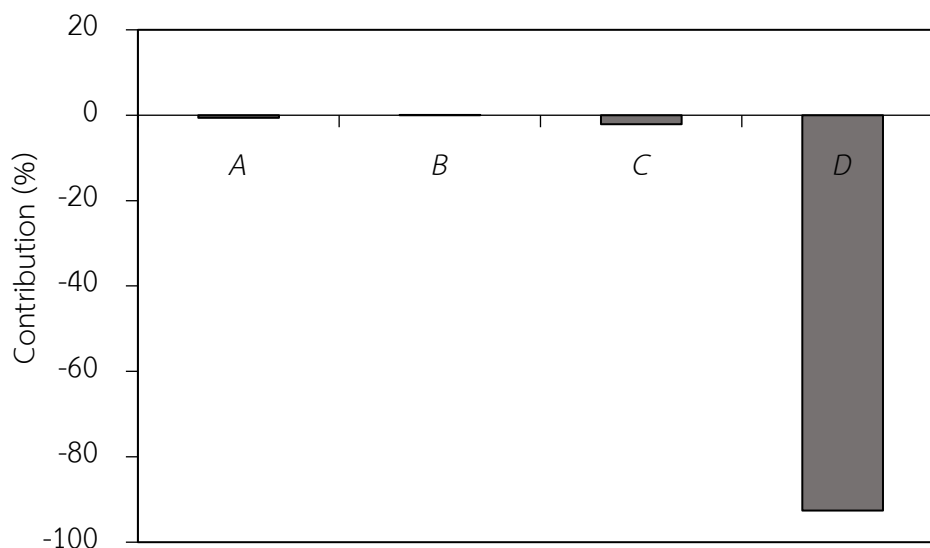


Figure 4.8 Plot of (a) predicted value and residual, and (b) Pareto analysis of GCD selectivity (Cont.).

4.3.4 Influence factors on GCA selectivity

As demonstrated in Table 4.9, the ANOVA analysis of GCA selectivity demonstrated that all investigated parameters and their interaction, including TiO_2 dosage, H_2O_2 concentration, light intensity, irradiation time and their interaction, influenced GCA selectivity. Eq.(4.12) gave the best fit among the experimental results with R^2 greater than 0.9716. A lack of structural residual distribution was obtained as shown in Figure 4.9(a).

$$S_{\text{GCA}}(\%) = 15.10 - 1.12A + 1.29B + 1.46C + 2.18D - 0.89AC - 1.08AD + 1.04BC + 1.31BD + 0.93BCD \quad (4.12)$$

where A , B , C and D are TiO_2 dosage, H_2O_2 concentration, light intensity and irradiation time, respectively.

The Pareto plot exhibits that H_2O_2 concentration, light intensity, irradiation time, interaction of H_2O_2 concentration-light intensity, H_2O_2 concentration-irradiation time

and H_2O_2 concentration-light intensity-irradiation time all had a positive effect, while TiO_2 dosage and its interaction with light intensity and irradiation time had a negative effect on GCA selectivity (Figure 4.9(b)). This suggested that the principal route for GCA formation was the radical-mediated route, consistent with the results obtained from the previous section. The negative effect of TiO_2 and its interaction with H_2O_2 and light intensity might be distributed for further oxidation of GCA via the photogenerated h^+ .

Table 4.9 ANOVA results for analysis of GCA selectivity.

| Sources of variation | Sum of squares | Degree of freedom | Mean squares | F_0 | P -value |
|---------------------------------|----------------|-------------------|--------------|-------|------------|
| Model | 246.69 | 9 | 27.41 | 22.78 | 0.0006 |
| A- TiO_2 Dosage | 20.23 | 1 | 20.23 | 16.81 | 0.0064 |
| B- H_2O_2 conc. | 26.45 | 1 | 26.45 | 21.97 | 0.0034 |
| C-Light intensity | 34.43 | 1 | 34.43 | 28.61 | 0.0017 |
| D-Irradiation Time | 75.99 | 1 | 75.99 | 63.15 | 0.0002 |
| AC | 12.62 | 1 | 12.62 | 10.49 | 0.0177 |
| AD | 18.51 | 1 | 18.51 | 15.38 | 0.0078 |
| BC | 17.20 | 1 | 17.20 | 14.29 | 0.0092 |
| BD | 27.33 | 1 | 27.33 | 22.71 | 0.0031 |
| BCD | 13.93 | 1 | 13.93 | 11.58 | 0.0145 |
| Residual | 7.22 | 6 | 1.20 | | |
| Total | 253.91 | 15 | | | |

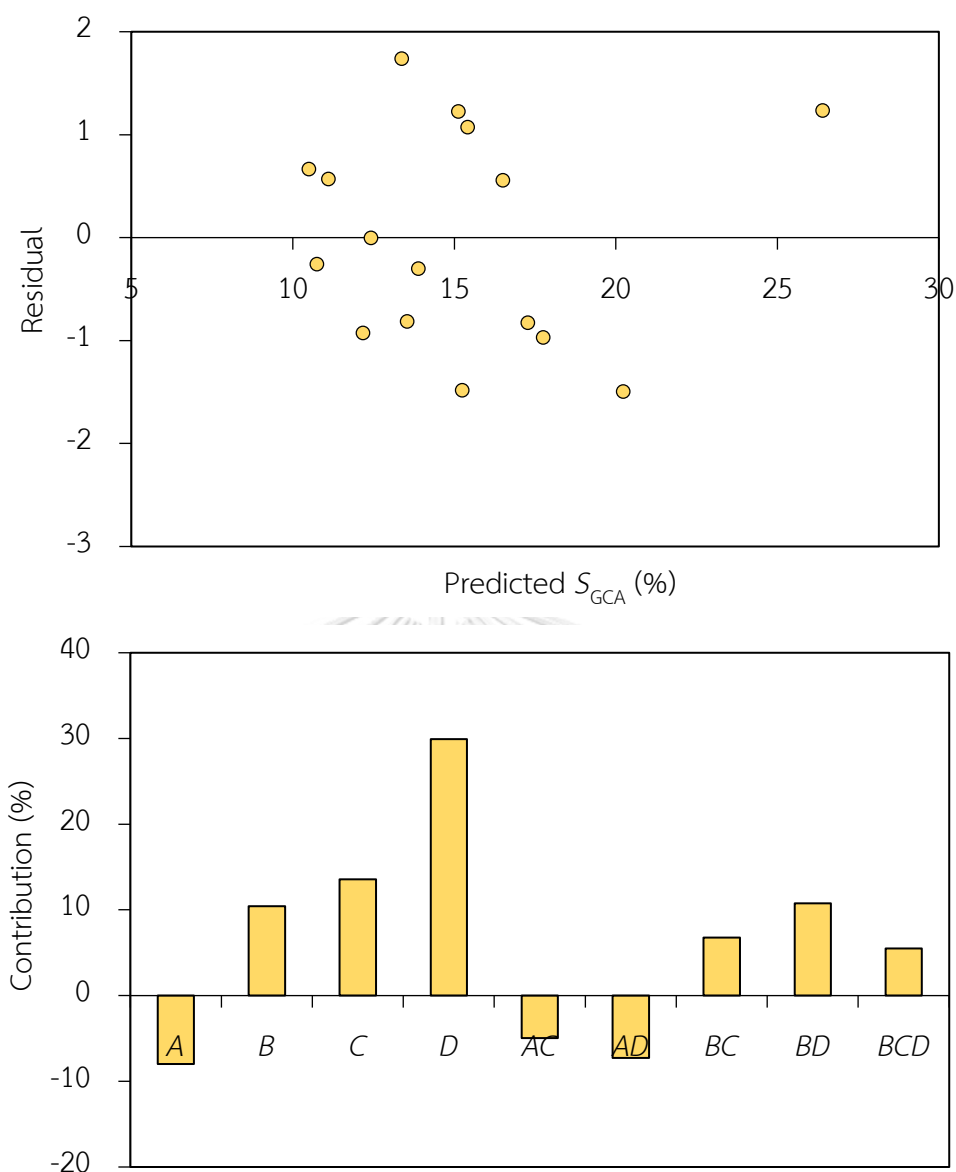


Figure 4.9 Plot of (a) predicted value and residual, and (b) Pareto analysis of GCA selectivity.

4.3.5 Influence factors on glycolic acid (GCOA) selectivity

For GCOA selectivity, ANOVA analysis showed that all investigated parameters and the interaction of H_2O_2 concentration and light intensity significantly affected GCOA selectivity (Table 4.10). The linear first order equation as expressed in Eq.(4.13) fit very well with the experimental data with R^2 greater than 0.9511. This developed regression

model was sufficient to represent the data over the experimental range due to its high R^2 value and non-structured residuals (Figure 4.10(a)).

$$S_{\text{GCOA}}(\%) = 58.94 + 1.99A + 0.30B + 0.62C + 9.58D - 2.39BC \quad (4.13)$$

where A , B , C and D are TiO_2 dosage, H_2O_2 concentration, light intensity and irradiation time, respectively.

The Pareto analysis also shows that both TiO_2 dosage and irradiation time had a positive effect on the selectivity of GCOA with irradiation time > TiO_2 dosage. However, the interaction of TiO_2 dosage and light intensity showed a negative influence on the selectivity of GCOA (Figure 4.10(b)). This might be due to the fact that GCOA is the product of GCA oxidation generated from the GCD. The presence of high strength TiO_2 dosage, H_2O_2 concentration, light intensity as well as long irradiation time could induce extremely high generation of oxidizing species (h^+ and/or OH^\bullet radicals), which can facilitate the oxidation of intermediate species to GCOA. However, the presence of too high oxidizing species, particular the OH^\bullet radicals, can enhance further oxidation of GCOA to other compounds, resulting in decreasing GCOA selectivity.

Table 4.10 ANOVA results for analysis of glycolic acid selectivity.

| Sources of variation | Sum of squares | Degree of freedom | Mean squares | F_0 | P -value |
|---------------------------------|----------------|-------------------|--------------|--------|------------|
| Model | 1629.81 | 5 | 325.96 | 38.86 | < 0.0001 |
| A- TiO_2 Dosage | 63.12 | 1 | 63.12 | 7.53 | 0.0207 |
| B- H_2O_2 conc. | 1.46 | 1 | 1.46 | 0.17 | 0.6849 |
| C-Light intensity | 6.18 | 1 | 6.18 | 0.74 | 0.4110 |
| D-Irradiation Time | 1468.04 | 1 | 1468.04 | 175.02 | < 0.0001 |
| BC | 91.01 | 1 | 91.01 | 10.85 | 0.0081 |
| Residual | 83.88 | 10 | 8.39 | | |
| Total | 1713.69 | 15 | | | |

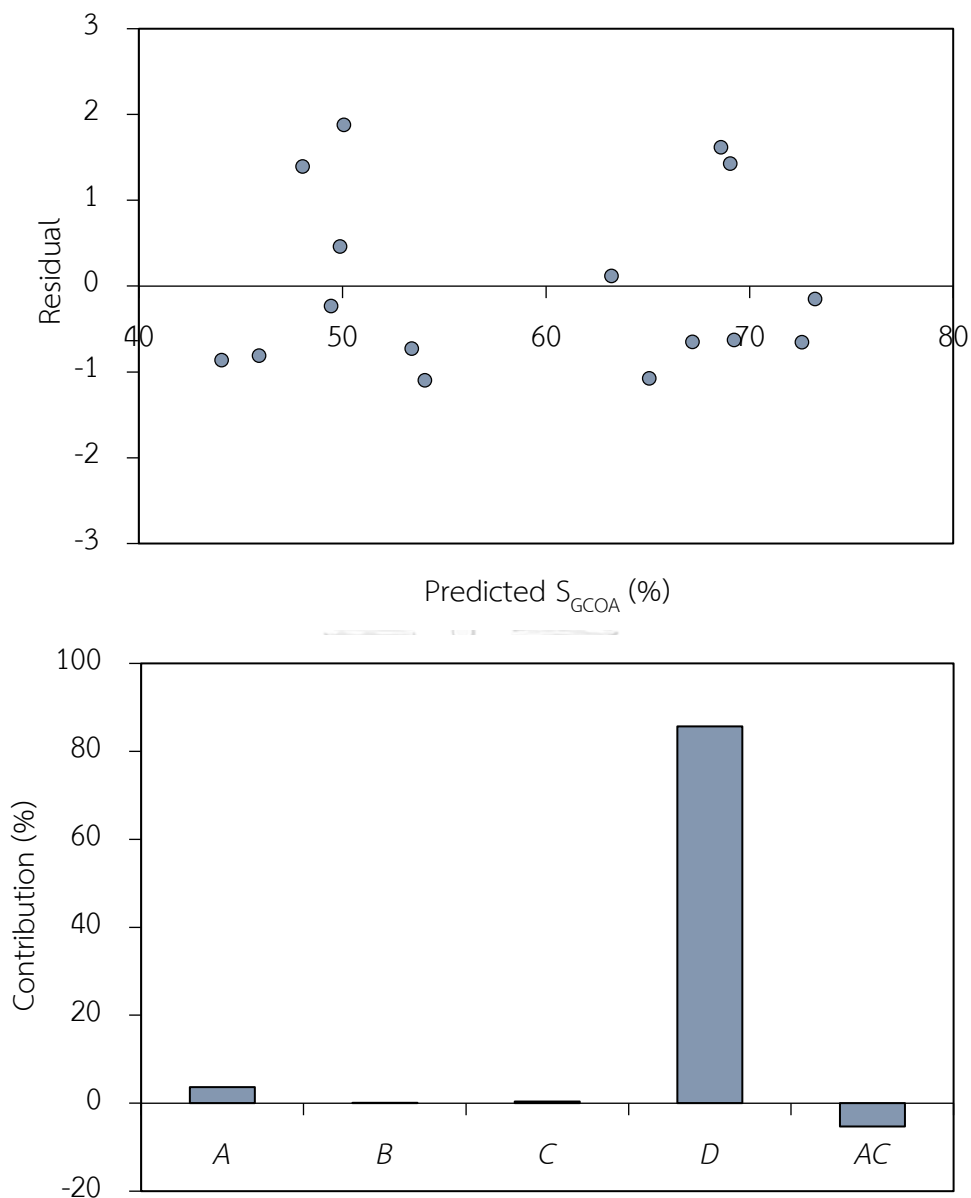


Figure 4.10 Plot of (a) predicted value and residual, and (b) Pareto analysis of GCOA selectivity.

According to the obtained results, it worth to mentioned that TiO_2 dosage had a positive effect on glycerol conversion and selectivity of DHA and GCOA, but a negative effect on GCD and GCA selectivity. Concentration of H_2O_2 had a positive influence on glycerol conversion and selectivity of GCD, GCA and GCOA, but had a negative influence on DHA selectivity. The intensity of UV light had a positive effect

on glycerol conversion and selectivity of GCA and GCOA but negative effect on the selectivity of DHA and GCD. Finally, irradiation time had the strongest effect on glycerol conversion and product selectivity. It had a positive impact on glycerol conversion and selectivity of GCA and GCOA, but had negative impact on the selectivity of DHA and GCD.

4.4 Effect of electron acceptor types on photocatalytic oxidation of glycerol

To explore the effect of electron acceptor on commercial TiO_2 -induced photocatalytic oxidation of glycerol, two types of electron acceptors, including H_2O_2 and O_2 , were utilized. A blank experiment was first carried out via the presence of either H_2O_2 or O_2 but absence of both UV light and TiO_2 . It was found that the presence of only H_2O_2 or O_2 could not facilitate the conversion of glycerol. However, the presence of irradiated-UV light and TiO_2 in the absence of either H_2O_2 or O_2 could promote the conversion of glycerol to four value-added compounds; DHA, GCA, GCD, and GCOA (Figure 4.11(a)). The addition of H_2O_2 in the irradiated-UV light and TiO_2 system could further enhance the conversion of glycerol with one additional formed product; FMA, compared with that in the absence of H_2O_2 (Figure 4.11(b)). Using O_2 as electron acceptor instead of H_2O_2 decreased the glycerol conversion almost twice (Figure 4.11(c)). The glycerol conversion was around 50% at 20 h. A similar three value-added compounds, including DHA, GCD, and GCOA, were still observed in the system, while two more compounds were generated in this system; hydroxypyruvic acid (HPA) and formaldehyde (FMD).

As previously reported, the oxidation of glycerol can be proceeded via the photogenerated oxidizing species, including photogenerated h^+ [142], OH^\bullet radical [144], and oxide radicals ($^1\text{O}_2/ \text{O}_2^{\bullet-}$) [143] formed via the photo-cleavage of water and H_2O_2

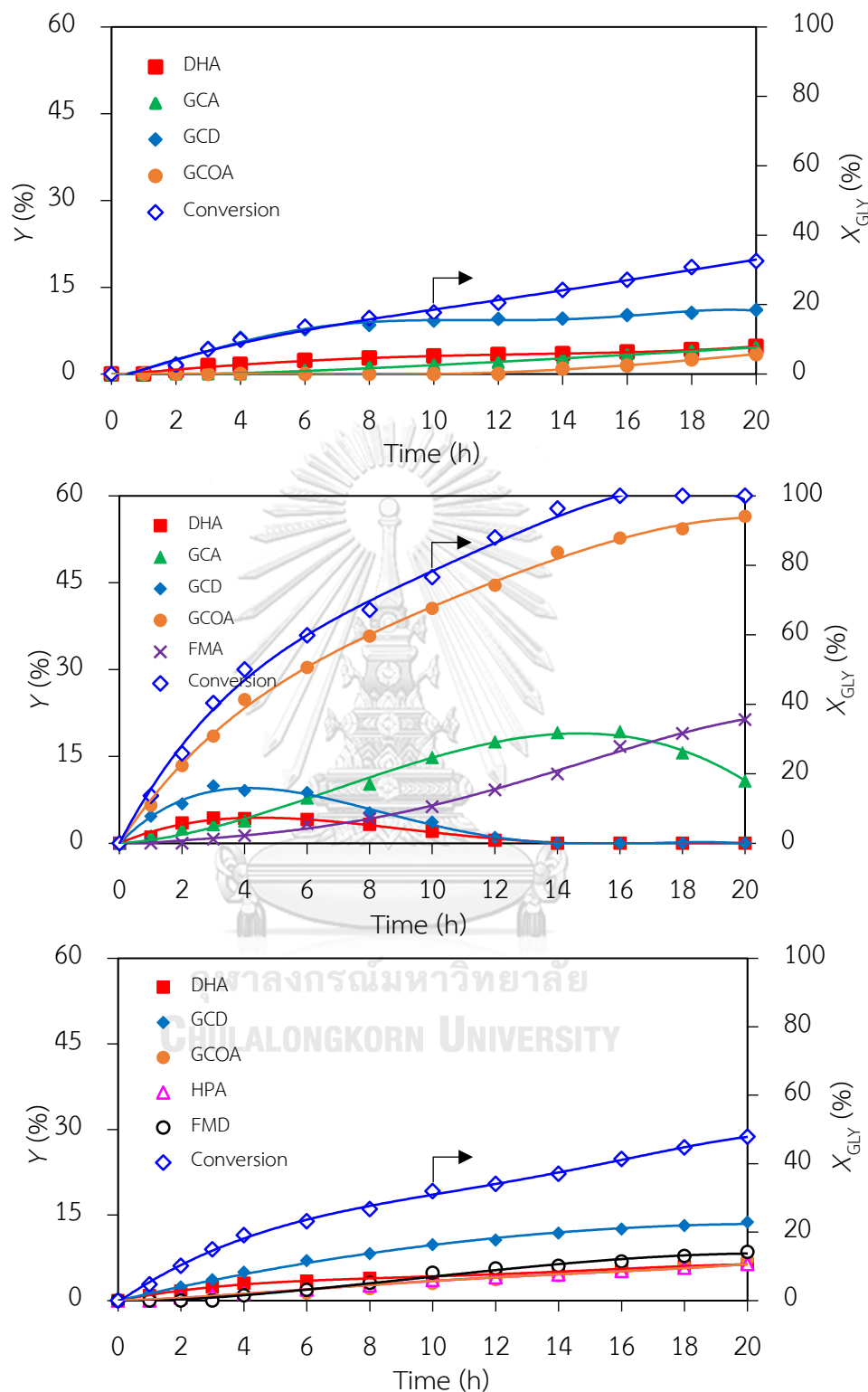


Figure 4.11 Variation of glycerol conversion and selected product yields at different experimental conditions of (a) UV light/TiO₂, (b) UV light/TiO₂/H₂O₂ (0.3 M) and (c) UV light/TiO₂/O₂.

[145]. To monitor the type of reactive oxygen species (ROS) generated in the system in the presence of both H_2O_2 and O_2 , the parallel reactions were carried out to monitor the production of two strong ROS, including the OH^\bullet radicals and $^1\text{O}_2$. The production of the former species was traced via the concentration loss of *p*CBA, while the generation of the latter species was monitored by the concentration loss of FFA [159, 160]. More decrease of *p*CBA- and FFA concentrations indicated a higher generation of OH^\bullet radical and $^1\text{O}_2$, respectively.

As demonstrated in Figure 4.12(a), under the irradiated-UV light with TiO_2 and absence of an electron acceptor, the concentration of *p*CBA decreased slightly as reaction time increased, while that of FFA remained constant (Figure 4.12(b)). This suggested the formation of OH^\bullet radicals in the irradiated-UV light and TiO_2 system, while the $^1\text{O}_2$ were not. When either H_2O_2 or O_2 were used as an electron acceptor, the concentration of *p*CBA and FFA decreased significantly, suggesting the formation of both OH^\bullet radical and $^1\text{O}_2$ in the system.

Based on the obtained results and literatures, the generation of OH^\bullet radicals and $^1\text{O}_2$ in this study system has been proposed as follows. When the TiO_2 absorbed the light having energy equal to or greater than its band gap energy, e^- is excited from the valence band to the conduction band, leaving a photogenerated h^+ in the valence band according to Eq.(4.1).

In the absence of an electron acceptor, the photogenerated h^+ is able to oxidize the surface-bond water molecules to produce highly reactive OH^\bullet radicals, while the generated e^- can further react with proton (H^+) to form gaseous H_2 according to Eqs.(4.14) and (4.15) [145, 161, 162].



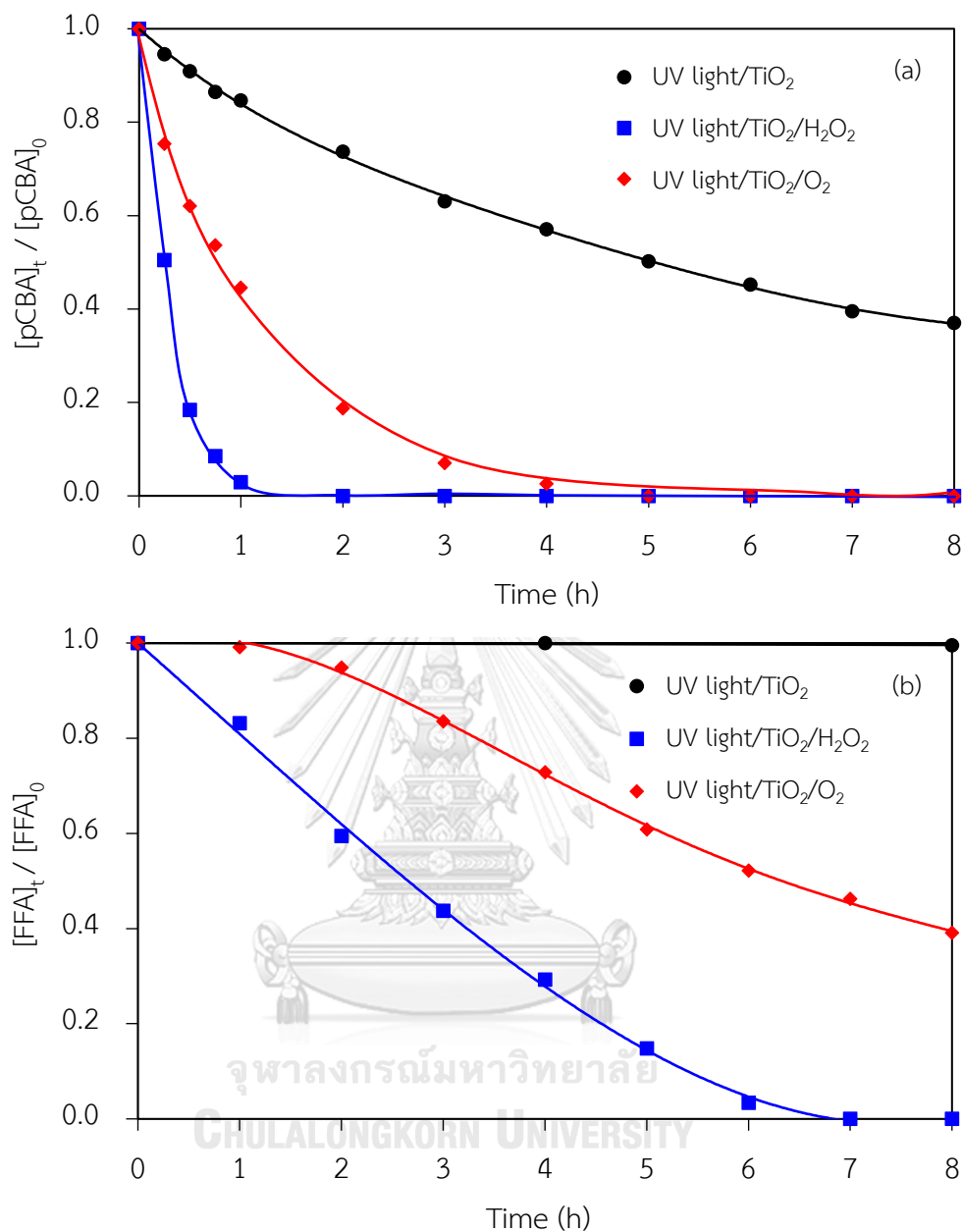
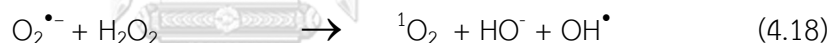
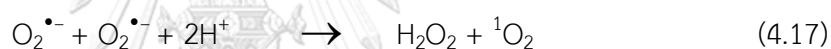
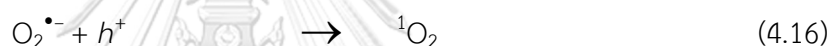


Figure 4.12 Variation of (a) pCBA and (b) FFA as a function of time in irradiated-UV light and TiO₂ system in the presence of H₂O₂ and O₂ as electron acceptors.

As exhibited in Figure 4.13(a), a low quantity of OH[•] radicals was produced in this case, probably due to the recombination of $h^+ - e^-$ pairs, which usually occurred in the absence of an electron acceptor, which can be confirmed by a low glycerol conversion and product yields as demonstrated in Figure 4.11(a).

In the presence of an electron acceptor, ex. H_2O_2 , both OH^\bullet radicals and $^1\text{O}_2$ were generated. Various elementary reactions can then proceed as follows. The H_2O_2 can break down to form OH^\bullet radicals (Eq.(4.2)) when it absorbs UV light. Besides, it can react via the photogenerated e^- or photogenerated h^+ according to Eqs. (4.2)-(4.4) to form OH^\bullet radicals.

Furthermore, it can oxidize via the formed HO^- and the photogenerated h^+ as well as the OH^\bullet radicals to form $\text{O}_2^{\bullet-}$ radicals, which readily react with H_2O_2 to form OH^\bullet radicals, according to Eqs.(4.5)-(4.7), respectively. Also, the generated $\text{O}_2^{\bullet-}$ radicals can further react with h^+ and H^+ as well as H_2O_2 to form $^1\text{O}_2$ and OH^\bullet radicals as mentioned above (Eqs.(4.16)-(4.18)). Both generated ROS had ability to oxidize glycerol to form various products as shown in Figure 4.12(b).



Regarding the use of O_2 as an electron acceptor, various possible reactions can be proposed. Initially, the supplied O_2 can react with the photogenerated e^- to form $\text{O}_2^{\bullet-}$ (Eq. (4.19)) and H_2O_2 (Eq. (4.20)) [161, 163]. The generated $\text{O}_2^{\bullet-}$ radicals can further react with h^+ and H^+ as well as H_2O_2 to form $^1\text{O}_2$ and OH^\bullet radicals (Eqs.(4.16)-(4.18)). Besides, the generated H_2O_2 in this system can dissociate after absorbing UV light or react with either photogenerated h^+ or e^- to form OH^\bullet radicals according to Eqs. (4.5)-(4.7).



With regard to the product generation in the presence of O_2 as electron acceptor, different value-added compounds were produced, particularly HPA and FMD. From the obtained results, it seems that the type of generated ROS including OH^\bullet

radical and $^1\text{O}_2$ did not affect the types of value-added compounds generated from glycerol conversion because both species were produced when either H_2O_2 or O_2 were used as an electron acceptor. This difference is probably due to the difference of the ROS concentration produced in the system.

To prove this hypothesis, additional experiment was carried out with low H_2O_2 concentration (0.075 M). As demonstrated in Figure 4.13, both OH^\bullet radical and $^1\text{O}_2$ were still generated in the presence of both low and high H_2O_2 concentrations but in different quantities observing from the different losses of *p*CBA and FFA concentrations. Large quantities of ROS were produced in the presence of high H_2O_2 concentration.

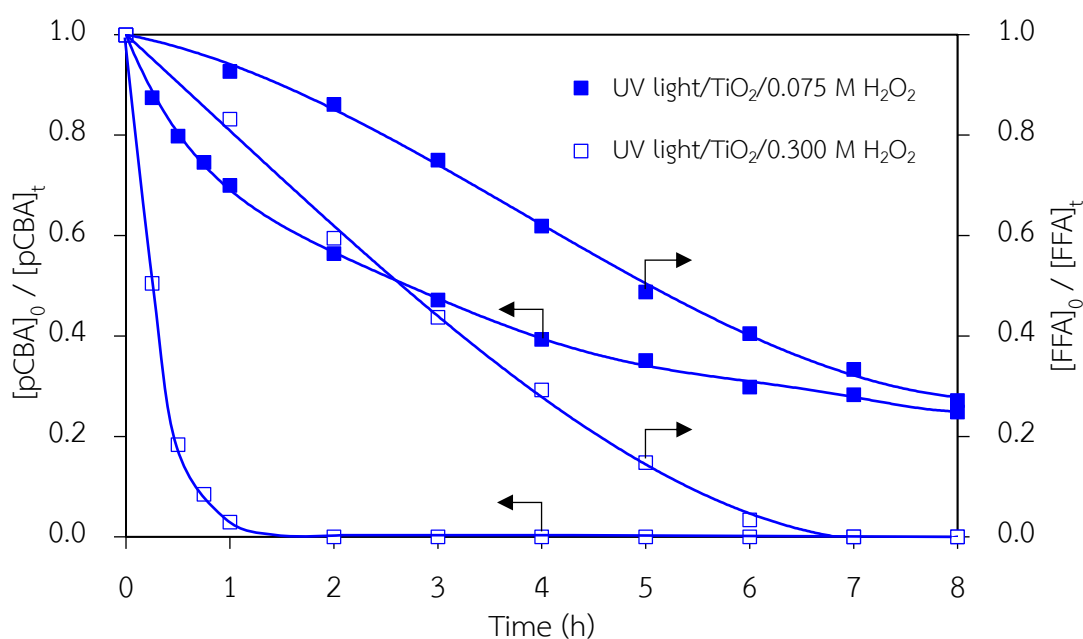


Figure 4.13 Variation of *p*CBA and FFA as a function of time in the presence of H_2O_2 at different concentrations.

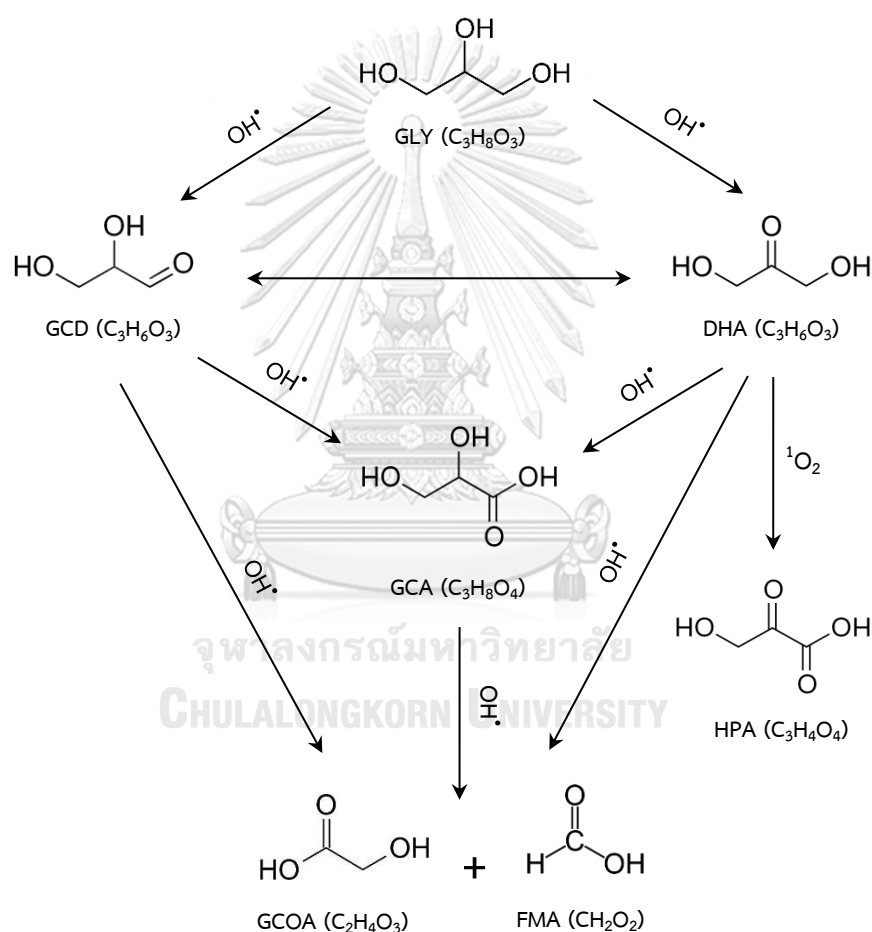
As far as the glycerol conversion and yield of value-added compounds produced at low H_2O_2 concentrations (Figure 4.14(a)), the types of value-added compounds were almost similar to those generated in the presence of high H_2O_2

concentration (Figure 4.14(b)) but with low quantity except with the FMA. Surprisingly, HPA was observed in this system, which indicates that the quantity of the present ROS affected the route of glycerol conversion as well as the type of generated products. In the presence of low OH^\bullet radical quantity, the $^1\text{O}_2$ can probably play as the principle ROS to attack the 1°-C atom of DHA to form HPA [164]. The threshold quantity of ROS that controls the route of glycerol conversion to form the different value-added compounds via the TiO_2 -induced photocatalytic oxidation was not determined at this stage. Thus, more extensive and expanded studies will be carried out to determine the threshold quantity of ROS.

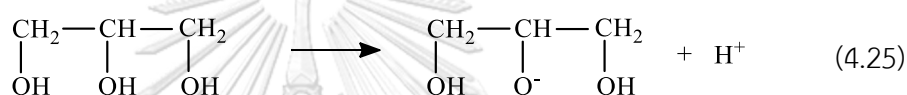
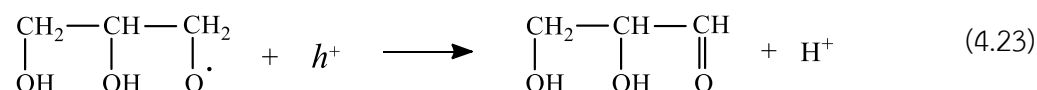
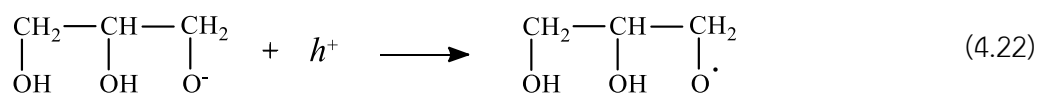
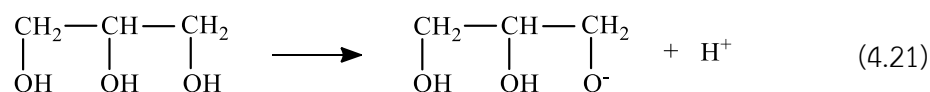
4.5 Mechanism of commercial TiO_2 -induced photocatalytic oxidation of glycerol

In summary, under the absence of electron acceptor (H_2O_2 or O_2), the photogenerated h^+ and the OH^\bullet radicals generated according to Eq.(4.1) and Eq.(4.14) can attach the 1° - or 2° - C atom of glycerol to form GCD or DHA, respectively [150]. Afterward, they can further oxidize the generated GCD to form GCA as well as cleave the C-C bond of GCA to form GCOA [151]. Besides, the DHA can be oxidized to GCA and GCOA. High glycerol conversion and yield of value-added compounds were observed in the presence of H_2O_2 , probably due to large amount of both OH^\bullet radical and $^1\text{O}_2$ generated as well as their high oxidizing power. The types of generated value-added compounds in this system are GCD, DHA, GCA, GCOA, and FMA. Whilst in the presence of O_2 , three identical value-added compounds were still observed including GCD, DHA and GCOA. Moreover, two more compounds were produced, including HPA and FMD. This difference is due to the difference of the ROS concentration generated in each system as illustrated in the previous section. Based on the experimental results and some literatures, the pathway of glycerol conversion and product generation via

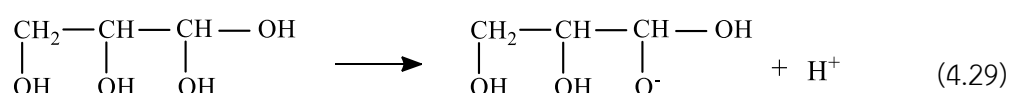
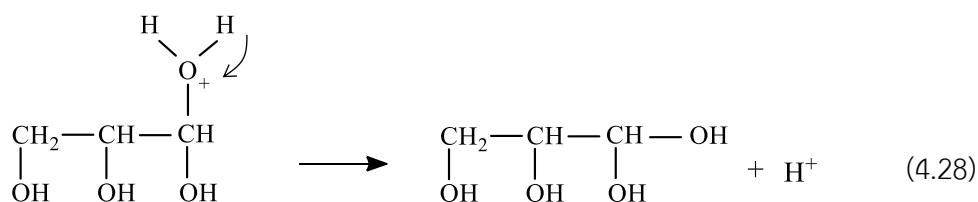
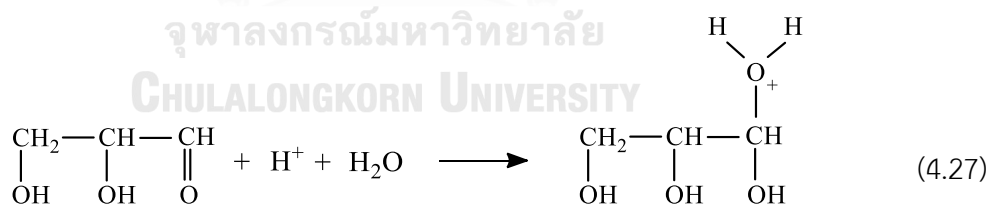
In the system with the presence of photogenerated h^+ , the glycerol molecule will act as an efficient scavenger of photogenerated h^+ , and then was oxidized to GCD and DHA, depending on the position of adsorbed -OH group. Namely, GCD was formed when the 1°-OH group of glycerol was selectively adsorbed and oxidized (Eqs. (4.21)-(4.23)), while DHA was generated when the 2°-OH group of glycerol is selectively adsorbed and oxidized (Eqs. (4.24)-(4.26)).

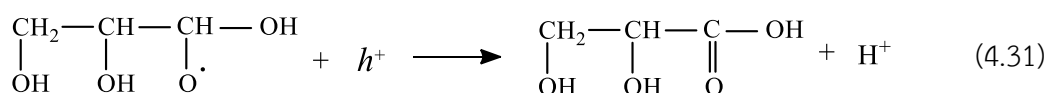
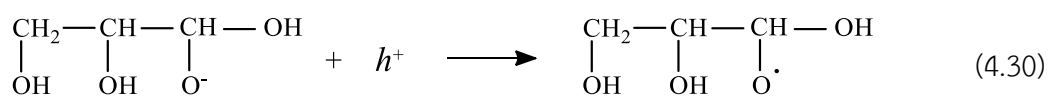


Scheme 3. Proposed reaction pathways with involving ROS for glycerol conversion via TiO₂-induced photocatalytic oxidation in the presence of H₂O₂ and O₂ as electron acceptors.

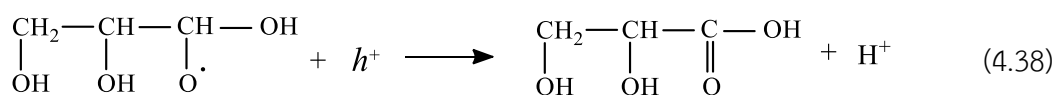
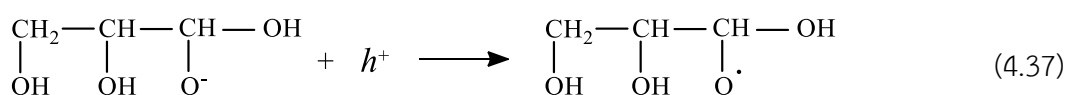
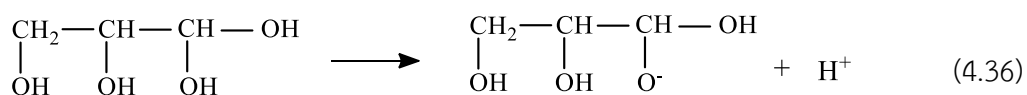
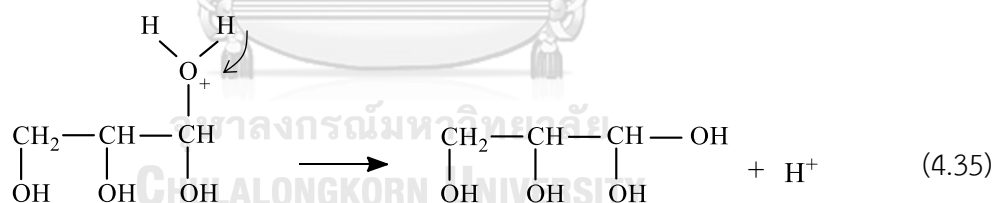
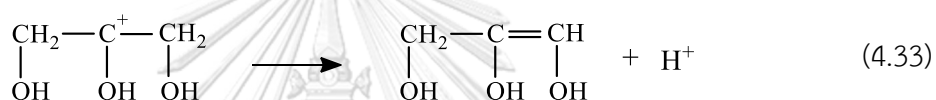


The generated GCD can be converted by a reaction with H^+ and the photogenerated h^+ as demonstrated as Eqs. (4.27)-(4.31) to form GCA.

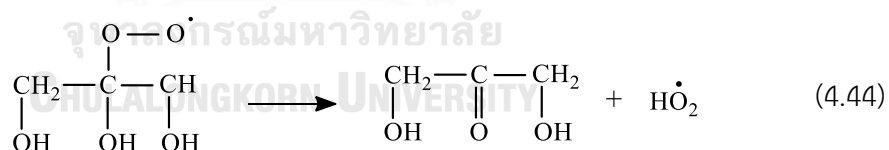
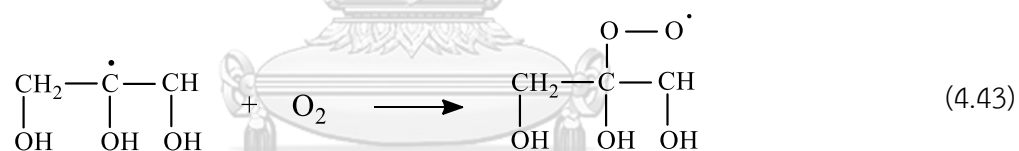
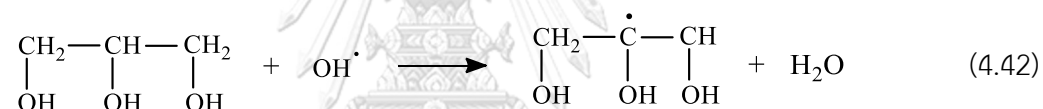
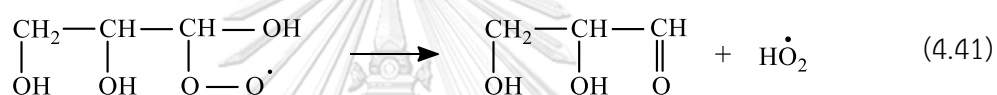
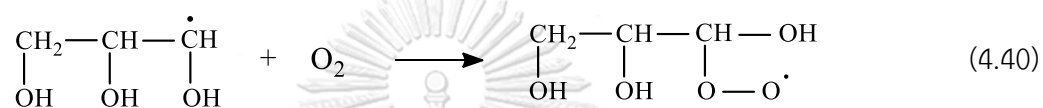
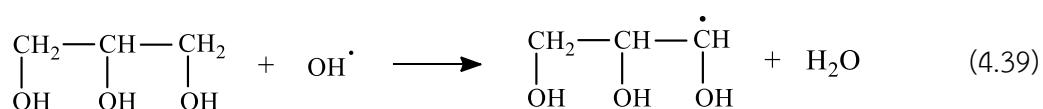




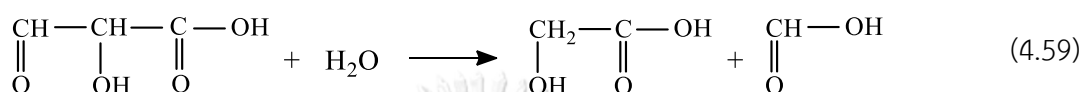
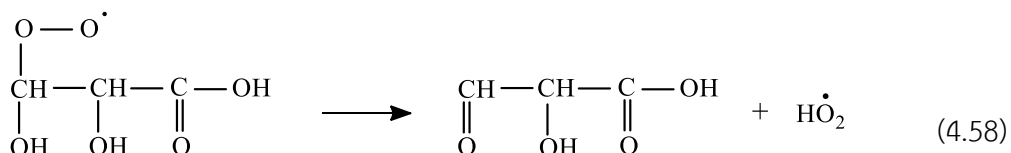
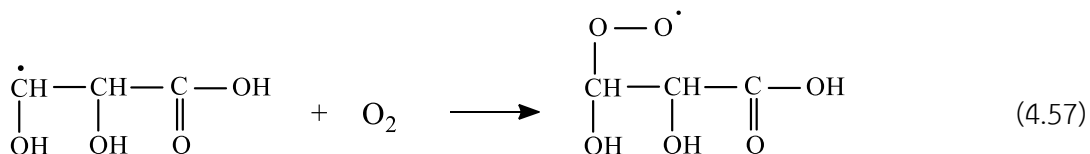
Furthermore, the generated DHA can be rearranged to GCD or oxidized to GCA via h^+ -mediated oxidation as Eqs. (4.32)-(4.38).



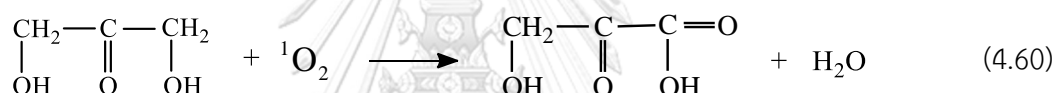
Under the presence the OH^\bullet radicals in the system, it is very reactive and can readily attach the C atom of glycerol to form GCD or DHA as Eqs. (4.39)-(4.41) or Eqs. (4.42)-(4.44), respectively, depending on the position of the attached C atom. That is, GCD and DHA were formed when the 1^o- and 2^o- C-atoms were respectively attached and oxidized.



The generated GCD can be further oxidized via the OH^\bullet radicals to GCA according to Eqs. (4.45)-(4.46), and the DHA can be oxidized to GCA and GCOA according to mechanism Eqs. (4.47)-(4.54) and Eq. (4.55), respectively. An excess OH^\bullet radical can also attach and cleave the C-C bond of GCA, resulting in the formation of GCOA and FMA (Eqs. (4.56)-(4.59)).



The generation of HPA in the system that exhibited $^1\text{O}_2$ as a major ROS might be caused by the attachment of $^1\text{O}_2$ at the primary carbon atom of DHA as Eq. (4.60)



This suggests that for the system having TiO_2 , UV light and either H_2O_2 or O_2 as electron acceptor, the conversion of glycerol and generation of products can proceed simultaneously by oxidation via the photogenerated h^+ and some radicals depending on the concentration of each ROS which will play a major role on the photocatalytic reaction.

CHAPTER V

METAL-DECORATED TiO₂ INDUCED PHOTOCATALYTIC OXIDATION OF GLYCEROL TO VALUE-ADDED COMPOUNDS

As well-known, the practical implementation of TiO₂ as a photocatalyst still faces two major obstructions due to its relatively large electronic band gap energy, which limits the effective photonic excitation under solar light and its low quantum efficiency in photocatalytic reactions, resulting in a high photogenerated e^-h^+ pairs recombination. This causes a decrease in the availability of the photogenerated charge carriers. Two strategies that can address this recombination problem are the use of an electron acceptor and the use of metal decorated on TiO₂ photocatalyst. In this chapter, it was focused on the latter strategy for enhance the glycerol conversion. The four types of monometallic NPs including bismuth (Bi), platinum (Pt), palladium (Pd), and gold (Au) and three types of bimetallic NPs including AuBi, AuPt and AuPd were selected to decorate on TiO₂ surface to enhance glycerol conversion and product distribution. The morphology and electronic properties of each prepared photocatalyst as well as their photocatalytic activity for glycerol conversion were studied throughout this work. Finally, the role of each decorated metal NPs in both mono- and bi-metallic system on photocatalytic activity was also evaluated.

5.1 Monometallic NPs decorated on TiO₂

5.1.1 Effect of decorated metal types

Four types of monometallic NPs including Bi, Pd, Pt, and Au, were selected to decorate on the surface of TiO₂ with the identical nominal content of 3 wt.% via the sol-immobilization technique. The as-prepared photocatalysts were donated as

Bi₃/TiO₂, Pd₃/TiO₂, Pt₃/TiO₂, and Au₃/TiO₂ for the decoration of Bi, Pd, Pt, and Au on TiO₂ support, respectively.

5.1.1.1 Crystallite structure analysis

The X-ray diffraction (XRD) patterns of as-prepared metal-decorated TiO₂ exhibited the main characteristic peaks of the crystalline structure of anatase phase at 2θ values of 25.3°, 37.8°, 48.0°, 53.9°, 55.3°, 62.7°, 68.7° and 70.5°, corresponding to the crystal planes of A(101), A(004), A(200), A(105), A(221), A(204), A(116) and A(220), respectively (Figure 5.1). Those of the metal-decorated TiO₂ photocatalysts still showed the main characteristic peaks of anatase TiO₂ along with the peaks of the respective doped metal. That is, the XRD of Bi/TiO₂ showed a peak of the Bi(110) plane at a 2θ of 39.7°, while that of Pd/TiO₂ showed peaks of the Pd(111) and Pd(200) planes at a 2θ of 40.14° and 46.8°, respectively. The XRD of Pt/TiO₂ exhibited two peaks at a 2θ of 39.8° and 46.3°, corresponding to the peaks of Pt(111) and Pt(200) planes, respectively, whilst Au/TiO₂ demonstrated peaks at 38.2°, 44.5° and 64.6°, relating to the characteristic peaks of the Au(111), Au(200) and Au(220) planes, respectively. No shift in the diffraction angles of anatase TiO₂ was observed, suggesting that the added metal species did not incorporate into the TiO₂ lattice but existed as a separate phase on the surface of the parent TiO₂.

The crystallite size of all the TiO₂ samples was estimated from the XRD patterns of A(101) crystallite plane using the Debye-Scherrer equation (Eq. 5.1).

$$D = K\lambda/(\beta\cos\theta) \quad (5.1)$$

where D is the mean size of the crystallite domain, K is dimensionless shape factor, λ is the X-ray wavelength, β is the line broadening at half the maximum intensity (FWHM) and θ is the Bragg angle (in degrees) [165]

As demonstrated in Table 5.1, the crystallite size of TiO_2 decorated by all respective metals had an almost similar crystallite size compared with the original TiO_2 , confirming that the addition of the respective metals did not affect the crystallite structure of TiO_2 .

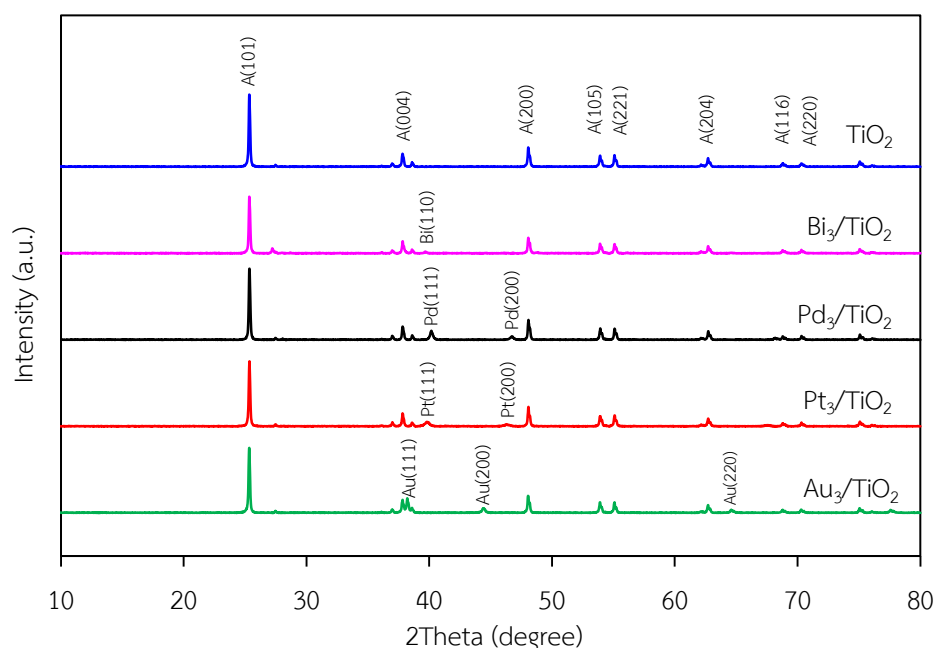


Figure 5.1 Representative XRD patterns of the TiO_2 and metal-decorated TiO_2 photocatalysts.

5.1.1.2 Morphology analysis

The particle size of all four decorated metals was estimated from the TEM images as demonstrated in Figure 5.2. The particle size of all metals was ranked as the order of $\text{Au} < \text{Pt} < \text{Pd} < \text{Bi}$ (Table 5.1). The entire quantity of decorated metals on the TiO_2 surface was then estimated by SEM-EDX analysis (Figure 5.3), where the actual metal content onto the TiO_2 surface was around 3.0 wt.% (Table 5.1), which closed to the set value. Regarding the textural property of all metal-decorated TiO_2 photocatalysts, as demonstrated in Table 5.1, their pore volume were closed to that

of commercial TiO₂, whilst their pore diameters were larger than that of commercial TiO₂. This is probably due to the pore widening during the preparation process when the decorated metal incorporated into the surface of TiO₂ under high temperature, which consequently reduce the BET surface area.

5.1.1.3 Chemical structure analysis

To estimate the bonding and chemical state of Ti, O and all doped-metals, XPS analysis was performed with the deconvolution and analysis of the peaks being performed by the XPSPEAK4.1 software. After Gaussian-Lorentzian fitting of the peak shape, it was found that the XPS spectra of the original TiO₂ photocatalyst showed two symmetric peak shapes of Ti2p at a binding energy of 465.2 and 459.4 eV, assigned to the Ti2p_{1/2} and Ti2p_{3/2} components, respectively (Figure 5.4(a1)), confirming the state of Ti as Ti⁴⁺ in the TiO₂ structures. For the metal-decorated TiO₂ photocatalysts, the principle peaks related to the Ti2p_{1/2} and Ti2p_{3/2} components were still observed at the same binding energy with respect to those of TiO₂. In addition, satellite features were observed at a lower binding energy of Ti2p peaks at around 463.8 and 457.9 eV (Figure 5.4(b1)-(e1)), indicating the formation of a Ti³⁺ state or defects on the surface of TiO₂, caused by the cooperation of the metal state on the surface of TiO₂. Recently, it was reported that the presence of Ti³⁺ defect states on the TiO₂ surface could form sublevel states below the conduction band that serve as adsorption sites or charge carrier traps, and so can prevent the recombination of the photogenerated e⁻ and h⁺ and reduce some portion of the TiO₂ band gap energy [166, 167].

With respect to the XPS spectra of O1s of the photocatalysts, an asymmetric shape peak was observed in all cases (Figure 5.4(a2)-(e2)). The main O1s peak appeared at a binding energy of 530.2-530.6 eV, assigned to the O²⁻ ions of the crystalline network. A small O1s peak was observed in the 531.8-532.0 eV range and was assigned

Table 5.1 Properties of metal-decorated TiO₂ photocatalysts.

| Type of photocatalyst | Crystallite size of TiO ₂ (nm) ^a | Size of decorated metal (nm) ^b | Metal content (wt. %) | Textural property | | | Band gap energy (E _g , eV) |
|-----------------------------------|--|---|-----------------------|---------------------------------------|----------------------------------|--------------------|---------------------------------------|
| | | | | BET surfaces area (m ² /g) | Pore volume (cm ³ /g) | Pore diameter (nm) | |
| TiO ₂ | 60.40 | - | - | 22.84 | 0.0461 | 8.07 | 3.21 |
| Bi ₃ /TiO ₂ | 60.60 | 58.3 ± 3.4 | 2.9 ± 0.0 | 13.17 | 0.0464 | 14.1 | 3.22 |
| Pd ₃ /TiO ₂ | 59.65 | 27.4 ± 1.7 | 3.0 ± 0.1 | 14.52 | 0.0535 | 14.7 | 3.21 |
| Pt ₃ /TiO ₂ | 61.04 | 14.8 ± 1.0 | 3.0 ± 0.2 | 11.37 | 0.0428 | 15.0 | 3.21 |
| Au ₃ /TiO ₂ | 59.53 | 7.51 ± 0.9 | 3.0 ± 0.1 | 10.46 | 0.0433 | 16.6 | 3.21 |

^a Calculated from Debye-Scherrer's equation

^b Calculated from TEM image with number of particles not less than 100 particles

SI
SITY

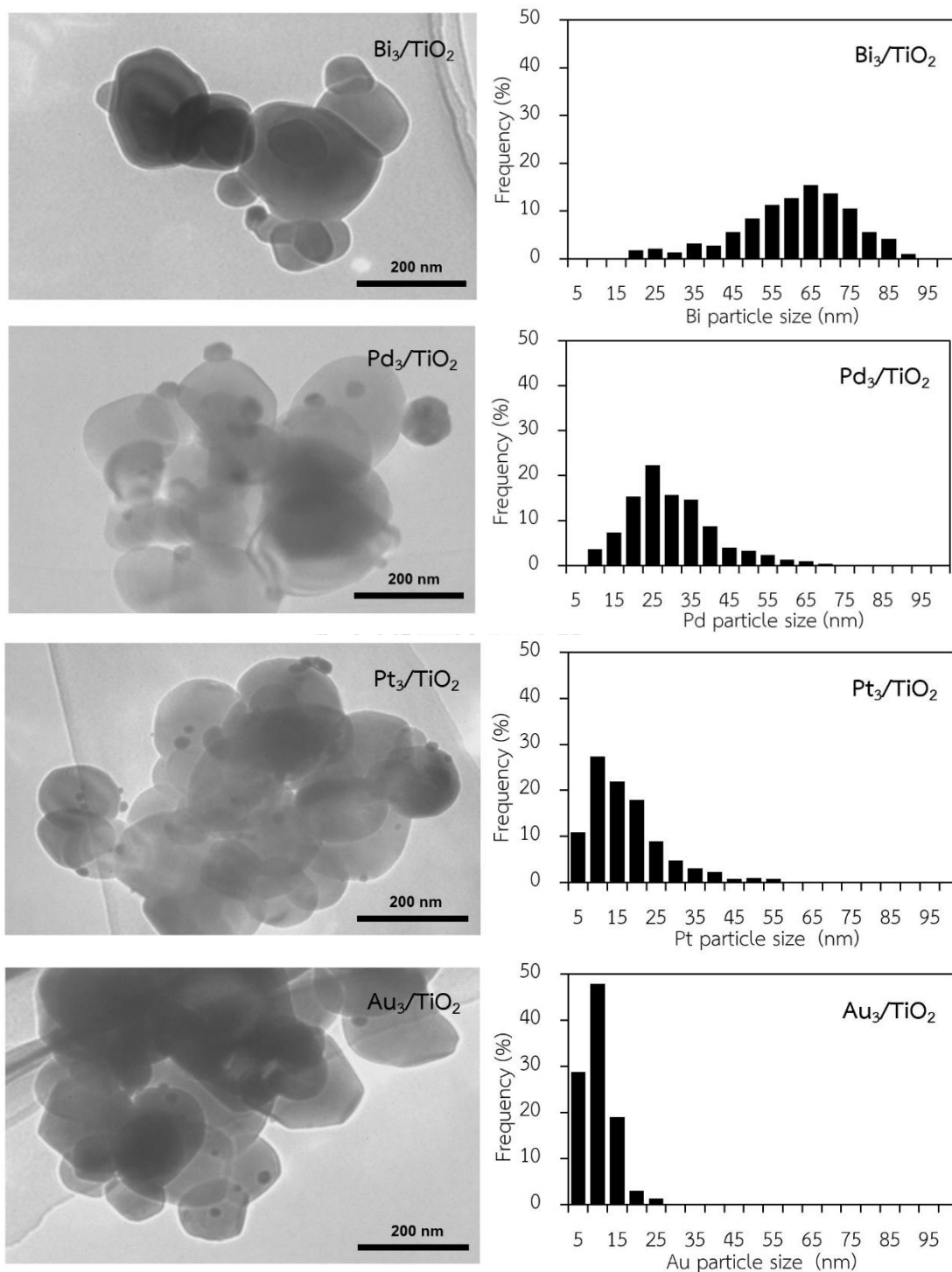


Figure 5.2 (Left) Representative TEM images of the TiO₂ and metal-decorated TiO₂ and (Right) their particle size distributions.

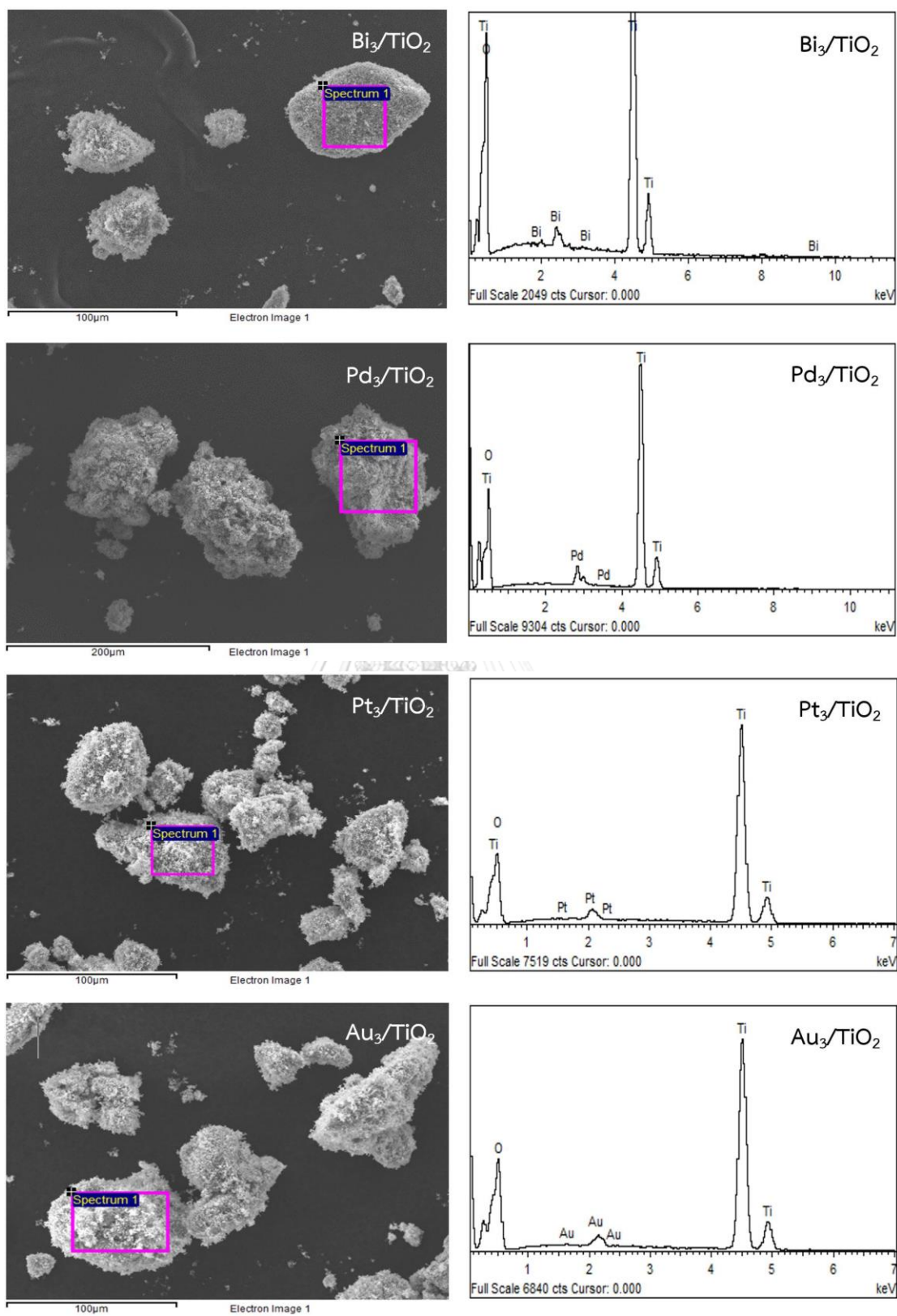


Figure 5.3 Representative of SEM-EDX of the metal-decorated TiO₂ photocatalyst.

to the OH⁻ ions of the crystalline network, while the third peak generated at a binding energy of 533.0 eV was due to the adsorbed H₂O. Interestingly, one additional O1s peak was observed for Bi₃/TiO₂ at a binding energy of 529.0 eV. Generally, the main bismuth oxide compound on Bi₃/TiO₂ was Bi₂O₃. However, no characteristic peaks of Bi₂O₃ (2θ of 31.8°) were observed in the XRD pattern. In addition, Bi₂O₃ is a semiconductor with a direct band gap of 2.8 eV that exhibited the ability to absorb visible light [168-170]. However, the Bi₃/TiO₂ photocatalyst did not absorb visible light (Figure 5.6(a)), indicating that no Bi₂O₃ was generated in its structure. Thus, the O1s peak at a binding energy of 529.0 eV in the Bi₃/TiO₂ photocatalyst can be considered as the non-bridging Bi-O- component [171].

With regard to the chemical state of the doped metals on the surface of the photocatalysts, the XPS spectra of Bi₃/TiO₂ showed the shoulder and main peaks of the Bi4f_{7/2} components at a binding energy of 157.9 and 159.6 eV, respectively, and also exhibited the shoulder and main peaks of the Bi4f_{5/2} components at a binding energy of 163.3 and 165 eV, respectively (Figure 5.4(b3)). These indicate the presence of Bi in both metallic (Bi⁰) and ionic (Bi³⁺) states. For Pd₃/TiO₂, the XPS spectra exhibited two asymmetric peaks at a maximum binding energy of 335.1 and 340.5 eV and also two shoulder peaks at a binding energy of 336.0 and 341.8 eV (Figure 5.4(c3)), suggesting that the Pd was present in both metallic (Pd⁰) and ionic (Pd²⁺) forms. An almost similar pattern of the XPS spectra to Pd₃/TiO₂ was observed for Pt₃/TiO₂, the main Pt4f_{7/2} and Pt4f_{3/2} components being located at a binding energy of 71.2 and 74.6 eV, assigned to the metallic state (Pt⁰) (Figure 5.4(d3)), and the two small shoulder peaks at 71.9 and 75.6 eV being assigned to the ionic state (Pt²⁺). For the Au₃/TiO₂ photocatalyst, two symmetric XPS signals were observed at a binding energy of 84.0 eV (Au4f_{7/2}) and 87.6 eV (Au4f_{5/2}), but no shoulder peak was observed at a higher binding energy (Figure 5.4(e3)), indicating the presence of Au only in the metallic state. The respective

presence of Bi^{3+} , Pd^{2+} and Pt^{2+} in the structure of the Bi_3/TiO_2 , Pd_3/TiO_2 and Pt_3/TiO_2 photocatalysts can play a role in their photocatalytic property. As mentioned previously, the presence of Bi^{3+} can trap electrons, affecting the simplicity/difficulty for e^-h^+ recombination [131, 172] and also induced the formation of Ti^{3+} that can form a sublevel state under the conduction band. On the other hand, the presence of either PdO or $\text{Pt}(\text{OH})_2$ components can enhance the visible light absorption [89, 173]. From the above results, the presence of their metal state provided a different step of electron transfer, which consequently affected the simplicity / difficulty for e^-h^+ recombination.

To explore the electron density state of the valence band of the photocatalysts, the valence band XPS was evaluated. The TiO_2 powder showed a typical valence band with the edge of the maximum energy at around 2.7 eV (Figure 5.5(a)). However, the band gap energy of TiO_2 is 3.21 eV, suggesting that the conduction band minimum would occur at -0.51 eV. The linear regions of the valence band spectra, which indicated the characteristic valence band edge of TiO_2 at a binding energy of at 2.7 eV, was still observed for all the metal-decorated TiO_2 photocatalysts (Figure 5.5). Moreover, a down-field linear portion of valence band spectra was also observed for the Pd_3/TiO_2 , Pt_3/TiO_2 and Au_3/TiO_2 photocatalysts at a binding energy of -1.5, -0.6 and 1.4 eV, respectively (Figure 5.5(b)-(e)), caused by the plasmon band of the Pd, Pt and Au metallic states. This is due to the oscillations of the conduction electrons in the metal under visible light irradiation or the LSPR effect [174-176]. However, the LSPR effect was not observed in the valence band spectra of Bi/TiO_2 , where only a slight increase with a binding energy of 1.0–3.2 eV was observed. The improved valence band edge indicated the localized valence band bending that resulted from the alteration of the overlapping $\text{Bi}6s$ and $\text{O}2p$ orbitals and demonstrated the formation of a band tail [169]. However, the band tail behavior of

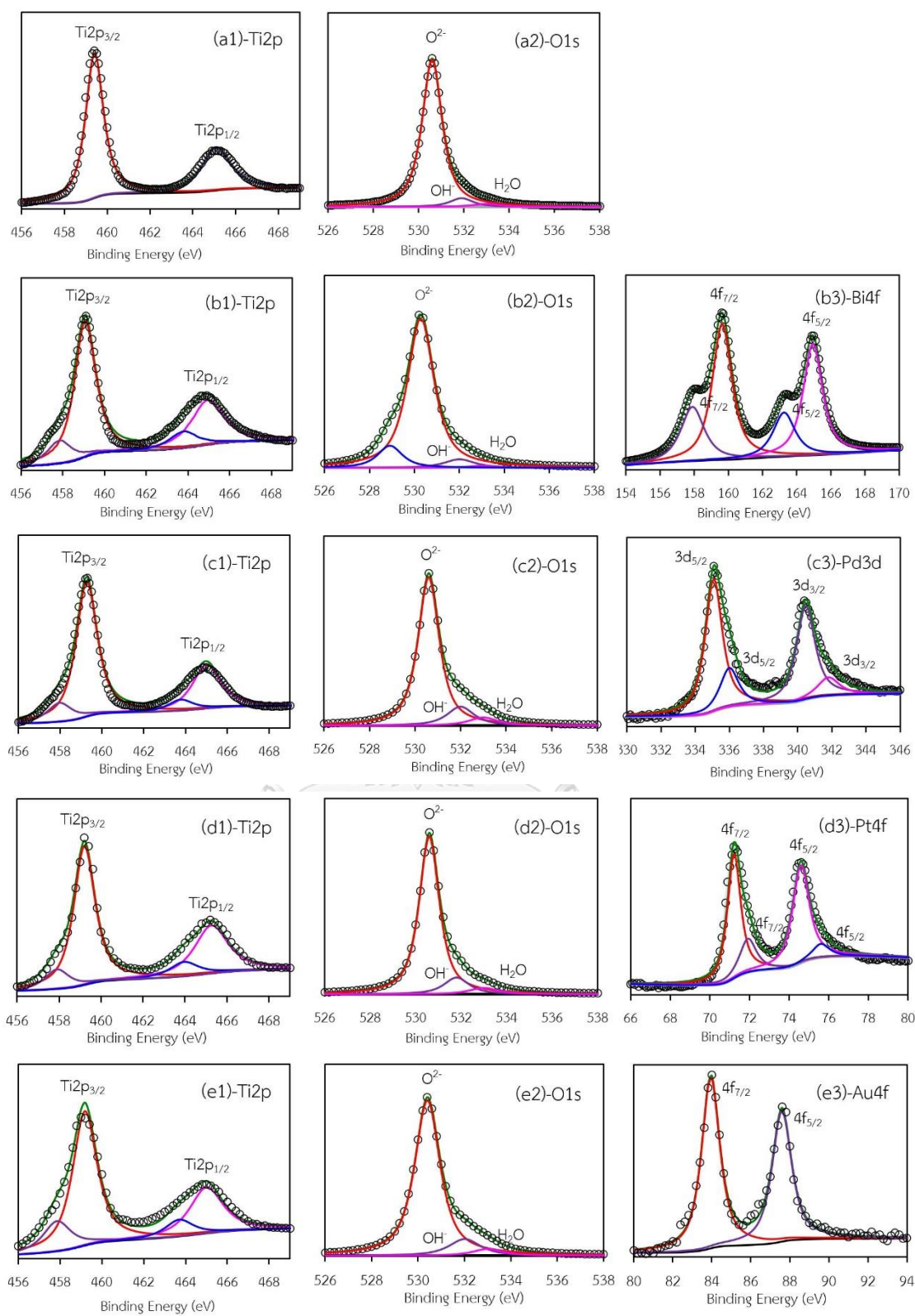


Figure 5.4 XPS spectra of (a) TiO_2 , (b) Bi_3/TiO_2 , (c) Pd_3/TiO_2 , (d) Pt_3/TiO_2 and (e) Au_3/TiO_2 .

TiO₂ was not observed in the valence band spectra of Pd₃/TiO₂, Pt₃/TiO₂ and Au₃/TiO₂, which might be due to their interference with the metallic state spectra of the decorated-metals.

5.1.1.4 Optical property analysis

Figure 5.6(a) represents the optical absorption spectra of parent TiO₂ and metal-decorated TiO₂ photocatalysts in the wavelength range of 300–800 nm at room temperature. All the as-prepared photocatalysts absorbed the UV light at a wavelength of <400 nm. A decay of absorbance to a zero value was observed for TiO₂ and the Bi/TiO₂ under the visible light region (> 450 nm), suggesting that the parent TiO₂ and Bi₃/TiO₂ doesn't have ability to adsorb light in the visible region. Interestingly, the absorption spectra of Pd₃/TiO₂, Pt₃/TiO₂ and Au₃/TiO₂ were observed in the visible light region, suggesting their ability to absorb visible light. This is probably due to the characteristics of nanoscale noble metals that can absorb visible light through the localized surface plasmon resonance effect (LSPR) due to the polarization and oscillation of the conduction electrons in the metal structure [177-180].

Taking into account the linear portion of the fundamental absorption edge of the UV-visible spectra (Figure 5.6(a)) and the plots of $(\alpha h\nu)^{1/n}$ against $(h\nu)$ (Figure 5.6(b)), where α is the optical absorption coefficient determined from the obtained absorbance, $h\nu$ is the energy of the incident photons and n is the nature of the electronic transition (equal to 2 for anatase TiO₂), yields the value of band gap energy (E_g) by drawing the tangent line to the slope. The E_g values of all the metal-decorated TiO₂ photocatalysts were close to that of TiO₂ (Table 5.1), which suggests that the addition of metals on the TiO₂ powder did not affect the main E_g of the obtained photocatalysts. This is attributed to the fact that the doped metals did not incorporate into the TiO₂ lattice, resulting in no alteration to the major electronic state as well as

the band gap between the valance band in the O2p state and conduction band in the Ti3d state.

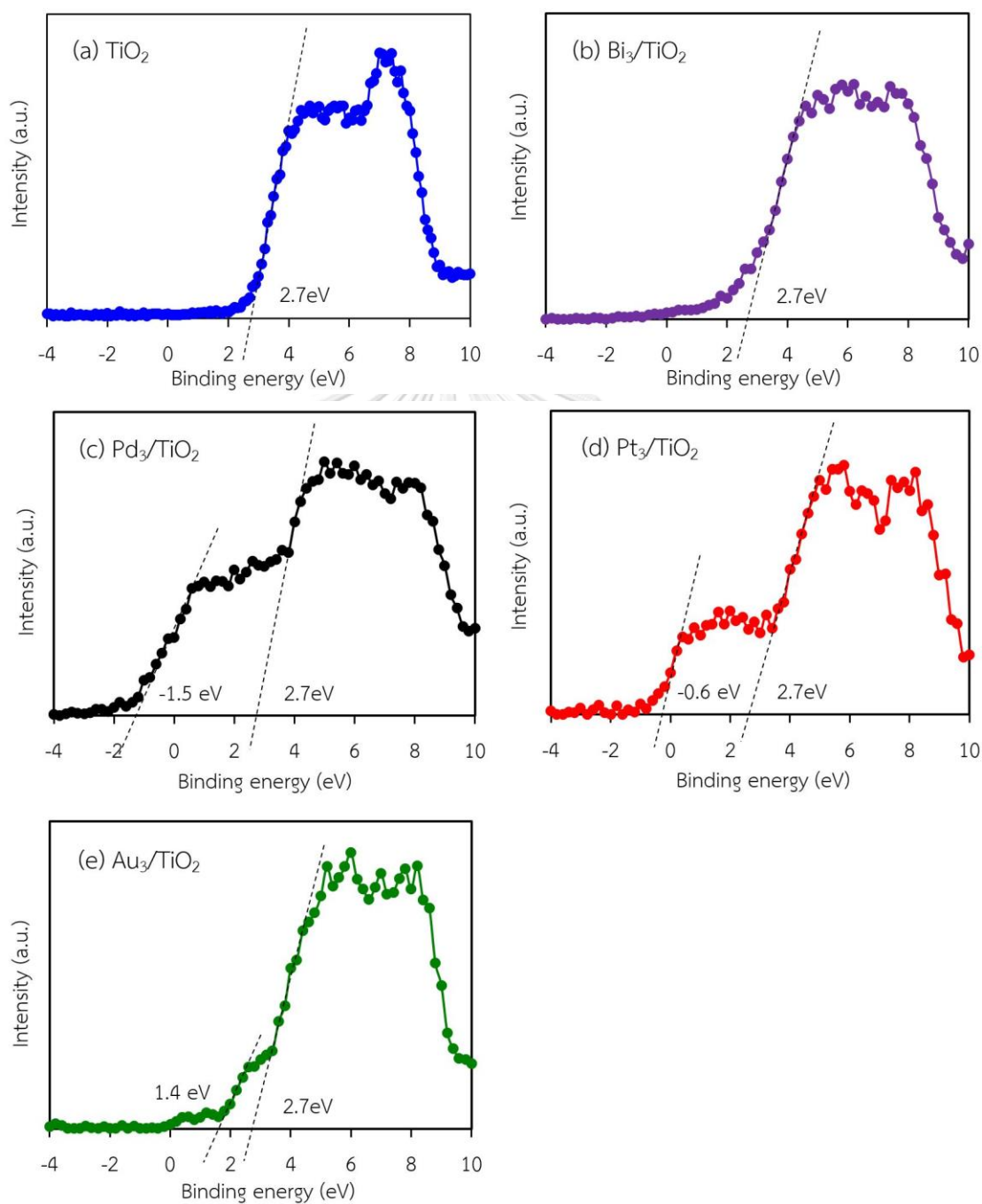


Figure 5.5 Valence band spectra of TiO_2 and metal-decorated TiO_2 photocatalysts.

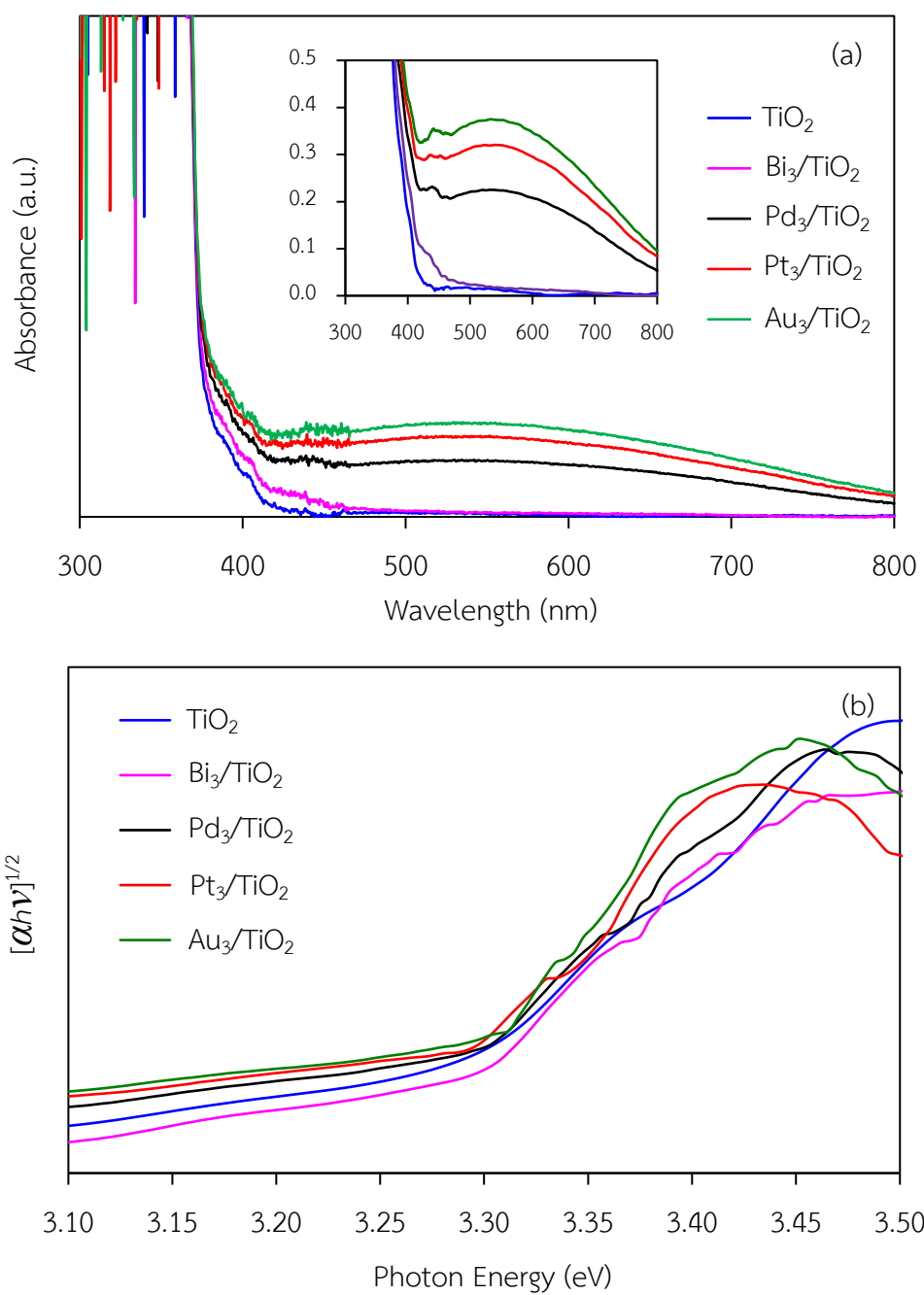


Figure 5.6 Representative (a) UV-visible spectra and the depended of $(\alpha h\nu)^{1/2}$ on photon energy of TiO₂ and metal-decorated TiO₂ photocatalysts.

5.1.1.5 Photocatalytic activity test for glycerol conversion

The activity of all the prepared photocatalysts in the glycerol conversion was tested in a photoreactor in the presence of a light intensity of 4.68 mW/cm^2 , catalyst loading of 3 g/L and reaction time of 14 h . As demonstrated in Figure 5.7, the conversion of glycerol was ranked in the order of $\text{Au}_3/\text{TiO}_2 > \text{Pt}_3/\text{TiO}_2 > \text{Pd}_3/\text{TiO}_2 > \text{Bi}_3/\text{TiO}_2 > \text{TiO}_2$ under the same test condition. This suggests that the Au_3/TiO_2 and TiO_2 had the highest and lowest activity, respectively, for glycerol conversion. The different activity for glycerol of each photocatalyst might be attributed to their differential ability to absorb visible light and their simplicity/difficulty for e^-h^+ recombination, not related to the BET surface area. The light source used in this work provided a wide wavelength of light spectrum ($100\text{--}600 \text{ nm}$), which consisted of both UV and visible lights. Also, as shown in Figure 5.6(a), the absorbance intensity of the metal-decorated TiO_2 photocatalysts at wavelengths of $480\text{--}800 \text{ nm}$ was ranked in the order of $\text{Au}_3/\text{TiO}_2 > \text{Pt}_3/\text{TiO}_2 > \text{Pd}_3/\text{TiO}_2 > \text{Bi}_3/\text{TiO}_2 > \text{TiO}_2$. This indicates the ability trend to absorb the photon energy as the order of $\text{Au}_3/\text{TiO}_2 > \text{Pt}_3/\text{TiO}_2 > \text{Pd}_3/\text{TiO}_2 > \text{Bi}_3/\text{TiO}_2 > \text{TiO}_2$. A high quantity of absorbed photons can achieve a high level of photogenerated h^+ and e^- on the TiO_2 surface. The plausible reason for different visible light absorbance intensity might be due to the particle size difference of decorated metals. As demonstrated in Table 5.1, the particle size of Au was smaller than other decorated metals, which can enhance a high LSPR effect [133, 181], compared with other photocatalysts.

As well-known that the active species generated via the photochemical process can oxidize glycerol effectively. As mentioned in previous chapter, once the photocatalyst absorbs the light, the h^+ and e^- are generated. The supplied O_2 can react with the e^- to form $\text{O}_2^{\bullet-}$ (Eq. (4.19)) and H_2O_2 (Eq. (4.20)) [161, 163]. Sequentially, the generated $\text{O}_2^{\bullet-}$ radicals can further react with h^+ and H^+ as well as H_2O_2 to form $^1\text{O}_2$ and OH^{\bullet} radicals (Eqs. (4.16) - (4.18)). In addition, the generated H_2O_2 in this system can

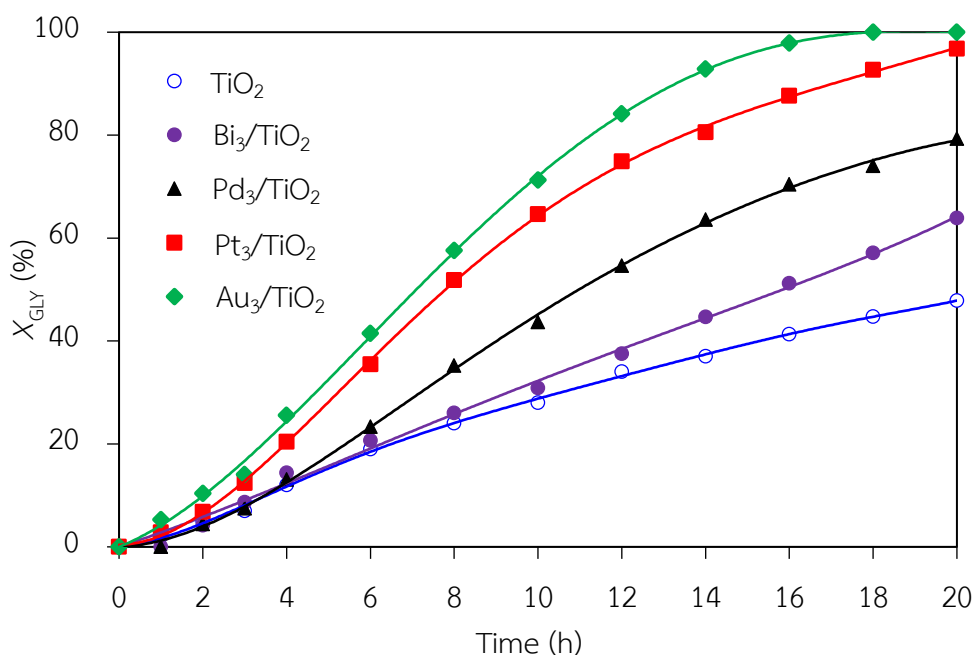


Figure 5.7 Variation of glycerol as a function of time in the presence of TiO₂ and metal-decorated TiO₂ under the irradiated UV light in the presence of O₂ as electron acceptor, a light intensity of 4.68 mW/cm², photocatalyst loading of 3 g/L.

dissociate after absorbing UV light or react with either photogenerated h^+ or e^- to form OH• radicals according to Eqs. (4.5)-(4.7).

To monitor the generation of some reactive oxygen species (ROS), the variation of two strong ROSs, including the OH• radicals and ¹O₂ against time was traced by the concentration loss of pCBA and FFA, respectively. As shown in Figure 5.8, the loss of both pCBA and FFA concentrations was ranked in the order of Au₃/TiO₂ > Pt₃/TiO₂ > Pd₃/TiO₂ > Bi₃/TiO₂ > TiO₂. This suggests that the quantity of OH• radicals and ¹O₂ formation was ranked as a similar trend. The generated species, including the h^+ , OH• radical and oxide radicals (¹O₂/ O₂•⁻), can act as oxidizing species [142-145], to oxidize organic compounds effectively, including glycerol.

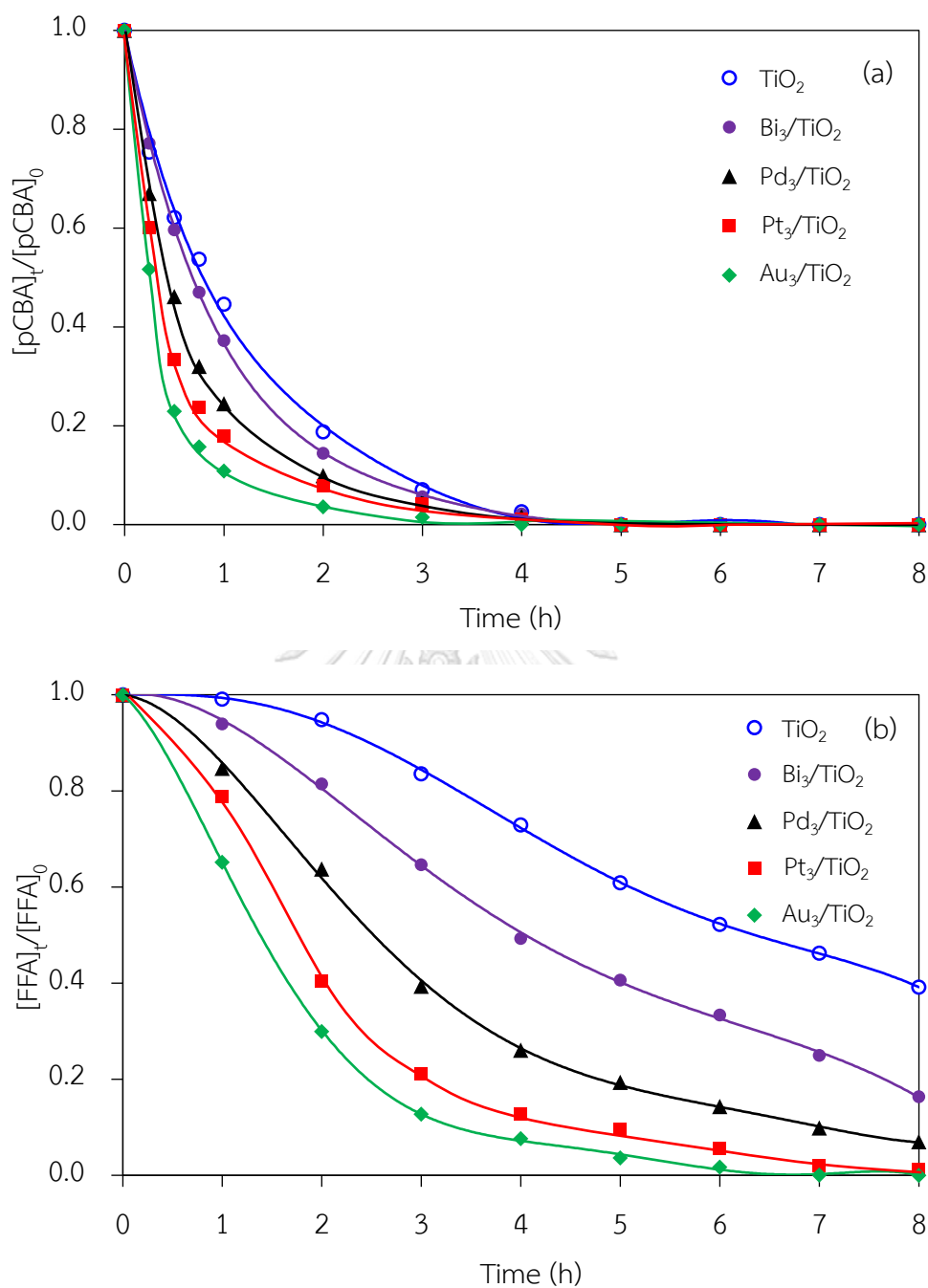


Figure 5.8 Variation of (a) pCBA and (b) FFA as a function of time in the irradiated UV light in the presence of different metal-decorated TiO₂ photocatalysts using O₂ as electron acceptors.

The mechanism of glycerol conversion to value-added compounds under UV light and photocatalyst was already proposed in previous chapter. Briefly, the photogenerated h^+ and the OH^\bullet radicals can attach to the 1°- or 2°-C atom of glycerol to form GCD or DHA, respectively. The generated GCD and DHA can be further oxidized to form GCOA and/or HPA. As obviously observed in Figure 5.9, the principle compound generated with all the photocatalysts was GCD. This suggests that the generated ROS from the as-prepared metal-decorated TiO_2 prefer to attach to the 1°-C atom of glycerol rather than the 2°-C atom. A long reaction time induced a decrease of GCD yield, but an increase of GCOA and FMD yield, particular in the presence of Au/TiO_2 catalysts. This might be attributed to the fact that a high content of ROS induced the conversion of GCD to GCOA, which is further converted to FMD. The selectivities of all monitored products at the end of reaction time (20 h) were listed in Table 5.2. It seems to be that the TiO_2 , Bi_3/TiO_2 and Pd_3/TiO_2 promoted the production of the GCD, while the Pt_3/TiO_2 and Au_3/TiO_2 preferred to produce the FMD.

Table 5.2 Glycerol conversions and product selectivity in the presence of TiO_2 and metal-decorated TiO_2 photocatalysts under the irradiated UV light in the presence of O_2 as electron acceptor^a.

| Type of photocatalyst | Glycerol conversion (%) | S (%) | | | | |
|-----------------------|-------------------------|-------|-------|-------|-------|-------|
| | | DHA | GCD | GCOA | HPA | FMD |
| TiO_2 | 47.84 | 15.08 | 32.54 | 17.01 | 15.14 | 20.23 |
| Bi/TiO_2 | 63.88 | 14.98 | 32.58 | 13.89 | 18.71 | 19.84 |
| Pd/TiO_2 | 79.22 | 12.61 | 33.22 | 14.31 | 19.51 | 20.36 |
| Pt/TiO_2 | 92.67 | 4.95 | 22.05 | 25.47 | 10.66 | 36.87 |
| Au/TiO_2 | 100.0 | 6.86 | 17.18 | 30.38 | 10.36 | 35.23 |

^a Light intensity of 4.68 mW/cm^2 , photocatalyst loading of 3 g/L, reaction time 20 h.

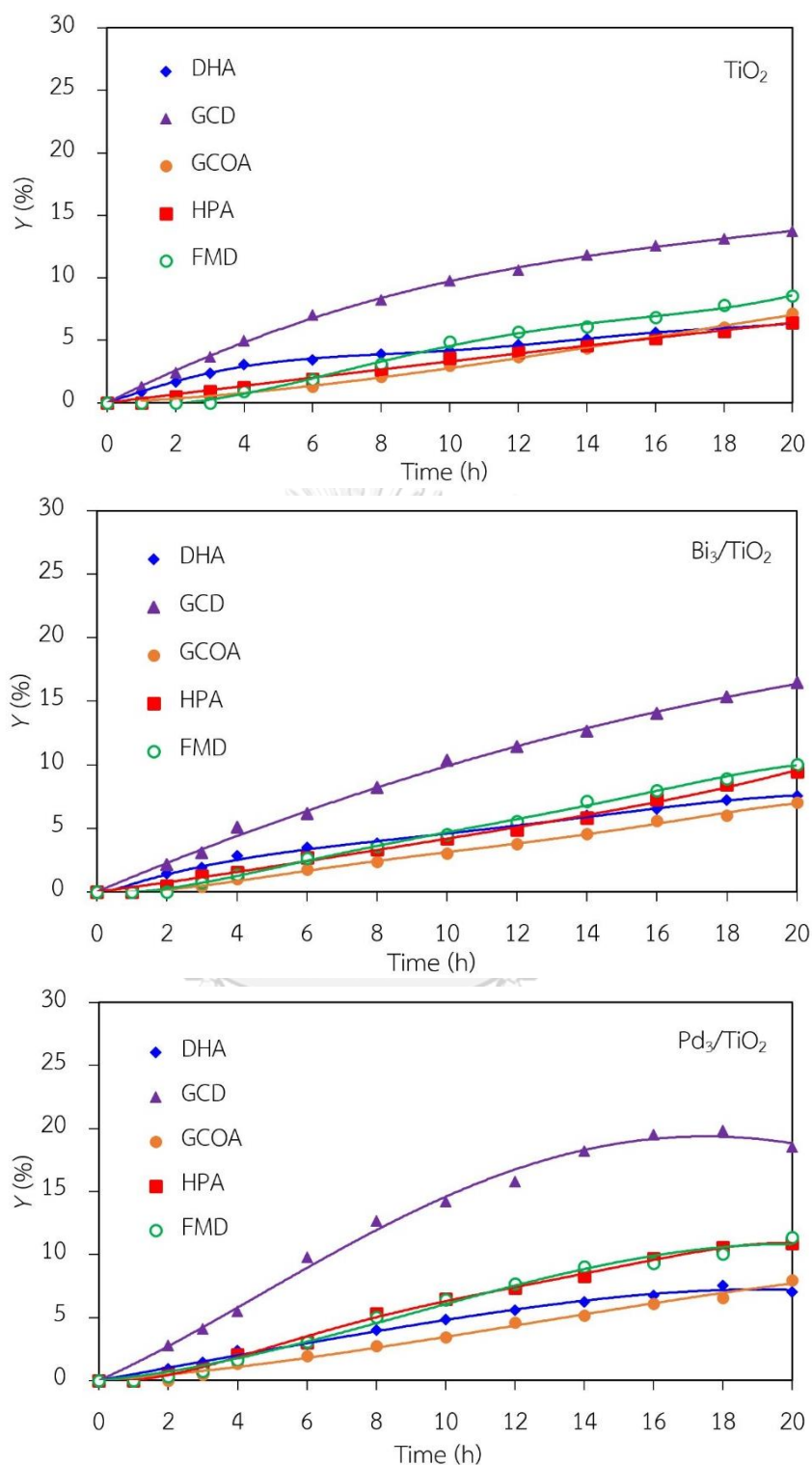


Figure 5.9 Yield of selected products obtained from glycerol photocatalytic conversion via TiO_2 and metal-decorated TiO_2 at loading of 3.0 g/L with an average light intensity of 4.7 mW/cm^2 and using O_2 as the electron acceptor.

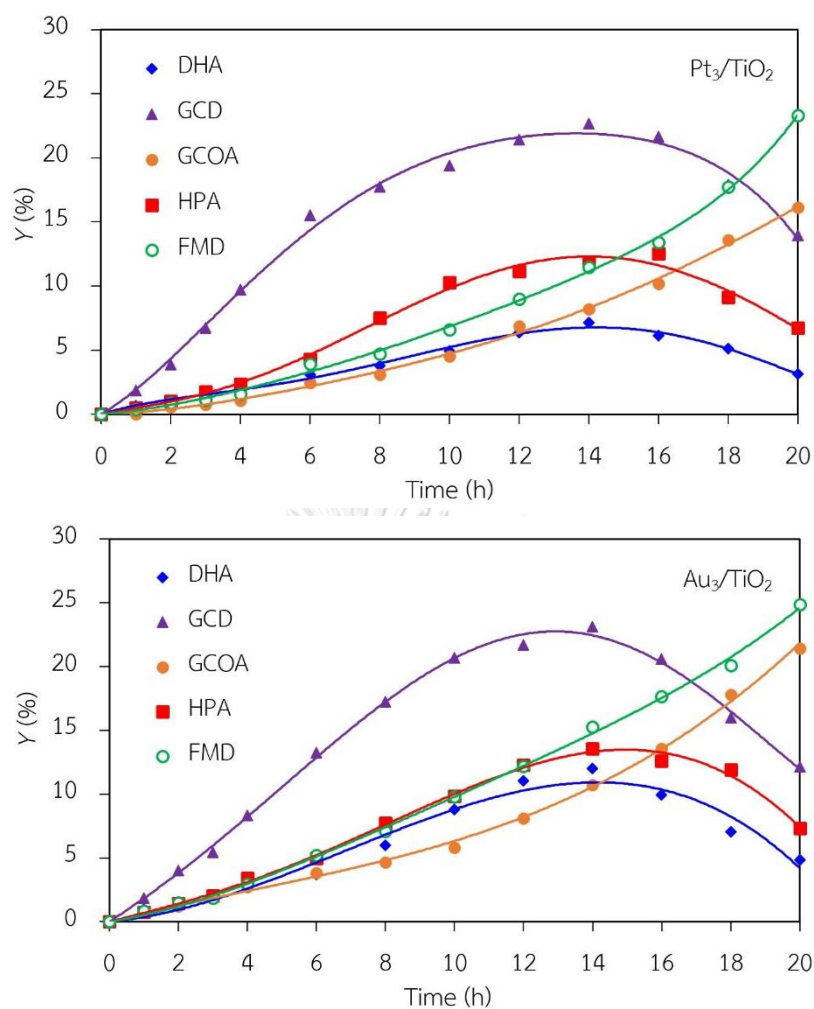


Figure 5.9 Yield of selected products obtained from glycerol photocatalytic conversion via TiO₂ and metal-decorated TiO₂ at loading of 3.0 g/L with an average light intensity of 4.7 mW/cm² and using O₂ as the electron acceptor (Cont.).

5.1.1.6 Mechanism of charge transfer in monometallic NPs decorated on TiO₂

The mechanism of the charge transfer in the monometallic metal NPs decorated on TiO₂ photocatalysts was also proposed based on the available literature [174, 182, 183] and the obtained results. The transfer mechanism of photogenerated h^+ and e^- on the bare TiO₂ surface after absorbing the photon energy of irradiated light is depicted in Figure 5.10(a). The h^+ and e^- can transfer in the valence and conduction bands, respectively, to allow the surface reaction. In the presence of doped metal, some electrons accumulated in the conduction band can localize to the adjacent metal. The e^- mobility pathway between TiO₂ and the adjacent metal seems to be another crucial factor on the photocatalytic activity of the as-prepared photocatalysts. For Bi₃/TiO₂, the LSPR phenomenon was not considered in this metal and the transfer of e^- between TiO₂ and Bi is still obscure. However, the high photocatalytic activity related to e^- transfer pathway of Bi₃/TiO₂ compared to that for TiO₂ is probably caused by a narrow band gap energy due to the presence of the valence band tail above the valence band and the Ti³⁺ state below the conduction band (Figure 5.10(b)). This allows an easy jump of photogenerated e^- from either the valence band tail level to either a shallow trap (Ti³⁺ state) or conduction band.

The Pd₃/TiO₂, Pt₃/TiO₂ and Au₃/TiO₂ photocatalysts provided a higher activity in the conversion of glycerol than Bi/TiO₂ although they all had the Ti³⁺ state. This might be due to the LSPR behavior in the metal structure, resulting in the transfer of e^- from the metallic nanoparticle to a shallow trap or conduction band or vice versa under the visible light adsorption. For Pd₃/TiO₂, the plasmon metallic state of Pd was above the conduction band of TiO₂ (~1.0 eV; Figure 5.10(c)), leading to an easy transfer of e^- from the Pd particle to the TiO₂ conduction band. However, the transfer of an e^- from the conduction band of TiO₂ to the Pd particle seemed to be a bit difficult, due to its requirement for more energy to transverse between two energy levels, resulting

in the accumulation of e^- on the conduction band preceding the reaction or sometimes recombining with the h^+ . This is not the case for the Pt_3/TiO_2 catalyst because the plasmon metallic state of Pt was slightly higher than the conduction band ($\sim 0.1\text{eV}$; Figure 5.10(d)). Thus, the transfer of e^- from the conduction band of TiO_2 to the Pt particle or *vice versa* to perform the surface reaction can proceed easily, and so the rate of the e^-h^+ recombination is expected to be lower than that in the Pd/TiO_2 photocatalyst. However, the slight difference between the conduction band and the metallic state energy level of Pt can promote the free shuttling of electron transfer between the Pt metal and TiO_2 compared with the transfer of electrons from the Au metal to TiO_2 because Au had a metallic state energy level that was lower than the conduction band of TiO_2 (Figure 5.10(e)). On the other hand, either the hot electron stimulated by the UV light or the electron driven by the LSPR in response to the visible light have opportunities to bind onto the conduction band of TiO_2 or the surface of Au and can then further participate in the surface reaction. In this case, it is possible that the appropriate thermodynamically feasible pathway of electron transfer can relieve the recombination of e^-h^+ pairs and remarkably promote the surface reaction and so contribute to the high performance of the photocatalyst.

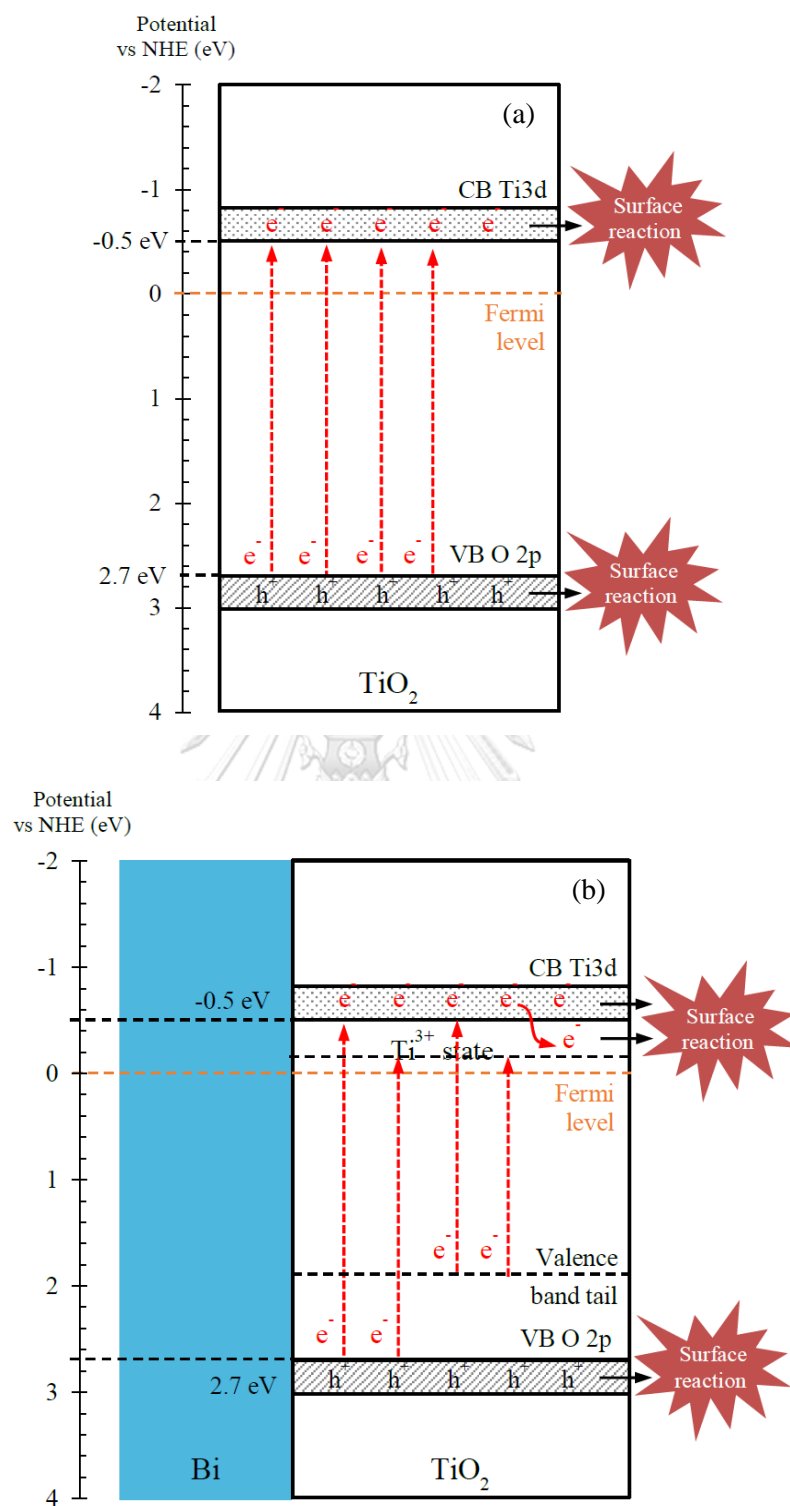


Figure 5.10 Mechanism of the charge transfer in (a) TiO₂, (b) Bi₃/TiO₂, (c) Pd₃/TiO₂, (d) Pt₃/TiO₂ and (e) Au₃/TiO₂ under UV-visible irradiation.

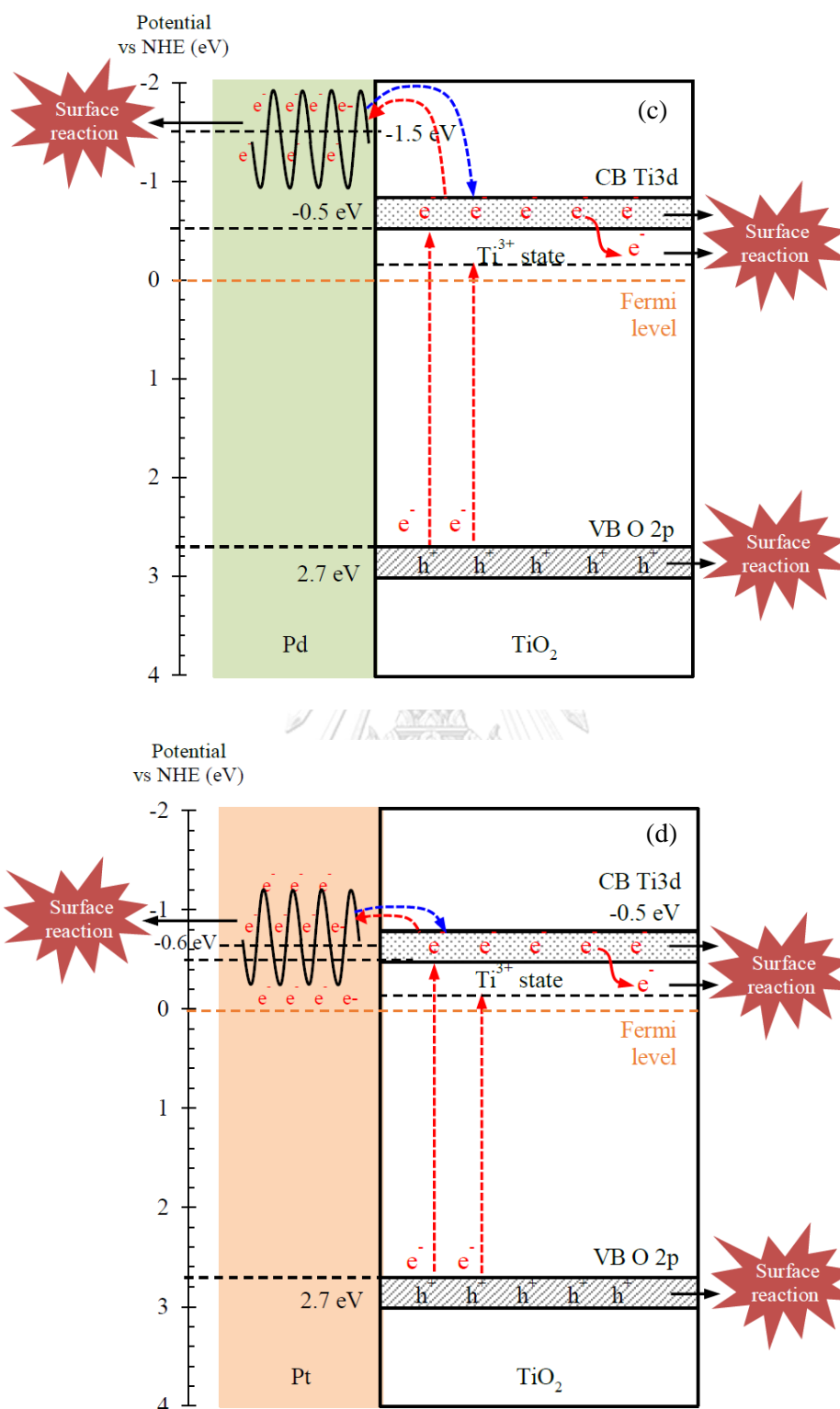


Figure 5.10 Mechanism of the charge transfer in (a) TiO₂, (b) Bi₃/TiO₂, (c) Pd₃/TiO₂, (d) Pt₃/TiO₂ and (e) Au₃/TiO₂ under UV-visible irradiation (Cont.).

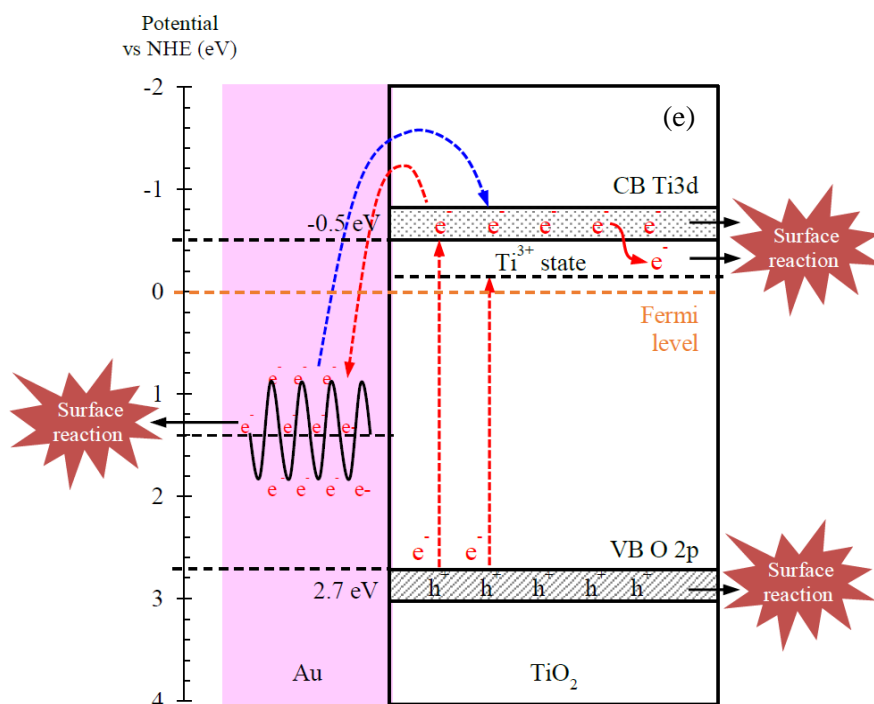


Figure 5.10 Mechanism of the charge transfer in (a) TiO₂, (b) Bi₃/TiO₂, (c) Pd₃/TiO₂, (d) Pt₃/TiO₂ and (e) Au₃/TiO₂ under UV-visible irradiation (Cont.).

5.1.2 Effect of Au metal content

As mentioned in previous section, Au decorated on TiO₂ exhibited the highest photocatalytic performance among other decorated metals. Thus, in this section, the expanded study on the amount of Au content in the range of 1.0-7.0 wt.% was then carried out. The as-prepared photocatalyst was denoted as Au_x/TiO₂, where x is Au content in wt.%

5.1.2.1 Crystallite structure analysis

Representative XRD patterns of the as-synthesized Au_x/TiO₂ photocatalysts with different metal contents are displayed in Figure 5.11. All photocatalysts still exhibited the main diffraction peaks of TiO₂ in the anatase phase at a 2θ of 25.3°, 37.0°, 37.9°,

38.6°, 48.1°, 53.9°, 55.1°, 62.7°, 68.8°, 70.3° and 75.1°, corresponding to the (101), (103), (004), (112), (200), (105), (221), (204), (116), (220) and (215) crystal planes, respectively (JCPDS No. 21-1272), with an additional rutile peak in trivial content at 27.5° corresponding to the (101) crystal plane (JCPDS No. 04-0802) (Figure 5.11(a)). In addition, the diffraction peaks of Au NPs appeared at about 38.2°, 44.4°, 64.6° and 77.6°, assigning to the face centered cubic structure of Au with (111), (200), (220) and (311) planes (JCPDS No. 002-1095), indicating the presence of metallic Au in the all as-synthesized Au_x/TiO_2 photocatalysts. The intensity of the Au peaks increased as the content of Au decorated on the TiO_2 surface increased, but without a shift in the peak position (Figure 5.11(b) and 1(c)).

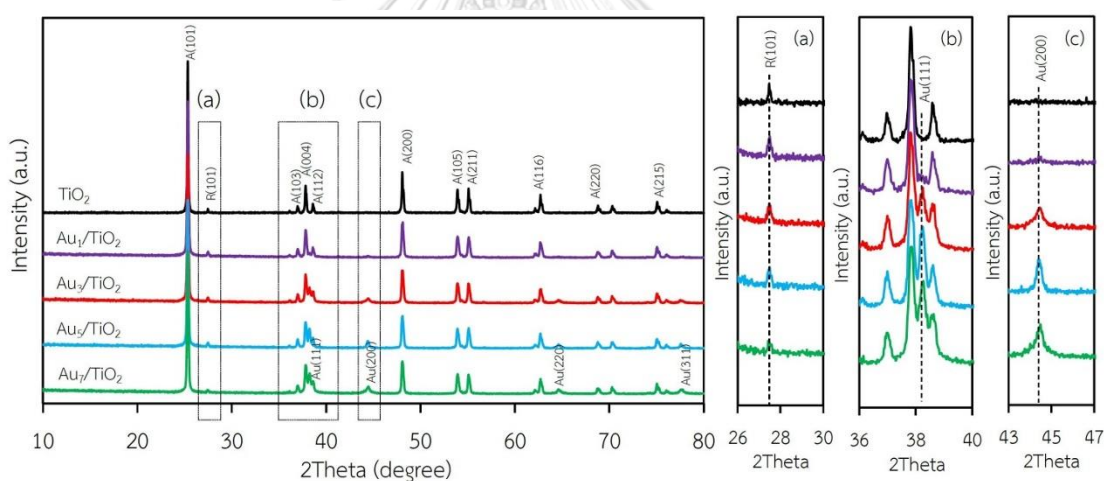


Figure 5.11 Representative XRD of monometallic Au_x/TiO_2 photocatalyst with different Au contents.

5.1.2.2 Morphology analysis

The qualitative presence of Au in all the Au_x/TiO_2 photocatalysts was also confirmed by SEM-EDX analysis (Figure 5.12). Quantitatively, as summarized in Table 5.3, the Au content in each Au_x/TiO_2 photocatalyst was close to the set value. The TEM images of the as-prepared photocatalysts with the derived Au NP size distribution

are displayed in Figure 5.13. They exhibited well-dispersed decorated Au NPs on the TiO₂ surface with a narrow size distribution. The average size of Au NPs increased slightly as the Au content increased, suggesting an agglomeration of Au NPs in the presence of a high Au contents.

Table 5.3 Properties of Au/TiO₂ photocatalysts with different Au contents.

| Photocatalyst | Au content (wt.%) ^a | Decorated metal particle size (nm) ^b | Band gap energy (eV) | Ti ³⁺ /Ti ⁴⁺ |
|-----------------------------------|--------------------------------|---|----------------------|------------------------------------|
| Au ₁ /TiO ₂ | 0.98 ± 0.10 | 6.36 ± 0.75 | 3.00 | 0.1220 |
| Au ₃ /TiO ₂ | 3.02 ± 0.21 | 6.69 ± 0.86 | 3.00 | 0.1478 |
| Au ₅ /TiO ₂ | 4.96 ± 0.19 | 10.04 ± 1.11 | 2.94 | 0.2198 |
| Au ₇ /TiO ₂ | 7.08 ± 0.35 | 10.84 ± 1.01 | 2.80 | 0.2412 |

^aEstimated from SEM-EDX

^bAveraged metal particle size obtained from TEM

5.1.2.3 Chemical structure analysis

To investigate the formation of defective structure of TiO₂ in the presence of Au NPs, XPS analysis with a high resolution (HR) Ti2p state was employed. As demonstrated in Figure 5.14, two symmetric peaks at 459.4 and 465.1 eV, assigned to Ti 2p_{3/2} and Ti 2p_{1/2}, were exhibited in the Ti2p core-level spectra of all the prepared Au_x/TiO₂ photocatalysts. The different binding energy of the observed spin-orbit splitting between the Ti 2p_{3/2} and Ti 2p_{1/2} was around 5.7 eV, in accordance with the typical value of Ti⁴⁺ sites coordinated to oxygen atoms in TiO₂ [184]. Interestingly, two additional tailored peaks were observed at a lower binding energy of around 457.9 and 464.0 eV, which can be ascribed to the existence of Ti³⁺ species. The generation

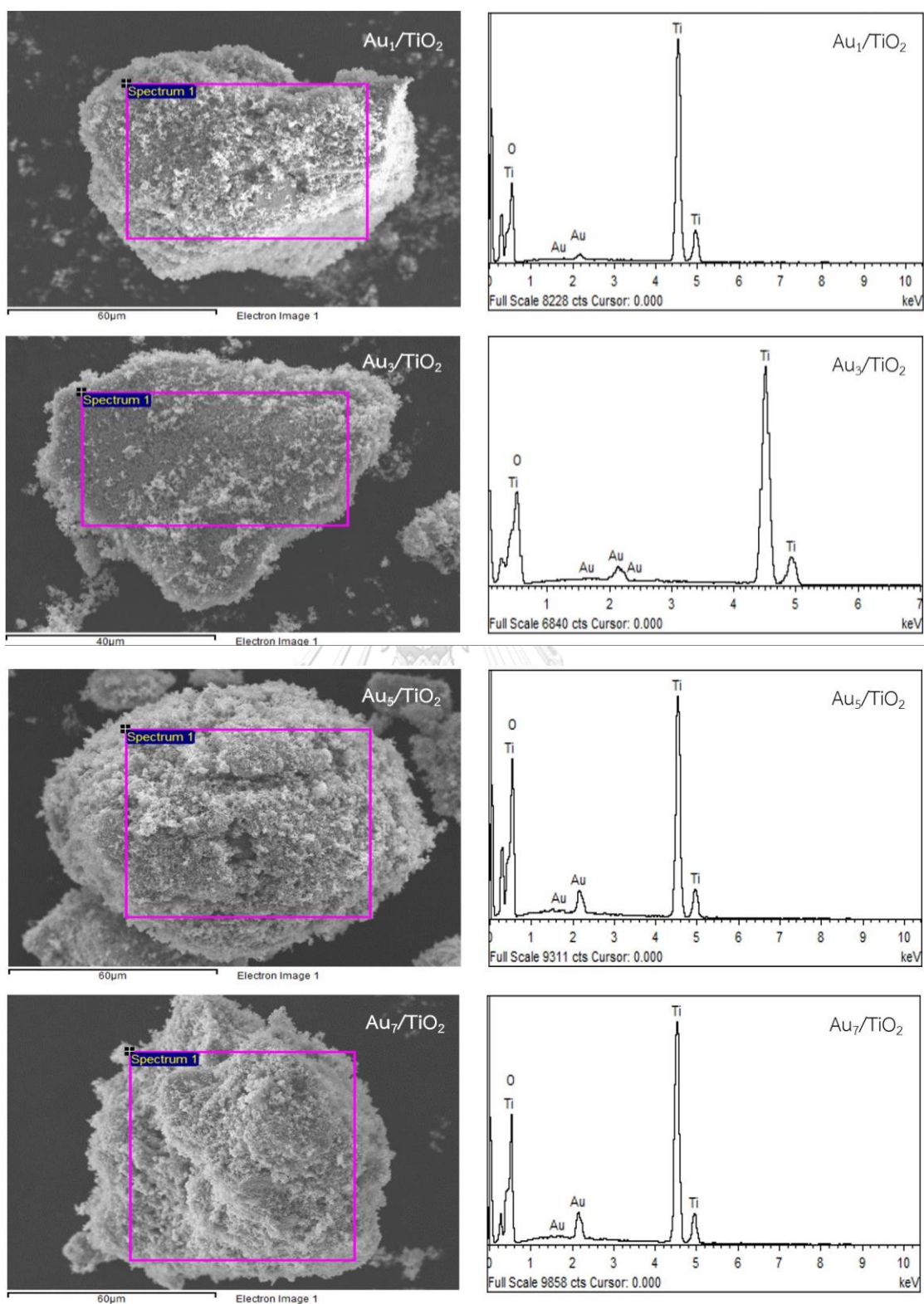


Figure 5.12 Representative SEM-EDX images of Au_x/TiO₂ photocatalyst with different Au contents.

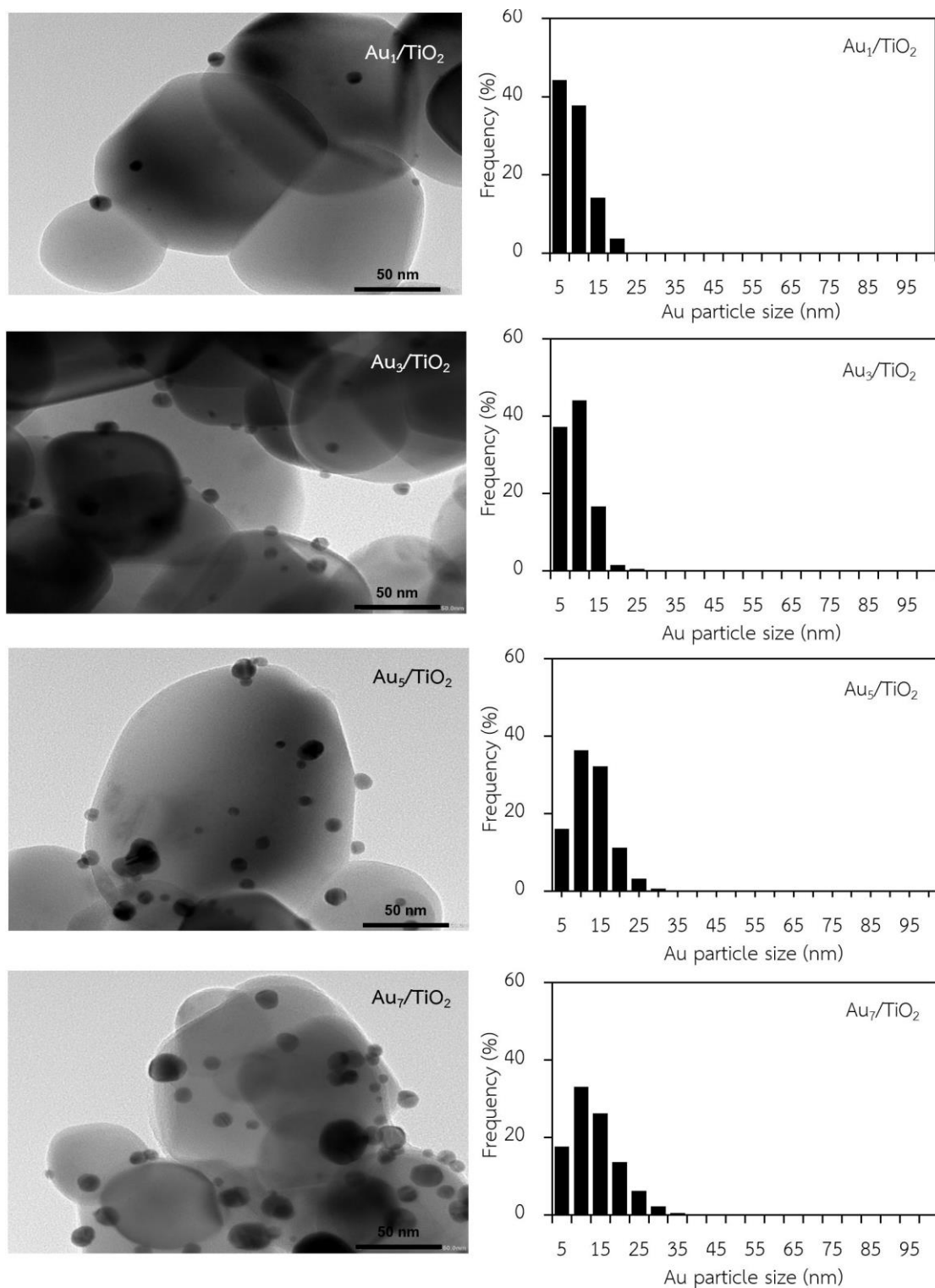


Figure 5.13 (Left) Representative TEM images of Au_x/TiO_2 photocatalyst with different Au contents and (Right) Au particle size distribution on the surface of TiO_2 .

of Ti^{3+} could have originated from the incorporation of the decorated-metal on the TiO_2 under the H_2 treatment [185, 186]. This is because the decorated metal, Au in this case, can induce the generation of oxygen vacancies that are subsequently essential to form the $\text{Ti}^{3+}\text{-O-Ti}^{4+}$ defect structures [187]. After deconvolution, the relative content of $\text{Ti}^{3+}/\text{Ti}^{4+}$ in all the Au_x/TiO_2 photocatalysts was obtained, and is summarized in Table 5.3. The $\text{Ti}^{3+}/\text{Ti}^{4+}$ ratio increased as the Au content increased, becoming almost two-fold higher in Au_7/TiO_2 than in Au_1/TiO_2 , suggesting that the decoration of TiO_2 with a high Au content induced a high level of Ti^{3+} defective structures in the TiO_2 .

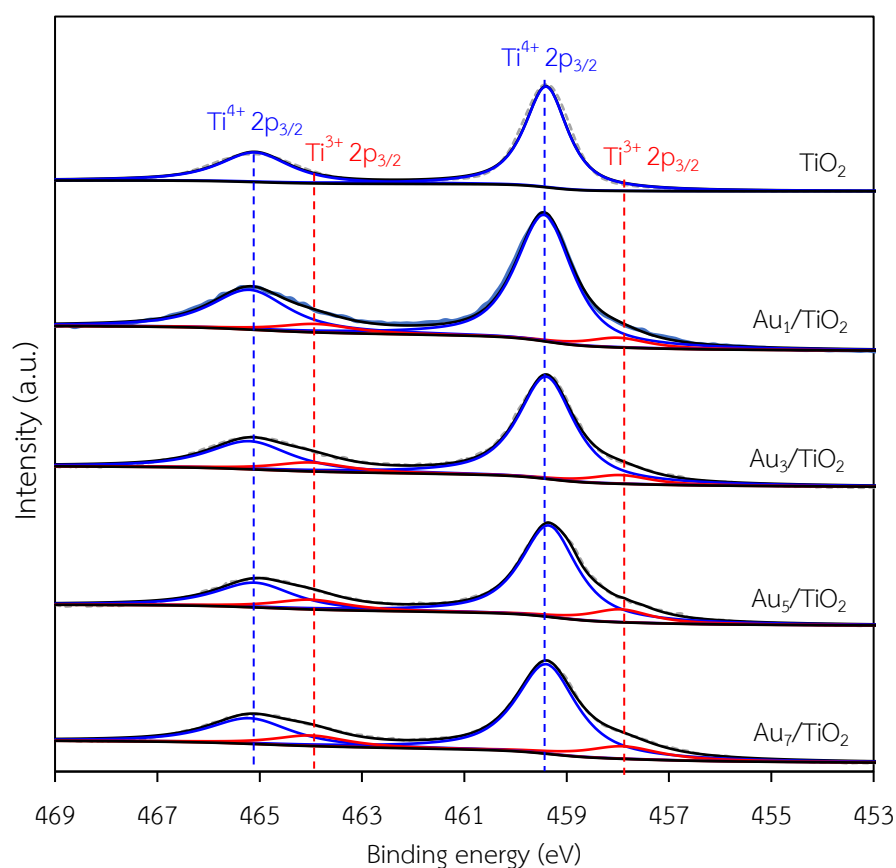


Figure 5.14 Representative HR-XPS spectra of $\text{Ti}2p$ of Au_x/TiO_2 photocatalyst with different Au contents.

With respect to the valence state of the decorated metal, the Au4f level spectra were also examined. All the prepared photocatalysts displayed the main Au 4f_{7/2} and Au 4f_{5/2} peaks at a binding energy of about 84.0 and 87.7 eV with a spin-orbit splitting of 3.7 eV (Figure 5.15), which are in excellent agreement with the values of the monometallic Au⁰ state [188]. Therefore, the Au NPs existed totally in metallic form on the surface of the as-prepared Au_x/TiO₂ photocatalysts. No shift in the Au 4f binding energy was observed, suggesting that the addition of Au within the investigated weight content (1–7 wt.%) did not alter the chemical state of the decorated Au NPs on the TiO₂.

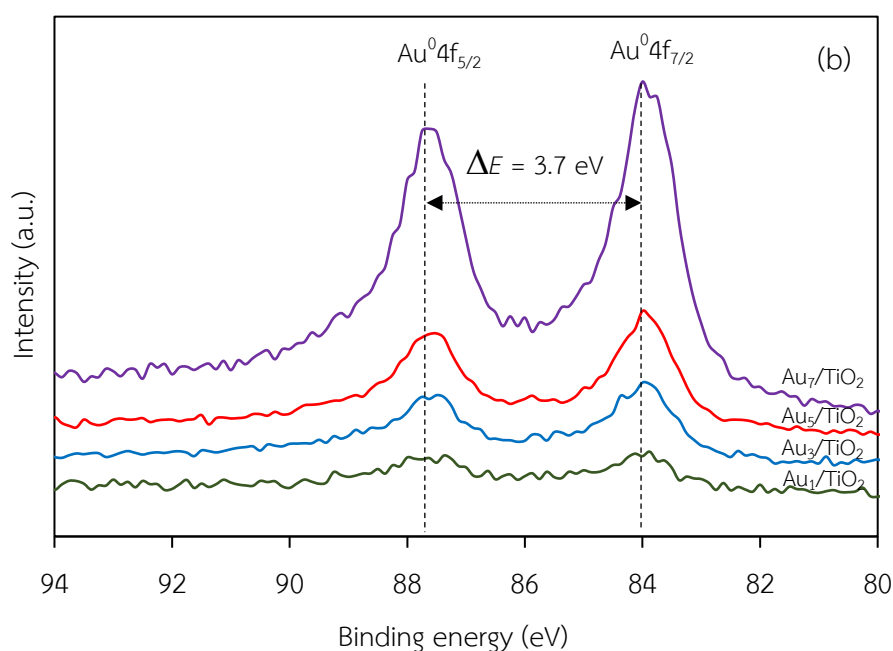


Figure 5.15 Representative HR-XPS spectra of Au4f of Au_x/TiO₂ photocatalyst with different Au contents.

5.1.2.4 Optical property analysis

Figure 5.16 exhibits the UV-vis absorption spectra of the Au_x/TiO₂ photocatalysts with different Au contents. As expected, the parent TiO₂ exhibited the

main intense UV absorption band at a wavelength of less than 400 nm with no absorption band in the visible light region or at a wavelength of greater than 400 nm. This was mainly due to its large electronic band gap energy that enabled the electron transfer from the filled valence O2p orbitals of the valence band to the vacant Ti3d orbitals of the conduction band only by the excitation of the photon energy from the UV light region. However, all the Au_x/TiO₂ photocatalysts exhibited an enhanced visible light absorption with an intense broad absorption band centered at wavelength around 540 nm. The peak intensity increased as the Au content increased from 1.0 to 7.0 wt.%. The presence of the visible light absorption of all Au_x/TiO₂ photocatalysts might be caused by the LSPR effect of the decorated Au NPs that can absorb visible light through the polarization and oscillation of the conduction electrons in the metal structure [177]. However, as reported previously, the LSPR band of well-dispersed spherical Au nanocrystals generally sharp and appears at a wavelength of 520 nm [189]. The absorption center of all the prepared Au_x/TiO₂ photocatalysts in this study deviated from the mentioned wavelength with a broad tail extending towards higher wavelengths, which might be attributed to the anisotropy of the trigonal/prismatic shape (non-spherical) of the Au nanocrystals [190]. The band gap values of all samples were determined from a Tauc's plot (inset of Figure 5.16), and are listed in Table 5.3. The addition of Au NPs decreased the band gap value of TiO₂ from 3.15 eV to 3.0, 3.0, 2.94 and 2.80 eV at an Au content of 1, 3, 5 and 7 wt.%, respectively. This might be caused by the presence of a defective TiO₂ structure in the presence of Au, which can alter the major electronic state of the valence band and conduction band position.

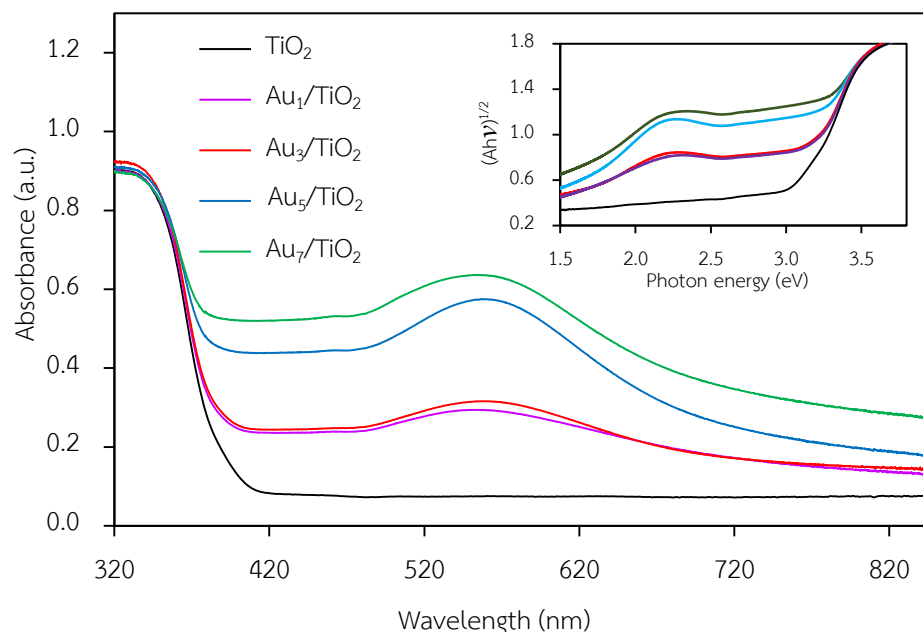


Figure 5.16 Representative UV-Vis spectra of Au_x/TiO_2 photocatalyst with different Au contents.

5.1.2.5 Photocatalytic activity test for glycerol conversion

The glycerol conversion level in the presence of the different Au_x/TiO_2 photocatalysts is summarized in Figure 5.17(a). All the Au_x/TiO_2 photocatalysts significantly enhanced the glycerol conversion level compared to the bare TiO_2 . The glycerol conversion increased as the Au content increased from 1 to 7 wt.%. Plotting the data to the pseudo first order reaction kinetic model (Figure 5.17(b)), where a plot of $\ln(C_t/C_0)$ versus t provided a straight line and allowed the determination of the kinetic rate constant (k), gave a good fit with a determination coefficient (R^2) of greater than 0.9879. Accordingly, the kinetic rate constant of glycerol conversion over the Au_1/TiO_2 , Au_3/TiO_2 , Au_5/TiO_2 and Au_7/TiO_2 photocatalysts were deduced to be 0.0340, 0.0537, 0.0606 and 0.0622 h^{-1} , respectively, compared to h^{-1} for TiO_2 (inset of Figure 5.17(b)). The enhanced glycerol conversion over Au-decorated TiO_2 could have arisen

from the plasmon induction effect of Au NPs. In addition, the presence of AuNPs were able to serve as electron sinks to facilitate interfacial electron transfer, which could effectively reduce the recombination rate of photogenerated h^+ and e^- [191].

With respect to the chemical species generated from the glycerol conversion via the photooxidation process in the presence of the Au_x/TiO_2 photocatalysts, similar chemical species, including GCD, DHA, HPA, GCOA, FMD and GCAD, were generated via photocatalytic oxidation with the Au_x/TiO_2 photocatalysts as well as with the parent TiO_2 (Figure 5.18), where GCD was the main product. However, the GCD yield as a function of reaction time varied with the different Au NP contents on the Au_x/TiO_2 photocatalysts. The yield of GCD increased continuously in the presence of 1 wt.% Au_1/TiO_2 from the initial time to the end of reaction time, but in the presence of a high Au content ($Au \geq 3$ wt.%), the yield of GCD increased continuously to reach a maximum value of around 22% and then dropped slightly. The Au_x/TiO_2 photocatalysts with a high Au NP content enhanced the fast generation of GCD to a maximum level and then accelerated the conversion of GCD to other chemical species, as seen by the decreased GCD yield in the later reaction times. This suggested that the Au_x/TiO_2 photocatalysts with a higher Au content had a higher photocatalytic activity than those with a lower Au content. This was presumably due to their higher level of defective structures, which could promote visible light absorption due to the narrowing of the electronic band gap via the continuum interstate between the Ti 3d states of the conduction band and the O 2p states of the valence band [192]. A high quantity of absorbed photons can achieve a high level of photogenerated h^+ and e^- on the TiO_2 surface. Moreover, the function of the decorated Au NPs as an electron sink can also promote the lifetime of the photogenerated h^+ and e^- , and so enhanced the photocatalytic activity for glycerol conversion.

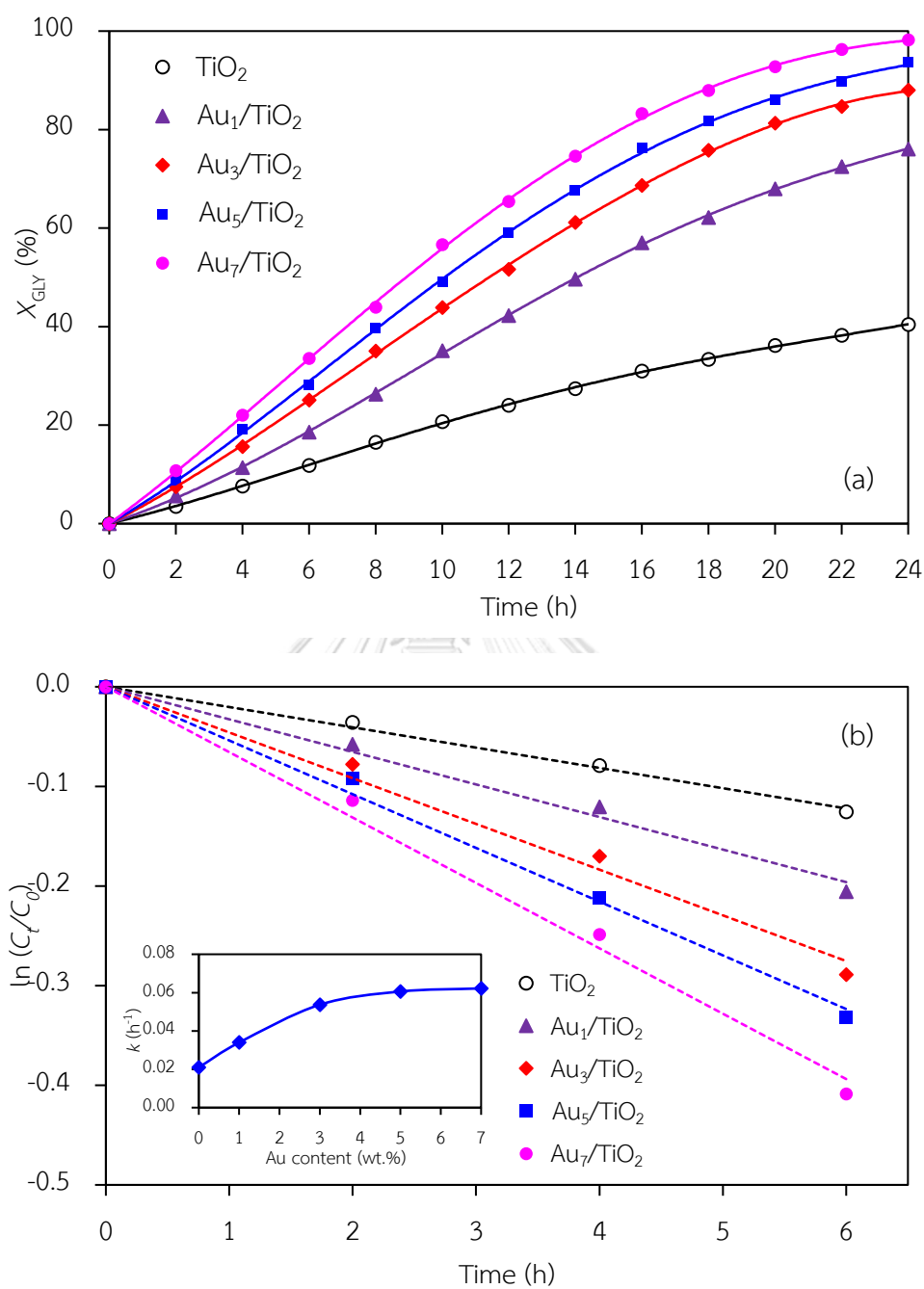


Figure 5.17 Representative (a) glycerol conversion and (b) plot of $\ln(C_t/C_0)$ as a function of time in the presence of Au_x/TiO_2 ($x = 1$ to 7) at photocatalyst loading of 3.0 g/L, light intensity of 4.7 mW/cm^2 and using O_2 as the electron acceptor.

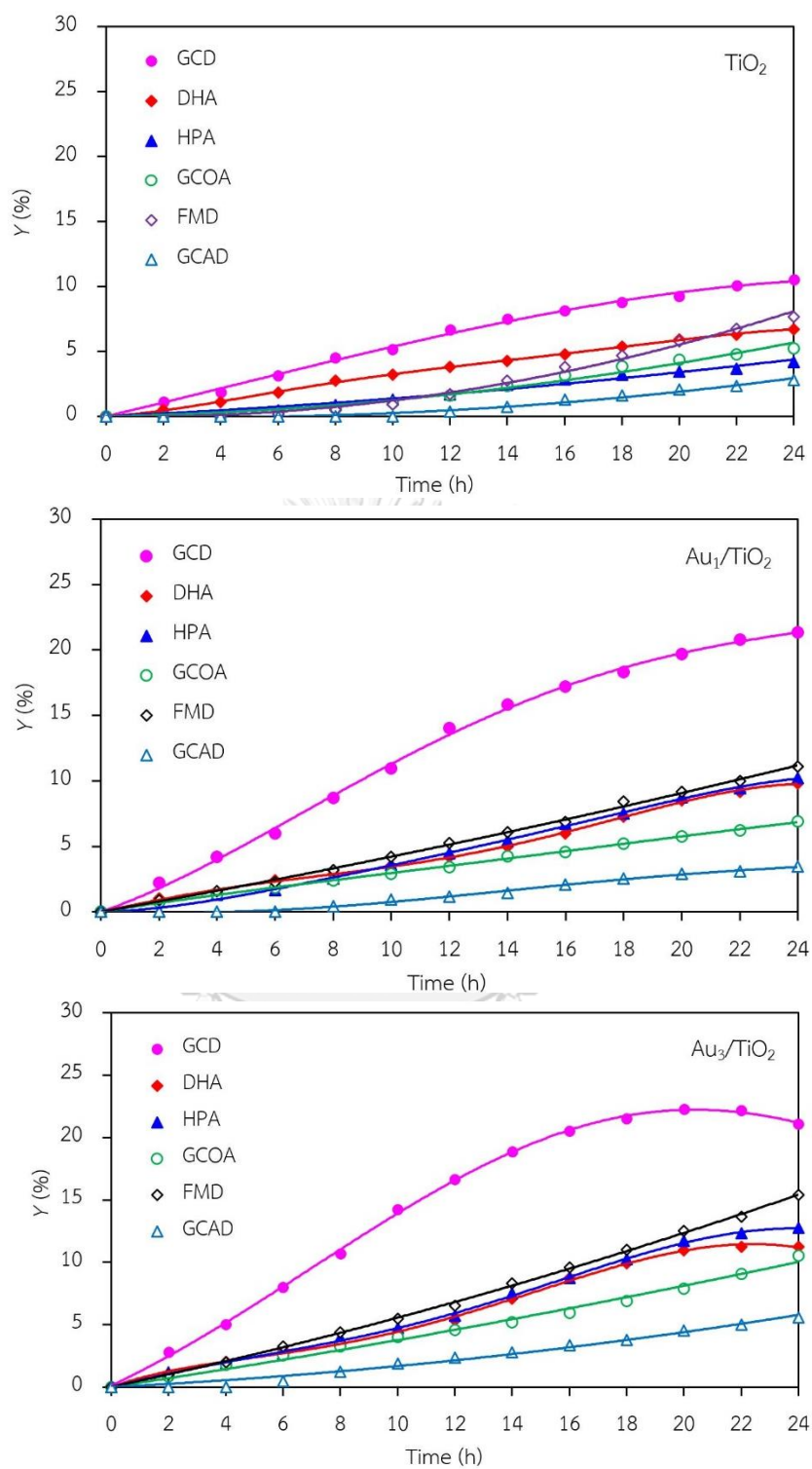


Figure 5.18 Yield of selected products obtained from glycerol photocatalytic conversion via Au_x/TiO_2 photocatalysts at loading of 3.0 g/L, light intensity of 4.7 mW/cm^2 and using O_2 as the electron acceptor.

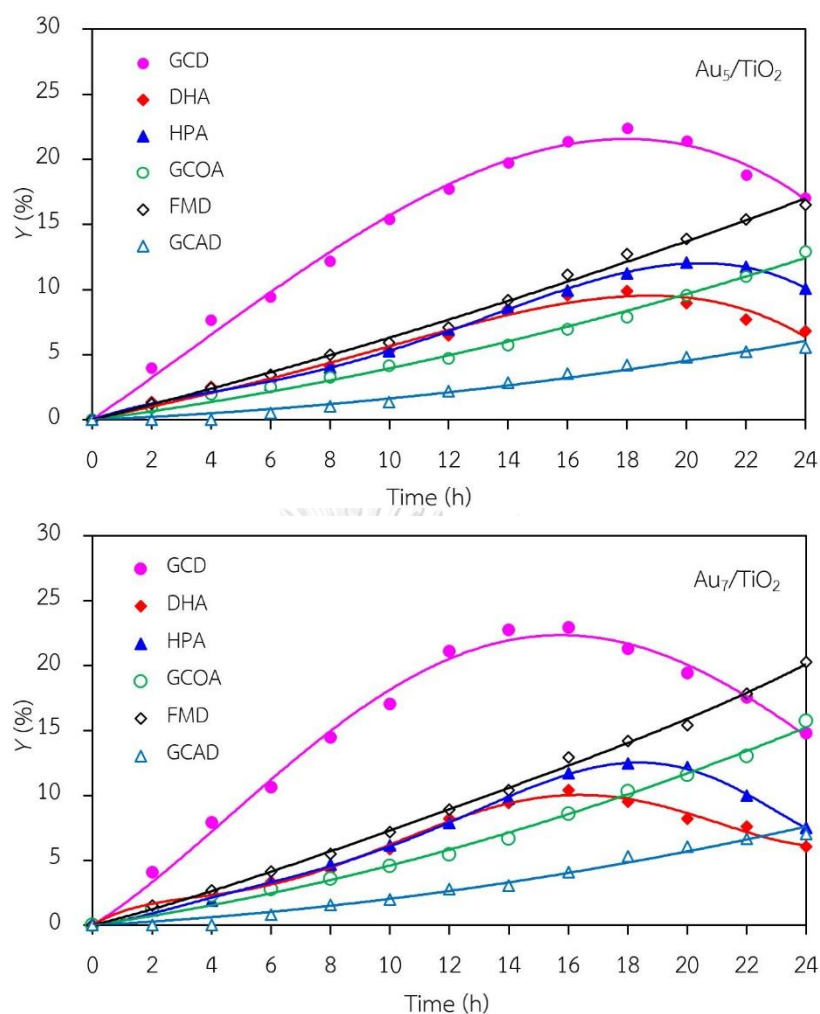


Figure 5.18 Yield of selected products obtained from glycerol photocatalytic conversion via Au_x/TiO₂ photocatalysts at loading of 3.0 g/L, light intensity of 4.7 mW/cm² and using O₂ as the electron acceptor (Cont.).

The mechanism of glycerol conversion to GCD, DHA, HPA, GCOA, FMD and GCAD was already proposed in the previous chapter. In brief, the photocatalytic oxidation of glycerol via TiO₂ occurred mainly at the 1°-OH groups to form GCD as the principle product and partially occurred at the 2°-OH group to form DHA. The generated GCD and DHA can be further oxidized to form GCOA, FMD or HPA. The generation of GCAD

in small content was probably occurred by the adsorption of two molecules of generated FMD on two neighboring Ti^{3+} defective sites and dimerized to form GCAD.

5.2 Bimetallic NPs decorated on TiO_2

According to the obtained results from the previous section, Au decorated on TiO_2 showed the best photocatalytic activity in monometallic system. Thus, in this section, to further explore the role of decorated bimetallic NPs and enhance glycerol conversion efficiency and yield of product distribution, the Au_3/TiO_2 was selected to composite with other metals (M) including Bi, Pt and Pd at identical loading of 3 wt.%. The photocatalyst denotation was $\text{Au}_3\text{Bi}_3/\text{TiO}_2$, $\text{Au}_3\text{Pt}_3/\text{TiO}_2$, and $\text{Au}_3\text{Pd}_3/\text{TiO}_2$ for 3 wt.% of Au and Bi decorated on TiO_2 , 3 wt.% of Au and Pt decorated on TiO_2 , and 3 wt.% of Au and Pd decorated on TiO_2 , respectively.

5.2.1 Crystallite structure analysis

The XRD patterns of the prepared $\text{Au}_3\text{M}_3/\text{TiO}_2$ photocatalysts are displayed in Figure 5.19. All three exhibited the main diffraction peaks of TiO_2 in the anatase phases, while the diffraction peaks of Au NPs were still clearly observed in the XRD patterns of the Au_3/TiO_2 and $\text{Au}_3\text{Bi}_3/\text{TiO}_2$ photocatalysts, but were not observed in the $\text{Au}_3\text{Pt}_3/\text{TiO}_2$ and $\text{Au}_3\text{Pd}_3/\text{TiO}_2$ photocatalysts (Figure 5.19(a)). A clear diffraction peak of Bi in the rhombohedral lattice appeared separately at a 2θ of 27.0° (PDF no. 01-085-1329) (Figure 5.19(a)), while no separate peaks of Pt and Pd were clearly observed, probably due to their alloy formation with AuNPs. The track of AuPt and AuPd peaks were detected, as shown in Figure 5.19(b) and 5.19(c). The presence of Au and the respective M in all three $\text{Au}_3\text{M}_3/\text{TiO}_2$ photocatalysts was close to the set values (3 wt.% of both Au and M), as confirmed by the SEM-EDX analysis (Figure 5.20), and are listed in Table 5.4.

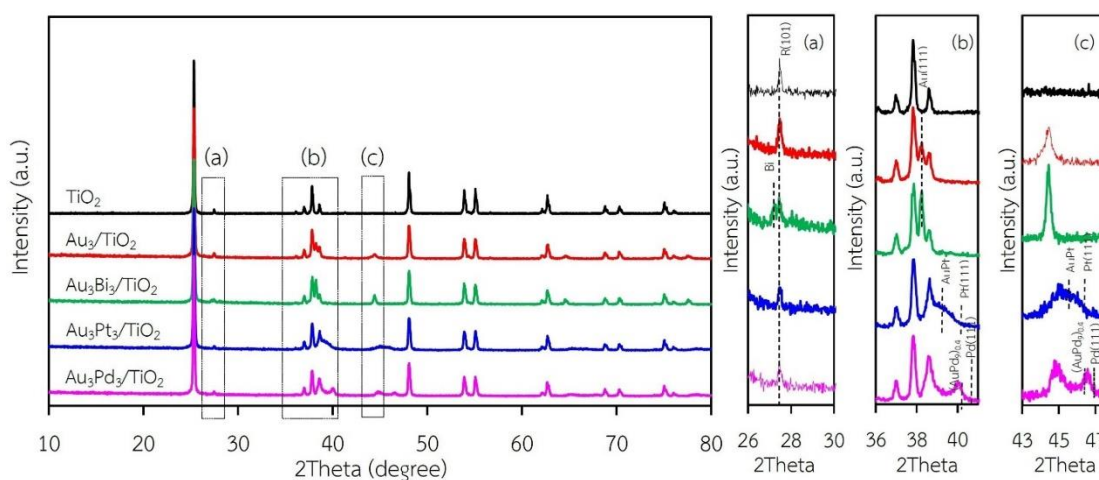


Figure 5.19 Representative XRD of $\text{Au}_3\text{M}_3/\text{TiO}_2$ photocatalysts compare with Au_3/TiO_2 photocatalyst.

Table 5.4 Properties of bimetallic $\text{Au}_3\text{M}_3/\text{TiO}_2$ photocatalysts.

| Photocatalyst | Au content (wt.%) ^a | M content (wt.%) ^a | Decorated metal particle size (nm) ^b | Band gap energy (eV) | Ti ³⁺ /Ti ⁴⁺ |
|---------------------------------------|--------------------------------|-------------------------------|---|----------------------|------------------------------------|
| $\text{Au}_3\text{Bi}_3/\text{TiO}_2$ | 2.96 ± 0.12 | 3.11 ± 0.28 | 11.84 ± 1.11 | 2.85 | 0.1960 |
| $\text{Au}_3\text{Pt}_3/\text{TiO}_2$ | 3.06 ± 0.10 | 3.01 ± 0.20 | 7.61 ± 0.91 | 2.85 | 0.1941 |
| $\text{Au}_3\text{Pd}_3/\text{TiO}_2$ | 3.09 ± 0.14 | 3.05 ± 0.22 | 9.66 ± 1.06 | 2.79 | 0.3561 |

^aEstimated from SEM-EDX,

^bAveraged metal particle size obtained from TEM

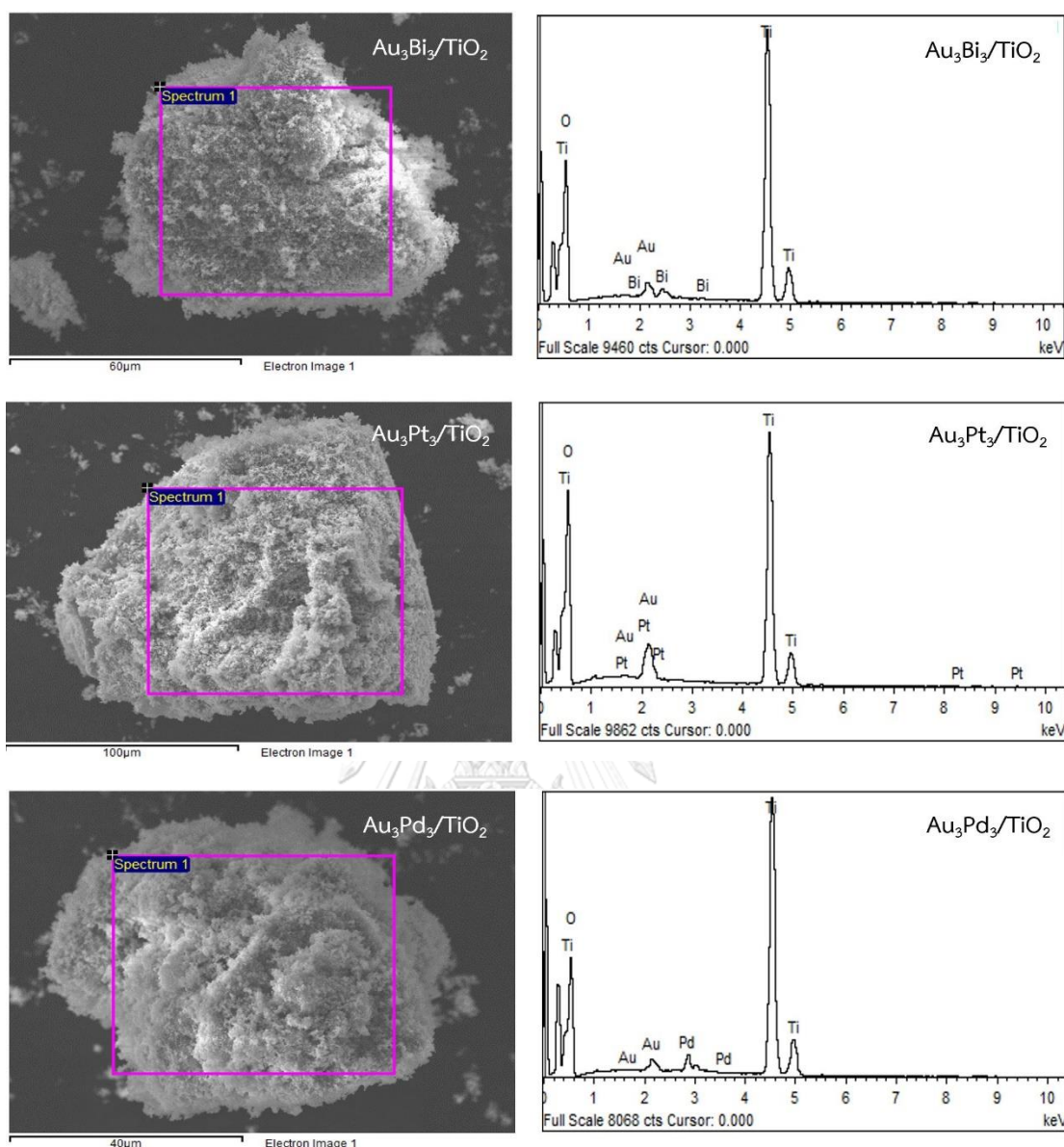


Figure 5.20 Representative SEM-EDX analysis of $\text{Au}_3\text{M}_3/\text{TiO}_2$ photocatalysts.

5.2.2 Morphology analysis

With respect to the particle size distribution, the TEM images (Figure 5.21) revealed a well-dispersed and narrow size distribution of the decorated AuM NPs on the TiO_2 surface, with a slightly larger particle size than that in Au_3/TiO_2 (Table 5.3 and 5.4). This suggests that the addition of the second metals induced a slight agglomeration

of the AuM NPs. To get insight into the morphology of the decorated metal NPs in the bimetallic catalysts, EDS line-scanning together with the elemental mapping analysis was performed. The compositional line scan of the Au₃Bi₃/TiO₂ photocatalyst showed that the concentration of Au increased from the edge to the center of the metal particle, whereas the Bi distribution was almost constant from the edge to the center of the selected particle (Figure 5.22(a)), indicating a core-shell structure of the Bi-Au particle with Au as the core and Bi as the shell. The onset position of the Bi signal was around 0.13 μm, which was 0.008 μm lower than that of Au, indicating a 8 nm thickness of the dendritic Bi shell. A core-shell structure was also observed for the Au₃Pd₃/TiO₂ photocatalyst, in which the high density of Au appeared at the center of the metal particle, while Pd was distributed uniformly from the edge to the center (Figure 5.22(c)), with the thickness of the dendritic Pt shell around the Au core being 7.5 nm. A different pattern of the line scan profile was observed for the Au₃Pt₃/TiO₂ photocatalyst, in which the density of both Au and Pt NPs increased from the edge to the center of the selected particle (Figure 5.22(b)). This indicated that the AuPt ensembles existed as a solid solution of arbitrary composition or as an AuPt alloy form.

5.2.3 Chemical structure analysis

To confirm the presence of the Ti³⁺ defective structures, Ti 2p HR-XPS spectra of the Au₃M₃/TiO₂ photocatalysts were investigated as shown in Figure 5.23. The core-level Ti2p spectra still exhibited the two main symmetric peaks of Ti 2p_{3/2} and Ti 2p_{1/2} at a binding energy of 459.4 and 465.1 eV, respectively, with a difference of 5.7 eV, in accordance with the typical value of the Ti⁴⁺ state in TiO₂. The shoulder peak of Ti2p at a low binding energy, assigned to the existence of the Ti³⁺ structure, was distinctly observed in all the Au₃M₃/TiO₂ photocatalysts. The Ti³⁺/Ti⁴⁺ ratios, as obtained from

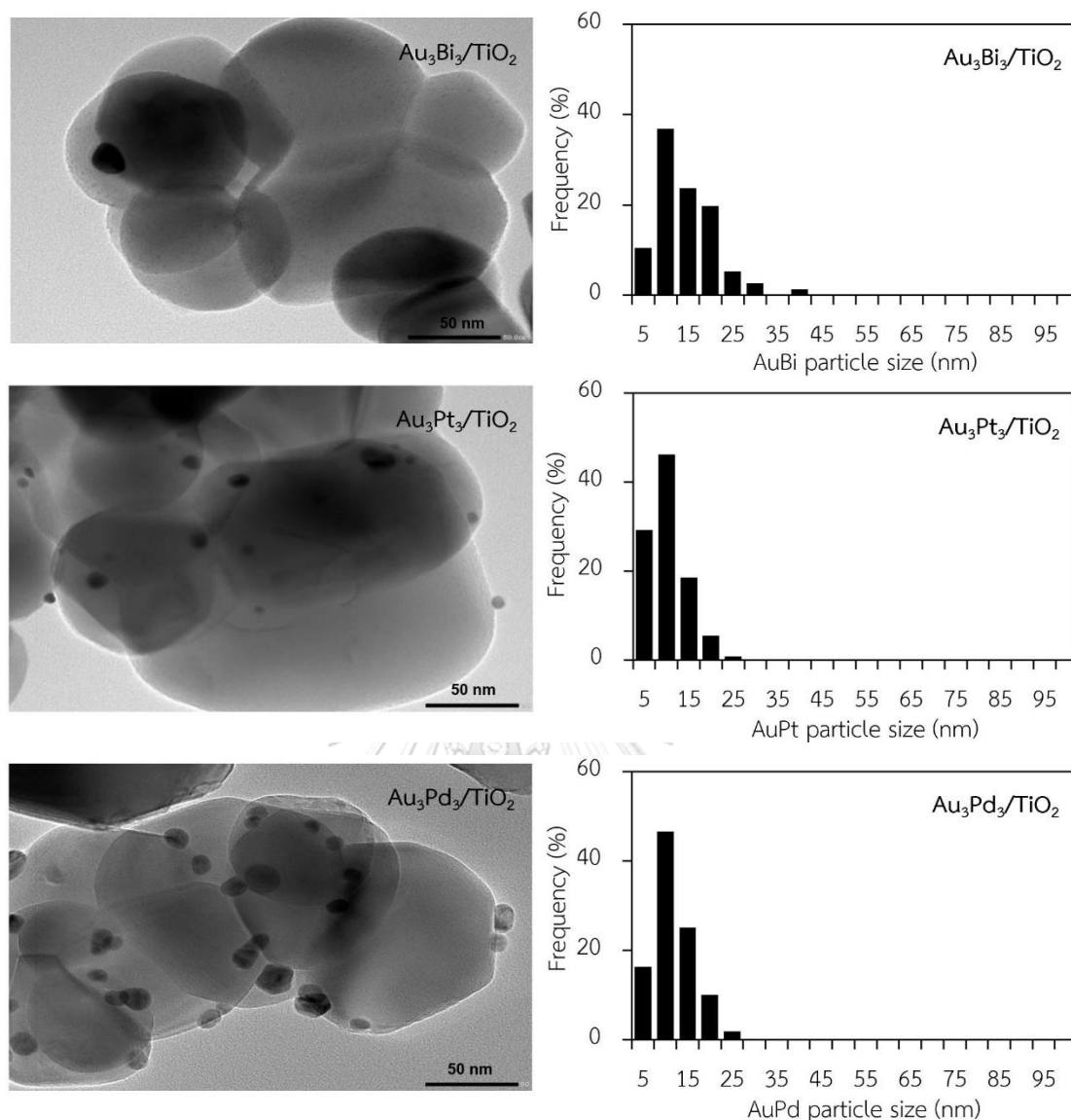


Figure 5.21 (Left) Representative TEM images of $\text{Au}_3\text{M}_3/\text{TiO}_2$ photocatalysts and (Right) respective decorated-metal particle size distribution.

the area under the deconvolution of both peaks, are listed in Table 5.4. The $\text{Au}_3\text{M}_3/\text{TiO}_2$ photocatalysts all exhibited a higher $\text{Ti}^{3+}/\text{Ti}^{4+}$ ratio than the Au_3/TiO_2 and parent TiO_2 photocatalysts, indicating that the addition of the bimetallic NPs (AuBi , AuPt and AuPd) induced a greater level of defective structures of TiO_2 than the addition of the monometallic Au NPs. Among all the $\text{Au}_3\text{M}_3/\text{TiO}_2$ photocatalysts, surprisingly, the $\text{Au}_3\text{Pd}_3/\text{TiO}_2$ photocatalyst exhibited the highest $\text{Ti}^{3+}/\text{Ti}^{4+}$ ratio of 0.3561, which was

2.41-, 1.82- and 1.83-fold higher than that of the Au_3/TiO_2 , $\text{Au}_3\text{Bi}_3/\text{TiO}_2$ and $\text{Au}_3\text{Pt}_3/\text{TiO}_2$ photocatalysts, respectively. The higher content of Ti^{3+} defect species in the bi- than mono-metallic system might be because the high content of decorated metal can incorporate into the TiO_2 structure and induce formation of the Ti^{3+} defect site by transferring electrons between the decorated metal and oxygen vacancies of TiO_2 in order to maintain the charge balance [193].

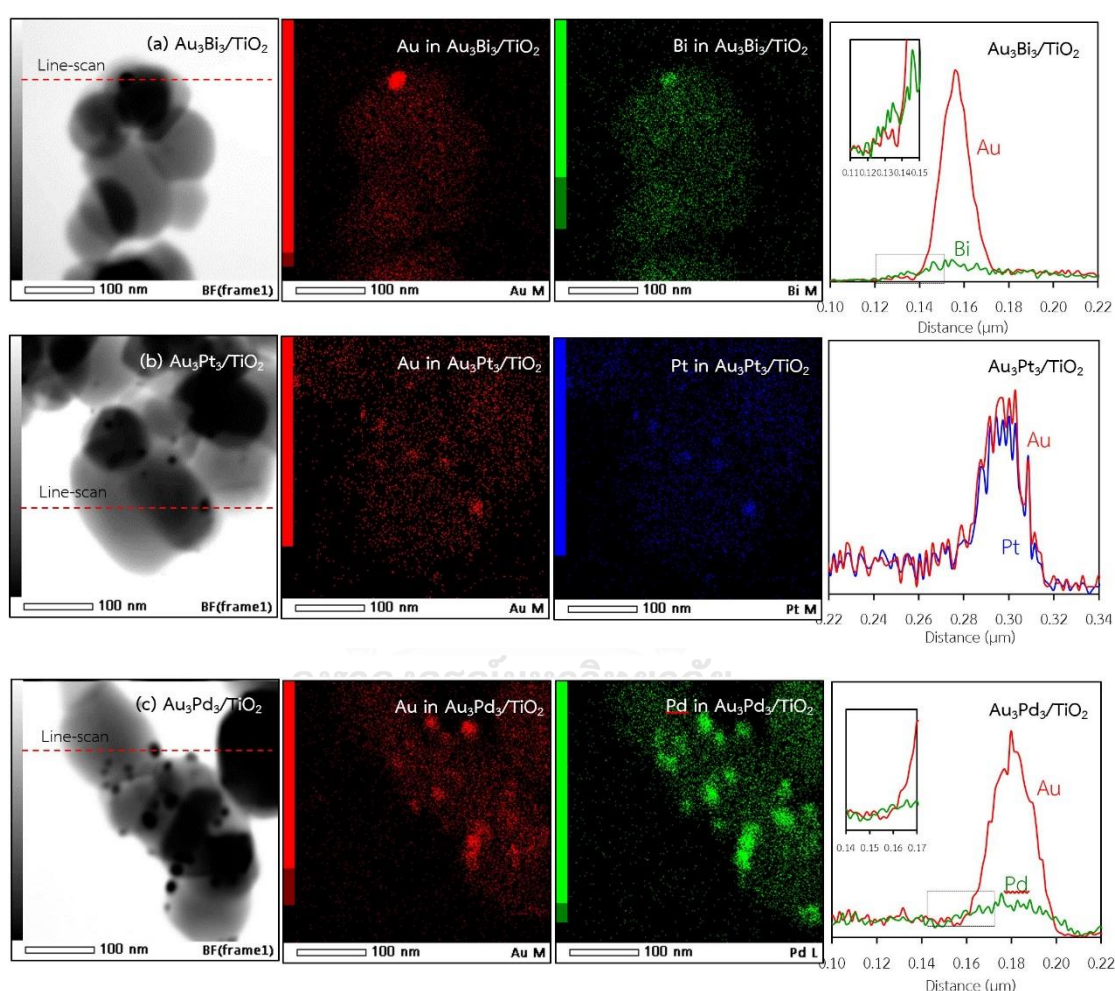


Figure 5.22 Representative TEM-EDX mapping images and line-scan profile of $\text{Au}_3\text{M}_3/\text{TiO}_2$ photocatalysts.

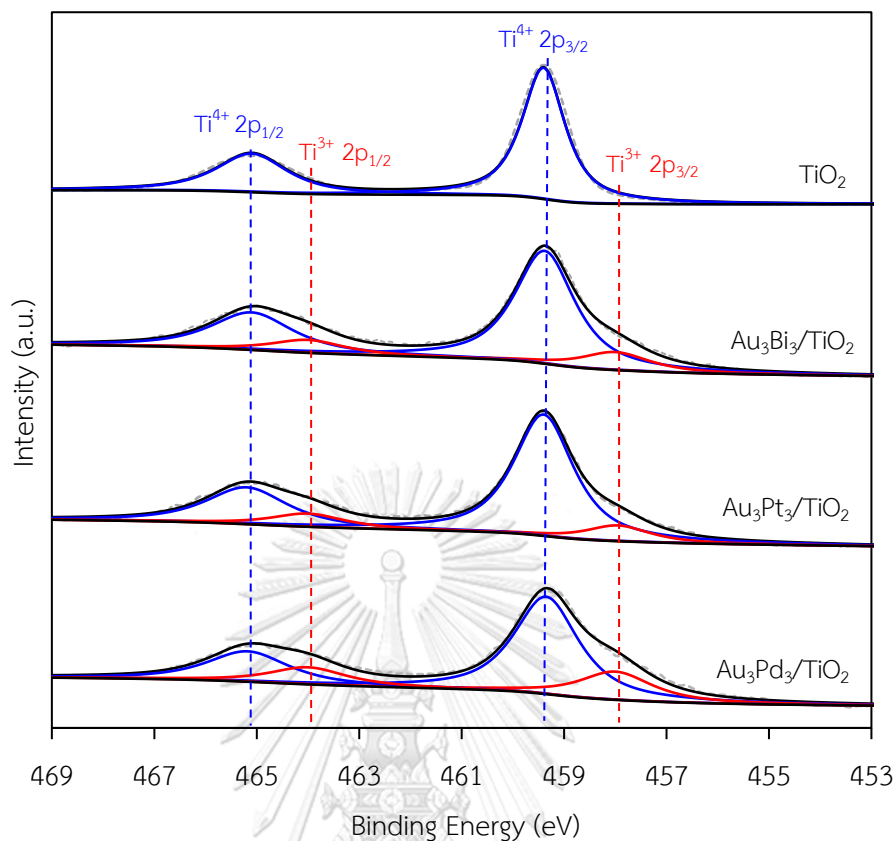


Figure 5.23 Representative HR-XPS spectra of Ti2p of $\text{Au}_3\text{M}_3/\text{TiO}_2$ photocatalysts.

To distinguish the valence states of the decorated metals, the Au 4f level spectra of all $\text{Au}_3\text{M}_3/\text{TiO}_2$ photocatalysts were analyzed, with respective examples shown in Figure 5.24. The two main characteristic peaks of Au $4f_{7/2}$ and Au $4f_{5/2}$ were still observed with a spin-orbit splitting of 3.7 eV, indicating the presence of Au in the metallic state. A slight blue shift in the Au 4f binding energy was observed for the $\text{Au}_3\text{Pt}_3/\text{TiO}_2$ and $\text{Au}_3\text{Pd}_3/\text{TiO}_2$ photocatalysts in comparison with that of Au_3/TiO_2 . Typically, the shift in the binding energy in each metal is attributed to various factors, such as a change in its chemical state or the charge compensation of added elements on the parent elements. However, in this case, the chemical state of Au in all the $\text{Au}_3\text{M}_3/\text{TiO}_2$ photocatalysts was still in the metallic state (Figure 5.24), and so this blue shift in the Au binding energy could be the result of charge compensation of the Pt or

Pd elements on Au elements [194], by which Au accepted sp-electrons from Pt or Pd, but donated d-electrons to Pt or Pd, and possibly due to the partial formation of AuM alloy structure, which are more negatively charged [195]. A low Au4f intensity was observed in the case of the $\text{Au}_3\text{Bi}_3/\text{TiO}_2$ photocatalyst compared with other two $\text{Au}_3\text{M}_3/\text{TiO}_2$ photocatalysts, due to the presence of the Bi-wrapped Au NPs as a core-shell structure.

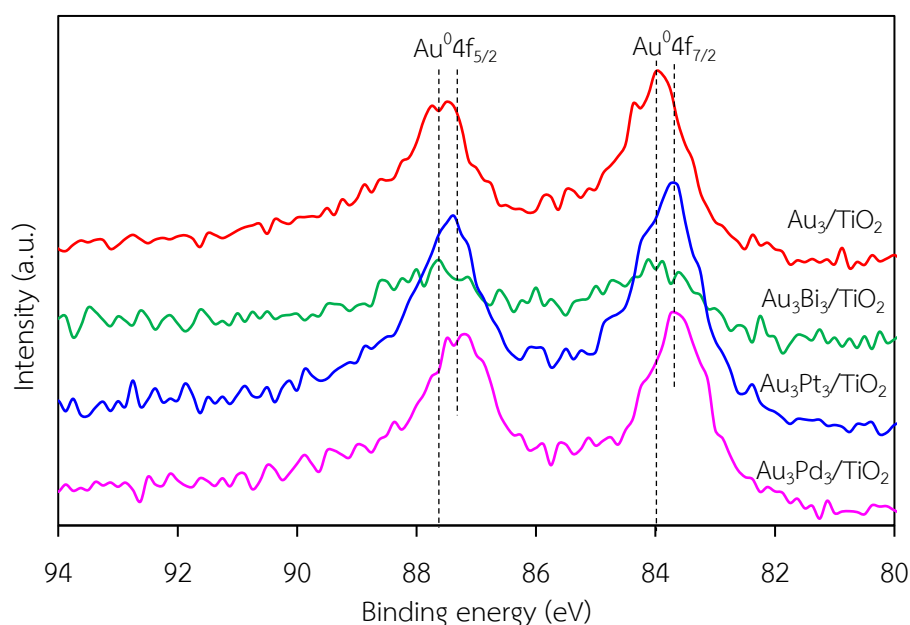


Figure 5.24 Representative HR-XPS spectra of Au4f of $\text{Au}_3\text{M}_3/\text{TiO}_2$ photocatalysts.

The chemical state of the second metals in all the photocatalysts was also analyzed by the HR-XPS. As demonstrated in Figure 5.25, all the second metals in the respective $\text{Au}_3\text{M}_3/\text{TiO}_2$ photocatalysts were presented in both a metallic and oxide form. The peaks located at 162.9 and 157.6 eV for the $\text{Au}_3\text{Bi}_3/\text{TiO}_2$ photocatalyst were assigned to $\text{Bi}^0 4f_{5/2}$ and $\text{Bi}^0 4f_{7/2}$, respectively, which is the characteristic value of the metallic Bi. A further two peaks at 164.5 and 159.2 eV were assigned to the $\text{Bi}^{3+} 4f_{5/2}$ and $\text{Bi}^{3+} 4f_{7/2}$ region, which are characteristic of Bi^{3+} in the as-prepared catalysts. These binding energy values of the Bi^{3+} ion-valent-form are too high to be assigned to the

typical Bi^{3+} in bismuth oxide (Bi_2O_3), but rather were assigned to bismuth hydroxylated oxide ($\text{BiO}(\text{OH})$) species on the photocatalyst surface [196]. For the $\text{Au}_3\text{Pt}_3/\text{TiO}_2$ photocatalyst, the Pt 4f signals consisted of three pairs of doublets; the Pt^0 $4f_{5/2}$ and Pt^0 $4f_{7/2}$ peaks at a binding energy of 74.2 and 70.9 eV, the Pt^{2+} $4f_{5/2}$ and Pt^{2+} $4f_{7/2}$ peaks at a binding energy of 75.3 and 72.0 eV and the Pt^{4+} $4f_{5/2}$ and Pt^{4+} $4f_{7/2}$ peaks at a binding energy of 76.5 and 73.2 eV, with an identical spin-orbit splitting of about 3.3 eV [197]. This suggests that the Pt NPs were present in both metallic zero-valent (Pt^0) and metallic ion-valent (Pt^{2+} and Pt^{4+}) forms. For the $\text{Au}_3\text{Pd}_3/\text{TiO}_2$ photocatalyst, the most intensive doublet, at binding energies of 340.6 (Pd^0 $3d_{3/2}$) and 335.3 eV (Pd^0 $3d_{5/2}$), was attributed to metallic Pd. The shoulder peaks located at binding energies of around 342.2 and 336.9 eV were assigned to Pd^{2+} $3d_{3/2}$ and Pd^{2+} $3d_{5/2}$, respectively, which is characteristic of Pd^{2+} in PdO in the achieved catalyst. The spin-orbit splitting of about 5.3 eV in both the metallic Pd and Pd^{2+} was well in accordance with the reported value [198]. All the second metal NPs in the respective $\text{Au}_3\text{M}_3/\text{TiO}_2$ catalysts existed predominantly in the metallic form, whereas the partial presence of the second metal in an oxide form might be attributed to the formation of a M-O bond driven by the oxygen chemisorption on the surface of the second metal nanostructure during the preparation process.

5.2.4 Optical property analysis

The capability of UV- and visible-light absorption of the $\text{Au}_3\text{M}_3/\text{TiO}_2$ photocatalysts is shown in Figure 5.26, where they all exhibited a high capability to absorb visible light at a wavelength of greater than 400 nm. The addition of Bi, Pt or Pd to the Au_3/TiO_2 attenuated an intense broad absorption band centered at around 540 nm of Au, probably due to the different dielectric function of the bimetals compared to the Au monometallic state [199]. Moreover, the strong interaction

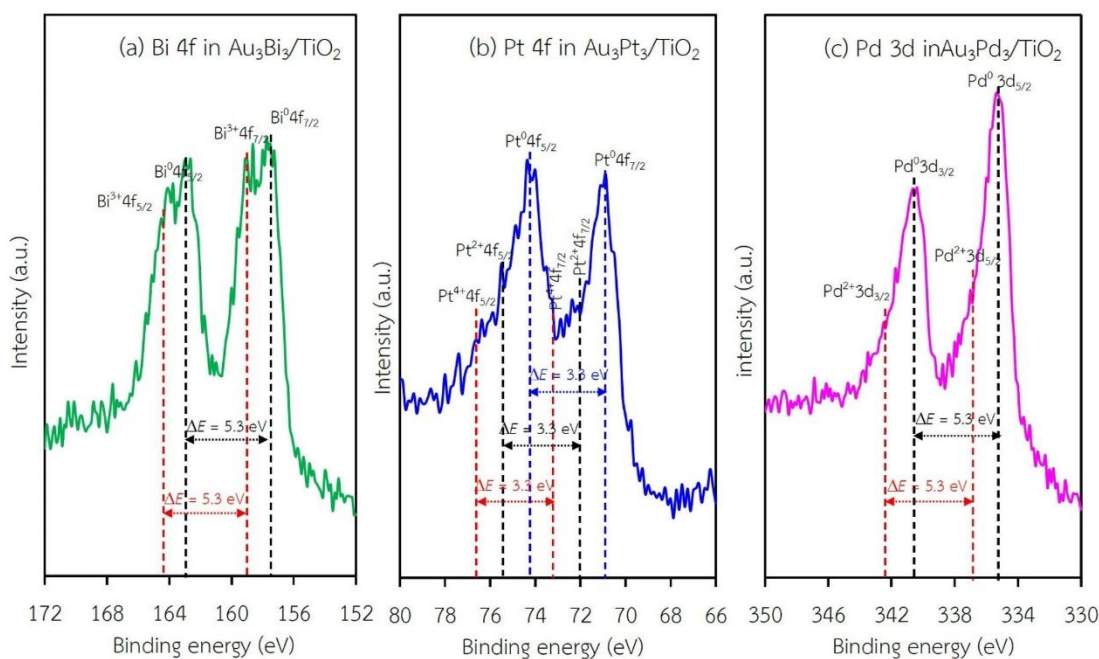


Figure 5.25 Representative HR-XPS spectra of Bi 4f, Pt 4f and Pd 3d in $\text{Au}_3\text{M}_3/\text{TiO}_2$ photocatalysts.

between the decorated Au-M can also influence the flattening of the Au LSPR band [200]. The band gap values of the $\text{Au}_3\text{Bi}_3/\text{TiO}_2$, $\text{Au}_3\text{Pt}_3/\text{TiO}_2$ and $\text{Au}_3\text{Pd}_3/\text{TiO}_2$ photocatalysts, as determined from a Tauc's plot (inset of Figure 5.26), were 2.85, 2.85 and 2.79 eV, respectively (Table 5.4), which suggested that the addition of the respective second metals caused the generation of the defective structure of TiO_2 . The formation of the Ti^{3+} defect structure likely induced an altered major electronic state of the valence band and conduction band, by which it formed a mid-gap state below the conduction band and also enabled the lengthening of the conduction band edge, resulting in the formation of the band tail structure and the narrowness of the band gap energy [201].

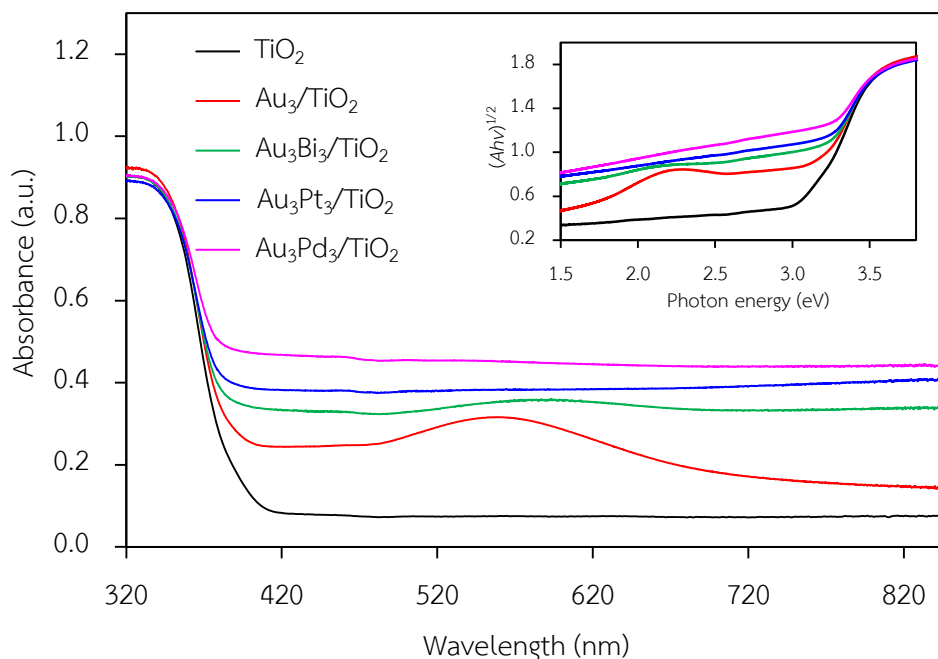


Figure 5.26 Representative UV-Vis spectra of $\text{Au}_3\text{M}_3/\text{TiO}_2$ photocatalysts.

5.2.5 Photocatalytic activity test for glycerol conversion

The photocatalytic activity of the $\text{Au}_3\text{M}_3/\text{TiO}_2$ photocatalysts was tested for the photocatalytic oxidation of glycerol to selected value-added compounds. As demonstrated in Figure 5.27(a), the addition of Pt or Pd NPs on the Au_3/TiO_2 photocatalyst to form $\text{Au}_3\text{Pt}_3/\text{TiO}_2$ and $\text{Au}_3\text{Pd}_3/\text{TiO}_2$, respectively, enhanced the glycerol conversion level, while the addition of Bi NPs retarded the reaction. The first order kinetic rate constants of glycerol conversion over $\text{Au}_3\text{Bi}_3/\text{TiO}_2$, $\text{Au}_3\text{Pt}_3/\text{TiO}_2$ and $\text{Au}_3\text{Pd}_3/\text{TiO}_2$ were 0.0396, 0.0644 and 0.0810 h^{-1} , respectively (Figure 5.27(b)). The $\text{Au}_3\text{Bi}_3/\text{TiO}_2$ photocatalyst exhibited a lower photocatalytic activity than the Au_3/TiO_2 photocatalyst despite having a lower band gap energy and higher defective structure, probably due to the core-shell structure of the AuBi NPs. That is, the LSPR behavior of the Au NPs was diminished when they were wrapped by the Bi species. Moreover, the decorated Bi NPs cannot extract the excited e^- from the Au or supported TiO_2 due to its lower work function (4.22 eV) than that of Au (5.1 eV) and TiO_2 (4.9 eV), resulting in

unalleviated e^-h^+ recombination (Figure 5.28(a)). The high photocatalytic activity of the $\text{Au}_3\text{Bi}_3/\text{TiO}_2$ compared to the parent TiO_2 was due to the presence of the valence band tail above the valence band, which was caused by the hybridization of the Bi 6s and O 2p orbital, and the existence of the Ti^{3+} state below the conduction band, which allowed an easy jump of photogenerated e^- from either the valence band tail level to either a shallow trap (Ti^{3+} state) or conduction band. In addition, as previously mentioned, the Bi6s is widely dispersed in the hybrid orbital of Bi6s-O2p leading to an increased charge mobility and consequently an improved photocatalytic activity of the parent photocatalyst [202].

For the $\text{Au}_3\text{Pt}_3/\text{TiO}_2$ and $\text{Au}_3\text{Pd}_3/\text{TiO}_2$ photocatalysts, the enhanced glycerol conversion level compared with the Au_3/TiO_2 photocatalyst was probably due to their lower band gap energy, which allowed the electron excitation at a lower photon energy and the presence of LSPR behavior in the decorated noble metal structure, resulting in the transfer of e^- from the metallic NPs to a shallow trap or conduction band of TiO_2 , or vice versa, under the visible light adsorption. Moreover, in fact, the excited electron can be transferred by the driven of work function. The difference in work function between Au and the second metal (Pt or Pd) can reduce the e^-h^+ recombination rate by transferring the e^- between the two metals after trapping the e^- from the conduction band of TiO_2 into equilibrium [203]. That is, the work function of Au is 5.1 eV and that of Pt and Pd are 5.65 and 5.22, respectively. The decorated AuPt NPs formed an alloy structure in the $\text{Au}_3\text{Pt}_3/\text{TiO}_2$ photocatalyst, which can initiate a new Fermi level of alloy NPs somewhere between the Fermi level of Au and Pt (Figure 5.28(b)) and so could prolong the e^-h^+ lifetime compared with the AuBi NPs. This was shorter than the two-stage transferring of an excited electron between the two Fermi levels of decorated metal in the core-shell structure generated in the $\text{Au}_3\text{Pd}_3/\text{TiO}_2$

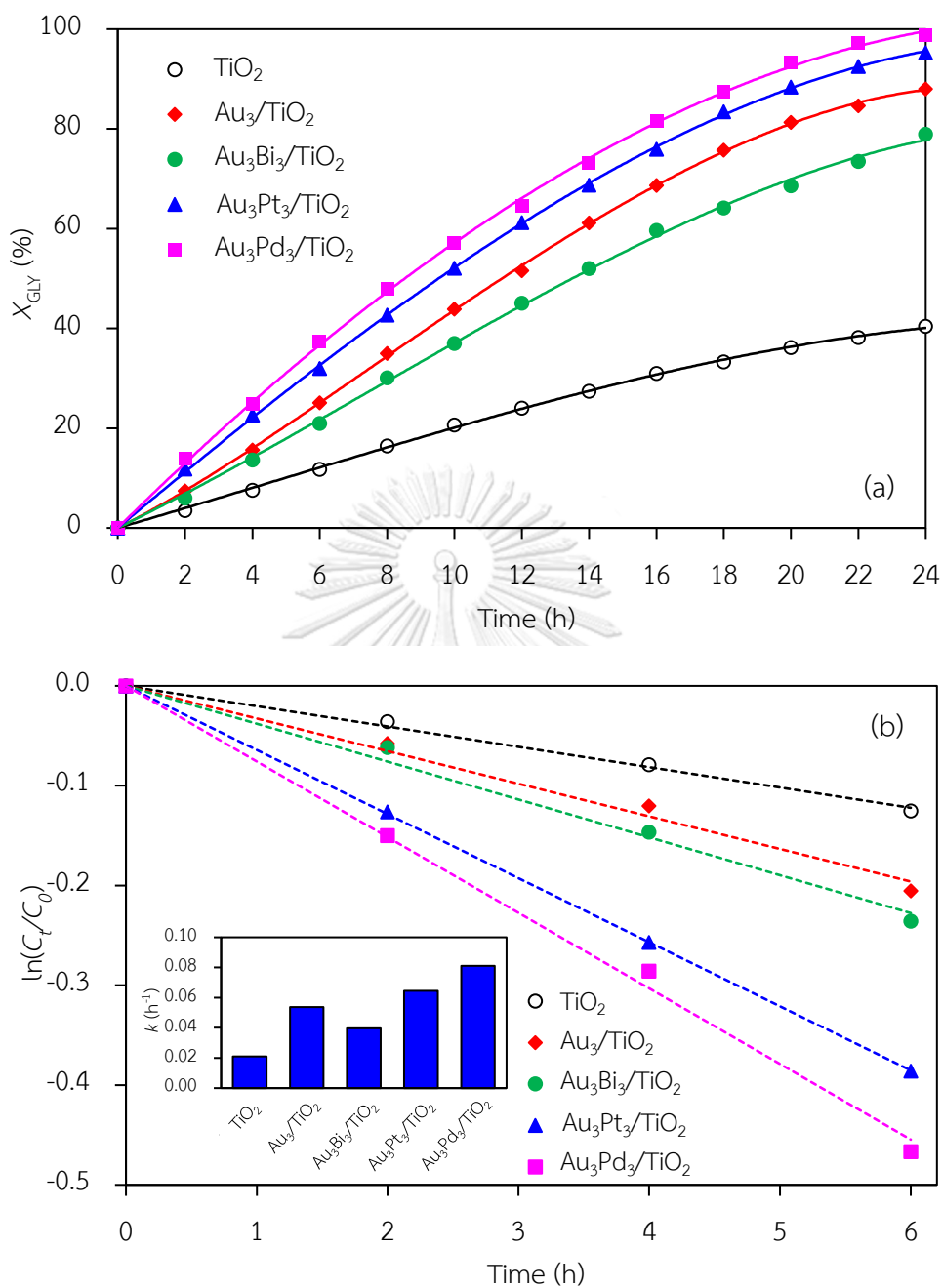


Figure 5.27 Representative (a) glycerol conversion and (b) plot of $\ln(C_t/C_0)$ as a function of time in the presence of Au_3M_3/TiO_2 compared with Au_3/TiO_2 at photocatalyst loading of 3.0 g/L, light intensity of 4.7 mW/cm^2 and using O_2 as the electron acceptor.

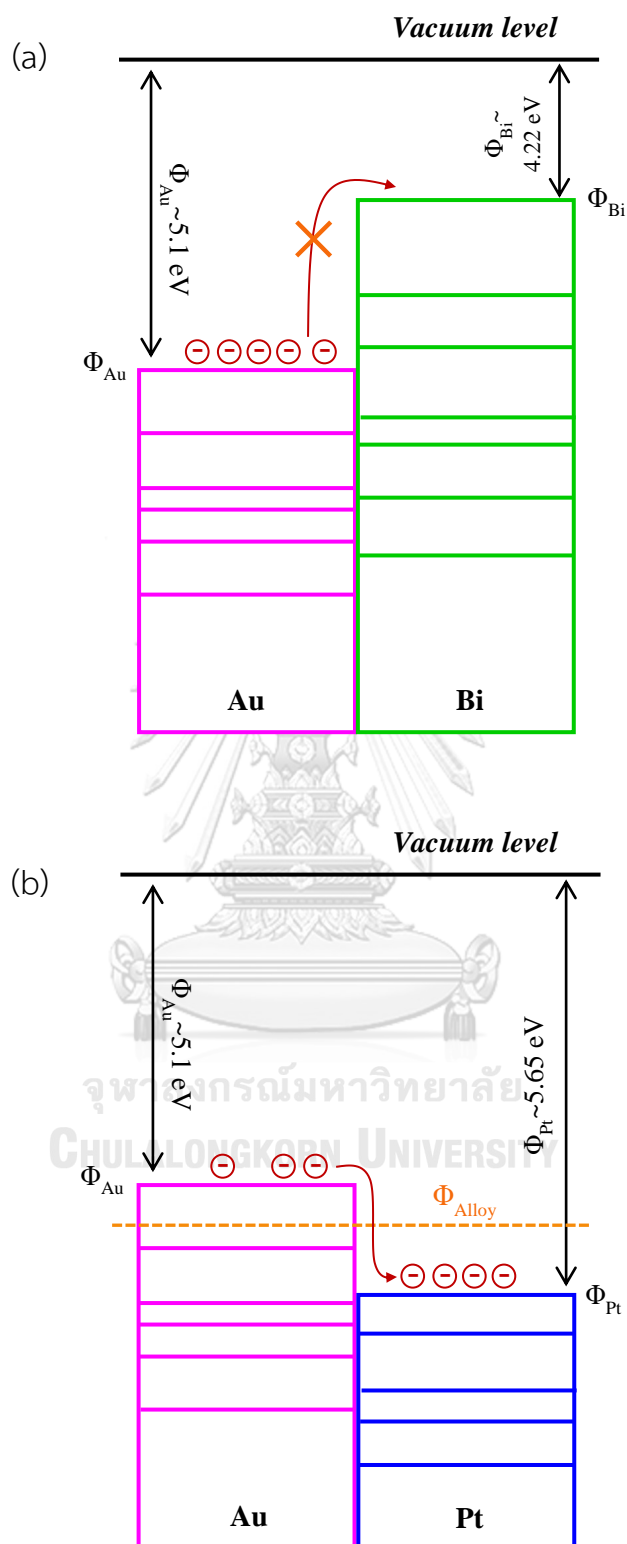


Figure 5.28 Schematic profiles of contact metal (a) AuBi, (b) AuPt and (c) AuPd with corresponding work-function in bimetallic NPs system.

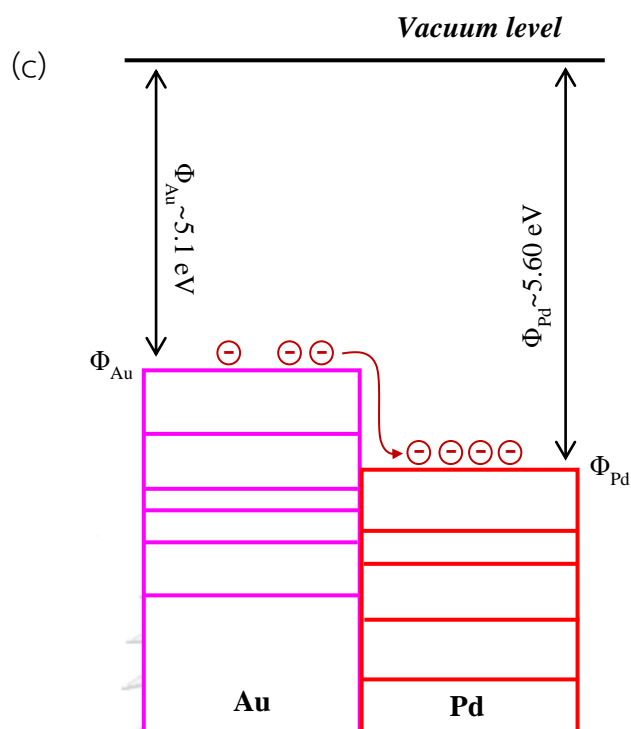


Figure 5.28 Schematic profiles of contact metal (a) AuBi, (b) AuPt and (c) AuPd with corresponding work-function in bimetallic NPs system (Cont.).

photocatalyst (Figure 5.28(c)). This reason is the reason why the $\text{Au}_3\text{Pd}_3/\text{TiO}_2$ exhibited a higher photocatalytic activity than the $\text{Au}_3\text{Pt}_3/\text{TiO}_2$ photocatalyst. The core-shell structure of the $\text{Au}_3\text{Pd}_3/\text{TiO}_2$ photocatalyst did not exhibit a negative effect on the LSPR behavior in this photocatalyst, probably because the plasmon metallic state of Pd can still occur, leading to an easy transfer of the e^- from the TiO_2 conduction band to Pd NPs and/or AuNPs and *vice versa*.

With respect to the generated products, the same products (GCD, DHA, HPA, GCOA, FMD and GCAD) were generated via all the $\text{Au}_3\text{M}_3/\text{TiO}_2$ photocatalysts and were similar to those generated in the presence of either the Au_3/TiO_2 or parent TiO_2 photocatalyst (Figure 5.29). The principle product was GCD in the presence of all the evaluated photocatalysts except for $\text{Au}_3\text{Bi}_3/\text{TiO}_2$, where GCAD was the principle

product. As reported in the previous section, monometallic Bi NPs decorated on TiO₂ did not promote the formation of GCAD as a major product. Accordingly, it is suggested that the synergism between the bimetallic Au-Bi was a vital factor in the formation of GCAD from glycerol. Various published works on the aerobic oxidation of glycerol over bimetallic catalysts with Bi NPs have proposed that Bi played a major role as a geometric blocking site, which can facilitate the activation and transformation of the secondary hydroxyl group of glycerol [204-206]. In this section, glycerol was mainly converted through the photo-oxidation reaction over Au₃Bi₃/TiO₂ to GCAD as the major product. It is hypothesized that the two terminal hydroxyl (-OH) groups of glycerol were bound on the surface of the AuBi NPs with Bi³⁺ species, whereas Bi adatoms function as blockers on the Au site, which is a high-energy site where the adsorption and reaction of the primary -OH group is preferred. This then serves to control the adsorbed orientation of glycerol molecules towards the preferential oxidation of the secondary -OH group to form DHA. In addition, due to the presence of various reactive oxygen species with a high oxidizing power in the photocatalytic system, the cleavage of the C-C bond of the generated DHA molecule to one molecule of GCAD and FMD is dramatically achieved. The generated FMD can eventually be oxidized to form CO₂ as a gas phase oxidation product. However, the synergetic role of Bi and the optimization of the Bi-promoted Au or other noble metals on TiO₂ photocatalyst with the corresponding reaction conditions to determine the highly selective oxidation of glycerol could also work to some extent that might be beneficial in academic research and the chemical industry.

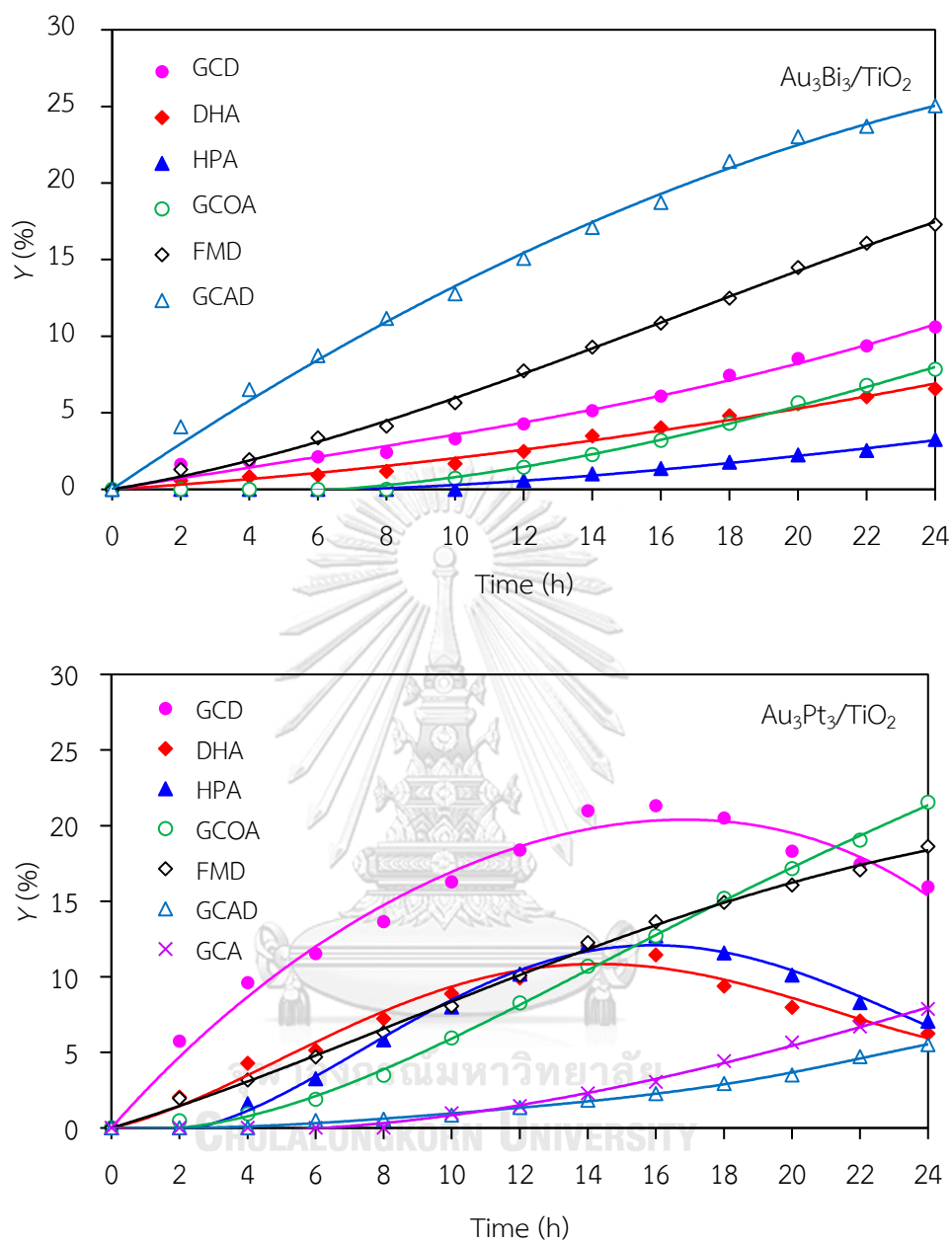


Figure 5.29 Yield of selected products obtained from glycerol photocatalytic conversion via $\text{Au}_3\text{M}_3/\text{TiO}_2$ at photocatalyst loading of 3.0 g/L, light intensity of 4.7 mW/cm^2 and using O_2 as the electron acceptor.

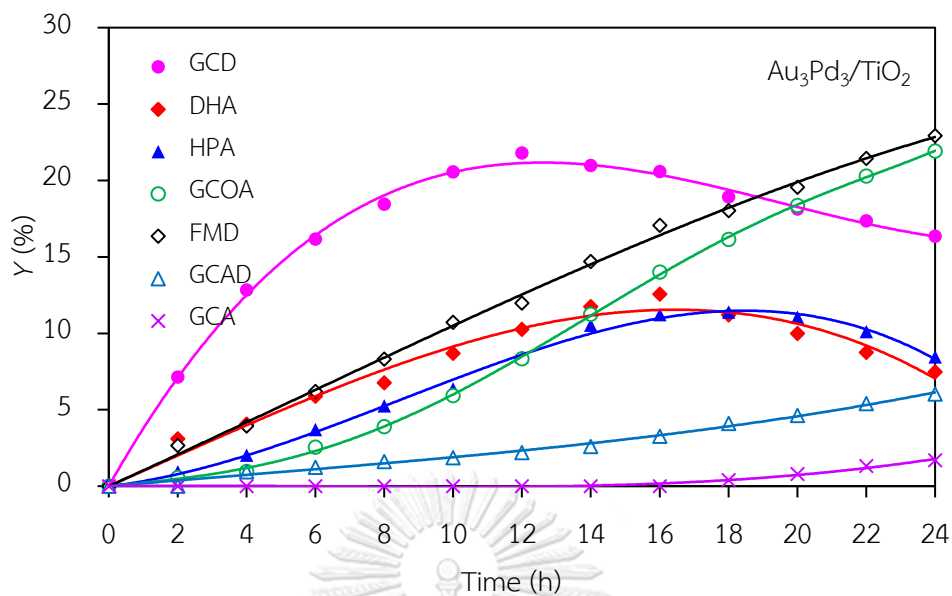


Figure 5.29 Yield of selected products obtained from glycerol photocatalytic conversion via $\text{Au}_3\text{M}_3/\text{TiO}_2$ photocatalyst loading of 3.0 g/L, light intensity of 4.7 mW/cm^2 and using O_2 as the electron acceptor (Cont.).

CHAPTER VI

PREPARATION OF BLACK TiO₂ VIA SOLUTION PLASMA PROCESS AND ITS PHOTOCATALYTIC OXIDATION OF GLYCEROL TO VALUE-ADDED COMPOUNDS

During the past few decades, enormous effort has been dedicated to synthesis a black or blue color of TiO₂, the so-called black TiO₂, by introducing the Ti³⁺ defect state and/or oxygen vacancies into the TiO₂ structure. This strategy has been highly regarded as a potential breakthrough in modulating the optical, chemical and electrical properties as well as a visible-light harvesting of TiO₂. Thus, in the present chapter, we introduce the novel technique named as “solution plasma process (SPP)” to synthesize black TiO₂ NPs. The effects of the plasma operating parameters, including the repetition frequency (20-80 kHz) and pulse width (0.5-2.0 μs) under two different solution medium concentrations of HNO₃ (0.3 mM and 3.0 mM) as well as plasma discharge time (1-4 h) on the morphology, structural and optical properties of the obtained black TiO₂ NPs were investigated. Finally, the photocatalytic activity of as-synthesized black TiO₂ was performed by using glycerol as a model compound and compared with commercial anatase TiO₂.

6.1 Formation of black TiO₂ NPs through solution plasma process

When the voltage pulse was applied across the metal electrodes, the current increased and some micro-gas bubbles were formed around the electrode tips due to the localized heating of the solution from the applied energy. During this stage, electrons flowed inside the bubble between the micro-gap, leading to its breakdown and subsequently a roughly circular discharge plasma occurred along the visible emission spectra in the gas-liquid interface, as shown schematically in Figure 6.1.

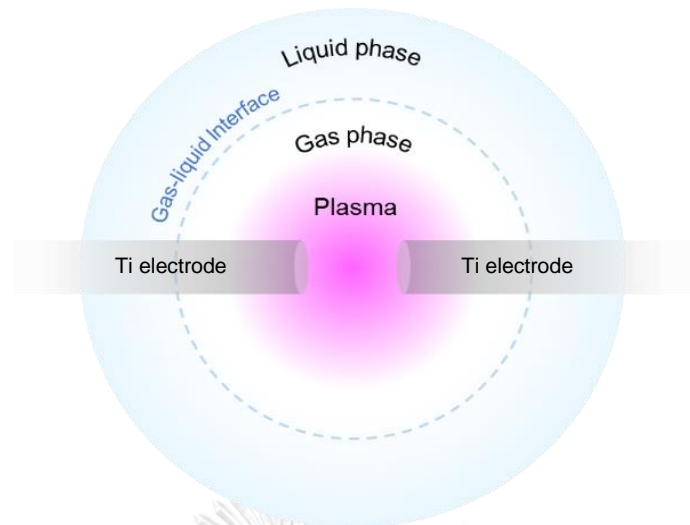


Figure 6.1 Model of the plasma generation.

To get an insight into the mechanism of black TiO₂ NPs formation via the SPP, the light emission spectra were evaluated. As shown in Figure 6.2, the majority of the active species obtained from the optical emission spectra (OES) were the H α , Ti I (neutral), Ti II (single-charge ions), and then H β and atomic O radicals. These highly energetic hydrogen and oxygen radicals were generated from the dissociation of water molecules in the acid solution and were responsible for the formation of the black TiO₂ NPs by bonding with the ionized Ti atom during the plasma generation. Another possible path for black TiO₂ NPs formation is the melting of Ti clusters disengaged from the Ti electrode surface. To test this hypothesis, the temperature of electrode tip was then calculated from the wavelength corresponding to the maximum blackbody radiation (λ_{max}) from the OES spectra according to Wien's law [207], as shown in Eq. (6.1).

$$\lambda_{\text{max}} = \frac{2.808 \times 10^3}{T} \quad (6.1)$$

where T is the absolute temperature (K)

It was found that the temperature between the electrode tips was around

4,996 K at the λ_{max} of 580 nm, which is higher than the boiling point (3,560 K) and the melting point (1,941 K) of titanium. Thus, molten Ti clusters could disengage from the Ti electrode surface and readily re-oxidize with some highly energetic atomic and electron bombardment in the plasma phase, yielding some black TiO₂ NPs after ejecting into the surrounded liquid phase. The high temperature difference between the plasma zone and solution resulted in the rapid quenching and frozen crystal growth, leading to the defective and disordered structure of the formed black TiO₂ NPs.

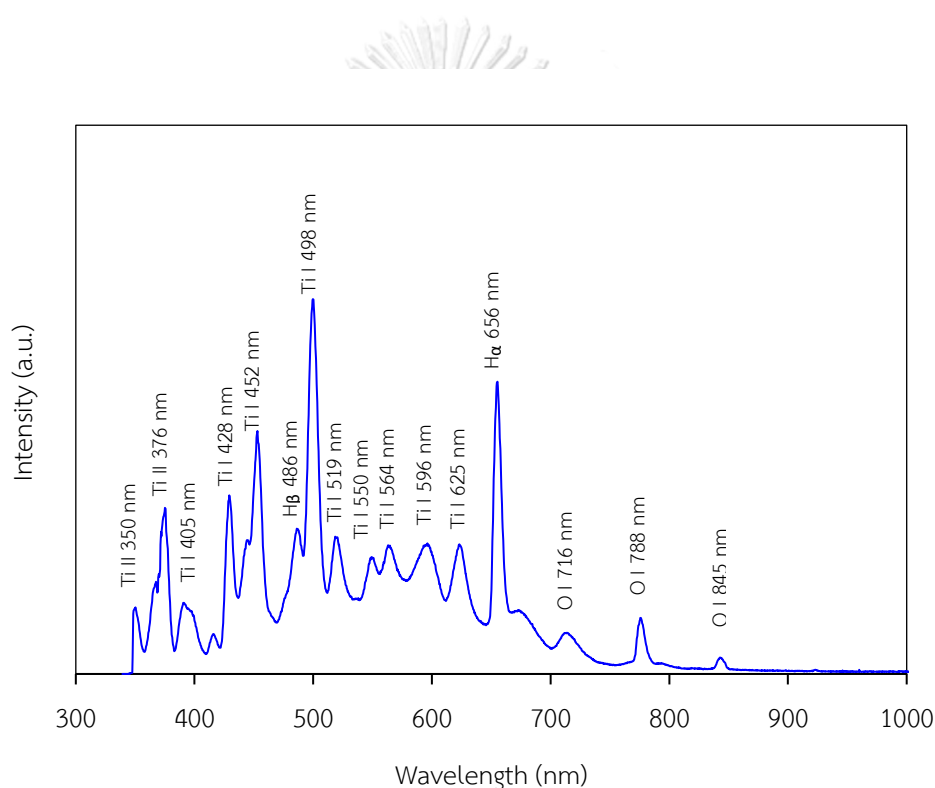


Figure 6.2 Representative OES of plasma discharge through a Ti electrode in HNO₃ solution.

6.2 Characterization of the as-synthesized black TiO₂ NPs

6.2.1 Effect of HNO₃ concentration, pulse width and repetition frequency

All of the influencing parameters including HNO₃ concentration, pulse width and repetition frequency are significantly influence on the plasma generation, which

affect the crystallinity, morphology, and optical properties of as-synthesized black TiO₂ NPs in terms of applied energy for discharged plasma.

The applied energy per pulse (E_p) and the applied energy per second (E_s) for discharged plasma were calculated according to Eqs. (6.2) and (6.3), respectively:

$$E_p = \int_0^t IV dt \quad (6.2)$$

$$E_s = E_p \times f \quad (6.3)$$

where I is current, V is voltage, t is the time per one pulse and f is the repetition frequency.

As presented in Table 6.1, the energy per pulse and the energy per second increased with increasing concentration of HNO₃ solution medium. The 3.0 mM HNO₃ solution provided the higher energy per second for discharging the plasma than 0.3 mM HNO₃ solution at identical repetition frequency and pulse width, probably due to its high acidic property and high conductivity. At the identical HNO₃ concentration, the energy per pulse and the energy per second both tend to be increased along with the increment of repetition frequency and pulse width.

6.2.1.1 Crystallite structure analysis

The crystal structure of the as-synthesized black TiO₂ NPs formed at different discharge plasma conditions with variation of HNO₃ concentration, pulse width and repetition frequency was detected by XRD analysis. As shown in Figure 6.3, all the prepared samples exhibited four diffraction peaks, matching well with the crystal structure of anatase TiO₂ in plane of (101), (200), (204) and (220) (JCPDS No. 21-1272), plus various diffraction peaks relating to the crystallite structure of the rutile phase (JCPDS No. 75-1751). This indicated that the as-synthesized black TiO₂ NPs contained both anatase and rutile phases. Interestingly, two additional peaks were observed at

2θ value of around 32.4° and 56.2° in all the prepared TiO_2 NP samples, which indicated the presence of the oxygen-deficient phases (ODP) in their structure [77].

Table 6.1 Plasma operating parameters for the synthesis of black TiO_2 NPs in HNO_3 solution medium.

| HNO_3 conc. (mM) | Frequency (f , kHz) | Pulse width (μs) | Energy per pulse (E_p , μJ) | Energy per second (E_s , J) |
|------------------------------|---------------------------|----------------------------------|---|-----------------------------------|
| 0.3 | 20 | 0.5 | 114 | 2.28 |
| 0.3 | 50 | 0.5 | 68.3 | 3.41 |
| 0.3 | 80 | 0.5 | 57.2 | 4.57 |
| 0.3 | 20 | 1.0 | 302 | 6.04 |
| 0.3 | 20 | 2.0 | 637 | 12.7 |
| 3.0 | 20 | 0.5 | 149 | 2.97 |
| 3.0 | 50 | 0.5 | 82.5 | 4.13 |
| 3.0 | 80 | 0.5 | 72.4 | 5.79 |
| 3.0 | 20 | 1.0 | 469 | 9.38 |
| 3.0 | 20 | 2.0 | 865 | 18.3 |

Typically, the ODP is identified as an absence of some oxygen atom compared with a normal stoichiometric TiO_2 , and was probably caused by (i) the rapid quenching and incomplete oxidation of the TiO_2 structure under the discharge SPP and (ii) the reaction between the hydrogen radicals that originated in plasma zone and the oxygen atom in the TiO_2 lattice. Although the diffraction peaks of the as-prepared black TiO_2 NPs still appeared at the standard position of the anatase and rutile phases, their intensity was weakened and broadened compared with the reference TiO_2 . This indicates the existence of oxygen vacancies and the formation of a Ti^{3+} defect state as

well as a decrease in the crystal lattice [208]. In addition, increasing the applied energy per second in both HNO₃ concentrations led to a weakened peak intensity, probably attributed to the rapid organization and structural growth of black TiO₂ NPs.

The crystal ratio of rutile and anatase phases was determined using Spurr's equation [209], as shown in Eq. (6.4), and the results are displayed in Table 6.2.

$$R = \left[\frac{1}{1 + 0.8(I_A / I_R)} \right] \quad (6.4)$$

where R is the mass fraction of the rutile phase in TiO₂, I_A is the integrated peak intensity of the main anatase (101) peak and I_R is the integrated peak intensity of the main rutile (110) peak.

The proportion of the rutile phase was considerably higher than the anatase phase when formed from a low utilized energy per second for discharged plasma, probably because the high temperature inside the plasma region preferably induced the transformation of the TiO₂ structure into the rutile phase [210]. The anatase phase was dominate under a high utilized energy per second might be because the high energy discharge plasma induced a dramatic quenching of the formed particles which had not transformed into the rutile phase in the plasma zone.

Compared to the XRD peak width of the rutile and anatase phase, the width of ODP looked significantly sharp, suggesting the formation of smaller crystallite size of rutile and anatase than the ODP. By using the Scherer equation (Eq. (5.1)), a crystallite sizes of anatase, rutile and ODP were calculated. As demonstrated in Table 6.2, the crystallite size of OPD were larger than those of anatase and rutile of around 7-10 folds, depending on the quantity of input energy per second. That is, increasing the input energy per second in both HNO₃ concentrations led to an increase of crystallite size of all anatase, rutile and ODP, probably attributed to the rapid organization and structural growth of black TiO₂ NPs.

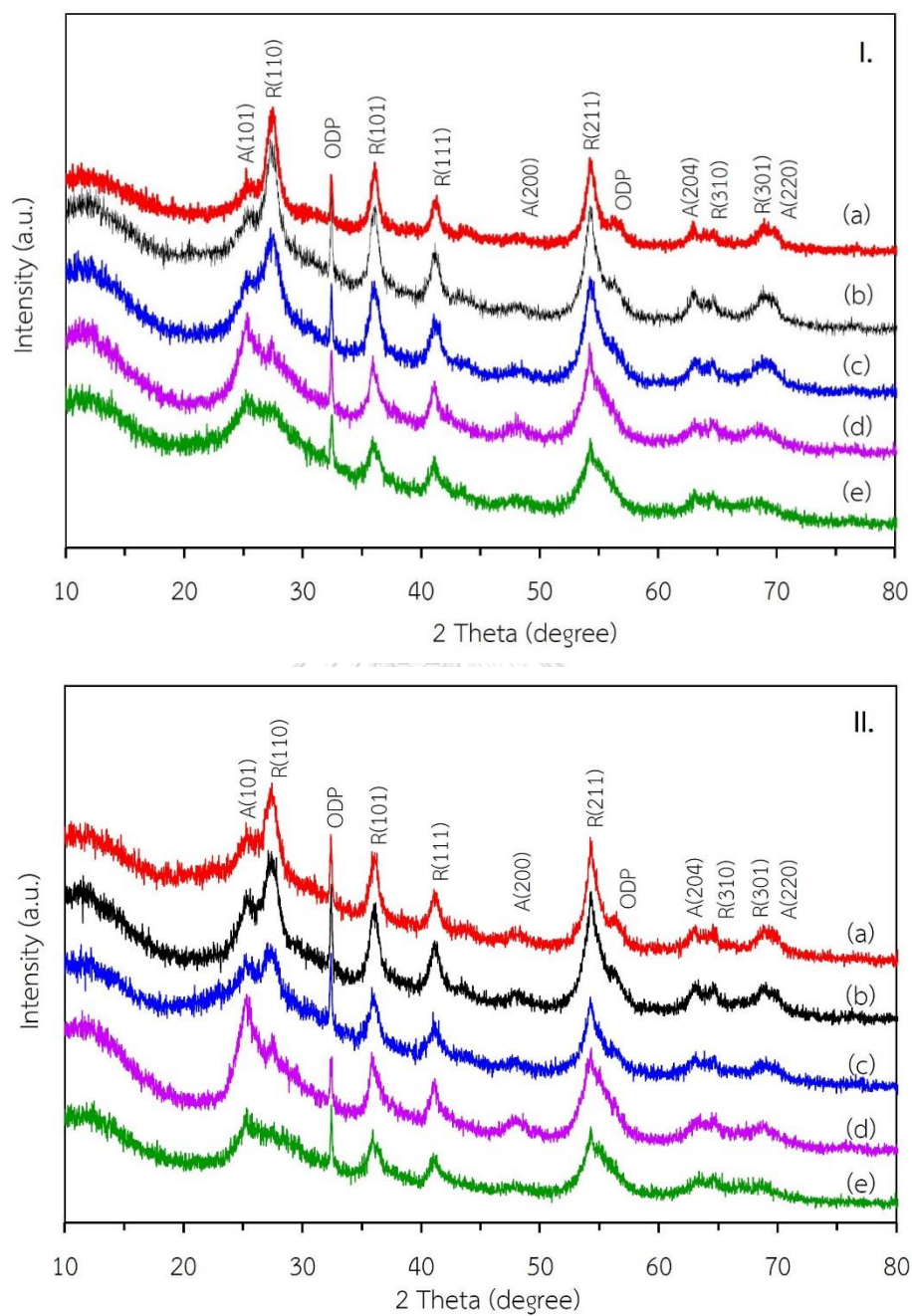


Figure 6.3 Representative XRD patterns of the as-synthesized black TiO_2 NPs formed from discharge plasma conditions of (a) 20 kHz and 0.5 μs , (b) 50 kHz and 0.5 μs , (c) 80 kHz and 0.5 μs , (d) 20 kHz and 1.0 μs and (e) 20 kHz and 2.0 μs in (I) 0.3 mM or (II) 3.0 mM HNO_3 as the discharge medium electrolyte solution.

Table 6.2 Structural information of the as-synthesized black TiO₂ NPs prepared under different discharge plasma operating parameters.

| Plasma operating parameters | | Mass fraction of rutile phase | | Crystallite size (nm) | | Stoichiometric ratio | | Mean volume diameter (nm) | | Synthesis rate (mg/h) | | Ti ³⁺ /Ti ⁴⁺ | | Ti-OH/TiO | | E _g (eV) | |
|--|--------------------|-------------------------------|--------------------------|-----------------------|--------------|----------------------|---------------|---------------------------|----------------------|-----------------------|------------------------------------|------------------------------------|---------------------|-----------|--|---------------------|--|
| HNO ₃ conc. (mM) | Frequency (f, kHz) | Pulse width (μs) | fraction of rutile phase | Anatase (101) | Rutile (110) | ODP at 2θ of 32.46° | Titanium (Ti) | Oxygen (O) | volume diameter (nm) | rate (mg/h) | Ti ³⁺ /Ti ⁴⁺ | Ti-OH/TiO | E _g (eV) | | | | |
| 0.3 | 20 | 0.5 | 0.77 | 5.94 | 8.17 | 46.20 | 1.00 | 1.85 | 325 | 7.23 | 0.179 | 0.211 | 2.97 | | | | |
| 0.3 | 50 | 0.5 | 0.76 | 5.94 | 7.78 | 46.72 | 1.00 | 1.82 | 387 | 8.20 | 0.203 | 0.142 | 2.95 | | | | |
| 0.3 | 80 | 0.5 | 0.72 | 5.81 | 6.19 | 47.52 | 1.00 | 1.79 | 675 | 15.2 | 0.241 | 0.122 | 2.83 | | | | |
| 0.3 | 20 | 1.0 | 0.36 | 4.84 | 5.84 | 48.64 | 1.00 | 1.73 | 1312 | 24.2 | 0.284 | 0.189 | 2.63 | | | | |
| 0.3 | 20 | 2.0 | 0.38 | 4.57 | 5.84 | 55.13 | 1.00 | 1.66 | 2642 | 32.2 | 0.311 | 0.070 | 2.50 | | | | |
| 3.0 | 20 | 0.5 | 0.67 | 5.94 | 8.34 | 42.85 | 1.00 | 1.82 | 389 | 7.40 | 0.188 | 0.302 | 2.71 | | | | |
| 3.0 | 50 | 0.5 | 0.66 | 5.94 | 7.43 | 43.53 | 1.00 | 1.80 | 513 | 8.65 | 0.210 | 0.273 | 2.69 | | | | |
| 3.0 | 80 | 0.5 | 0.62 | 5.94 | 7.11 | 45.19 | 1.00 | 1.74 | 998 | 22.5 | 0.276 | 0.145 | 2.62 | | | | |
| 3.0 | 20 | 0.5 | 0.25 | 5.50 | 7.43 | 46.99 | 1.00 | 1.65 | 1488 | 30.0 | 0.350 | 0.197 | 2.49 | | | | |
| 3.0 | 20 | 2.0 | 0.26 | 5.15 | 6.81 | 52.34 | 1.00 | 1.59 | 2810 | 46.9 | 0.401 | 0.082 | 2.44 | | | | |
| Reference TiO ₂ (anatase TiO ₂) | | | N/A | N/A | N/A | N/A | N/A | N/A | 550 | | 0.000 | 0.032 | 3.21 | | | | |

6.2.1.2 Morphology analysis

Regarding the appearance feature of the as-synthesized black TiO₂, it appeared in spherical shape (Figure 6.4(a) and (b)), which was likely reflected by the surface tension effect of the molten particles during the rapid ejection of the as-synthesized black TiO₂ NPs from the plasma region to the lower temperature region of the surrounding solution (the so-called quenching step). In terms of atomic composition evaluated by EDX spectroscopy, it was composed of only titanium (Ti) and oxygen (O) species (Figure 6.4(c)), suggesting that a high purity of black TiO₂ was successfully synthesized using the SPP. The stoichiometric ratio of Ti and O species at different synthesis conditions were summarized in Table 6.2. It showed the non-stoichiometric ratio of Ti and O atoms, confirming the presence of the oxygen deficiencies in the black TiO₂ structure. In addition, a well-crystallized black TiO₂ with a lattice spacing of 0.352 nm and 0.325 nm, corresponding to the anatase (101) and rutile (110) planes (JPCDS 21-276), respectively, was observed in the high-resolution TEM image (Figure 6.4(d)). The disordered structure of the as-synthesized TiO₂ NPs was also clearly observed, for example as marked with the dashed circle in Figure 6.4(d). These results also emphasize that the crystal defects were formed inside the black TiO₂ structure, in accord with the XRD patterns.

The mean volume diameter of the as-prepared TiO₂ NPs was examined by DLS, where it tended to increase as the applied energy per second increased (Table 6.2), presumably due to the joule heating in a vast local hot spot surface in the presence of a high energy input, which induced the electrothermal instability and made the electrode tip surface rough, causing a melt-off and facile agglomeration of the formed black TiO₂ NPs [211]. Moreover, numerous Ti atoms can vaporize from the Ti electrode when the electrode temperature exceeded the boiling point, and these can then grow from this hot plasma zone, resulting in the formation of large particles. These large

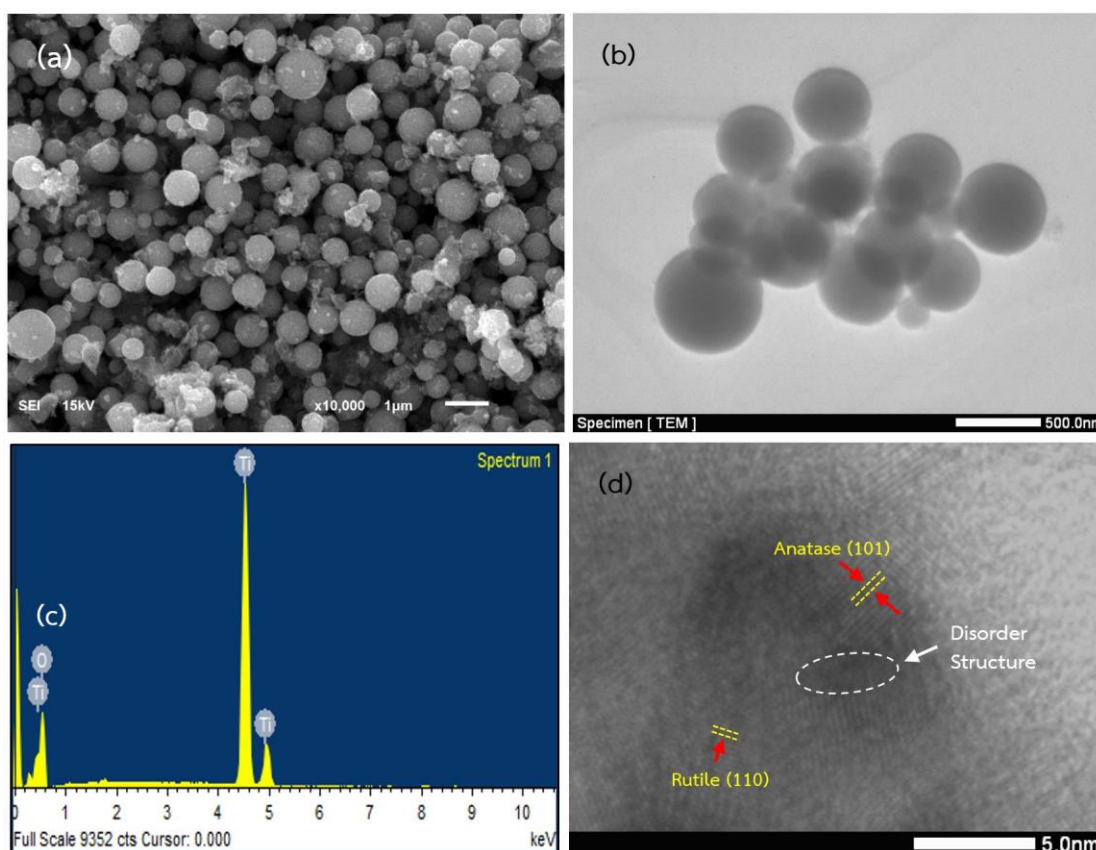


Figure 6.4 Representative (a) SEM, (b) TEM and (c) high-resolution TEM images of the as-synthesized black TiO_2 NPs formed with a 20 kHz, 2.0 μs discharge plasma in 3.0 mM HNO_3 .

black TiO_2 NPs were obtained in the presence of the higher HNO_3 concentration, probably due to the fact that a high electrolyte concentration could promote a high current flow. With regard to the synthesis rate, the discharged plasma under 3.0 mM HNO_3 solution at frequency of 20 kHz and pulse width of 20 μs also provided the high synthesis rate of black TiO_2 (46.9 mg/h) compared with other synthesis conditions (Table 6.2). This is probably due to the fact that this acid medium can provide high energy per second to generate the plasma, resulting in a high generation of high energetic atoms and electrons to promote the formation of black TiO_2 in the high yield. This is in line with the principle of plasma discharging into the solution medium on the

basis of the electric current [212]. The coloration of the as-synthesized TiO₂ NPs were black, due to the presence of the lattice disorder Ti³⁺ in their bulk structure [213], and no color changed of these as-synthesized TiO₂ NPs was observed over at least 6 months after synthesis.

6.2.1.3 Chemical structure analysis

The existence of Ti³⁺ in all as synthesized black TiO₂ NPs was revealed qualitatively by the EPR spectroscopy. No signal in the EPR spectra was observed for the reference TiO₂, while the signal was observed for all the as-synthesized black TiO₂ NP samples as illustrated in Figure 6.5. This gave a *g*-value of 1.99, which is a typical feature of paramagnetic Ti³⁺ centers [213, 214]. This indicated the presence of Ti³⁺ in the structure of all prepared black TiO₂ NP samples, resulting in the formation of their defective and disordered structure. A high intensity of the EPR spectra was observed in the presence of the high input energy per second plasma generation, suggesting the formation of a high Ti³⁺ content in those as-synthesized samples.

Figure 6.6 shows the XPS survey of black TiO₂, in which all peaks can be assigned to the Ti, O and C elements (from background carbon tape). This suggests that the pure black TiO₂ was synthesized at all different plasma conditions using the SPP. To quantitatively determine the presence of Ti³⁺ as well as the chemical bonding state of the as-synthesized black TiO₂ NPs, HR-XPS analysis was then performed. The reference TiO₂ (Anatase TiO₂) exhibited two symmetric main peaks (Figure 6.7) at a binding energy of 458.7 eV and 464.4 eV, corresponding to the spin-orbital doublet of Ti 2p_{3/2} and Ti 2p_{1/2} of Ti⁴⁺, respectively. All the as-synthesized samples also exhibited these two main peaks, but with rather broader peaks and a slight shift towards a lower

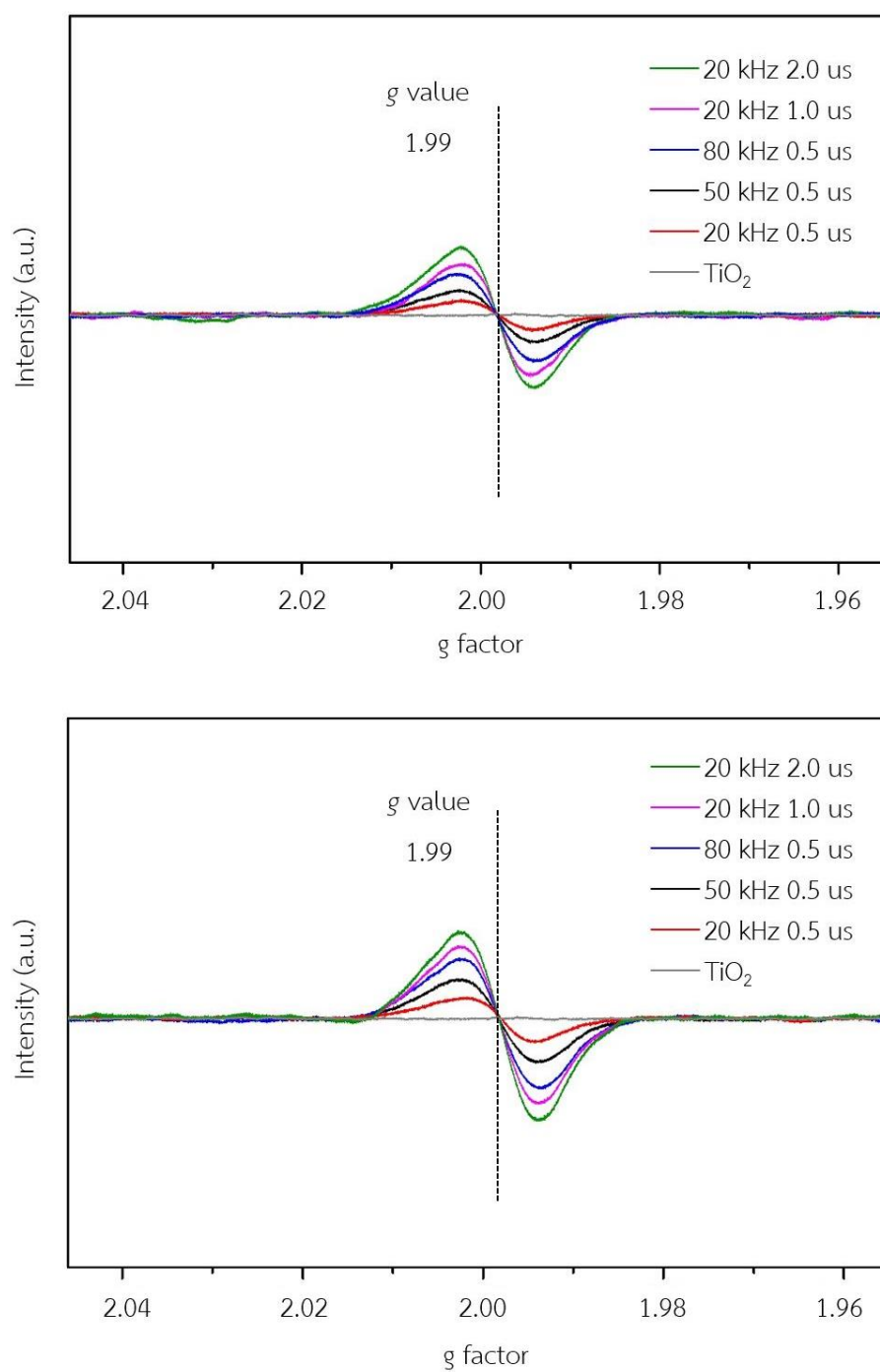


Figure 6.5 Representative EPR spectra of the as-synthesized black TiO₂ NPs formed from different discharge plasma conditions in (a) 0.3 mM and (b) 3.0 mM HNO₃.

binding energy than the reference TiO_2 . This distinctive blue shift indicates the chemical bonding of the Ti atoms with other species, besides O atoms, or/and the presence of a lower oxidation state (Ti^{3+}) species. As mentioned earlier, various high energetic species, such as hydrogen, oxygen, and hydroxyl radicals, were produced during the SPP. A black TiO_2 lattice might be structured with the generated hydrogen to form O-Ti-H bonds. The oxygen atom has a high electronegativity compared with the hydrogen atom, resulting in the shift of the partial electron from the H to Ti and O, and so enriching the electron of Ti 2p, which consequently led to the negative shift of the XPS spectrum towards a lower binding energy [215]. In addition, as mentioned elsewhere, the negative blue shift of the XPS spectrum is also achieved by the presence of some defect disorder structure or the presence of Ti^{3+} [216].

After deconvolution using a symmetrical Gauss distribution, two main peaks of as synthesized black TiO_2 NPs still appeared at a binding energy of 458.7 eV and 464.4 eV (Figure 6.7), which were assigned to the $\text{Ti}2p_{3/2}$ and $\text{Ti}2p_{1/2}$ of the Ti^{4+} species, respectively. Two additional tailored peaks appeared at a lower binding energy of 457.9 eV and 463.6 eV, respectively, indicating the presence of $\text{Ti} 2p_{3/2}$ and $\text{Ti} 2p_{1/2}$ of the Ti^{3+} species [213, 217]. This confirms the presence of the disorder structure or Ti^{3+} in all the as-synthesized black TiO_2 NPs. The self-assembled Ti^{3+} defects could be generated from the reaction between the lattice oxygen in the TiO_2 structure and energetic H atoms produced during the SPP, which led to well established oxygen vacancies, and simultaneously left two electrons in one oxygen vacancy site. These leftover electrons can allocate to the titanium atom position, yielding the formation of the lattice disorder Ti^{3+} in the structure of black TiO_2 NPs.

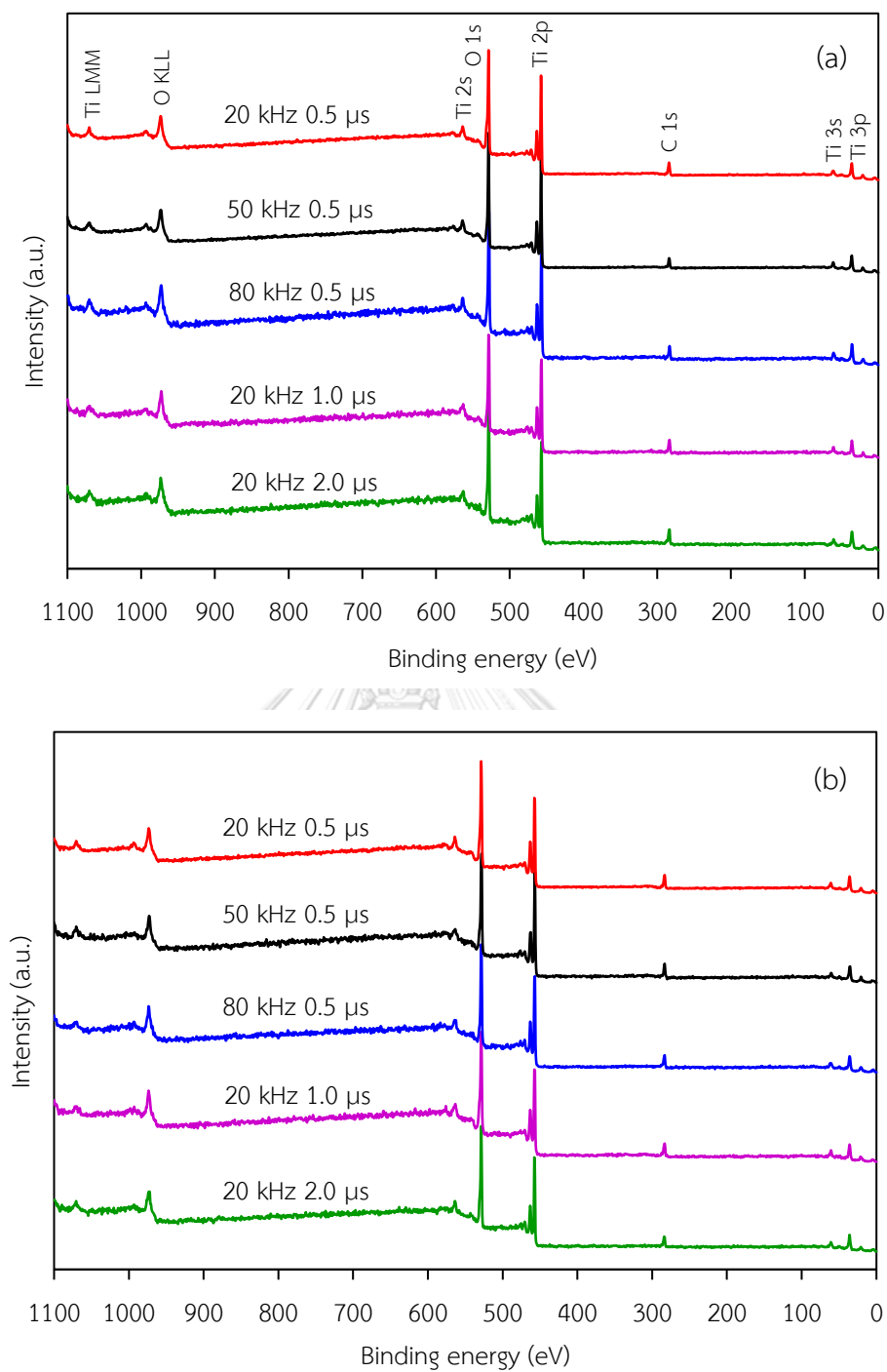


Figure 6.6 Representative XPS survey spectra of the as-synthesized black TiO₂ NPs formed in (a) 0.3 mM and (b) 3.0 mM HNO₃ under different discharge plasma conditions.

The relative Ti^{3+} to Ti^{4+} content in the TiO_2 NPs synthesized in the presence of different discharge plasma conditions was roughly estimated from the XPS deconvoluted areas and listed in Table 6.2. For each frequency and pulse width, a high $\text{Ti}^{3+}/\text{Ti}^{4+}$ ratio was obtained in a high HNO_3 concentration, while it also increased as the input energy per second increased, consistent with results obtained from the EPR spectra. Thus, the Ti^{3+} defect concentration clearly increased with a higher applied energy for the discharge plasma. This is because a high applied energy for the discharge plasma enhances the current flow, which can boost not only the highly generated energetic charges in the plasma but also disengage the molten particles from the electrode. This then resulted in an enrichment of generated black TiO_2 NPs, which were speedily removed from the plasma zone due to their high flux in the solution. The abrupt quenching and oxidation of the engendered particles can restrain the crystal structure, resulting in the formation of a high metastable defect content and disordered structure as Ti^{3+} or oxygen vacancies in the obtained samples.

To explore the oxygen chemical state in the as-prepared samples, the high-resolution O 1s spectra was examined by XPS. As demonstrated in Figure 6.8, the reference TiO_2 exhibited an almost symmetric O 1s spectrum at a binding energy between 530.2–530.6 eV, assigned to the O1s peaks characteristic of O^{2-} ions in the crystalline network. The small O 1s peak at 531.8–532.0 eV was the characteristic of the OH^- ions of the crystalline network. All the as-prepared TiO_2 NPs exhibited three single O 1s peaks at a binding energy of 529.8, 531.1 and 532.2 eV, assigned to the lattice oxygen in TiO_2 ($\text{Ti}^{4+}\text{-O}$), oxygen vacancies of TiO_2 ($\text{Ti}^{3+}\text{-O}$) and surface hydroxyl (Ti-OH), respectively. Two humped peaks at the high binding energy can be directly linked with the presence of the defect disordered structure of the black TiO_2 NPs, and were accordingly not observed in the reference stoichiometric TiO_2 . The concentration of hydroxyl species on the surface of the as-synthesized black TiO_2 NPs, estimated

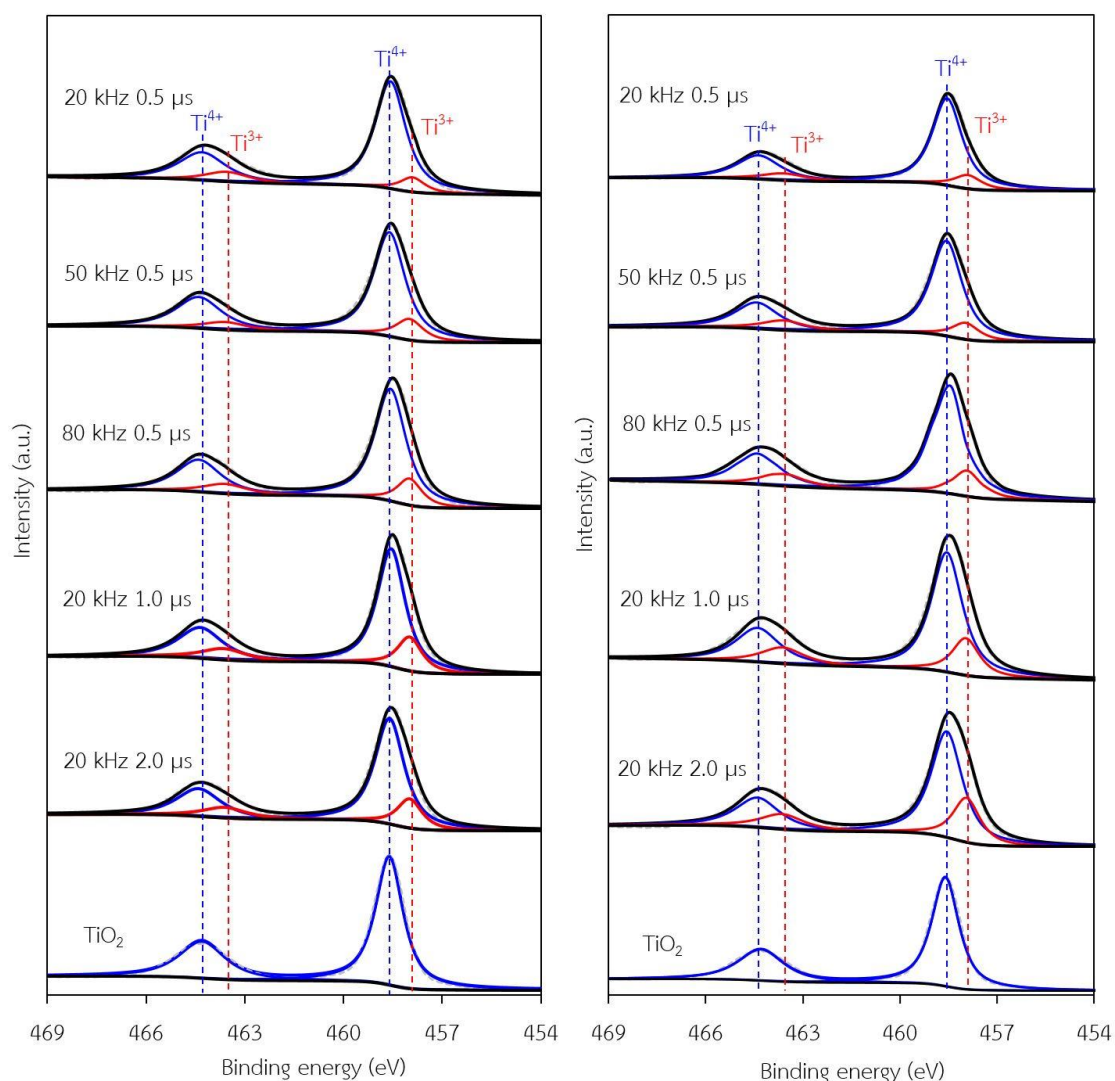


Figure 6.7 Representative deconvoluted peak area of high resolution Ti 2p XPS spectra of the reference TiO_2 and the as-synthesized black TiO_2 NPs formed in (a) 0.3 mM or (b) 3.0 mM HNO_3 under different discharge plasma conditions.

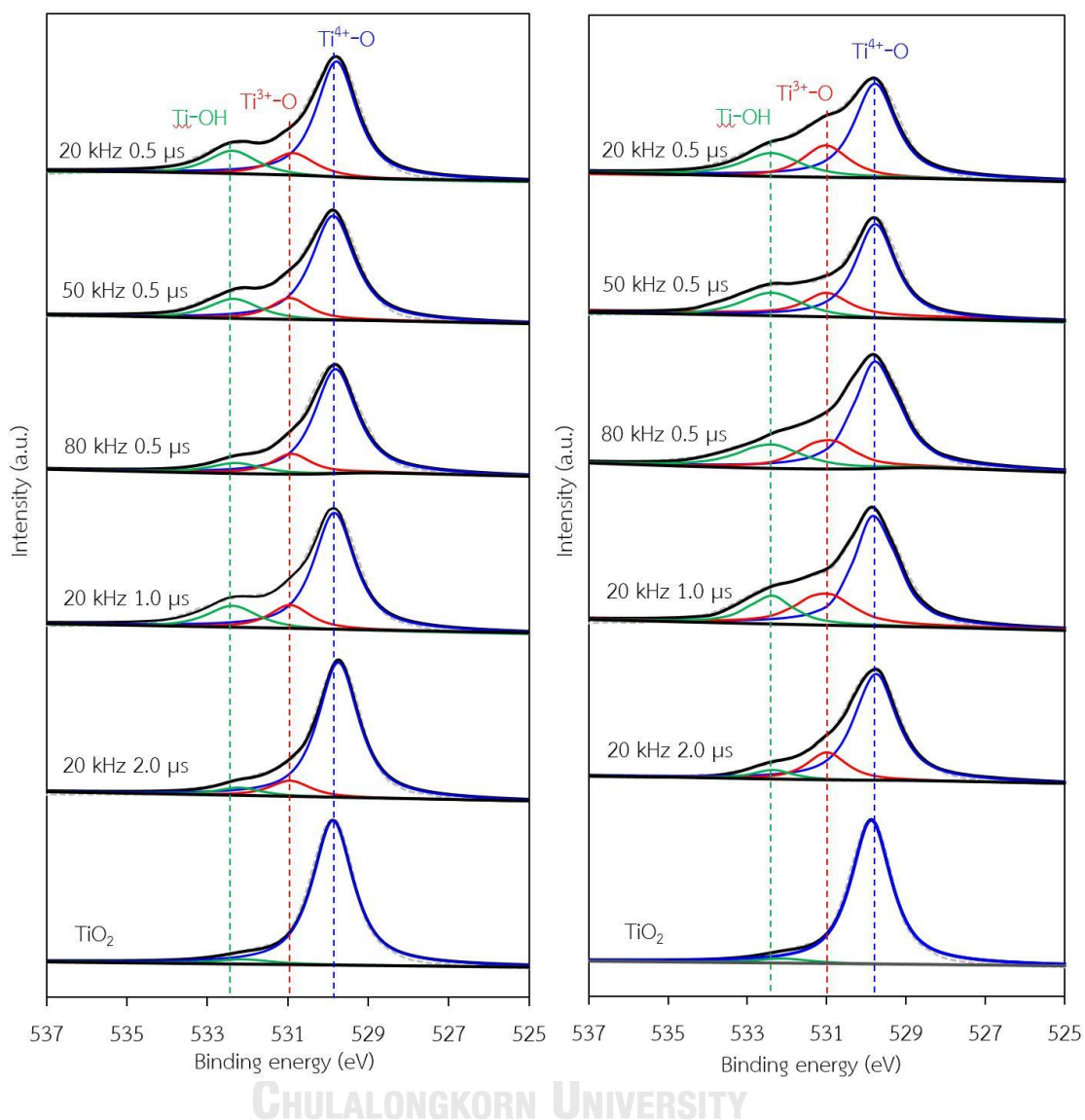


Figure 6.8 Representative deconvoluted peak area O1s XPS spectra of the reference TiO_2 and the as-synthesized black TiO_2 NPs formed in (a) 0.3 mM or (b) 3.0 mM HNO_3 under different discharge plasma conditions.

from the deconvoluted area of the XPS spectra and demonstrated in terms of the Ti-OH/Ti-O ratio, were listed in Table 6.2. The Ti-OH/Ti-O ratio tended to decrease with an increased applied input energy for plasma generation. Presumably, a high input energy can facilitate a high reaction rate between the surface hydroxyl species and the

generated charge species in the plasma region during the formation of the black TiO₂ NPs. Furthermore, the surface hydroxyl groups of the generated the black TiO₂ NPs suspended in the liquid phase can be re-oxidized by the various charged species that were formed at the plasma near the gas-liquid interface, resulting in a low concentration of Ti-OH on the obtained black TiO₂ surface.

To gain further insight into the chemical bonding species of as-synthesized black TiO₂ NPs, FTIR analysis was performed. As illustrated in Figure 6.9, all the as-synthesized black TiO₂ NPs showed similar absorption features in the wavenumber range of 500-4,000 cm⁻¹. A characteristic feature of all these spectra was the presence of a broad band in the frequency range of 500-1,000 cm⁻¹ from the symmetric stretching vibrations of Ti-O bonds [218], and the band located at 1,384 cm⁻¹ that corresponded to the vibration of the Ti-ligand bond [219]. The peaks at around 1,627 cm⁻¹, assigned to the O-H bending mode, and the broad band observed in range of 3,100-3,600 cm⁻¹ indicated the stretching and wagging vibration modes of hydroxyl groups (-OH). The wider IR-active hydroxyl vibration peak denoted that the -OH group of the as-synthesized black TiO₂ NPs experienced a diverse environment, which will mainly be due to the disordered structure [220].

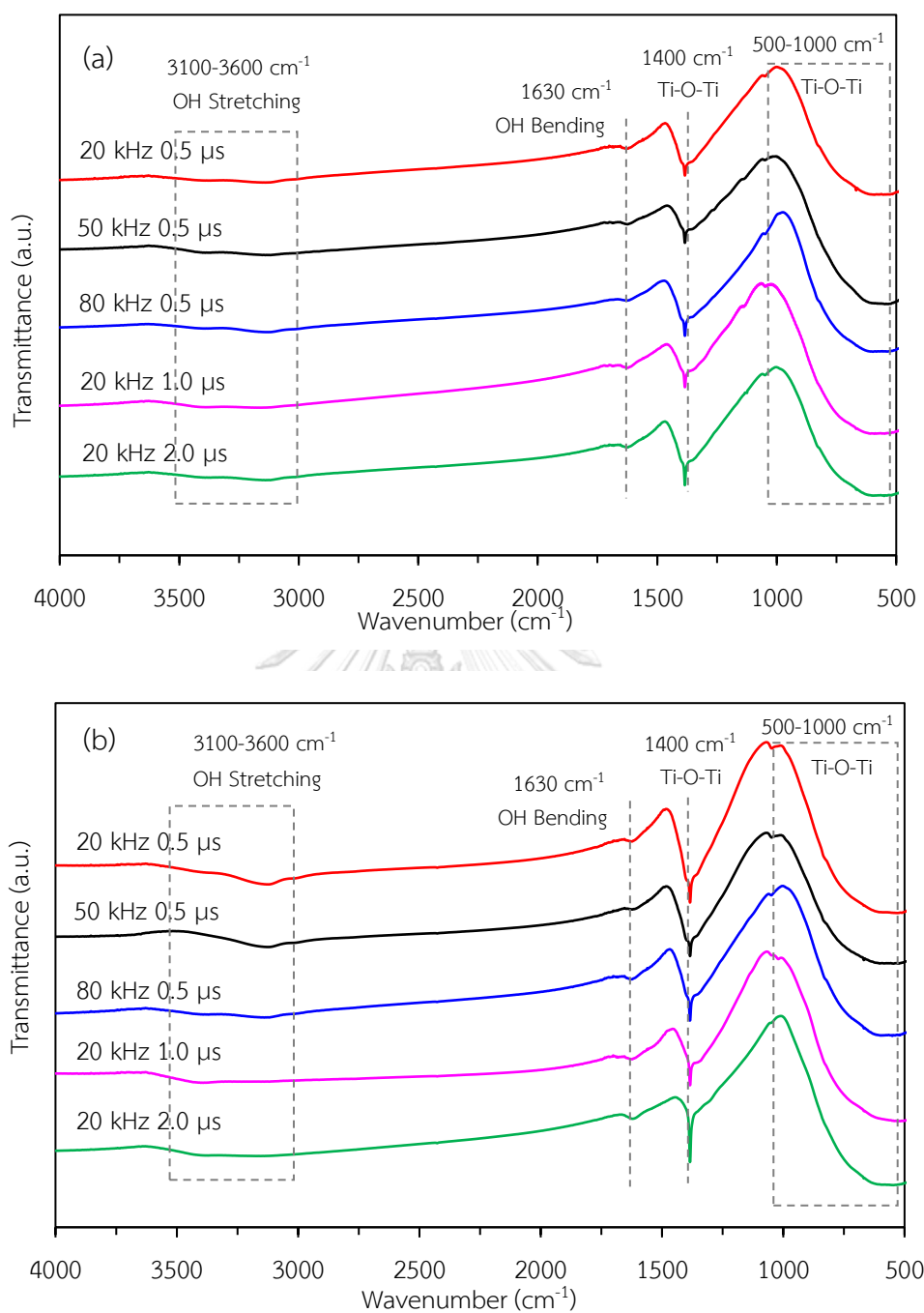


Figure 6.9 Representative FTIR spectra of the as-synthesized black TiO_2 NPs formed in (a) 0.3 mM or (b) 3.0 mM HNO_3 under different discharge plasma conditions.

6.2.1.4 Optical property analysis

The optical property of all the as-synthesized black TiO₂ NPs was investigated by UV-Visible spectrophotometry. As shown in Figure 6.10, compared with the reference TiO₂, all the synthesized black TiO₂ NPs exhibited a high absorbance intensity through the whole visible and ultraviolet light range, suggesting an ability to absorb visible light with a substantial red shift of the absorption band-edge and large absorption tail in the visible light regions in all the prepared samples that tended to increase with increasing input energy for the discharge plasma. This is in agreement with the concentration of Ti³⁺ defects. The absorbance information from Figure 6.10 was used to determine the band gap energy of the as-synthesized samples according to Eq. (6.5), which for ease can be rearranged to Eq. (6.6):

$$\alpha = \frac{A(h\nu - E_g)^n}{h\nu} \quad (6.5)$$

$$(\alpha h\nu)^{1/n} = Ah\nu - AE_g \quad (6.6)$$

where α is the optical absorption coefficient determined from the obtained absorbance, A is a constant, h is Plank's constant, ν is the frequency of light, E_g is the optical band gap and n is the nature of the electron transition, which is assumed to be 2 as the indirect band gap of TiO₂ [221, 222].

Plots of the photon energy ($h\nu$) again $(\alpha h\nu)^{1/2}$ are displayed in the inset of Figure 6.10. Extrapolation the linear part of the inset curve to intercept the x-axis gives the band gap energy, which is summarized in Table 6.2. The band gap energy of the reference TiO₂ was around 3.21, in accordance with the characteristic value of commercial TiO₂. The band gap energy of the as-synthesized black TiO₂ NPs decreased with increasing plasma discharge input energy. The lowest band gap energy of 2.44 eV was obtained from the sample synthesized with a frequency of 20 kHz, pulse width of 2.0 μ s and discharged in 3.0 mM HNO₃ aqueous solution.

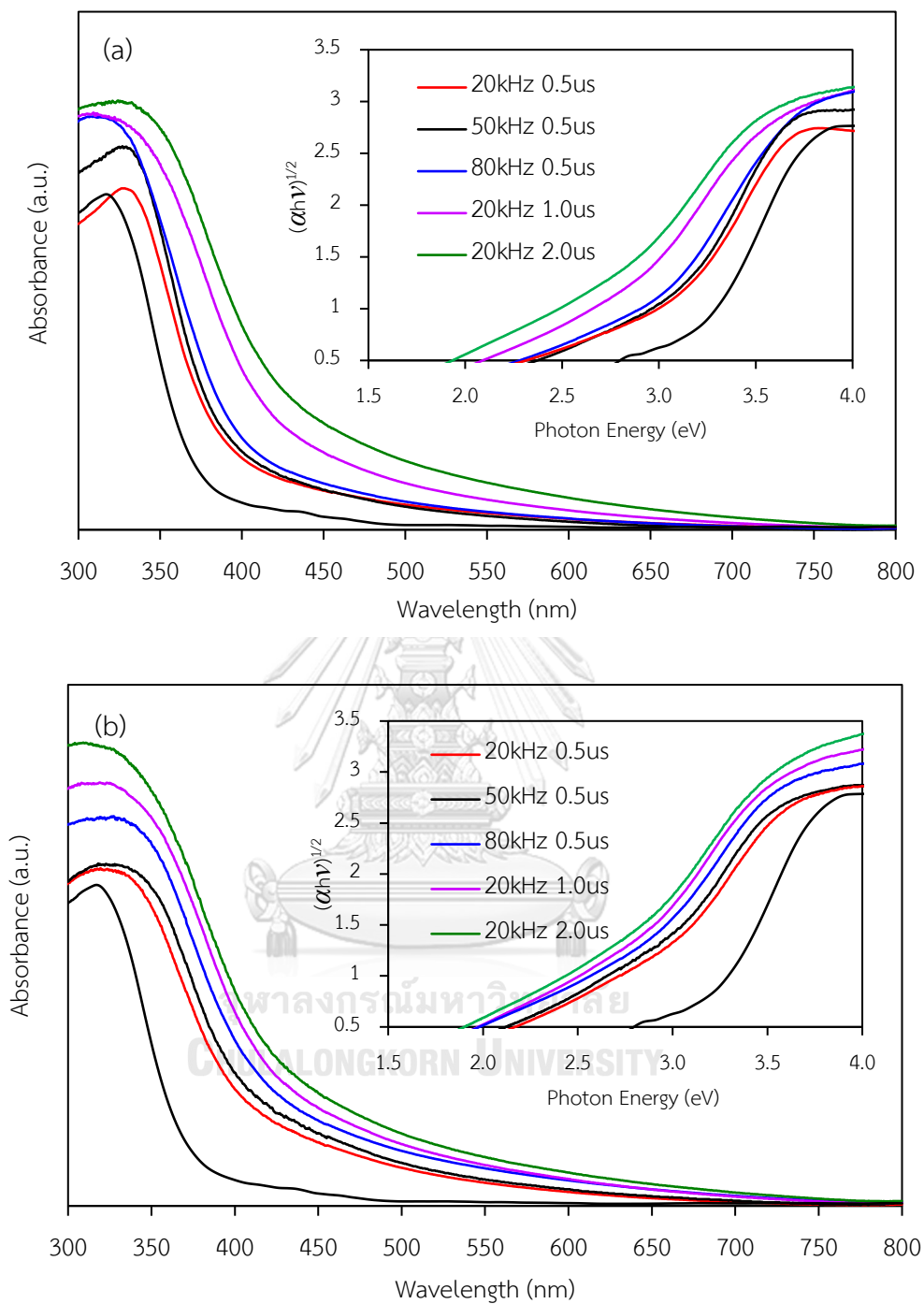


Figure 6.10 Representative UV-Vis spectra and Tauc's plot (inset) of the as-synthesized black TiO₂ NPs formed in (a) 0.3 mM and (b) 3.0 mM HNO₃ under different discharge plasma conditions.

Based on the obtained results, it is worth pointing out that the strong red shift of the UV-Vis spectra indicated a low band gap energy of the tested material. The significant red shift and enlarged absorption tail of the as-synthesized black TiO₂ NPs was related to the concentration of Ti³⁺, which was controlled by the input energy for discharge plasma.

As demonstrated in Figure 6.11, the variation in the band gap energy seemed to depend more strongly on the Ti³⁺/Ti⁴⁺ ratio than the Ti-OH/Ti-O one. Theoretically, a flawless TiO₂ lattice has a band gap energy of just over 3 eV due to the disjunction between the occupied valence band O 2p states and the empty Ti 3d orbital states as the conduction band. The presence of the lattice disordered Ti³⁺ in the TiO₂ matrix could also generate oxygen vacancies in order to maintain the electrostatic balance according to the reactions outlined in Eq. (6.7) [217];



where V_o denotes the oxygen vacancies, caused by the absence of O²⁻ in the lattice matrix.

The existence of Ti³⁺ and accompanying oxygen vacancies could yield an isolated mid-gap defect state [79], which induces the occupied 3d states to act as the electron donor at levels below the minimum conduction band. In addition, it also enables the lengthening of the continuum conduction band edge, resulting in the formation of band tail states [223]. Likewise, a large amount of Ti³⁺ defect disorder can yield not only the generated mid-gap isolated states and the conduction band tail but also an upshifted valance band edge of the black TiO₂ crystal, which leads to the narrowness of the electronic band gap seen in the as-synthesized materials [224, 225]. These phenomena can enhance the electron transportation and facilitate the generation of strongly reductive electrons. Namely, the electron in this occupied 3d isolated state can be stimulated to vacate the Ti 3d orbital of the conduction band

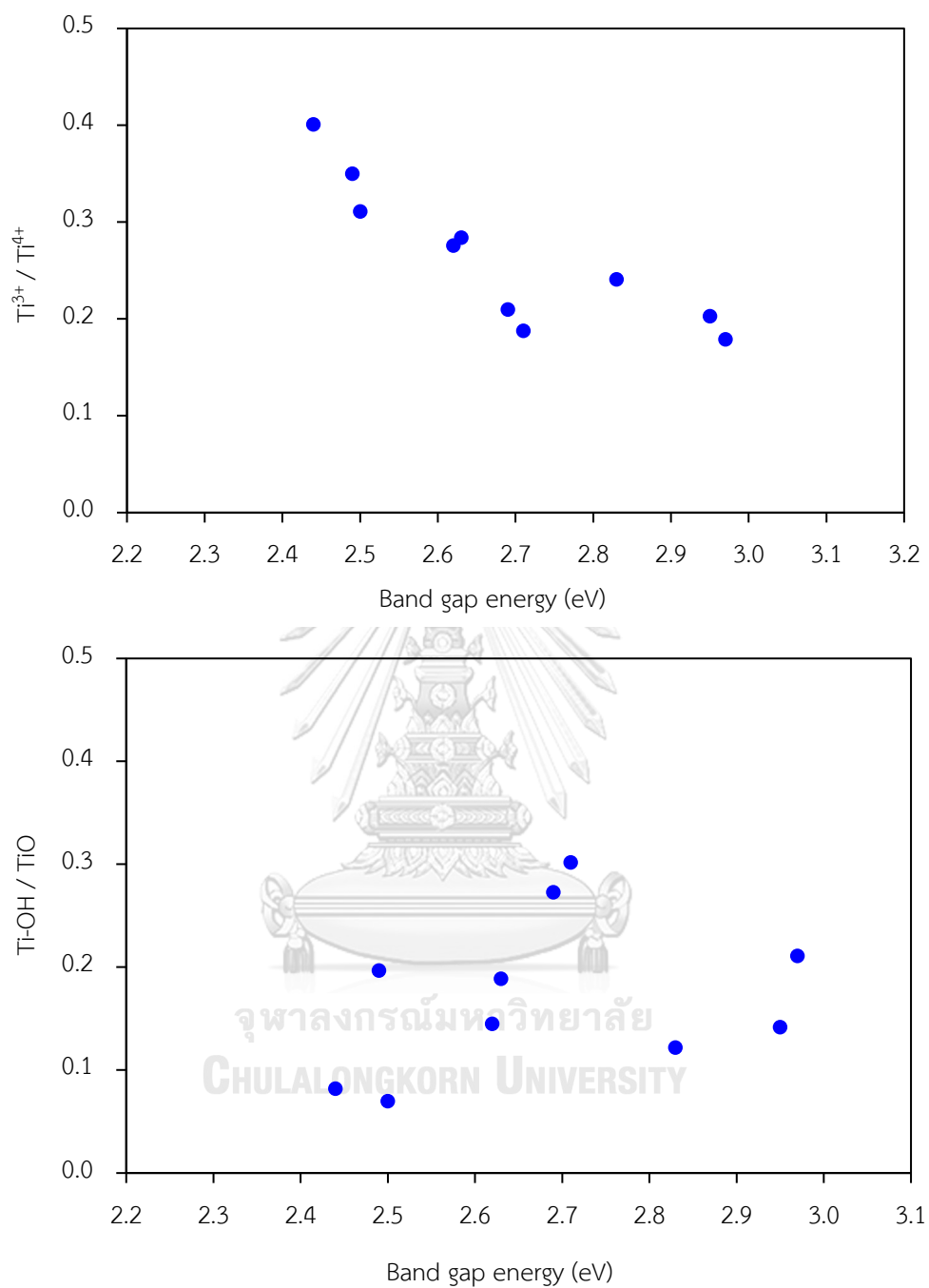


Figure 6.11 Alternation of the band gap energy of the as-prepared black TiO₂ NPs via (a) the Ti³⁺/Ti⁴⁺ and (b) Ti-OH/TiO ratios.

by photon excitation at wavelengths over the visible region, while the occupied electron in the O 2p state of the valence band can concurrently be excited to either the vacant sites of these Ti^{3+} defect isolated states or long-tailed conduction band by visible light illumination. Furthermore, the Ti^{3+} defect state can suppress the electron-hole recombination by acting as a trapping site for excited electrons from the conduction band due to the fact that it preferentially transfers electrons rather than transitions them back into the valence band to recombine with the photogenerated- h^+ [226]. Accordingly, the influence of the Ti^{3+} defective structure is a critical factor for the efficient visible light absorption and photogenerated charge transfer, which should enhance the electronic and photonic properties of TiO_2 NPs.

6.2.2 Effect of plasma discharge time

The effect of plasma discharge time on the morphology and optical property of black TiO_2 NPs was then explored in the range of 1-4 h in 3.0 mM HNO_3 solution medium at the repetition frequency of 20 kHz and pulse width of 2.0 μs . The samples prepared in this section were denoted as $\text{BT}_{\text{N-301}}$, $\text{BT}_{\text{N-302}}$, $\text{BT}_{\text{N-303}}$ and $\text{BT}_{\text{N-304}}$ for different plasma discharge time of 1, 2, 3 and 4 h, respectively.

6.2.2.1 Crystallite structure analysis

Regarding the effect of the plasma discharge time on the crystal structure of all as-synthesized black TiO_2 NPs, as demonstrated in Figure 6.12, all as-prepared samples still exhibited peaks of the both anatase and rutile phases or, in other words, they were in a mixed phase. As the plasma discharge time was prolonged, no shift of any diffraction peaks from the standard 2θ position was observed. However, their intensities were relatively poor, indicating the high formation of the defective structure inside the black TiO_2 NPs.

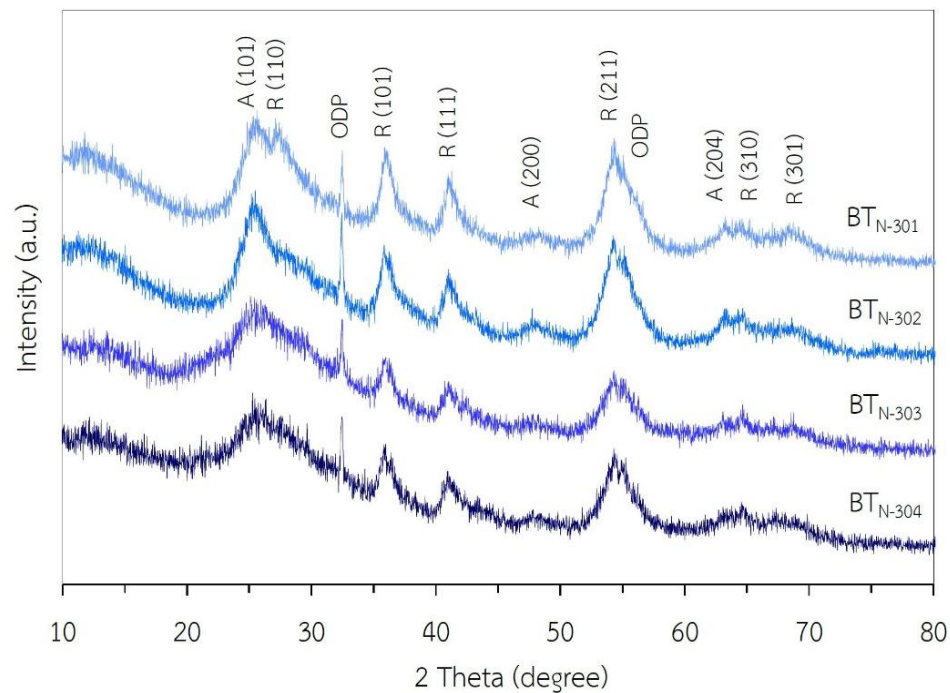


Figure 6.12 Representative XRD patterns of the as-synthesized black TiO_2 NPs through the solution plasma process at frequency of 20 kHz and pulse width of 2.0 μs at different plasma discharge times.

6.2.2.2 Morphology analysis

As demonstrated in Figure 6.13, most synthesized samples were still found to be spherical in shape, which was caused by the surface tension effect during the rapid ejection of generated particles from the plasma phase to the surrounded liquid phase. A long plasma discharge time induced the agglomeration and structural growth of the synthesized particles, leading to the generation of as-synthesized particles in the micrometer scale.

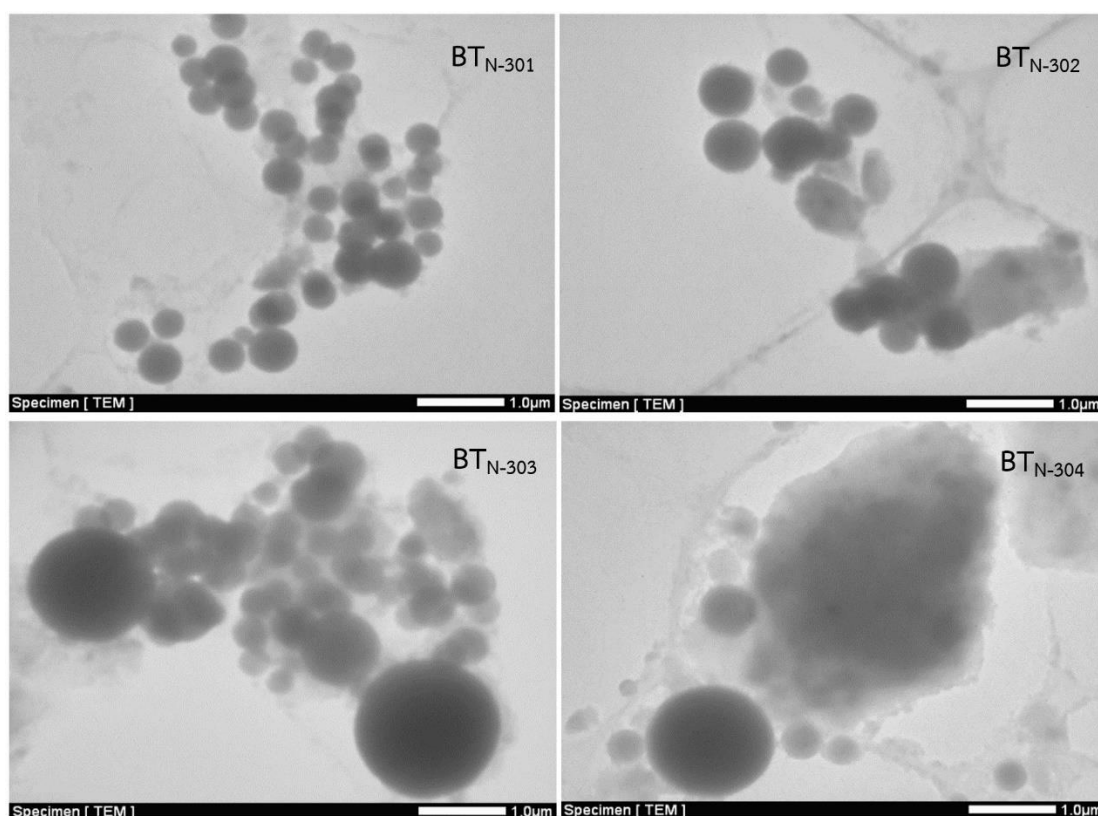


Figure 6.13 Representative TEM images of the as-synthesized black TiO_2 NPs through the solution plasma process at the frequency of 20 kHz and the pulse width of 2.0 μs at different plasma discharge times.

By using the DLS technique, as demonstrated in Figure 6.14, it was found that a short plasma discharge time provided a small particle size of the black TiO_2 NPs with a narrow distribution range. At a time equal to or greater than 2 h, the obtained particles were distributed into two ranges: a small size range and a big size range. The particle size of black TiO_2 in a big size range tended to increase with increasing the plasma discharge time. This was probably caused by an agglomeration and/or crystal growth of the previously formed black TiO_2 of small particle size to a larger particle size near the plasma-gas interface under the solution plasma process. In addition, a long plasma discharge time might cause a high roughness on electrode surface,

resulting in the formation of a big molten particle disengaging from the electrode surface. The mean volume diameter of all black TiO₂ particles synthesized at different plasma discharge times is summarized in Table 6.3.

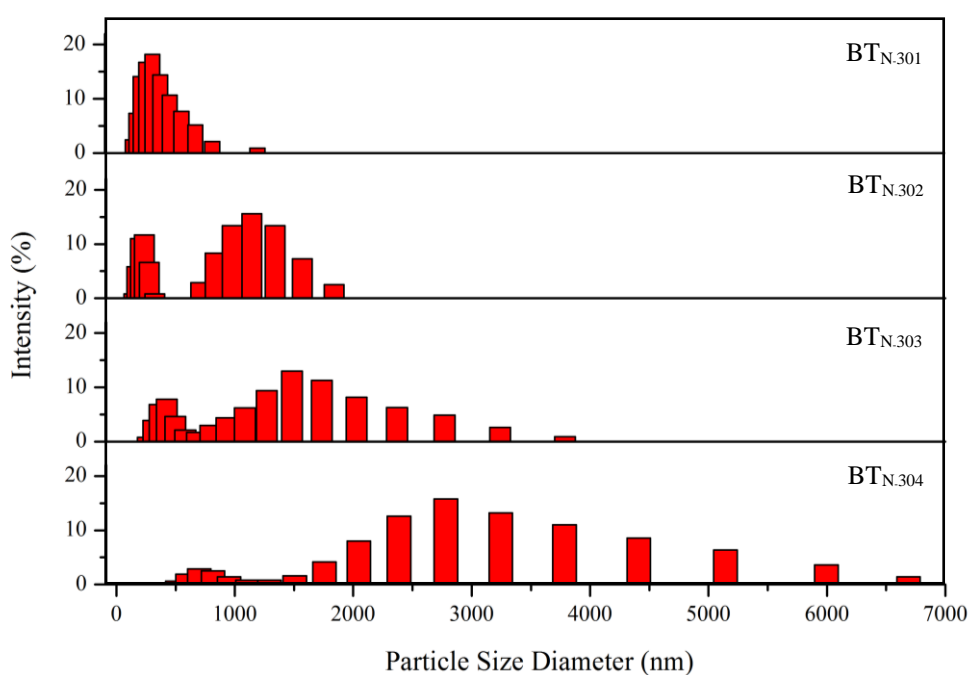


Figure 6.14 Particle size distribution from DLS technique of the as-synthesized black TiO₂ NPs through the solution plasma process at the frequency of 20 kHz and the pulse width of 2.0 μ s at different plasma discharge times.

Table 6.3 Structural information of the as-synthesized black TiO₂ NPs prepared with solution plasma in 3.0 mM HNO₃ at different plasma discharge times.

| Photo-catalyst | Mean volume diameter (nm) | Ti ³⁺ /Ti ⁴⁺ | E_g (eV) | Valence band maximum (eV) |
|---------------------|---------------------------|------------------------------------|------------|---------------------------|
| BT _{N-301} | 407 | 0.280 | 2.75 | 0.95 |
| BT _{N-302} | 926 | 0.321 | 2.63 | 0.80 |
| BT _{N-303} | 1,628 | 0.361 | 2.57 | 0.75 |
| BT _{N-304} | 3,219 | 0.411 | 2.44 | 0.60 |

6.2.2.3 Chemical structure analysis

The chemical nature and elemental binding of the Ti element of as-synthesized black TiO₂ NPs with different plasma discharge times were investigated by HR-XPS spectra in the Ti2p state. Two main peaks were observed at the binding energy of 458.7 eV and 464.4 eV, which indicated the presence of a Ti⁴⁺-O bond in the Ti 2p spectrum (Figure 6.15). After deconvolution, the Ti³⁺/Ti⁴⁺ ratio calculated from the area of the deconvoluted peaks was summarized in Table 6.3. This ratio tended to increase with the increase of the plasma discharge time, suggesting the formation of a high content of the Ti³⁺ defective structure.

6.2.2.4 Optical property analysis

The UV-Vis spectroscopy was also performed in order to examine the optical property of as-synthesized black TiO₂ with different plasma discharge times. As expected, all synthesized black TiO₂ NPs possessed an absorption response in the region of visible light (Figure 6.16). When the discharge plasma time was increased, the ability to absorb visible light also increased. From the Tauc's plot, the BT_{N-304} sample exhibited the lowest band gap energy of 2.44 eV while the BT_{N-301} sample had the highest band gap energy of 2.75 eV (Table 6.3).

To propose the density of states (DOS) of as-synthesized black TiO₂ NPs, the valence band (VB) position was estimated by an extrapolation of the main onset XPS peaks to intercept the x-axis baseline (Figure 6.17). The obtained values were 1.6, 1.5, 1.5 and 1.4 eV for BT_{N-301}, BT_{N-302}, BT_{N-303} and BT_{N-304}, respectively, below the Fermi energy level. The obtained schematic diagram of the DOS of all synthesized black TiO₂ NPs at different plasma discharge times is shown in Figure 6.18.

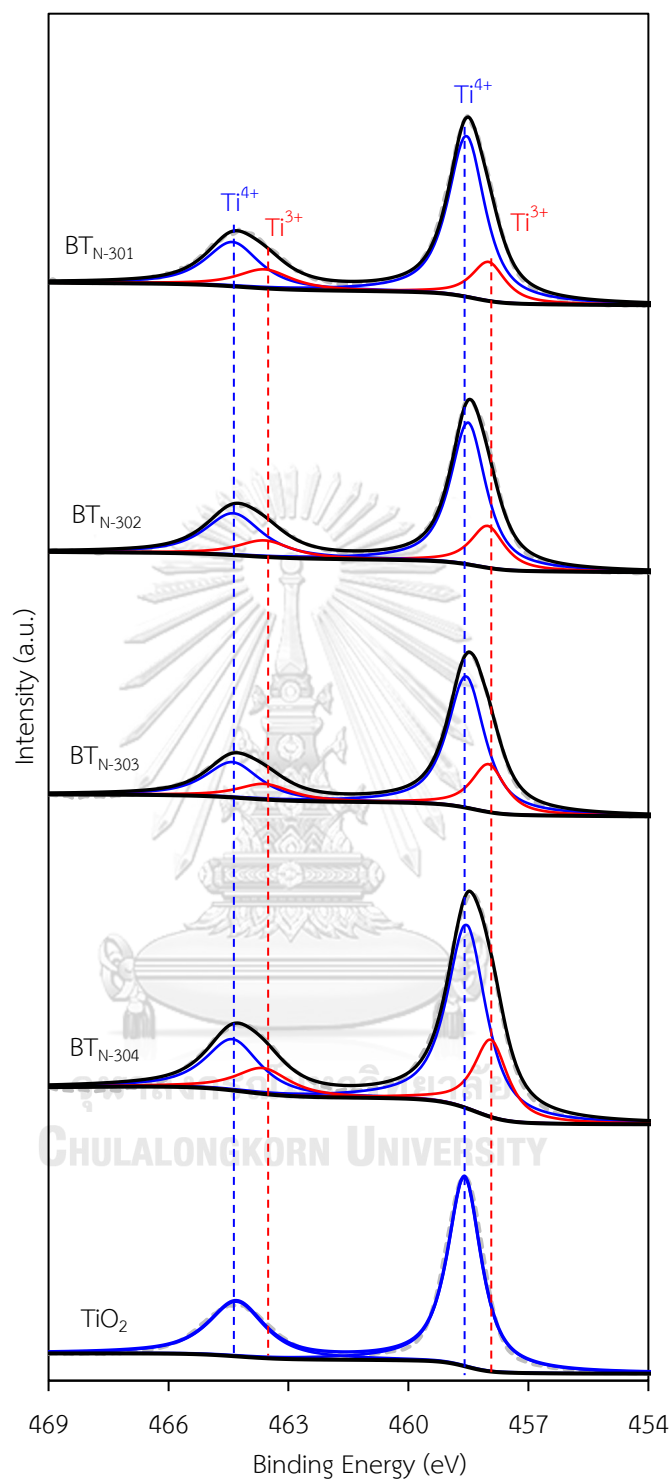


Figure 6.15 Representative deconvoluted peak area Ti₂p XPS spectra of the as-synthesized black TiO₂ NPs through the solution plasma process at the frequency of 20 kHz and the pulse width of 2.0 μ s at different plasma discharge times.

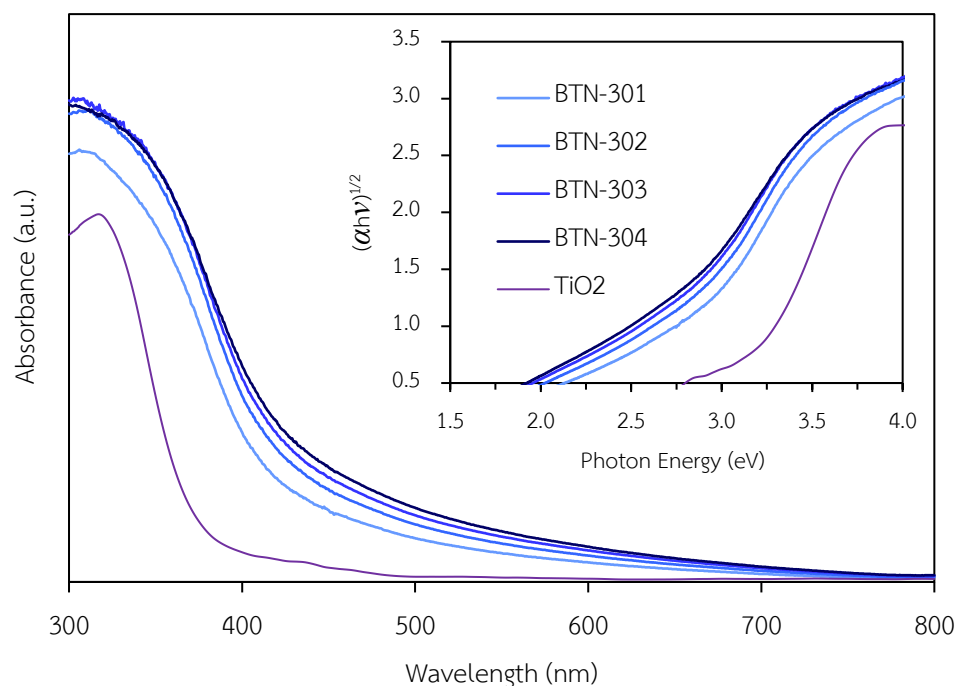


Figure 6.16 Representative UV-Vis spectra of the as-synthesized black TiO₂ NPs through the solution plasma process at the frequency of 20 kHz and the pulse width of 2.0 μs at different plasma discharge times.

Interestingly, the improvement of absorption properties toward the visible light region and narrowed band gap energy of all synthesized black TiO₂ NPs should be caused by the localized band bending by the shift of the valence band maximum toward the Fermi energy level. In addition, the rising conduction band (CB) tail, which extended below the CB minimum, might be attributed to the loss of lattice periodicity from the disorder structure of TiO₂ and break in the octahedral symmetry of TiO₆ [227, 228]. The localized band bending of the valence band by 0.65 eV was observed for the BT_{N-301} sample, resulting in the position of valence band maximum of around 0.95 eV while the shift was enlarged by 0.7-0.8 eV for the BT_{N-302}, BT_{N-303} and BT_{N-304}, resulting in the narrowing of its band gap energy. This is due to the greater formation of a Ti³⁺ defect structure which is analogous with the Ti³⁺ defect concentration from the

previous finding in the XPS spectra. Therefore, the large blue shift of valence band maximum in the presence of long plasma discharge time, induced by the Ti^{3+} disorder structure, can be postulated as responsible for the narrowed band gap by the alteration of orbital overlapping and extension of the continuum band tail structure.

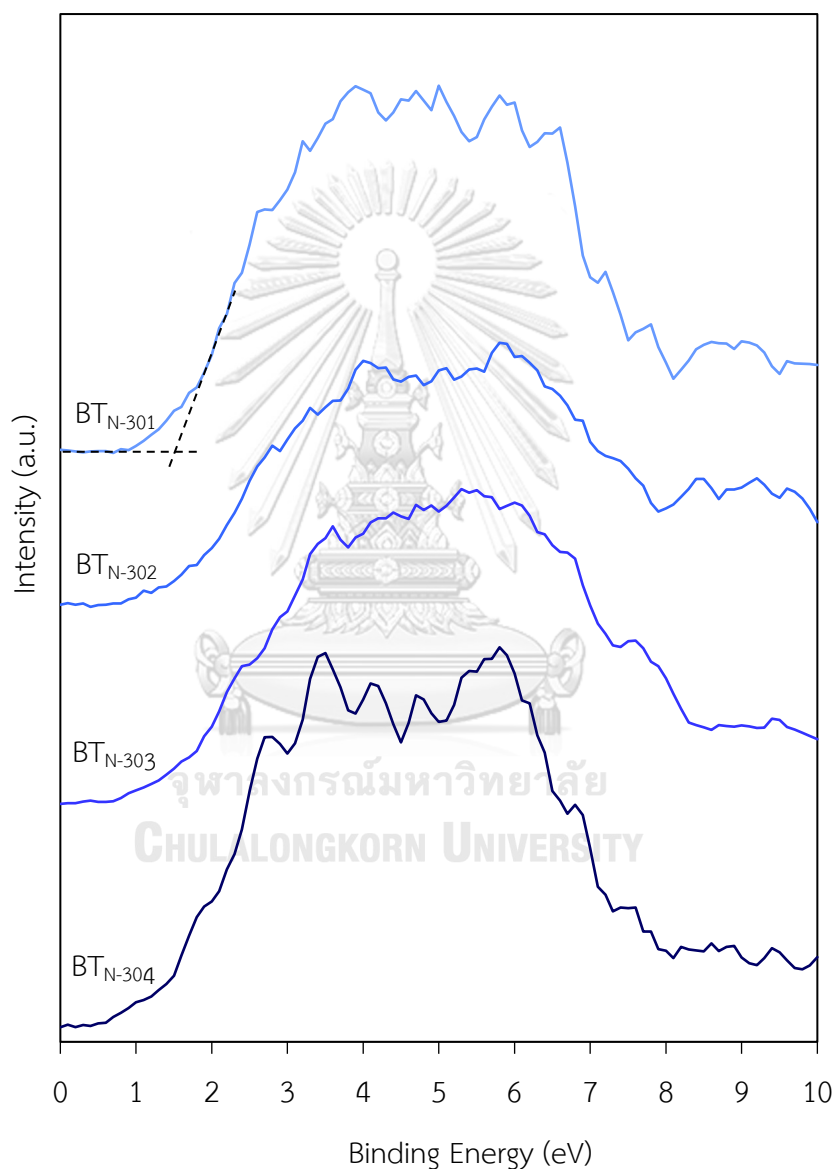


Figure 6.17 Representative valence band spectra of the as-synthesized black TiO_2 NPs through the solution plasma process at the frequency of 20 kHz and the pulse width of 2.0 μs at different plasma discharge times.

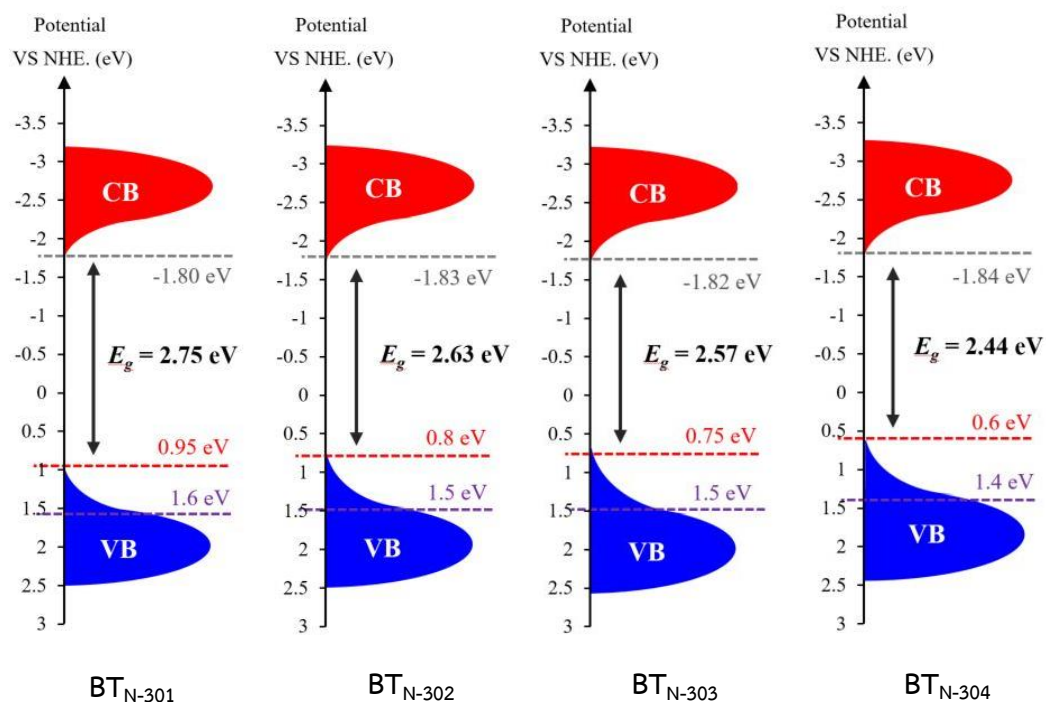


Figure 6.18 Schematic diagram of DOS of the as-synthesized black TiO₂ NPs through the solution plasma process at the frequency of 20 kHz and the pulse width of 2.0 μ s at different plasma discharge times.

6.3 Photocatalytic activity of as-synthesized black TiO₂ NPs

The photocatalytic activity was finally evaluated via the conversion of glycerol at a catalyst loading of 3.0 g/L and a light intensity of 4.7 mW/cm² and irradiation time of 24 h with the as-synthesized black TiO₂ NPs that synthesized through the solution plasma process at the frequency of 20 kHz and the pulse width of 2.0 μ s with different plasma discharge times under 3.0 mM of HNO₃ solution and compared with the commercial anatase TiO₂. Only as-synthesized black TiO₂ with different plasma discharge times was selected as a photocatalyst model to perform the activity test because it covers all of various band gap energy and defect structure concentration that might be effect on the photocatalytic activity.

As demonstrated in Figure 6.19, the highest glycerol conversion was observed in the presence of black TiO₂ formed from the longest plasma discharge time (4 h), being photocatalyzed in the order BT_{N-304} > BT_{N-303} > BT_{N-302} > BT_{N-301} > TiO₂ with a pseudo first-order rate constant of 7.94 × 10⁻³, 7.01 × 10⁻³, 6.19 × 10⁻³, 5.36 × 10⁻³ and 3.58 × 10⁻³ min⁻¹, respectively. This indicated that the BT_{N-304} had the highest photocatalytic activity for glycerol conversion compared with other as-synthesized black TiO₂ and commercial anatase TiO₂, although it had larger particle size than other black TiO₂. This is because the BT_{N-304} had the highest Ti³⁺ concentration and the lowest E_g , and so could create a mid-gap state level with an energy somewhat lower than the minimum CB, existing in the form of [O_vTi³⁺]⁺, which can prolong the life time of photogenerated e⁻-h⁺ pairs, resulting in the amelioration of photocatalytic performance [229]. Moreover, these defect sites can serve as the surface-absorbed site of the glycerol molecules to absorb oxygen, which can facilitate the kinetic chemical reaction [230]. In addition, the agglomerated TiO₂ NPs can extend the e⁻ - h⁺ life due to the interparticle charge transport [231]. In summary, a high photocatalytic activity of the BT_{N-304} compared with other TiO₂ was attributed to its high defective structure, low E_g and long e⁻ - h⁺ lifetime.

To confirm the photocatalytic oxidation of glycerol via the BT_{N-304}, the additional experiments were carried out with (i) BT_{N-304} in the absence of light and (ii) with light in the absence of catalyst. As also demonstrated in Figure 6.19, less than 4.5 % of glycerol were disappeared at 24 h via the BT_{N-304} in the absence of light, attributing to the adsorption of glycerol on the black TiO₂ surface. However, no glycerol was disappeared in the presence of light and absence of catalyst, suggesting that the photolysis cannot enhance the conversion of glycerol to value-added compounds.

As shown in Figure 6.20, similar compounds, including GCD, DHA, HPA, GCOA, FMD and glycolaldehyde (GCAD), were generated via the photocatalytic oxidation with

the black TiO₂ prepared at different reaction time and the GCAD and FMD were the principle generated products. A high yield of all selected products was observed as the order of BT_{N-304} > BT_{N-303} > BT_{N-302} > BT_{N-301}.

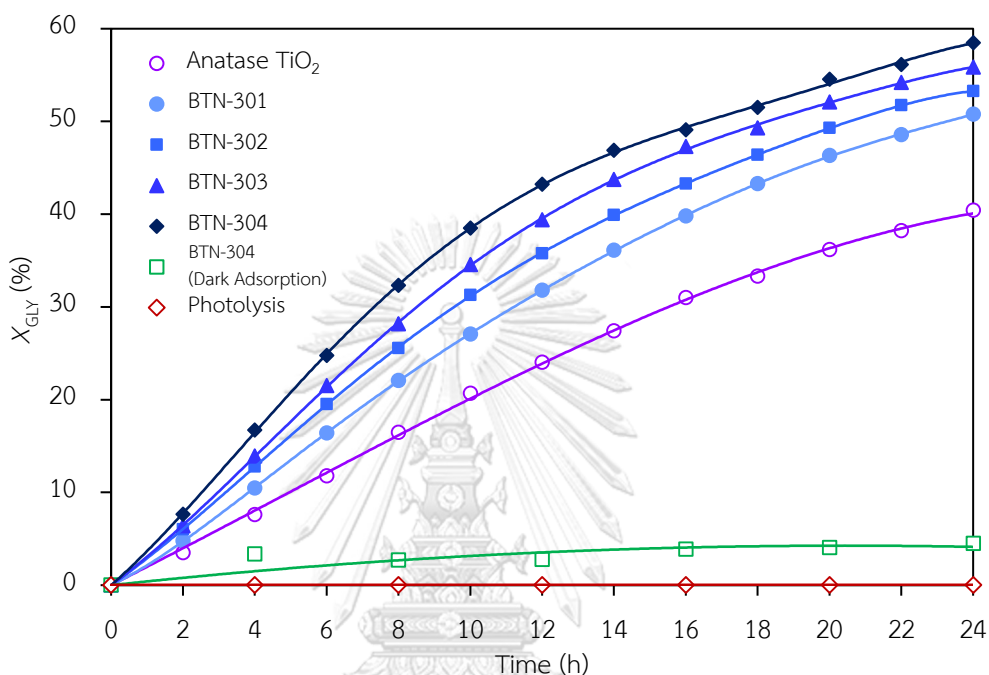


Figure 6.19 Variation of glycerol conversion as a function of time via as-synthesized black TiO₂ NPs under the irradiated UV light at catalyst loading of 3.0 g/L with an average light intensity of 4.7 mW/cm² and using O₂ as the electron acceptor.

As mentioned in previous chapter, photocatalytic oxidation of glycerol via TiO₂ occurred mainly at the 1°-OH groups to form GCD as the principle product and partially occurred at the 2°-OH group to form DHA. The generated GCD can be further oxidized with hydroxyl radicals (HO•) to form GCOA and FMD, while the DHA was further oxidized with the oxygen species (O₂^{•-} / ¹O₂) to form HPA. The yield of FMD was around 10% at a reaction time of 20 h and no GCAD was generated. However, with the BT_{N-304} photocatalyst, approximately 21% and 33% of FMD and GCAD were produced at the same time. This suggested the probable presence of another parallel glycerol

conversion route to form FMD and GCAD. As reported by Minero et al. [232], glycerol can be converted to FMD and GCAD by C-C bond cleavage via the direct electron transfer route on the defective TiO₂ (P25) pristine. In addition, two generated FMD molecules can easily be adsorbed on two neighboring Ti³⁺ defective sites and dimerized to form GCAD [233].

These phenomena likely then considerably promoted the formation of GCAD as the main product in our system. Thus, it can be hypothesized that the major reaction pathway for glycerol conversion on these as-synthesized black TiO₂ catalysts was C-C bond cleavage to produce FMD and GCAD, while the minor pathway is the oxidation of primary and/or secondary hydroxyl groups of glycerol molecules to form GCD and DHA. In addition, we also hypothesized that the different observed types of product might be depended on the nature of the oxidizing species involved in the glycerol oxidation mechanism. This hypothesis was proved and discussed in the next section.

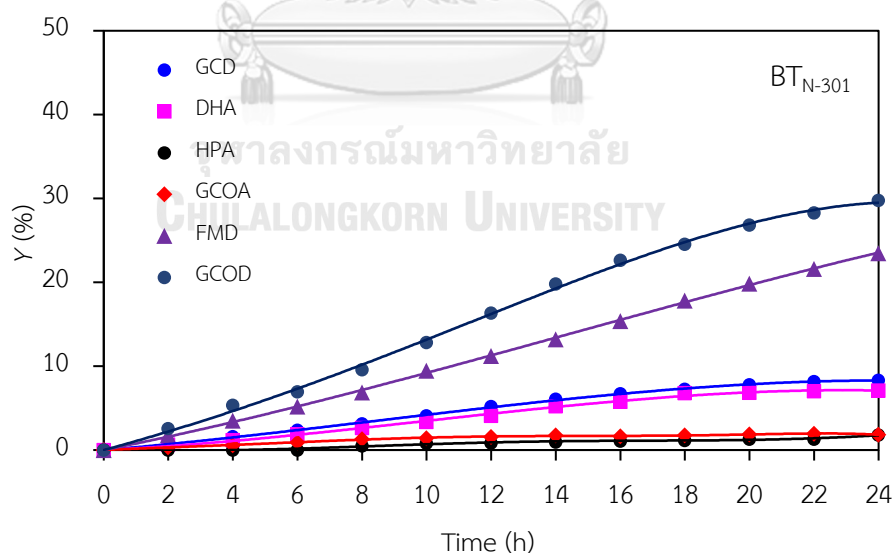


Figure 6.20 Yield of selected products obtained from glycerol photocatalytic conversion via as-synthesized black TiO₂ NPs at catalyst loading of 3.0 g/L with an average light intensity of 4.7 mW/cm² and using O₂ as the electron acceptor.

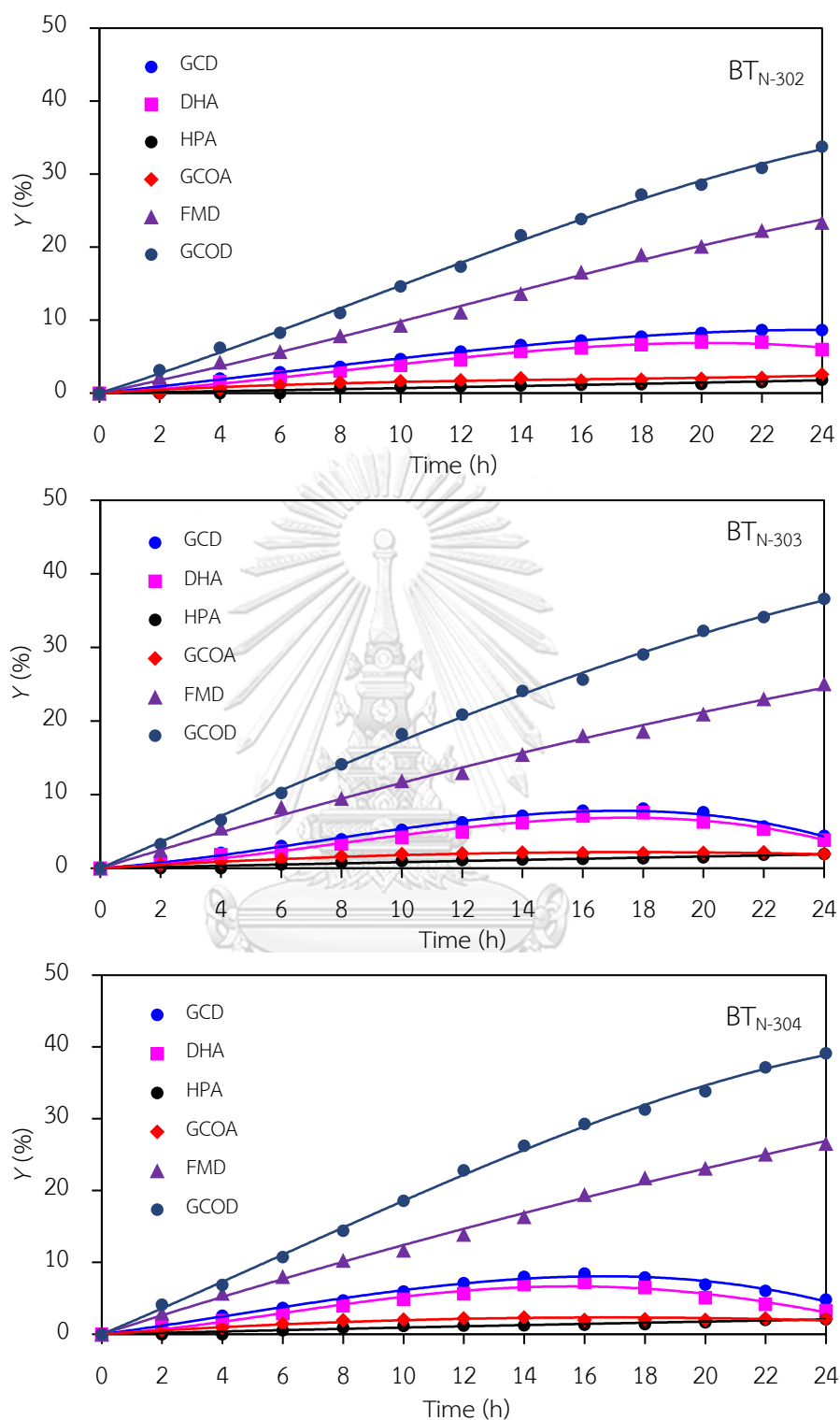


Figure 6.20 Yield of selected products obtained from glycerol photocatalytic conversion via as-synthesized black TiO₂ NPs at catalyst loading of 3.0 g/L with an average light intensity of 4.7 mW/cm² and using O₂ as the electron acceptor (Cont.).

6.4 Mechanism and role of generated ROS in the photooxidation of glycerol by using black TiO₂

As mentioned earlier, the photocatalytic oxidation of glycerol via commercial TiO₂ occurred mainly at the 1°-OH groups to form GCD as the principle product and also partially occurred at the 2°-OH group to form DHA. The generated GCD can then be further oxidized with the generated ROS to form FMD and GCOA [234, 235]. To confirm the exact chemical species generated from GCD and DHA conversion, both chemical species were used as the raw substrate and subjected to the photocatalyst oxidation with black TiO₂ (3.0 g/L) at a light intensity of 4.7 mW/cm² and O₂ as the electron acceptor. The photocatalytic oxidation of GCD provided GCAD as the main product with a trace of DHA and GCOA (Figure 6.21). A large amount of FMD was produced after an 8 h reaction time. With DHA as the substrate, the principle generated products were FMD and GCAD plus a trace of GCD and GCOA.

Although both GCD and DHA have the same molecular formula (C₃H₆O₃) with two hydroxide groups (-OH) and one carbonyl group (C=O) in their structure, they provided different amounts of generated FMD and GCAD via the photooxidation reaction. This is probably due to the different position of the carbonyl group (C=O) in the GCD and DHA structure, which altered the adsorption characteristics of carbonyl group of these molecules onto the surface defect structure, promoting different dissociative over molecular adsorption. That is, the GCD has the carbonyl group at the 1°-C atom and the C-C cleavage could provide one molecule of FMD and one molecule of GCAD. In case of DHA, with the carbonyl group at the 2°-C atom, the C-C cleavage could induce the formation of two molecules of FMD and one molecule of CO. The diminishing level of FMD at a reaction time greater than 8 h in the presence of DHA as the substrate is probably due to it being converted to other chemical species, such as formic acid (HCOOH) or carbon dioxide (CO₂) [236, 237]. As already

mentioned, glycerol can be converted directly to GCAD and FMD by C-C bond cleavage via a direct electron transfer route on the defective TiO₂ (P25) pristine [232]. Two generated FMD molecules can easily be adsorbed on two neighboring Ti³⁺ defective sites and dimerized to form GCAD [233]. These phenomena likely then considerably promoted the formation of GCAD as the main product in our system.

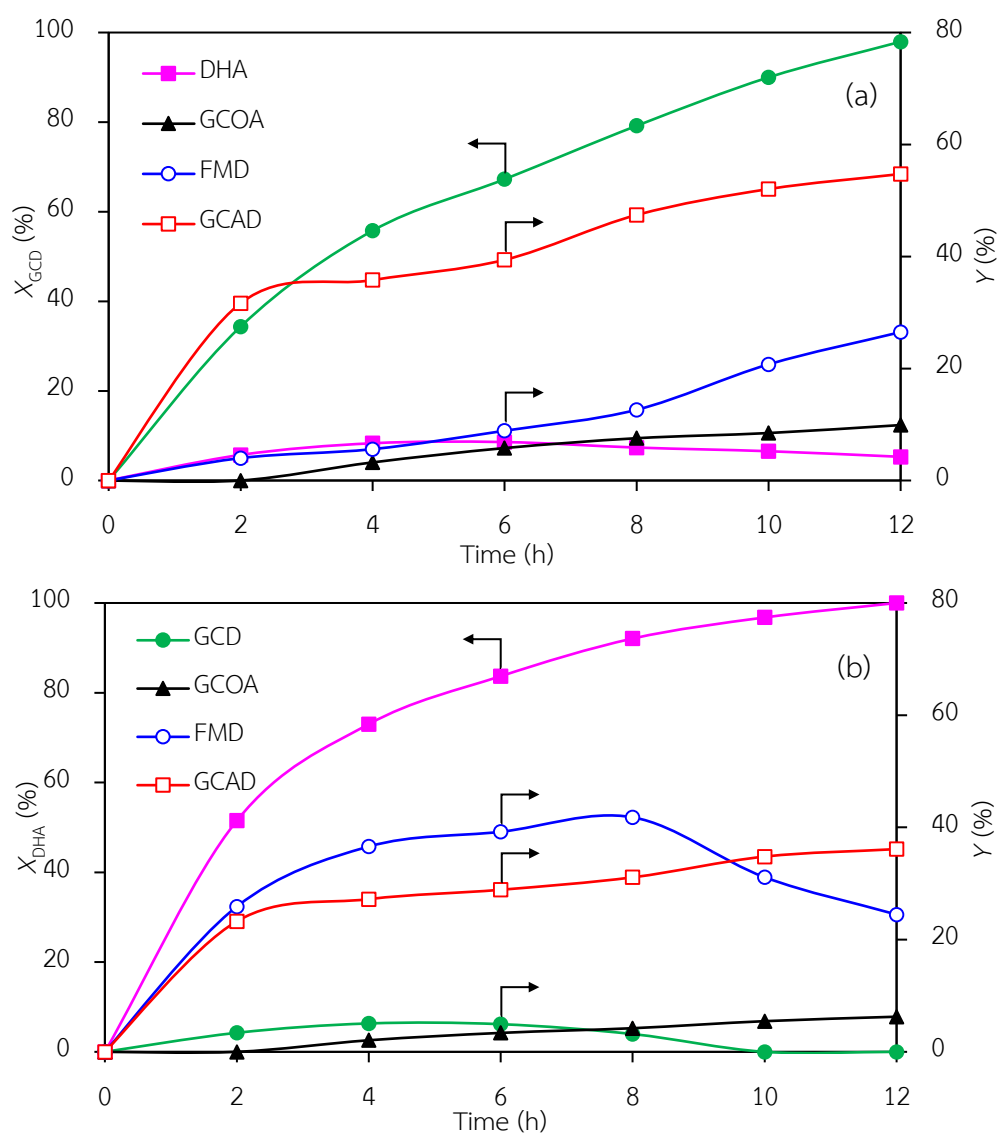


Figure 6.21 Variation conversion levels of (a) GCD and (b) DHA and selected product yield obtained with the black TiO₂ photocatalyst at 3.0 g/L, a light intensity of 4.7 mW/cm² using O₂ as the electron acceptor.

As reported previously, the ROS generated via the photocatalytic process can act as the oxidizing species to oxidize organic compounds effectively, including glycerol. To explore in-depth the photocatalytic mechanism, the dominate active species related in the step of glycerol conversion to the different products were explored by the separate addition of AO, KI, IPA, FFA and BQ in order to trap the photogenerated h^+ , photogenerated h^+ and surface hydroxyl radicals (h^+ / OH^{\bullet}_b), bulk hydroxyl radicals (OH^{\bullet}_b), singlet oxygen (1O_2) and generated superoxide radicals ($O_2^{\bullet-}$), respectively, [238-241].

As exhibited in Figure 6.22(a), the glycerol conversion was not significantly changed in the presence of AO, suggesting that the h^+ was not an essential species for glycerol conversion. However, the glycerol conversion was inhibited by the addition of KI, IPA, FFA and BQ, decreasing it from 32.8% without any inhibitor to 27.8%, 18.8%, 14.0% and 10.6%, respectively, while the rate constant of glycerol conversion was decreased from 0.0504 min^{-1} to 0.0459, 0.0260, 0.0189 and 0.0140 min^{-1} , respectively (Inset of Figure 6.22(a)). This indicated that h^+ / OH^{\bullet}_s , OH^{\bullet}_b , 1O_2 and $O_2^{\bullet-}$ were the important ROS for glycerol conversion, and were ranked in the order of $O_2^{\bullet-} > ^1O_2 > OH^{\bullet}_b > h^+ / OH^{\bullet}_s$. The main reason that $O_2^{\bullet-}$ is the major ROS in the photocatalytic oxidation of glycerol catalyzed by black TiO_2 can be described as follows. During the photocatalytic process, the adsorption of dissolved O_2 molecule on the surface of TiO_2 is a prevailing key step in the reaction [225]. As revealed previously [242], O_2 does not adsorb on the perfectly neutral TiO_2 surface, but only on the TiO_2 surface when a negative charge is available to form O-Ti bonds. This can be provided by a surface-oxygen vacancy, in which the adsorption energy is -2.52 eV [243]. Thus, the presence of the defective structure on the surface of black TiO_2 could promote the adsorption of O_2 , which can then enable the capturing of photogenerated electrons as well as the free electrons located on oxygen vacancy state, simultaneously generating a huge

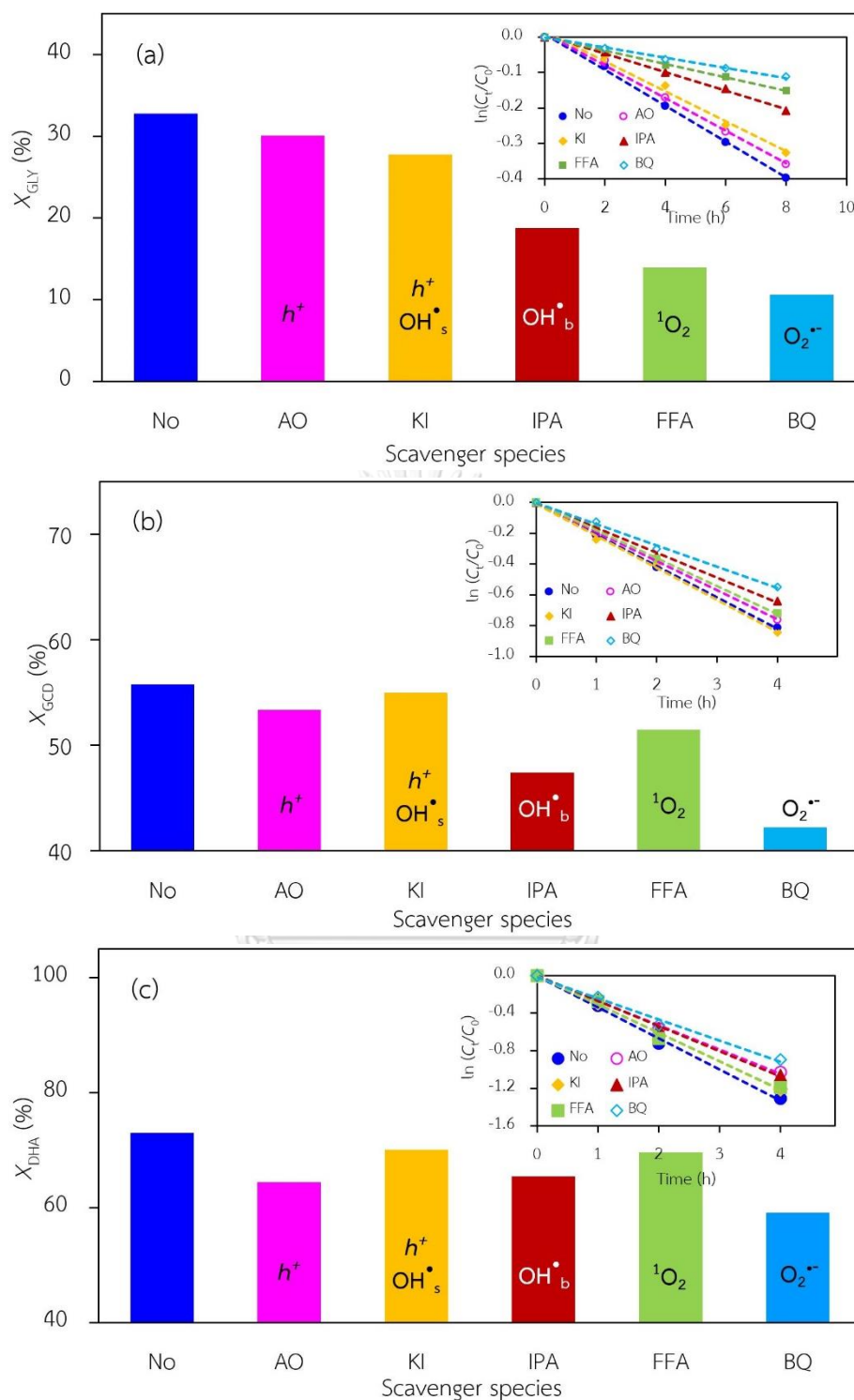
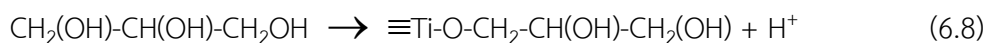


Figure 6.22 Representative conversion levels of (a) glycerol, (b) GCD and (c) DHA in the presence of various scavenger species (10 mM) with the black TiO_2 photocatalyst at 3.0 g/L, light intensity of 4.7 mW/cm^2 , and using O_2 as the electron acceptor.

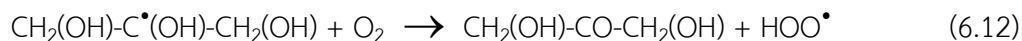
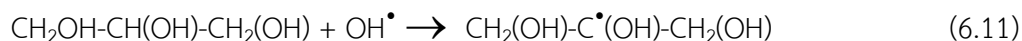
amount of $O_2^{\bullet-}$. The superior generation of this ROS then actively promotes the charge separation process as well as the oxidation of glycerol molecules. Therefore, it becomes the main ROS in the defected black TiO_2 system.

With regard to the yield of the main generated products (Figure 6.23), in the absence of scavengers, their yields gradually increased with increasing reaction time in the ranked order of $GCAD > FMD > GCD > DHA$. In the presence of AO, the yields of all monitored products were not changed significantly, indicating that the h^+ was not the principal ROS converting glycerol to all the main compounds, in accordance with the results displayed in Figure 6.22. The yield of GCD decreased from 0.59% to 0.00, 0.17 and 0.50% after 1 h in the presence of BQ, FFA and IPA, respectively. Principally, 1O_2 is the oxidative product of the $O_2^{\bullet-}$ species. Thus, the addition of BQ in the system to trap the $O_2^{\bullet-}$ species can terminate the generation of both $O_2^{\bullet-}$ and 1O_2 species. However, from Figure 6.23(f), no GCD was generated at an early reaction time in the presence of BQ, while it was generated in the presence of FFA (Figure 6.23(e)), suggesting that the conversion of glycerol to GCD was more dependent upon the presence of $O_2^{\bullet-}$ than on 1O_2 . In other words, the dominate ROS for glycerol conversion to GCD was ranked as $O_2^{\bullet-} > ^1O_2 > OH^{\bullet}_b$. The reaction mechanism of glycerol conversion to GCD via the $O_2^{\bullet-}$ can then be written as in Eqs. (6.8)-(6.10).

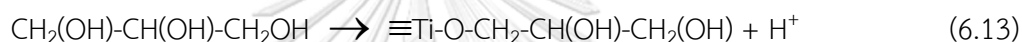


For DHA, its low yield was more pronounced in the presence of KI and IPA by decreasing the DHA yield from 0.49% to 0.00% (Figure 6.23(c)) and 0.21% (Figure 6.23(d)) after 1 h, respectively. This suggested that the h^+ / OH^{\bullet}_s and OH^{\bullet}_b were the principle species to convert glycerol to DHA. However, as shown in Figure 6.23(b), h^+

was not the main oxidizing species to convert glycerol. Thus, it can be concluded that the OH^\bullet was the dominate active species for glycerol conversion to DHA, as shown in Eqs. (6.11) and (6.12).



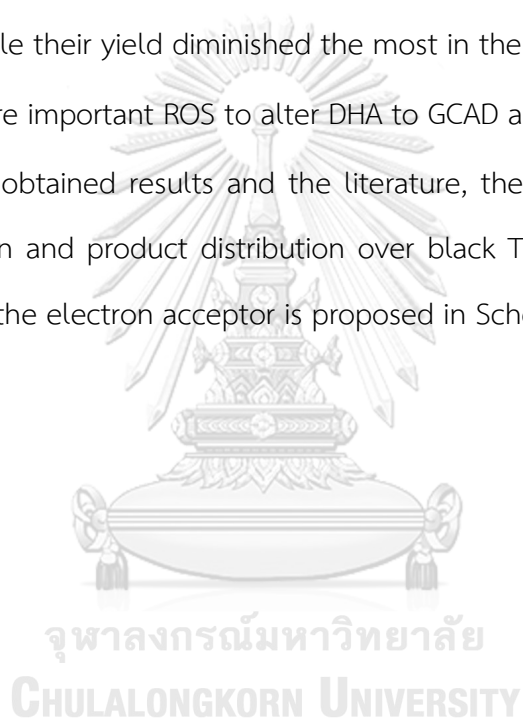
In the case of GCAD, no apparent yield was observed following the addition of IPA after a 1 h reaction time (Figure 6.23(d)), suggesting that the OH_b^\bullet species was the dominant active species to transform glycerol directly to GCAD, and the reaction mechanism is shown in Eqs. (6.13)–(6.16):



To further find out the dominate species that effectively convert the intermediates GCD and DHA, the parallel photocatalytic experiments were performed using GCD or DHA as the initial substrate instead of glycerol, a black TiO_2 loading level of 3.0 g/L, light intensity of 4.7 mW/cm^2 , using O_2 as the electron acceptor and a reaction time of 4 h in the presence of the respective scavenger species. As demonstrated in Figure 6.22(b), the GCD conversion level decreased in the presence of IPA, FFA and BQ, suggesting that OH_b^\bullet , $^1\text{O}_2$ and O_2^\bullet were the important ROS to convert GCD, and were ranked as $\text{O}_2^\bullet > \text{OH}_b^\bullet > ^1\text{O}_2$. As to the product yields, as demonstrated in Figure 6.24(a), GCAD was the principle product of GCD conversion in the absence of any chemical scavengers (36.7%), and this was decreased the most in the presence of BQ (26.4%) and IPA (33.2%), indicating that the O_2^\bullet and OH_b^\bullet were the dominate ROS to convert GCD to GCAD. In the presence of the h^+ scavenger AO (Figure

6.24(b)), the yield of GCAD was still the same as in its absence, but no GCOA was produced, suggesting that h^+ was the dominate ROS to convert GCD to GCOA.

In the case of DHA, its conversion diminished in the presence of AO, IPA and BQ (Figure 6.22(c)), indicating the h^+ , OH^{\bullet}_b and $\text{O}_2^{\bullet-}$ were essential ROS for DHA conversion, and were ranked in the order of $\text{O}_2^{\bullet-} > \text{OH}^{\bullet}_b \geq h^+$. In terms of the product yield, both GCAD and FMD were the main generated products from DHA conversion in the absence of scavengers (Figure 6.25). Their yield decreased slightly in the presence of IPA and AO, while their yield diminished the most in the presence of BQ, indicating the $\text{O}_2^{\bullet-}$ was a more important ROS to alter DHA to GCAD and FMD than the OH^{\bullet}_b and h^+ . According the obtained results and the literature, the reaction pathway for the glycerol conversion and product distribution over black TiO_2 via various ROS in the presence of O_2 as the electron acceptor is proposed in Scheme 4.



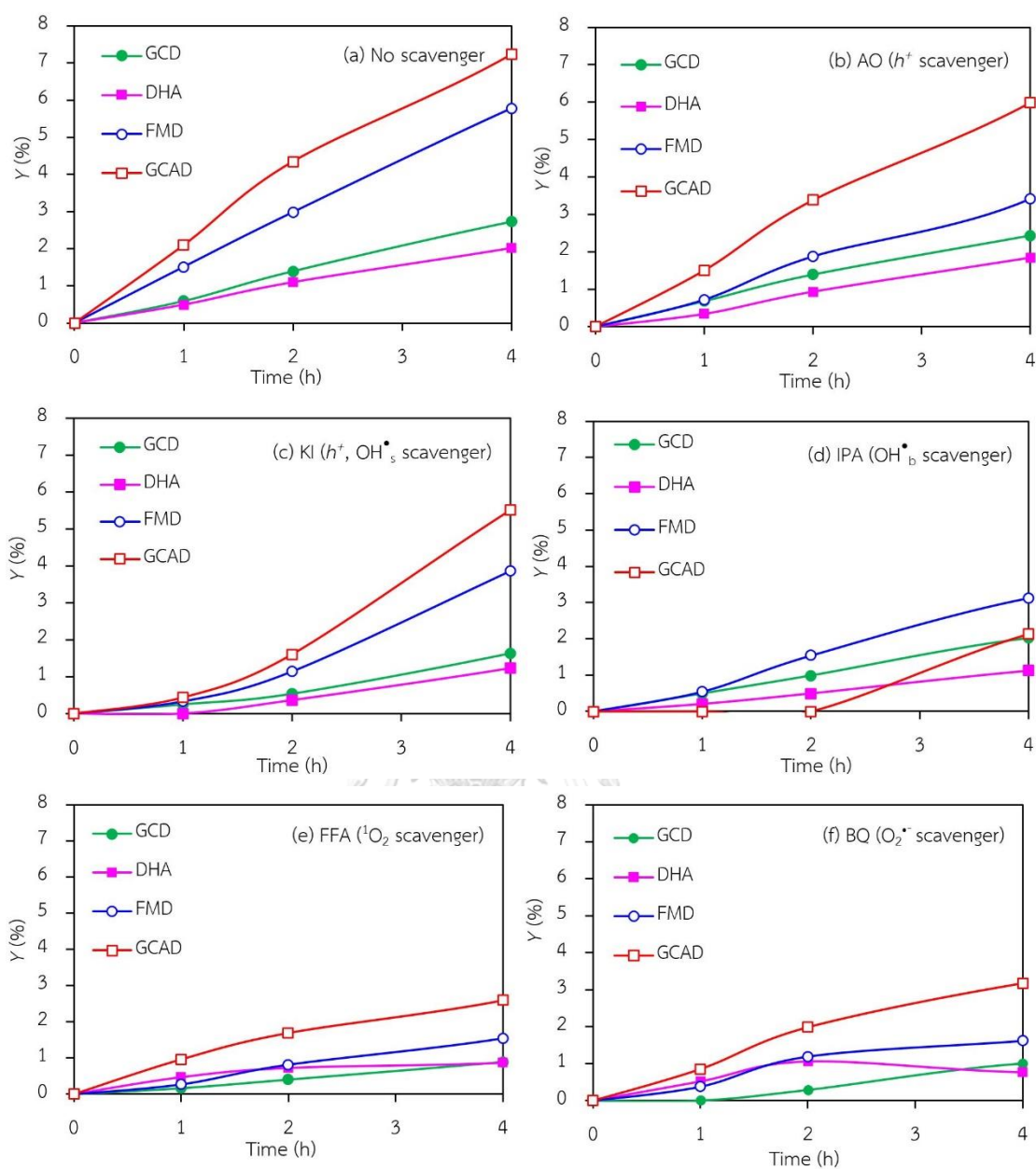


Figure 6.23 Yield of selected products obtained from glycerol photocatalytic conversion in the presence of various scavengers via black TiO_2 NPs at loading of 3.0 g/L with light intensity of 4.7 mW/cm^2 and using O_2 as the electron acceptor.

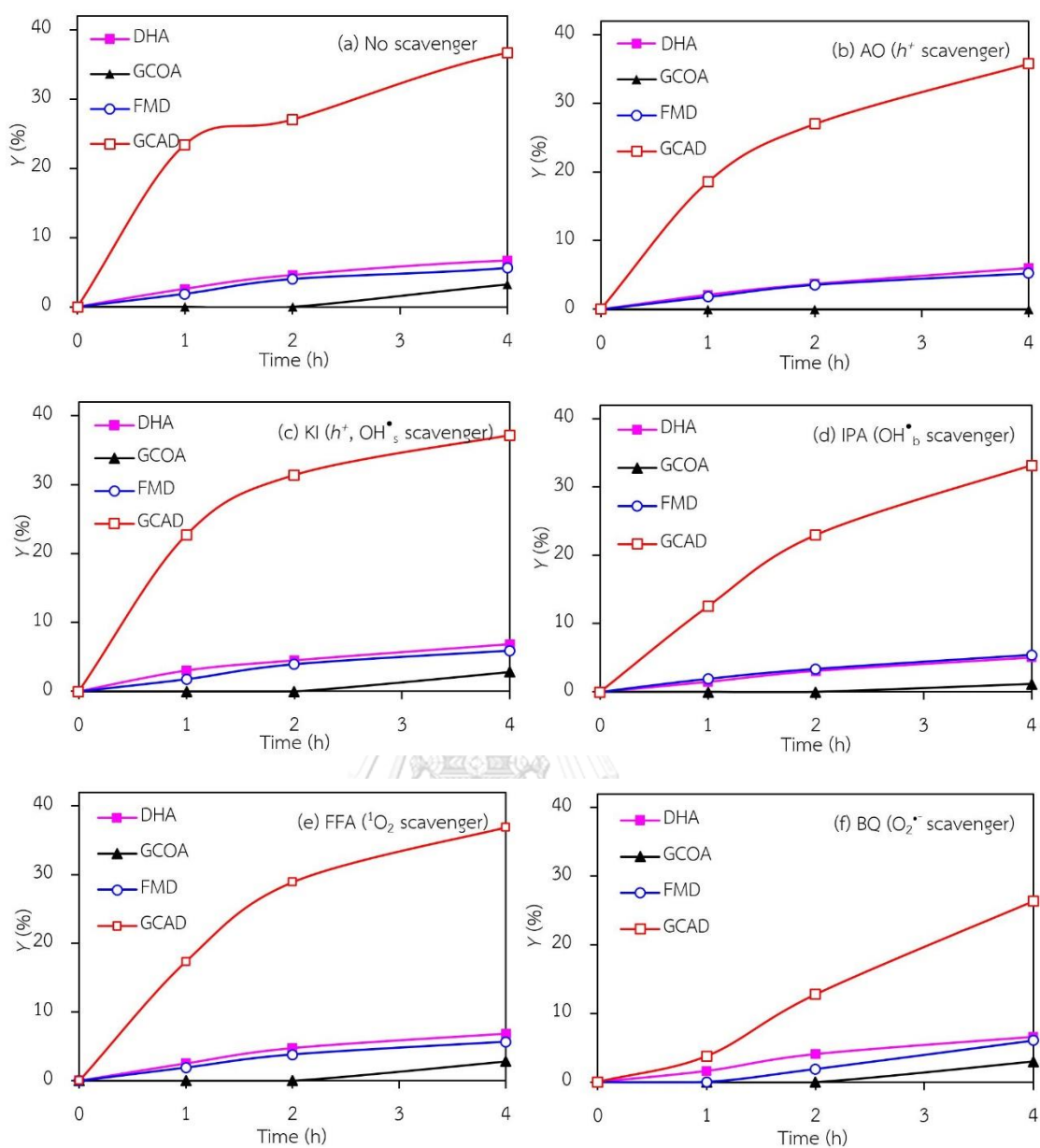


Figure 6.24 Yield of selected products obtained from GCD photocatalytic conversion in the presence of various scavengers via black TiO₂ NPs at loading of 3.0 g/L with light intensity of 4.7 mW/cm² and using O₂ as the electron acceptor.

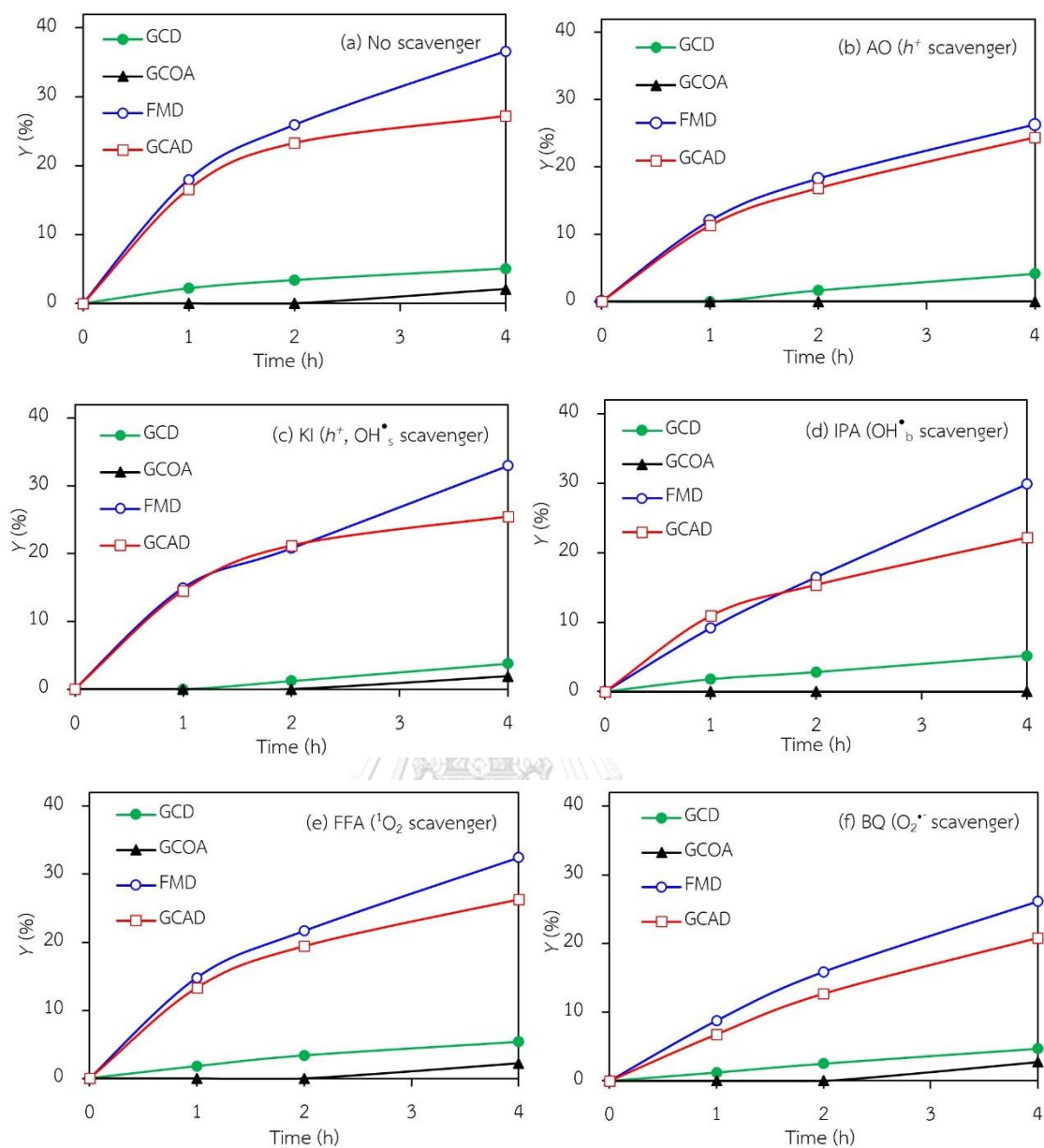
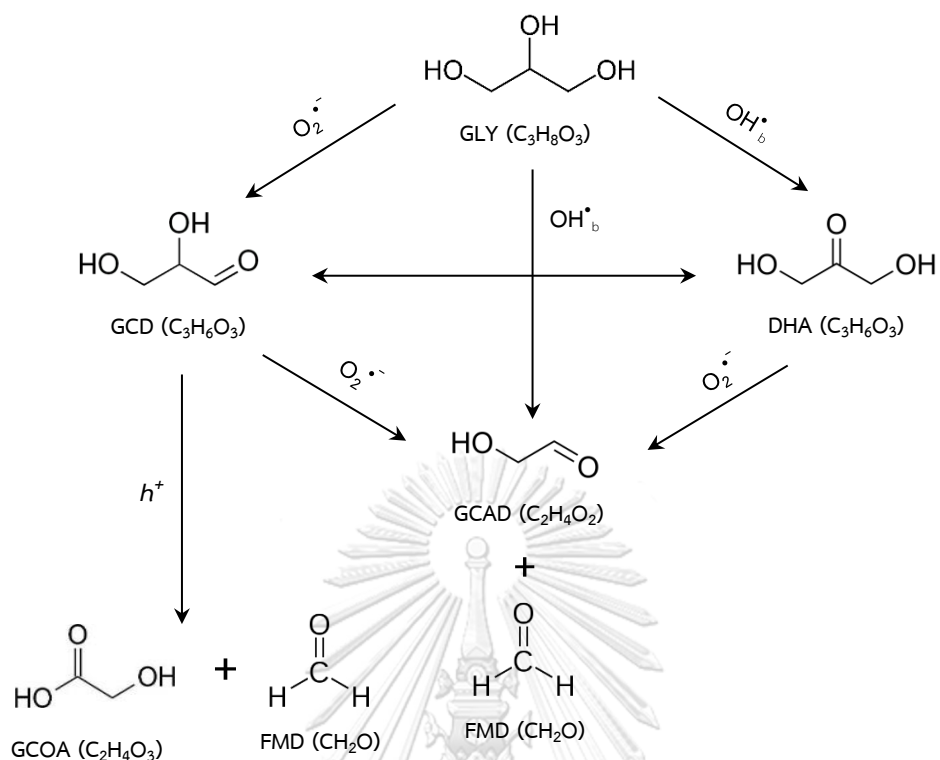


Figure 6.25 Yield of selected products obtained from DHA photocatalytic conversion in the presence of various scavengers via black TiO_2 NPs at loading of 3.0 g/L with light intensity of 4.7 mW/cm^2 and using O_2 as the electron acceptor.



Scheme 4. Proposed reaction pathways with involving ROS for glycerol conversion and product distribution via black TiO_2 NPs-induced photocatalytic oxidation in the presence of O_2 as electron acceptors.

CHAPTER VII

CONCLUSIONS AND RECOMMENDATIONS

7.1 Conclusions

This work was carried out to investigate the effect of several operating parameters for the conversion of glycerol to value-added compounds via photocatalytic process with TiO₂-based photocatalyst. According to all obtained results, the conclusions can be highlighted as the following.

7.1.1 Commercial TiO₂-induced photocatalytic oxidation of glycerol to value-added compounds

In this part, the photocatalytic conversion of glycerol to value-added compounds in liquid phase system was carried out by using the commercial TiO₂ photocatalyst. The commercial TiO₂ in pure anatase phase structure exhibited the higher photocatalytic activity than commercial TiO₂ in pure rutile and mixture of anatase-rutile phase structure. Moreover, the effect of operating parameters, including light intensity, catalyst dosage, irradiation time, and types of electron acceptor was successfully explored. The types of generated value-added products in liquid phase were GCD, DHA, GCA, GCOA, HPA, FMA and FMD. The most important parameter that affected the glycerol conversion and product selectivity was the irradiation time, which had a positive effect on glycerol conversion and selectivity of GCA and GCOA, while having a negative effect on the selectivity of DHA and GCD. The use of H₂O₂ as electron acceptor can further enhance conversion of glycerol and product generation than that use of O₂ as electron acceptor. In the presence of H₂O₂, the conversion of glycerol mainly proceeded via radical-mediated oxidation route and provided GCOA as the principle product. While in the presence of O₂, GCD was generated as a major product.

The concentration of the generated ROS in the system was significantly affected the route of glycerol conversion and types of product generation.

7.1.2 Metal-decorated TiO₂-induced photocatalytic oxidation of glycerol to value-added compounds

In this part, the addition of decorated metals in both mono- and bi-metallic system on the surface of TiO₂ photocatalyst was achieved and utilized for the conversion of glycerol to value-added compounds. The decoration of monometallic NPs, including Au, Pt, Pd and Bi, with 3 wt.% metal content on the surface of TiO₂ photocatalyst can enhance the photocatalytic activity for glycerol conversion. 3 wt.% Au decorated on TiO₂ (Au/TiO₂) exhibited the highest photocatalytic activity among other decorated monometallic metals, providing the conversion of glycerol up to 88.02% and the yield of GCD, DHA, HPA, GCOA, FMD and GCAD of 21.10, 11.25, 12.76, 10.52, 15.41 and 5.59%, respectively. In addition, the rate of glycerol conversion over the Au/TiO₂ photocatalyst can be explained by a pseudo-first order reaction, which was increased when increasing Au content in the range of 1-7 wt.%. The combination of decorated metal toward bimetallic system, including AuBi, AuPt and AuPd on the TiO₂ photocatalyst with 3 wt.% of each decorated metal can alter the photocatalytic activity and route of glycerol conversion. Both Au₃Pt₃/TiO₂ and Au₃Pd₃/TiO₂ can further enhance the photocatalytic activity for glycerol conversion, while Au₃Bi₃/TiO₂ retarded the photocatalytic conversion of glycerol compared with the monometallic Au NPs decorated on TiO₂. Au₃Pd₃/TiO₂ exhibited the highest glycerol conversion among all prepared metal-decorated photocatalyst with 98.75% glycerol conversion and provided the FMD with 22.94% of yield as a main product at 24 h of irradiation time. Although Au₃Bi₃/TiO₂ did not provided the highest photocatalytic conversion of glycerol. It raised the generation of GCAD (25.04% of yield) as a principle value-added

products instead of FMD, which might be attributed to the promotional geometric effect in the presence Bi species.

7.1.3 Preparation of black TiO₂ via solution plasma process and its photocatalytic oxidation of glycerol to value-added compounds

The black TiO₂ NPs was successfully synthesized through the novel simple green process named as “Solution Plasma”. The several generated-plasma operating parameters including pulse width, repetition frequency, HNO₃ solution medium concentration and plasma discharge time were significantly affected on the structural, morphological and optical property of as-synthesized black TiO₂. Increasing the pulse width, repetition frequency and HNO₃ solution medium concentration increased the energy per second for discharge plasma, which induced the formation of black TiO₂ NPs with a large mean volume diameter at a high synthesis rate and high Ti³⁺/Ti⁴⁺ ratio. In addition, it also reduced the band gap energy of the obtained black TiO₂, resulting in the capability of the visible light absorption. Moreover, long plasma discharge time also induced an agglomeration and/or structural growth of the synthesized black TiO₂ particles and the high formation of Ti³⁺ defect structure. Among all as-synthesized black TiO₂ photocatalysts, the black TiO₂ synthesized through the SPP with plasma discharge time of 4 h at the repetition frequency of 20 kHz and pulse width of 2.0 μs under 3.0 mM HNO₃ solution medium exhibited the lowest band gap energy of around 2.44 eV and provided the highest photocatalytic activity for glycerol conversion (58.49% at 24 h) with the yield of GCD, DHA, HPA, GCOA, GCOD and FMD of 4.85, 3.32, 2.11, 2.15, 39.15 and 26.61%, respectively.

7.2 Recommendations

Further research on the photocatalytic conversion of glycerol over TiO_2 -based photocatalyst should be concerned with the following aspects:

1. It is clear that the concentration of ROS was significantly affected on the type of product generation. Therefore, the threshold quantity of each ROS on each type of generated value-added compounds via the photocatalytic oxidation over TiO_2 -based photocatalyst was suggested for the further study in order to achieve the controllable route of glycerol conversion and the high yield of desired products.
2. To achieve the desirable glycerol conversion in the early operation time and improve the yield of desired products over bimetallic NPs decorated on TiO_2 , the optimization of metal ratio should be carried out.
3. It is worth noting that the metal-decorated on TiO_2 and defective black TiO_2 can adsorb the light in visible region. Thus, the use of solar light for the photocatalytic conversion of glycerol over these photocatalysts should be evaluated.

REFERENCES



จุฬาลงกรณ์มหาวิทยาลัย
CHULALONGKORN UNIVERSITY

REFERENCES

- [1] L. He, J.M.S. Parra, E.A. Blekkan, D. Chen, Towards efficient hydrogen production from glycerol by sorption enhanced steam reforming, *Energy & Environmental Science*, 3 (2010) 1046-1056.
- [2] A. Villa, N. Dimitratos, C.E. Chan-Thaw, C. Hammond, L. Prati, G.J. Hutchings, Glycerol oxidation using gold-containing catalysts, *Accounts of chemical research*, 48 (2015) 1403-1412.
- [3] E. Skrzyńska, S. Zaid, J.S. Girardon, M. Capron, F. Dumeignil, Catalytic behaviour of four different supported noble metals in the crude glycerol oxidation, *Applied Catalysis A: General*, 499 (2015) 89-100.
- [4] F.F. Wang, S. Shao, C.L. Liu, C.L. Xu, R.Z. Yang, W.S. Dong, Selective oxidation of glycerol over Pt supported on mesoporous carbon nitride in base-free aqueous solution, *Chemical Engineering Journal*, 264 (2015) 336-343.
- [5] A.L. Linsebigler, G. Lu, J.T. Yates, Photocatalysis on TiO₂ Surfaces: Principles, Mechanisms, and Selected Results, *Chemical Reviews*, 95 (1995) 735-758.
- [6] S.G. Kumar, K.K. Rao, Polymorphic phase transition among the titania crystal structures using a solution-based approach: from precursor chemistry to nucleation process, *Nanoscale*, 6 (2014) 11574-11632.
- [7] S. Livraghi, K. Elghniji, A.M. Czoska, M.C. Paganini, E. Giamello, M. Ksibi, Nitrogen-doped and nitrogen-fluorine-codoped titanium dioxide. Nature and concentration of the photoactive species and their role in determining the photocatalytic activity under visible light, *Journal of Photochemistry and Photobiology A: Chemistry*, 205 (2009) 93-97.
- [8] T. Torimoto, Y. Okawa, N. Takeda, H. Yoneyama, Effect of activated carbon content in TiO₂-loaded activated carbon on photodegradation behaviors of dichloromethane, *Journal of Photochemistry and Photobiology A: Chemistry*, 103 (1997) 153-157.
- [9] R.F. Howe, EPR spectroscopy in surface chemistry: recent developments, *Advances in Colloid and Interface Science*, 18 (1982) 1-55.

- [10] Y. Nakaoka, Y. Nosaka, ESR investigation into the effects of heat treatment and crystal structure on radicals produced over irradiated TiO₂ powder, *Journal of Photochemistry and Photobiology A: Chemistry*, 110 (1997) 299-305.
- [11] J. Conti, P. Holtberg, J. Diefenderfer, A. LaRose, J.T. Turnure, L. Westfall, *International Energy Outlook 2016 With Projections to 2040*, in, USDOE Energy Information Administration (EIA), Washington, DC (United States). Office of Energy Analysis, 2016.
- [12] N.R. Council, *Renewable fuel standard: potential economic and environmental effects of US biofuel policy*, National Academies Press, 2012.
- [13] H.W. Tan, A.R. Abdul Aziz, M.K. Aroua, Glycerol production and its applications as a raw material: A review, *Renewable and Sustainable Energy Reviews*, 27 (2013) 118-127.
- [14] L. He, J.M. Salamanca Parra, E.A. Blekkan, D. Chen, Towards efficient hydrogen production from glycerol by sorption enhanced steam reforming, *Energy & Environmental Science*, 3 (2010) 1046-1056.
- [15] A. Behr, *The Future of Glycerol. New Usages for a Versatile Raw Material*. By Mario Pagliaro and Michele Rossi, *ChemSusChem*, 1 (2008) 653-653.
- [16] C.S.K. Lin, L.A. Pfaltzgraff, L. Herrero-Davila, E.B. Mubofu, S. Abderrahim, J.H. Clark, A.A. Koutinas, N. Kopsahelis, K. Stamatelatou, F. Dickson, Food waste as a valuable resource for the production of chemicals, materials and fuels. Current situation and global perspective, *Energy & Environmental Science*, 6 (2013) 426-464.
- [17] R. Fillières, B. Benjelloun-Mlayah, M. Delmas, Ethanolysis of rapeseed oil: Quantitation of ethyl esters, mono-, di-, and triglycerides and glycerol by high-performance size-exclusion chromatography, *Journal of the American Oil Chemists' Society*, 72 (1995) 427-432.
- [18] S. Shah, S. Sharma, M.N. Gupta, Biodiesel Preparation by Lipase-Catalyzed Transesterification of Jatropha Oil, *Energy & Fuels*, 18 (2004) 154-159.

- [19] A. Alhanash, E.F. Kozhevnikova, I.V. Kozhevnikov, Gas-phase dehydration of glycerol to acrolein catalysed by caesium heteropoly salt, *Applied Catalysis A: General*, 378 (2010) 11-18.
- [20] J. Feng, Y. Zhang, W. Xiong, H. Ding, B. He, Hydrogenolysis of Glycerol to 1,2-Propanediol and Ethylene Glycol over Ru-Co/ZrO₂ Catalysts, *Catalysts*, 6 (2016) 51.
- [21] R. Huang, E.Y. Kim, Catalytic Synthesis of Glycerol tert-Butyl Ethers as Fuel Additives from the Biodiesel By-Product Glycerol, *Journal of Chemistry*, 2015 (2015) 6.
- [22] C. Márquez-Alvarez, E. Sastre, J. Pérez-Pariente, Solid Catalysts for the Synthesis of Fatty Esters of Glycerol, Polyglycerols and Sorbitol from Renewable Resources, *Topics in Catalysis*, 27 (2004) 105-117.
- [23] M.V. Sivaiah, S. Robles-Manuel, S. Valange, J. Barrault, Recent developments in acid and base-catalyzed etherification of glycerol to polyglycerols, *Catalysis Today*, 198 (2012) 305-313.
- [24] M. Pagliaro, M. Rossi, Chapter 1 Glycerol: Properties and Production, in: *The Future of Glycerol: New Usages for a Versatile Raw Material*, The Royal Society of Chemistry, 2008, pp. 1-17.
- [25] J.G. van Bennekom, R.H. Venderbosch, D. Assink, K.P.J. Lemmens, H.J. Heeres, Bench scale demonstration of the Supermethanol concept: The synthesis of methanol from glycerol derived syngas, *Chemical Engineering Journal*, 207 (2012) 245-253.
- [26] B. Katryniok, S. Paul, V. Bellière-Baca, P. Rey, F. Dumeignil, Glycerol dehydration to acrolein in the context of new uses of glycerol, *Green Chemistry*, 12 (2010) 2079-2098.
- [27] B. Katryniok, H. Kimura, E. Skrzynska, J.-S. Girardon, P. Fongarland, M. Capron, R. Ducoulombier, N. Mimura, S. Paul, F. Dumeignil, Selective catalytic oxidation of glycerol: perspectives for high value chemicals, *Green Chemistry*, 13 (2011) 1960-1979.

- [28] P.T. Anastas, A. Perosa, M. Selva, *Green Processes: Green Nanoscience*, Wiley, 2014.
- [29] S.N. Habisreutinger, L. Schmidt-Mende, J.K. Stolarczyk, Photocatalytic Reduction of CO₂ on TiO₂ and Other Semiconductors, *Angewandte Chemie International Edition*, 52 (2013) 7372-7408.
- [30] B.G. Yacobi, *Semiconductor Materials*, Springer US, 2003.
- [31] O. Ola, M.M. Maroto-Valer, Review of material design and reactor engineering on TiO₂ photocatalysis for CO₂ reduction, *Journal of Photochemistry and Photobiology C: Photochemistry Reviews*, 24 (2015) 16-42.
- [32] D. Chatterjee, S. Dasgupta, Visible light induced photocatalytic degradation of organic pollutants, *Journal of Photochemistry and Photobiology C: Photochemistry Reviews*, 6 (2005) 186-205.
- [33] D.T. Cromer, K. Herrington, The Structures of Anatase and Rutile, *Journal of the American Chemical Society*, 77 (1955) 4708-4709.
- [34] S.-D. Mo, W.Y. Ching, Electronic and optical properties of three phases of titanium dioxide: Rutile, anatase, and brookite, *Physical Review B*, 51 (1995) 13023-13032.
- [35] U. Diebold, The surface science of titanium dioxide, *Surface Science Reports*, 48 (2003) 53-229.
- [36] A.T. Paxton, L. Thiën-Nga, Electronic structure of reduced titanium dioxide, *Physical Review B*, 57 (1998) 1579-1584.
- [37] A. Fujishima, T.N. Rao, D.A. Tryk, Titanium dioxide photocatalysis, *Journal of Photochemistry and Photobiology C: Photochemistry Reviews*, 1 (2000) 1-21.
- [38] M. Kitano, M. Matsuoka, M. Ueshima, M. Anpo, Recent developments in titanium oxide-based photocatalysts, *Applied Catalysis A: General*, 325 (2007) 1-14.
- [39] W. Sigmund, H. El-Shall, D.O. Shah, B.M. Moudgil, *Particulate systems in nano- and biotechnologies*, CRC Press, 2008.
- [40] M. Schiavello, *Heterogeneous photocatalysis*, Wiley, 1997.
- [41] A.L. Linsebigler, G. Lu, J.T. Yates Jr, Photocatalysis on TiO₂ surfaces: principles, mechanisms, and selected results, *Chemical reviews*, 95 (1995) 735-758.

- [42] T. Umebayashi, T. Yamaki, H. Itoh, K. Asai, Analysis of electronic structures of 3d transition metal-doped TiO₂ based on band calculations, *Journal of Physics and Chemistry of Solids*, 63 (2002) 1909-1920.
- [43] W. Choi, A. Termin, M.R. Hoffmann, The role of metal ion dopants in quantum-sized TiO₂: correlation between photoreactivity and charge carrier recombination dynamics, *The Journal of Physical Chemistry*, 98 (1994) 13669-13679.
- [44] M.M. Joshi, N.K. Labhsetwar, P.A. Mangrulkar, S.N. Tijare, S.P. Kamble, S.S. Rayalu, Visible light induced photoreduction of methyl orange by N-doped mesoporous titania, *Applied Catalysis A: General*, 357 (2009) 26-33.
- [45] S.M. Gupta, M. Tripathi, A review of TiO₂ nanoparticles, *Chinese Science Bulletin*, 56 (2011) 1639.
- [46] S. Linic, P. Christopher, D.B. Ingram, Plasmonic-metal nanostructures for efficient conversion of solar to chemical energy, *Nature Material*, 10 (2011) 911-921.
- [47] A.V. Rupa, D. Divakar, T. Sivakumar, Titania and Noble Metals Deposited Titania Catalysts in the Photodegradation of Tartazine, *Catalysis Letters*, 132 (2009) 259-267.
- [48] S. Krejčíková, L. Matejová, K. Kočí, L. Obalová, Z. Matej, L. Čapek, O. Šolcová, Preparation and characterization of Ag-doped crystalline titania for photocatalysis applications, *Applied Catalysis B: Environmental*, 111 (2012) 119-125.
- [49] Y. Nosaka, K. Norimatsu, H. Miyama, The function of metals in metal-compounded semiconductor photocatalysts, *Chemical Physics Letters*, 106 (1984) 128-131.
- [50] H.B. Michaelson, The work function of the elements and its periodicity, *Journal of Applied Physics*, 48 (1977) 4729-4733.
- [51] R. Asahi, T. Morikawa, T. Ohwaki, K. Aoki, Y. Taga, Visible-light photocatalysis in nitrogen-doped titanium oxides, *science*, 293 (2001) 269-271.
- [52] J.H. Park, S. Kim, A.J. Bard, Novel carbon-doped TiO₂ nanotube arrays with high aspect ratios for efficient solar water splitting, *Nano letters*, 6 (2006) 24-28.
- [53] K. Kondo, N. Murakami, C. Ye, T. Tsubota, T. Ohno, Development of highly efficient sulfur-doped TiO₂ photocatalysts hybridized with graphitic carbon nitride, *Applied Catalysis B: Environmental*, 142 (2013) 362-367.

- [54] T. Ohno, M. Akiyoshi, T. Umebayashi, K. Asai, T. Mitsui, M. Matsumura, Preparation of S-doped TiO₂ photocatalysts and their photocatalytic activities under visible light, *Applied Catalysis A: General*, 265 (2004) 115-121.
- [55] J.C. Yu, J. Yu, W. Ho, Z. Jiang, L. Zhang, Effects of F-doping on the photocatalytic activity and microstructures of nanocrystalline TiO₂ powders, *Chemistry of materials*, 14 (2002) 3808-3816.
- [56] G. Liu, L. Wang, H.G. Yang, H.M. Cheng, G.Q.M. Lu, Titania-based photocatalysts—crystal growth, doping and heterostructuring, *Journal of Materials Chemistry*, 20 (2010) 831-843.
- [57] R. Asahi, T. Morikawa, Nitrogen complex species and its chemical nature in TiO₂ for visible-light sensitized photocatalysis, *Chemical Physics*, 339 (2007) 57-63.
- [58] H. Irie, Y. Watanabe, K. Hashimoto, Nitrogen-concentration dependence on photocatalytic activity of TiO_{2-x}N_x powders, *The Journal of Physical Chemistry B*, 107 (2003) 5483-5486.
- [59] C. Di Valentin, G. Pacchioni, A. Selloni, Theory of carbon doping of titanium dioxide, *Chemistry of Materials*, 17 (2005) 6656-6665.
- [60] M.S. Vohra, S. Kim, W. Choi, Effects of surface fluorination of TiO₂ on the photocatalytic degradation of tetramethylammonium, *Journal of Photochemistry and Photobiology A: Chemistry*, 160 (2003) 55-60.
- [61] X. Zong, G. Lu, L. Wang, Nonmetal Doping in TiO₂ Toward Visible-Light-Induced Photocatalysis, in: D.W. Bahnemann, P.K.J. Robertson (Eds.) *Environmental Photochemistry Part III*, Springer Berlin Heidelberg, Berlin, Heidelberg, 2015, pp. 87-113.
- [62] T. Bak, J. Nowotny, N.J. Sucher, E. Wachsman, Effect of crystal imperfections on reactivity and photoreactivity of TiO₂ (rutile) with oxygen, water, and bacteria, *The Journal of Physical Chemistry C*, 115 (2011) 15711-15738.
- [63] J. Nowotny, M.A. Alim, T. Bak, M.A. Idris, M. Ionescu, K. Prince, M.Z. Sahdan, K. Sopian, M.A.M. Teridi, W. Sigmund, Defect chemistry and defect engineering of TiO₂-based semiconductors for solar energy conversion, *Chemical Society Reviews*, 44 (2015) 8424-8442.

- [64] J. Nowotny, W. Li, T. Bak, Effect of oxygen activity on semiconducting properties of TiO₂ (rutile), *Ionics*, 21 (2015) 1399-1406.
- [65] I. Nakamura, N. Negishi, S. Kutsuna, T. Ihara, S. Sugihara, K. Takeuchi, Role of oxygen vacancy in the plasma-treated TiO₂ photocatalyst with visible light activity for NO removal, *Journal of Molecular Catalysis A: Chemical*, 161 (2000) 205-212.
- [66] G. Liu, F. Li, D.W. Wang, D.M. Tang, C. Liu, X. Ma, G.Q. Lu, H.M. Cheng, Electron field emission of a nitrogen-doped TiO₂ nanotube array, *Nanotechnology*, 19 (2007) 025606.
- [67] G.U. von Oertzen, A.R. Gerson, The effects of O deficiency on the electronic structure of rutile TiO₂, *Journal of Physics and Chemistry of Solids*, 68 (2007) 324-330.
- [68] N. Serpone, Is the Band Gap of Pristine TiO₂ Narrowed by Anion- and Cation-Doping of Titanium Dioxide in Second-Generation Photocatalysts?, *The Journal of Physical Chemistry B*, 110 (2006) 24287-24293.
- [69] H. Liu, H. Ma, X. Li, W. Li, M. Wu, X. Bao, The enhancement of TiO₂ photocatalytic activity by hydrogen thermal treatment, *Chemosphere*, 50 (2003) 39-46.
- [70] A. Sirisuk, E. Klansorn, P. Praserttham, Effects of reaction medium and crystallite size on Ti³⁺ surface defects in titanium dioxide nanoparticles prepared by solvothermal method, *Catalysis Communications*, 9 (2008) 1810-1814.
- [71] D.R. Park, J. Zhang, K. Ikeue, H. Yamashita, M. Anpo, Photocatalytic oxidation of ethylene to CO₂ and H₂O on ultrafine powdered TiO₂ photocatalysts in the presence of O₂ and H₂O, *Journal of catalysis*, 185 (1999) 114-119.
- [72] X. Yu, B. Kim, Y.K. Kim, Highly enhanced photoactivity of anatase TiO₂ nanocrystals by controlled hydrogenation-induced surface defects, *ACS Catalysis*, 3 (2013) 2479-2486.
- [73] B.J. Morgan, G.W. Watson, Intrinsic n-type defect formation in TiO₂: a comparison of rutile and anatase from GGA+ U calculations, *The Journal of Physical Chemistry C*, 114 (2010) 2321-2328.
- [74] Z. Zheng, B. Huang, X. Meng, J. Wang, S. Wang, Z. Lou, Z. Wang, X. Qin, X. Zhang, Y. Dai, Metallic zinc- assisted synthesis of Ti³⁺ self-doped TiO₂ with tunable phase

- composition and visible-light photocatalytic activity, *Chemical Communications*, 49 (2013) 868-870.
- [75] F.N. Sayed, O. Jayakumar, R. Sasikala, R. Kadam, S.R. Bharadwaj, L. Kienle, U. Schürmann, S.r. Kaps, R. Adelung, J. Mittal, Photochemical hydrogen generation using nitrogen-doped TiO₂-Pd nanoparticles: facile synthesis and effect of Ti³⁺ incorporation, *The Journal of Physical Chemistry C*, 116 (2012) 12462-12467.
- [76] Q. Kang, J. Cao, Y. Zhang, L. Liu, H. Xu, J. Ye, Reduced TiO₂ nanotube arrays for photoelectrochemical water splitting, *Journal of Materials Chemistry A*, 1 (2013) 5766-5774.
- [77] Z.K. Zhang, M.L. Bai, D.Z. Guo, S.M. Hou, G.M. Zhang, Plasma-electrolysis synthesis of TiO₂ nano/microspheres with optical absorption extended into the infra-red region, *Chemical Communications*, 47 (2011) 8439-8441.
- [78] M.S. Kim, W.J. Jo, D. Lee, S.H. Baeck, J.H. Shin, B.C. Lee, Enhanced photocatalytic activity of TiO₂ modified by e-beam irradiation, *Bulletin of the Korean Chemical Society*, 34 (2013) 1397-1400.
- [79] L.R. Grabstanowicz, S. Gao, T. Li, R.M. Rickard, T. Rajh, D.J. Liu, T. Xu, Facile Oxidative Conversion of TiH₂ to High-Concentration Ti³⁺-Self-Doped Rutile TiO₂ with Visible-Light Photoactivity, *Inorganic Chemistry*, 52 (2013) 3884-3890.
- [80] Z. Pei, L. Ding, H. Lin, S. Weng, Z. Zheng, Y. Hou, P. Liu, Facile synthesis of defect-mediated TiO_{2-x} with enhanced visible light photocatalytic activity, *Journal of Materials Chemistry A*, 1 (2013) 10099-10102.
- [81] F. Zuo, K. Bozhilov, R.J. Dillon, L. Wang, P. Smith, X. Zhao, C. Bardeen, P. Feng, Active Facets on Titanium(III)-Doped TiO₂: An Effective Strategy to Improve the Visible-Light Photocatalytic Activity, *Angewandte Chemie International Edition*, 51 (2012) 6223-6226.
- [82] A.I. Morozov, *Introduction to plasma dynamics*, CRC Press, 2012.
- [83] O. Takai, Solution plasma processing (SPP), *Pure and Applied Chemistry*, 80 (2008) 2003-2011.
- [84] A. Hickling, M. Ingram, Contact glow-discharge electrolysis, *Transactions of the Faraday Society*, 60 (1964) 783-793.

- [85] K. Azumi, T. Mizuno, T. Akimoto, T. Ohmori, Light Emission from Pt during High-Voltage Cathodic Polarization, *Journal of the Electrochemical Society*, 146 (1999) 3374-3377.
- [86] S.K. Sengupta, R. Singh, A.K. Srivastava, A Study on the Origin of Nonfaradaic Behavior of Anodic Contact Glow Discharge Electrolysis The Relationship Between Power Dissipated in Glow Discharges and Nonfaradaic Yields, *Journal of the Electrochemical Society*, 145 (1998) 2209-2213.
- [87] S. Campbell, V. Cunnane, D. Schiffrin, Cathodic contact glow discharge electrolysis under reduced pressure, *Journal of Electroanalytical Chemistry*, 325 (1992) 257-268.
- [88] T. Tsuji, T. Mizuki, S. Ozono, M. Tsuji, Laser-induced silver nanocrystal formation in polyvinylpyrrolidone solutions, *Journal of Photochemistry and Photobiology A: Chemistry*, 206 (2009) 134-139.
- [89] K. Siuzdak, M. Sawczak, M. Klein, G. Nowaczyk, S. Jurga, A. Cenian, Preparation of platinum modified titanium dioxide nanoparticles with the use of laser ablation in water, *Physical Chemistry Chemical Physics*, 16 (2014) 15199-15206.
- [90] I.B. Gornushkin, U. Panne, Radiative models of laser-induced plasma and pump-probe diagnostics relevant to laser-induced breakdown spectroscopy, *Spectrochimica Acta Part B: Atomic Spectroscopy*, 65 (2010) 345-359.
- [91] S. Horikoshi, N. Serpone, In-liquid plasma: a novel tool in the fabrication of nanomaterials and in the treatment of wastewaters, *RSC Advances*, 7 (2017) 47196-47218.
- [92] X. Hu, O. Takai, N. Saito, Simple synthesis of platinum nanoparticles by plasma sputtering in water, *Japanese Journal of Applied Physics*, 52 (2013) 01AN05.
- [93] A. Watthanaphanit, G. Panomsuwan, N. Saito, A novel one-step synthesis of gold nanoparticles in an alginate gel matrix by solution plasma sputtering, *RSC Advances*, 4 (2014) 1622-1629.
- [94] S.P. Cho, M.A. Bratescu, N. Saito, O. Takai, Microstructural characterization of gold nanoparticles synthesized by solution plasma processing, *Nanotechnology*, 22 (2011) 455701.

- [95] M.A. Bratescu, S.P. Cho, O. Takai, N. Saito, Size-controlled gold nanoparticles synthesized in solution plasma, *The Journal of Physical Chemistry C*, 115 (2011) 24569-24576.
- [96] N. Saito, J. Hieda, O. Takai, Synthesis process of gold nanoparticles in solution plasma, *Thin Solid Films*, 518 (2009) 912-917.
- [97] P. Pootawang, N. Saito, S.Y. Lee, Discharge time dependence of a solution plasma process for colloidal copper nanoparticle synthesis and particle characteristics, *Nanotechnology*, 24 (2013) 055604.
- [98] J. Kang, O.L. Li, N. Saito, Synthesis of structure-controlled carbon nano spheres by solution plasma process, *Carbon*, 60 (2013) 292-298.
- [99] T. Morishita, T. Ueno, G. Panomsuwan, J. Hieda, A. Yoshida, M.A. Bratescu, N. Saito, Fastest Formation Routes of Nanocarbons in Solution Plasma Processes, *Scientific reports*, 6 (2016) 36880.
- [100] X. Hu, X. Zhang, X. Shen, H. Li, O. Takai, N. Saito, Plasma-induced synthesis of CuO nanofibers and ZnO nanoflowers in water, *Plasma Chemistry and Plasma Processing*, 34 (2014) 1129-1139.
- [101] X. Hu, X. Shen, O. Takai, N. Saito, Facile fabrication of PtAu alloy clusters using solution plasma sputtering and their electrocatalytic activity, *Journal of Alloys and Compounds*, 552 (2013) 351-355.
- [102] P. Pootawang, N. Saito, O. Takai, S.Y. Lee, Synthesis and characteristics of Ag/Pt bimetallic nanocomposites by arc-discharge solution plasma processing, *Nanotechnology*, 23 (2012) 395602.
- [103] P. Pootawang, S.Y. Lee, Rapid synthesis of Ag nanoparticles-embedded mesoporous silica via solution plasma and its catalysis for 4-nitrophenol reduction, *Materials Letters*, 80 (2012) 1-4.
- [104] P. Pootawang, N. Saito, O. Takai, Ag nanoparticle incorporation in mesoporous silica synthesized by solution plasma and their catalysis for oleic acid hydrogenation, *Materials Letters*, 65 (2011) 1037-1040.
- [105] T. Shirafuji, Y. Noguchi, T. Yamamoto, J. Hieda, N. Saito, O. Takai, A. Tsuchimoto, K. Nojima, Y. Okabe, Functionalization of multiwalled carbon nanotubes by

- solution plasma processing in ammonia aqueous solution and preparation of composite material with polyamide 6, *Japanese Journal of Applied Physics*, 52 (2013) 125101.
- [106] V. Burakov, A. Nevar, M. Nedel'ko, N. Tarasenko, Formation of zinc oxide nanoparticles during electric discharge in water, *Technical Physics Letters*, 34 (2008) 679-681.
- [107] V. Burakov, N. Savastenko, N. Tarasenko, E. Nevar, Synthesis of nanoparticles using a pulsed electrical discharge in a liquid, *Journal of Applied Spectroscopy*, 75 (2008) 114-124.
- [108] N. Tarasenko, A. Nevar, M. Nedelko, Properties of zinc-oxide nanoparticles synthesized by electrical-discharge technique in liquids, *physica status solidi (a)*, 207 (2010) 2319-2322.
- [109] T. Okada, T. Kaneko, R. Hatakeyama, Conversion of toluene into carbon nanotubes using arc discharge plasmas in solution, *Thin Solid Films*, 515 (2007) 4262-4265.
- [110] Z. Kelgenbaeva, E. Omurzak, S. Takebe, Z. Abdullaeva, S. Sulaimankulova, C. Iwamoto, T. Mashimo, Magnetite nanoparticles synthesized using pulsed plasma in liquid, *Japanese Journal of Applied Physics*, 52 (2013) 11NJ02.
- [111] Z. Abdullaeva, E. Omurzak, C. Iwamoto, H.S. Ganapathy, S. Sulaimankulova, C. Liliang, T. Mashimo, Onion-like carbon-encapsulated Co, Ni, and Fe magnetic nanoparticles with low cytotoxicity synthesized by a pulsed plasma in a liquid, *Carbon*, 50 (2012) 1776-1785.
- [112] Z. Abdullaeva, E. Omurzak, C. Iwamoto, H. Ihara, H.S. Ganapathy, S. Sulaimankulova, M. Koinuma, T. Mashimo, Pulsed plasma synthesis of iron and nickel nanoparticles coated by carbon for medical applications, *Japanese Journal of Applied Physics*, 52 (2013) 01AJ01.
- [113] Y. Matsui, N. Takeuchi, K. Sasaki, R. Hayashi, K. Yasuoka, Experimental and theoretical study of acetic-acid decomposition by a pulsed dielectric-barrier plasma in a gas-liquid two-phase flow, *Plasma Sources Science and Technology*, 20 (2011) 034015.

- [114] S. Horikoshi, S. Sato, M. Abe, N. Serpone, A novel liquid plasma AOP device integrating microwaves and ultrasounds and its evaluation in defluorinating perfluorooctanoic acid in aqueous media, *Ultrasonics sonochemistry*, 18 (2011) 938-942.
- [115] X.L. Hao, X.W. Zhang, L.C. Lei, Degradation characteristics of toxic contaminant with modified activated carbons in aqueous pulsed discharge plasma process, *Carbon*, 47 (2009) 153-161.
- [116] G. Qu, D. Liang, D. Qu, Y. Huang, T. Liu, H. Mao, P. Ji, D. Huang, Simultaneous removal of cadmium ions and phenol from water solution by pulsed corona discharge plasma combined with activated carbon, *Chemical Engineering Journal*, 228 (2013) 28-35.
- [117] A.J. Bard, R. Parsons, J. Jordan, *Standard Potentials in Aqueous Solution*, Taylor & Francis, 1985.
- [118] Y. Nosaka, A.Y. Nosaka, Generation and Detection of Reactive Oxygen Species in Photocatalysis, *Chemical Reviews*, 117 (2017) 11302-11336.
- [119] B.H.J. Bielski, D.E. Cabelli, R.L. Arudi, A.B. Ross, Reactivity of HO_2/O_2^- Radicals in Aqueous Solution, *Journal of Physical and Chemical Reference Data*, 14 (1985) 1041-1100.
- [120] R. Nakamura, A. Imanishi, K. Murakoshi, Y. Nakato, In Situ FTIR Studies of Primary Intermediates of Photocatalytic Reactions on Nanocrystalline TiO_2 Films in Contact with Aqueous Solutions, *Journal of the American Chemical Society*, 125 (2003) 7443-7450.
- [121] Y. Murakami, K. Endo, I. Ohta, A.Y. Nosaka, Y. Nosaka, Can OH Radicals Diffuse from the UV-Irradiated Photocatalytic TiO_2 Surfaces? Laser-Induced-Fluorescence Study, *The Journal of Physical Chemistry C*, 111 (2007) 11339-11346.
- [122] B.G. Kwon, J.H. Kwon, Measurement of the hydroxyl radical formation from H_2O_2 , NO_3^- , and Fe(III) using a continuous flow injection analysis, *Journal of Industrial and Engineering Chemistry*, 16 (2010) 193-199.
- [123] G.V. Buxton, C.L. Greenstock, W.P. Helman, A.B. Ross, Critical Review of rate constants for reactions of hydrated electrons, hydrogen atoms and hydroxyl

- radicals ($\cdot\text{OH}/\cdot\text{O}_2^-$) in Aqueous Solution, *Journal of Physical and Chemical Reference Data*, 17 (1988) 513-886.
- [124] G.L. Vaghjiani, A.R. Ravishankara, Photodissociation of H_2O_2 and CH_3OOH at 248 nm and 298 K: Quantum yields for OH, $\text{O}(^3\text{P})$ and $\text{H}(^2\text{S})$, *The Journal of Chemical Physics*, 92 (1990) 996-1003.
- [125] Y. Nosaka, T. Daimon, A.Y. Nosaka, Y. Murakami, Singlet oxygen formation in photocatalytic TiO_2 aqueous suspension, *Physical Chemistry Chemical Physics*, 6 (2004) 2917-2918.
- [126] V. Augugliaro, H.A.H. El Nazer, V. Loddo, A. Mele, G. Palmisano, L. Palmisano, S. Yurdakal, Partial photocatalytic oxidation of glycerol in TiO_2 water suspensions, *Catalysis Today*, 151 (2010) 21-28.
- [127] C. Minero, A. Bedini, V. Maurino, Glycerol as a probe molecule to uncover oxidation mechanism in photocatalysis, *Applied Catalysis B: Environmental*, 128 (2012) 135-143.
- [128] R. Chong, J. Li, X. Zhou, Y. Ma, J. Yang, L. Huang, H. Han, F. Zhang, C. Li, Selective photocatalytic conversion of glycerol to hydroxyacetaldehyde in aqueous solution on facet tuned TiO_2 -based catalysts, *Chemical Communications*, 50 (2014) 165-167.
- [129] P. Panagiotopoulou, E.E. Karamerou, D.I. Kondarides, Kinetics and mechanism of glycerol photo-oxidation and photo-reforming reactions in aqueous TiO_2 and Pt/TiO_2 suspensions, *Catalysis Today*, 209 (2013) 91-98.
- [130] F.J. López-Tenllado, J. Hidalgo-Carrillo, V. Montes, A. Marinas, F.J. Urbano, J.M. Marinas, L. Ilieva, T. Tabakova, F. Reid, A comparative study of hydrogen photocatalytic production from glycerol and propan-2-ol on M/TiO_2 systems ($M=\text{Au}, \text{Pt}, \text{Pd}$), *Catalysis Today*, 280 (2017) 58-64.
- [131] W. Zhao, X. Wang, H. Sang, K. Wang, Synthesis of Bi-doped TiO_2 Nanotubes and Enhanced Photocatalytic Activity for Hydrogen Evolution from Glycerol Solution, *Chinese Journal of Chemistry*, 31 (2013) 415-420.

- [132] S. Bagwasi, Y. Niu, M. Nasir, B. Tian, J. Zhang, The study of visible light active bismuth modified nitrogen doped titanium dioxide photocatalysts: Role of bismuth, *Applied Surface Science*, 264 (2013) 139-147.
- [133] D. Tsukamoto, Y. Shiraishi, Y. Sugano, S. Ichikawa, S. Tanaka, T. Hirai, Gold nanoparticles located at the interface of anatase/rutile TiO₂ particles as active plasmonic photocatalysts for aerobic oxidation, *Journal of the American Chemical Society*, 134 (2012) 6309-6315.
- [134] S. Bashir, H. Idriss, Mechanistic study of the role of Au, Pd and Au-Pd in the surface reactions of ethanol over TiO₂ in the dark and under photo-excitation, *Catalysis Science & Technology*, 7 (2017) 5301-5320.
- [135] X. Chen, L. Liu, P.Y. Yu, S.S. Mao, Increasing Solar Absorption for Photocatalysis with Black Hydrogenated Titanium Dioxide Nanocrystals, *Science*, 331 (2011) 746-750.
- [136] A. Sinhamahapatra, J.P. Jeon, J.S. Yu, A new approach to prepare highly active and stable black titania for visible light-assisted hydrogen production, *Energy & Environmental Science*, 8 (2015) 3539-3544.
- [137] Y. Zhang, N. Zhang, Z.R. Tang, Y.J. Xu, Identification of Bi₂WO₆ as a highly selective visible-light photocatalyst toward oxidation of glycerol to dihydroxyacetone in water, *Chemical Science*, 4 (2013) 1820-1824.
- [138] Y. Guo, C. Cheng, J. Wang, Z. Wang, X. Jin, K. Li, P. Kang, J. Gao, Detection of reactive oxygen species (ROS) generated by TiO₂(R), TiO₂(R/A) and TiO₂(A) under ultrasonic and solar light irradiation and application in degradation of organic dyes, *Journal of Hazardous Materials*, 192 (2011) 786-793.
- [139] L. Kuang, Y. Zhao, W. Zhang, S. Ge, Roles of Reactive Oxygen Species and Holes in the Photodegradation of Cationic and Anionic Dyes by TiO₂ under UV Irradiation, *Journal of Environmental Engineering*, 142 (2015) 04015065.
- [140] M. Batzill, Fundamental aspects of surface engineering of transition metal oxide photocatalysts, *Energy & Environmental Science*, 4 (2011) 3275-3286.

- [141] T. Luttrell, S. Halpegamage, J. Tao, A. Kramer, E. Sutter, M. Batzill, Why is anatase a better photocatalyst than rutile?-Model studies on epitaxial TiO₂ films, *Scientific reports*, 4 (2014) 4043.
- [142] A. Yamakata, T.A. Ishibashi, H. Onishi, Effects of water addition on the methanol oxidation on Pt/TiO₂ photocatalyst studied by time-resolved infrared absorption spectroscopy, *The Journal of Physical Chemistry B*, 107 (2003) 9820-9823.
- [143] M. Styliadi, D.I. Kondarides, X.E. Verykios, Visible light-induced photocatalytic degradation of Acid Orange 7 in aqueous TiO₂ suspensions, *Applied Catalysis B: Environmental*, 47 (2004) 189-201.
- [144] R. Gao, J. Stark, D.W. Bahnemann, J. Rabani, Quantum yields of hydroxyl radicals in illuminated TiO₂ nanocrystallite layers, *Journal of Photochemistry and Photobiology A: Chemistry*, 148 (2002) 387-391.
- [145] V.M. Daskalaki, P. Panagiotopoulou, D.I. Kondarides, Production of peroxide species in Pt/TiO₂ suspensions under conditions of photocatalytic water splitting and glycerol photoreforming, *Chemical Engineering Journal*, 170 (2011) 433-439.
- [146] F.L. Rosario-Ortiz, E.C. Wert, S.A. Snyder, Evaluation of UV/H₂O₂ treatment for the oxidation of pharmaceuticals in wastewater, *Water research*, 44 (2010) 1440-1448.
- [147] O. Shadyro, A. Sosnovskaya, I. Edimecheva, N. Ostrovskaya, K. Kazem, I. Hryntsevich, A. Alekseev, Effects of quinones on free-radical processes of oxidation and fragmentation of hydroxyl-containing organic compounds, *Bioorganic & medicinal chemistry letters*, 17 (2007) 6383-6386.
- [148] M. Simões, S. Baranton, C. Coutanceau, Enhancement of catalytic properties for glycerol electrooxidation on Pt and Pd nanoparticles induced by Bi surface modification, *Applied Catalysis B: Environmental*, 110 (2011) 40-49.
- [149] W.C. Ketchie, M. Murayama, R.J. Davis, Promotional effect of hydroxyl on the aqueous phase oxidation of carbon monoxide and glycerol over supported Au catalysts, *Topics in Catalysis*, 44 (2007) 307-317.
- [150] S. Carrettin, P. McMorn, P. Johnston, K. Griffin, C.J. Kiely, G.J. Hutchings, Oxidation of glycerol using supported Pt, Pd and Au catalysts, *Physical Chemistry Chemical Physics*, 5 (2003) 1329-1336.

- [151] S. Gil, M. Marchena, L. Sánchez-Silva, A. Romero, P. Sánchez, J.L. Valverde, Effect of the operation conditions on the selective oxidation of glycerol with catalysts based on Au supported on carbonaceous materials, *Chemical engineering journal*, 178 (2011) 423-435.
- [152] M. Zhao, C. Rice, R.I. Masel, P. Waszczuk, A. Wieckowski, Kinetic Study of Electro-oxidation of Formic Acid on Spontaneously-Deposited Pt/Pd Nanoparticles CO Tolerant Fuel Cell Chemistry, *Journal of The Electrochemical Society*, 151 (2004) A131-A136.
- [153] T. McMurray, J. Byrne, P. Dunlop, J. Winkelman, B. Eggins, E. McAdams, Intrinsic kinetics of photocatalytic oxidation of formic and oxalic acid on immobilised TiO₂ films, *Applied Catalysis A: General*, 262 (2004) 105-110.
- [154] D.S. Muggli, M.J. Backes, Two active sites for photocatalytic oxidation of formic acid on TiO₂: effects of H₂O and temperature, *Journal of Catalysis*, 209 (2002) 105-113.
- [155] T. Abe, E. Suzuki, K. Nagoshi, K. Miyashita, M. Kaneko, Electron source in photoinduced hydrogen production on Pt-supported TiO₂ particles, *The Journal of Physical Chemistry B*, 103 (1999) 1119-1123.
- [156] S. Parra, V. Sarria, S. Malato, P. Péringier, C. Pulgarin, Photochemical versus coupled photochemical–biological flow system for the treatment of two biorecalcitrant herbicides: metobromuron and isoproturon, *Applied catalysis B: environmental*, 27 (2000) 153-168.
- [157] T. Hirakawa, K. Yawata, Y. Nosaka, Photocatalytic reactivity for O₂⁻ and OH radical formation in anatase and rutile TiO₂ suspension as the effect of H₂O₂ addition, *Applied Catalysis A: General*, 325 (2007) 105-111.
- [158] M.R. Hoffmann, S.T. Martin, W. Choi, D.W. Bahnemann, Environmental applications of semiconductor photocatalysis, *Chemical reviews*, 95 (1995) 69-96.
- [159] W. Han, P. Zhang, W. Zhu, J. Yin, L. Li, Photocatalysis of p-chlorobenzoic acid in aqueous solution under irradiation of 254 nm and 185 nm UV light, *Water research*, 38 (2004) 4197-4203.

- [160] W.R. Haag, J. Hoigne, Singlet oxygen in surface waters. 3. Photochemical formation and steady-state concentrations in various types of waters, *Environmental science & technology*, 20 (1986) 341-348.
- [161] D.H. Tseng, L.C. Juang, H.H. Huang, Effect of oxygen and hydrogen peroxide on the photocatalytic degradation of monochlorobenzene in aqueous suspension, *International Journal of Photoenergy*, 2012 (2012).
- [162] G.N. Nomikos, P. Panagiotopoulou, D.I. Kondarides, X.E. Verykios, Kinetic and mechanistic study of the photocatalytic reforming of methanol over Pt/TiO₂ catalyst, *Applied Catalysis B: Environmental*, 146 (2014) 249-257.
- [163] X. Guo, Q. Li, M. Zhang, M. Long, L. Kong, Q. Zhou, H. Shao, W. Hu, T. Wei, Enhanced photocatalytic performance of N-nitrosodimethylamine on TiO₂ nanotube based on the role of singlet oxygen, *Chemosphere*, 120 (2015) 521-526.
- [164] J. Deleplanque, J.L. Dubois, J.F. Devaux, W. Ueda, Production of acrolein and acrylic acid through dehydration and oxydehydration of glycerol with mixed oxide catalysts, *Catalysis Today*, 157 (2010) 351-358.
- [165] J. Lee, Y.H. Lee, J.S. Choi, K.S. Park, K.S. Chang, M. Yoon, Hydrothermal synthesis of defective TiO₂ nanoparticles for long-wavelength visible light-photocatalytic killing of cancer cells, *RSC Advances*, 5 (2015) 99789-99796.
- [166] J. Zhuang, W. Dai, Q. Tian, Z. Li, L. Xie, J. Wang, P. Liu, X. Shi, D. Wang, Photocatalytic degradation of RhB over TiO₂ bilayer films: effect of defects and their location, *Langmuir*, 26 (2010) 9686-9694.
- [167] M. Kong, Y. Li, X. Chen, T. Tian, P. Fang, F. Zheng, X. Zhao, Tuning the relative concentration ratio of bulk defects to surface defects in TiO₂ nanocrystals leads to high photocatalytic efficiency, *Journal of the American Chemical Society*, 133 (2011) 16414-16417.
- [168] W. Wang, D. Zhu, Z. Shen, J. Peng, J. Luo, X. Liu, One-pot hydrothermal route to synthesize the Bi-doped anatase TiO₂ hollow thin sheets with prior facet exposed for enhanced visible-light-driven photocatalytic activity, *Industrial & Engineering Chemistry Research*, 55 (2016) 6373-6383.

- [169] J. Yang, X. Wang, J. Dai, J. Li, Efficient visible-light-driven photocatalytic degradation with Bi_2O_3 coupling silica doped TiO_2 , *Industrial & Engineering Chemistry Research*, 53 (2014) 12575-12586.
- [170] Y. Liu, F. Xin, F. Wang, S. Luo, X. Yin, Synthesis, characterization, and activities of visible light-driven Bi_2O_3 - TiO_2 composite photocatalysts, *Journal of Alloys and Compounds*, 498 (2010) 179-184.
- [171] B. Oprea, T. Radu, S. Simon, XPS investigation of atomic environment changes on surface of B_2O_3 - Bi_2O_3 glasses, *Journal of Non-Crystalline Solids*, 379 (2013) 35-39.
- [172] T.S. Natarajan, K. Natarajan, H.C. Bajaj, R.J. Tayade, Enhanced photocatalytic activity of bismuth-doped TiO_2 nanotubes under direct sunlight irradiation for degradation of Rhodamine B dye, *Journal of nanoparticle research*, 15 (2013) 1669.
- [173] Y. Yu, T. He, L. Guo, Y. Yang, L. Guo, Y. Tang, Y. Cao, Efficient visible-light photocatalytic degradation system assisted by conventional Pd catalysis, *Scientific reports*, 5 (2015) 9561.
- [174] Z. Lin, X. Wang, J. Liu, Z. Tian, L. Dai, B. He, C. Han, Y. Wu, Z. Zeng, Z. Hu, On the role of localized surface plasmon resonance in UV-Vis light irradiated Au/ TiO_2 photocatalysis systems: pros and cons, *Nanoscale*, 7 (2015) 4114-4123.
- [175] J. Yan, G. Wu, N. Guan, L. Li, Synergetic promotion of the photocatalytic activity of TiO_2 by gold deposition under UV-visible light irradiation, *Chemical Communications*, 49 (2013) 11767-11769.
- [176] A. Polman, Plasmonics applied, *Science*, 322 (2008) 868-869.
- [177] A. Naldoni, F. Riboni, M. Marelli, F. Bossola, G. Ulisse, A. Di Carlo, I. Piš, S. Nappini, M. Malvestuto, M.V. Dozzi, Influence of TiO_2 electronic structure and strong metal-support interaction on plasmonic Au photocatalytic oxidations, *Catalysis Science & Technology*, 6 (2016) 3220-3229.
- [178] K.H. Leong, H.Y. Chu, S. Ibrahim, P. Saravanan, Palladium nanoparticles anchored to anatase TiO_2 for enhanced surface plasmon resonance-stimulated, visible-light-driven photocatalytic activity, *Beilstein journal of nanotechnology*, 6 (2015) 428.

- [179] C. Langhammer, Z. Yuan, I. Zorić, B. Kasemo, Plasmonic properties of supported Pt and Pd nanostructures, *Nano letters*, 6 (2006) 833-838.
- [180] N. Zhang, C. Han, Y.J. Xu, J.J. Foley IV, D. Zhang, J. Codrington, S.K. Gray, Y. Sun, Near-field dielectric scattering promotes optical absorption by platinum nanoparticles, *Nature Photonics*, 10 (2016) 473-482.
- [181] M.V. Dozzi, L. Prati, P. Canton, E. Selli, Effects of gold nanoparticles deposition on the photocatalytic activity of titanium dioxide under visible light, *Physical chemistry chemical physics*, 11 (2009) 7171-7180.
- [182] S.A. Ansari, M.M. Khan, S. Kalathil, A. Nisar, J. Lee, M.H. Cho, Oxygen vacancy induced band gap narrowing of ZnO nanostructures by an electrochemically active biofilm, *Nanoscale*, 5 (2013) 9238-9246.
- [183] X. Pan, M.Q. Yang, X. Fu, N. Zhang, Y.J. Xu, Defective TiO₂ with oxygen vacancies: synthesis, properties and photocatalytic applications, *Nanoscale*, 5 (2013) 3601-3614.
- [184] M.C. Biesinger, L.W. Lau, A.R. Gerson, R.S.C. Smart, Resolving surface chemical states in XPS analysis of first row transition metals, oxides and hydroxides: Sc, Ti, V, Cu and Zn, *Applied Surface Science*, 257 (2010) 887-898.
- [185] Y. Xu, C. Zhang, L. Zhang, X. Zhang, H. Yao, J. Shi, Pd-catalyzed instant hydrogenation of TiO₂ with enhanced photocatalytic performance, *Energy & Environmental Science*, 9 (2016) 2410-2417.
- [186] A. Gallo, T. Montini, M. Marelli, A. Minguzzi, V. Gombac, R. Psaro, P. Fornasiero, V. Dal Santo, H₂ production by renewables photoreforming on Pt–Au/TiO₂ catalysts activated by reduction, *ChemSusChem*, 5 (2012) 1800-1811.
- [187] C. Ma, G. Pang, G. He, Y. Li, C. He, Z. Hao, Layered sphere-shaped TiO₂ capped with gold nanoparticles on structural defects and their catalysis of formaldehyde oxidation, *Journal of Environmental Sciences*, 39 (2016) 77-85.
- [188] H.G. Boyen, G. Kästle, F. Weigl, B. Koslowski, C. Dietrich, P. Ziemann, J.P. Spatz, S. Riethmüller, C. Hartmann, M. Möller, Oxidation-resistant gold-55 clusters, *Science*, 297 (2002) 1533-1536.

- [189] S. Link, M.A. El-Sayed, Size and temperature dependence of the plasmon absorption of colloidal gold nanoparticles, *The Journal of Physical Chemistry B*, 103 (1999) 4212-4217.
- [190] G. De, C. Rao, Au-Pt alloy nanocrystals incorporated in silica films, *Journal of Materials Chemistry*, 15 (2005) 891-894.
- [191] X. Gao, X. Liu, Z. Zhu, Y. Gao, Q. Wang, F. Zhu, Z. Xie, Enhanced visible light photocatalytic performance of CdS sensitized TiO₂ nanorod arrays decorated with Au nanoparticles as electron sinks, *Scientific reports*, 7 (2017) 973.
- [192] Y.-Q. Wang, Y. Liu, M.X. Zhang, F.F. Min, Electronic Structure and Visible-Light Absorption of Transition Metals (TM= Cr, Mn, Fe, Co) and Zn-Codoped SrTiO₃: a First-Principles Study, *Chinese Physics Letters*, 35 (2018) 017101.
- [193] H. Zhao, F. Pan, Y. Li, A review on the effects of TiO₂ surface point defects on CO₂ photoreduction with H₂O, *Journal of Materiomics*, 3 (2017) 17-32.
- [194] C.W. Yi, K. Luo, T. Wei, D.W. Goodman, The Composition and Structure of Pd-Au Surfaces, *The Journal of Physical Chemistry B*, 109 (2005) 18535-18540.
- [195] H. Yu, X. Wang, H. Sun, M. Huo, Photocatalytic degradation of malathion in aqueous solution using an Au-Pd-TiO₂ nanotube film, *Journal of hazardous materials*, 184 (2010) 753-758.
- [196] A. Tripković, K.D. Popović, R. Stevanović, R. Socha, A. Kowal, Activity of a PtBi alloy in the electrochemical oxidation of formic acid, *Electrochemistry Communications*, 8 (2006) 1492-1498.
- [197] L.M. Zhang, Z.B. Wang, X.L. Sui, C.Z. Li, L. Zhao, D.M. Gu, Nitrogen-doped carbon with mesoporous structure as high surface area catalyst support for methanol oxidation reaction, *RSC Advances*, 6 (2016) 39310-39316.
- [198] S. Bashir, H. Idriss, Mechanistic study of the role of Au, Pd and Au-Pd in the surface reactions of ethanol over TiO₂ in the dark and under photo-excitation, *Catalysis Science & Technology*, 7 (2017) 5301-5320.
- [199] S. Devarajan, P. Bera, S. Sampath, Bimetallic nanoparticles: a single step synthesis, stabilization, and characterization of Au-Ag, Au-Pd, and Au-Pt in sol-gel derived silicates, *Journal of colloid and interface science*, 290 (2005) 117-129.

- [200] L.M. Liz-Marzan, A.P. Philipse, Stable hydrosols of metallic and bimetallic nanoparticles immobilized on imogolite fibers, *The Journal of Physical Chemistry*, 99 (1995) 15120-15128.
- [201] N. Feng, F. Liu, M. Huang, A. Zheng, Q. Wang, T. Chen, G. Cao, J. Xu, J. Fan, F. Deng, Unravelling the Efficient Photocatalytic Activity of Boron-induced Ti^{3+} Species in the Surface Layer of TiO_2 , *Scientific reports*, 6 (2016) 34765.
- [202] H. Cheng, B. Huang, Y. Dai, X. Qin, X. Zhang, Z. Wang, M. Jiang, Visible-light photocatalytic activity of the metastable $\text{Bi}_{20}\text{TiO}_{32}$ synthesized by a high-temperature quenching method, *Journal of Solid State Chemistry*, 182 (2009) 2274-2278.
- [203] R.J. Wong, J. Scott, P. Kappen, G.K.C. Low, J.N. Hart, R. Amal, Enhancing bimetallic synergy with light: the effect of UV light pre-treatment on catalytic oxygen activation by bimetallic Au-Pt nanoparticles on a TiO_2 support, *Catalysis Science & Technology*, 7 (2017) 4792-4805.
- [204] X. Ning, Y. Li, H. Yu, F. Peng, H. Wang, Y. Yang, Promoting role of bismuth and antimony on Pt catalysts for the selective oxidation of glycerol to dihydroxyacetone, *Journal of Catalysis*, 335 (2016) 95-104.
- [205] A. Brandner, K. Lehnert, A. Bienholz, M. Lucas, P. Claus, Production of biomass-derived chemicals and energy: chemocatalytic conversions of glycerol, *Topics in Catalysis*, 52 (2009) 278-287.
- [206] W. Xue, Z. Wang, Y. Liang, H. Xu, L. Liu, J. Dong, Promoting Role of Bismuth on Hydrotalcite-Supported Platinum Catalysts in Aqueous Phase Oxidation of Glycerol to Dihydroxyacetone, *Catalysts*, 8 (2018) 20.
- [207] H. Lee, M.A. Bratescu, T. Ueno, N. Saito, Solution plasma exfoliation of graphene flakes from graphite electrodes, *RSC Advances*, 4 (2014) 51758-51765.
- [208] L. Han, Z. Ma, Z. Luo, G. Liu, J. Ma, X. An, Enhanced visible light and photocatalytic performance of TiO_2 nanotubes by hydrogenation at lower temperature, *RSC Advances*, 6 (2016) 6643-6650.

- [209] N.T. Nolan, M.K. Seery, S.C. Pillai, Spectroscopic investigation of the anatase-to-rutile transformation of sol–gel-synthesized TiO₂ photocatalysts, *The Journal of Physical Chemistry C*, 113 (2009) 16151-16157.
- [210] Z. Ding, G. Lu, P. Greenfield, Role of the crystallite phase of TiO₂ in heterogeneous photocatalysis for phenol oxidation in water, *The Journal of Physical Chemistry B*, 104 (2000) 4815-4820.
- [211] G. Saito, Y. Nakasugi, T. Akiyama, Excitation temperature of a solution plasma during nanoparticle synthesis, *Journal of Applied Physics*, 116 (2014) 083301.
- [212] Y. Nakasugi, G. Saito, T. Yamashita, T. Akiyama, Synthesis of nonstoichiometric titanium oxide nanoparticles using discharge in HCl solution, *Journal of Applied Physics*, 115 (2014) 123303.
- [213] J. Huo, Y. Hu, H. Jiang, C. Li, In situ surface hydrogenation synthesis of Ti³⁺ self-doped TiO₂ with enhanced visible light photoactivity, *Nanoscale*, 6 (2014) 9078-9084.
- [214] F. Zuo, L. Wang, T. Wu, Z. Zhang, D. Borchardt, P. Feng, Self-doped Ti³⁺ enhanced photocatalyst for hydrogen production under visible light, *Journal of the American Chemical Society*, 132 (2010) 11856-11857.
- [215] E.M. Samsudin, S.B.A. Hamid, J.C. Juan, W.J. Basirun, G. Centi, Enhancement of the intrinsic photocatalytic activity of TiO₂ in the degradation of 1, 3, 5-triazine herbicides by doping with N, F, *Chemical Engineering Journal*, 280 (2015) 330-343.
- [216] A.F. Carley, P.R. Chalker, J.C. Riviere, M.W. Roberts, The identification and characterisation of mixed oxidation states at oxidised titanium surfaces by analysis of X-ray photoelectron spectra, *Journal of the Chemical Society, Faraday Transactions 1: Physical Chemistry in Condensed Phases*, 83 (1987) 351-370.
- [217] X. Jiang, Y. Zhang, J. Jiang, Y. Rong, Y. Wang, Y. Wu, C. Pan, Characterization of oxygen vacancy associates within hydrogenated TiO₂: a positron annihilation study, *The Journal of Physical Chemistry C*, 116 (2012) 22619-22624.
- [218] V.A. Zeitler, C.A. Brown, The infrared spectra of some Ti-O-Si, Ti-O-Ti and Si-O-Si compounds, *The Journal of Physical Chemistry*, 61 (1957) 1174-1177.

- [219] C. Huang, H. Bai, Y. Huang, S. Liu, S. Yen, Y. Tseng, Synthesis of Neutral SiO₂, International Journal of Photoenergy, 2012 (2012).
- [220] X. Chen, L. Liu, Z. Liu, M.A. Marcus, W.C. Wang, N.A. Oyler, M.E. Grass, B. Mao, P.-A. Glans, Y.Y. Peter, Properties of disorder-engineered black titanium dioxide nanoparticles through hydrogenation, Scientific reports, 3 (2013) 1510.
- [221] H. Tang, K. Prasad, R. Sanjines, P. Schmid, F. Levy, Electrical and optical properties of TiO₂ anatase thin films, Journal of applied physics, 75 (1994) 2042-2047.
- [222] R. Beranek, H. Kisch, Tuning the optical and photoelectrochemical properties of surface-modified TiO₂, Photochemical & photobiological sciences, 7 (2008) 40-48.
- [223] X. Chen, L. Liu, Y.Y. Peter, S.S. Mao, Increasing solar absorption for photocatalysis with black hydrogenated titanium dioxide nanocrystals, Science, 331 (2011) 746-750.
- [224] U. Diebold, The surface science of titanium dioxide, Surface science reports, 48 (2003) 53-229.
- [225] T.L. Thompson, J.T. Yates, Surface science studies of the photoactivation of TiO₂ new photochemical processes, Chemical Reviews, 106 (2006) 4428-4453.
- [226] J. Wang, P. Yang, B. Huang, Self-doped TiO_{2-x} nanowires with enhanced photocatalytic activity: facile synthesis and effects of the Ti³⁺, Applied Surface Science, 356 (2015) 391-398.
- [227] A. Naldoni, M. Allieta, S. Santangelo, M. Marelli, F. Fabbri, S. Cappelli, C.L. Bianchi, R. Psaro, V. Dal Santo, Effect of nature and location of defects on bandgap narrowing in black TiO₂ nanoparticles, Journal of the American Chemical Society, 134 (2012) 7600-7603.
- [228] Z. Wang, C. Yang, T. Lin, H. Yin, P. Chen, D. Wan, F. Xu, F. Huang, J. Lin, X. Xie, Visible-light photocatalytic, solar thermal and photoelectrochemical properties of aluminium-reduced black titania, Energy & Environmental Science, 6 (2013) 3007-3014.
- [229] W. Fang, Y. Zhou, C. Dong, M. Xing, J. Zhang, Enhanced photocatalytic activities of vacuum activated TiO₂ catalysts with Ti³⁺ and N co-doped, Catalysis Today, 266 (2016) 188-196.

- [230] M.S. Hamdy, R. Amrollahi, G. Mul, Surface Ti^{3+} -containing (blue) titania: A unique photocatalyst with high activity and selectivity in visible light-stimulated selective oxidation, *ACS catalysis*, 2 (2012) 2641-2647.
- [231] N. Lakshminarasimhan, W. Kim, W. Choi, Effect of the agglomerated state on the photocatalytic hydrogen production with in situ agglomeration of colloidal TiO_2 nanoparticles, *The Journal of Physical Chemistry C*, 112 (2008) 20451-20457.
- [232] C. Minero, A. Bedini, V. Maurino, Glycerol as a probe molecule to uncover oxidation mechanism in photocatalysis, *Applied Catalysis B: Environmental*, 128 (2012) 135-143.
- [233] S. Civiš, R. Szabla, B.M. Szyja, D. Smykowski, O. Ivanek, A. Knížek, P. Kubelík, J. Šponer, M. Ferus, J.E. Šponer, TiO_2 -catalyzed synthesis of sugars from formaldehyde in extraterrestrial impacts on the early Earth, *Scientific reports*, 6 (2016) 23199.
- [234] T. Jedsukontorn, V. Meeyoo, N. Saito, M. Hunsom, Route of glycerol conversion and product generation via TiO_2 -induced photocatalytic oxidation in the presence of H_2O_2 , *Chemical Engineering Journal*, 281 (2015) 252-264.
- [235] T. Jedsukontorn, V. Meeyoo, N. Saito, M. Hunsom, Effect of electron acceptors H_2O_2 and O_2 on the generated reactive oxygen species $^1\text{O}_2$ and OH in TiO_2 -catalyzed photocatalytic oxidation of glycerol, *Chinese Journal of Catalysis*, 37 (2016) 1975-1981.
- [236] C. Ao, S. Lee, J. Yu, J. Xu, Photodegradation of formaldehyde by photocatalyst TiO_2 : effects on the presences of NO , SO_2 and VOCs, *Applied catalysis B: environmental*, 54 (2004) 41-50.
- [237] S. Sun, J. Ding, J. Bao, C. Gao, Z. Qi, C. Li, Photocatalytic oxidation of gaseous formaldehyde on TiO_2 : an in situ DRIFTS study, *Catalysis letters*, 137 (2010) 239-246.
- [238] W.R. Haag, E. Gassman, Singlet oxygen in surface waters—Part I: Furfuryl alcohol as a trapping agent, *Chemosphere*, 13 (1984) 631-640.

- [239] S. Li, J. Zhang, S. Hu, K. Xu, W. Jiang, J. Liu, Synthesis of flower-like Ta₃N₅-Au heterojunction with enhanced visible light photocatalytic activity, *Journal of Alloys and Compounds*, 695 (2017) 1137-1144.
- [240] Y. Chen, G. Tian, Y. Shi, Y. Xiao, H. Fu, Hierarchical MoS₂/Bi₂MoO₆ composites with synergistic effect for enhanced visible photocatalytic activity, *Applied Catalysis B: Environmental*, 164 (2015) 40-47.
- [241] G. Li, J. Qu, X. Zhang, H. Liu, H. Liu, Electrochemically assisted photocatalytic degradation of Orange II: influence of initial pH values, *Journal of Molecular Catalysis A: Chemical*, 259 (2006) 238-244.
- [242] E. Lira, S. Wendt, P. Huo, J.Ø. Hansen, R. Streber, S. Porsgaard, Y. Wei, R. Bechstein, E. Lægsgaard, F. Besenbacher, The importance of bulk Ti³⁺ defects in the oxygen chemistry on titania surfaces, *Journal of the American Chemical Society*, 133 (2011) 6529-6532.
- [243] C.L. Muhich, Y. Zhou, A.M. Holder, A.W. Weimer, C.B. Musgrave, Effect of surface deposited Pt on the photoactivity of TiO₂, *The Journal of Physical Chemistry C*, 116 (2012) 10138-10149.



APPENDIX A
CALIBRATION CURVE

A.1 Calibration curve of glycerol solution

Table A.1 Data of different glycerol concentrations for calibration curve.

| Glycerol concentration (mol/L) | Peak Area | | |
|--------------------------------------|-----------|---------|---------|
| | 1 | 2 | Average |
| 0.0 | 0 | 0 | 0 |
| 0.1 | 914577 | 886449 | 900513 |
| 0.2 | 1649442 | 1686752 | 1668097 |
| 0.3 | 2505019 | 2518953 | 2511986 |
| 0.4 | 3357854 | 3314534 | 3336194 |

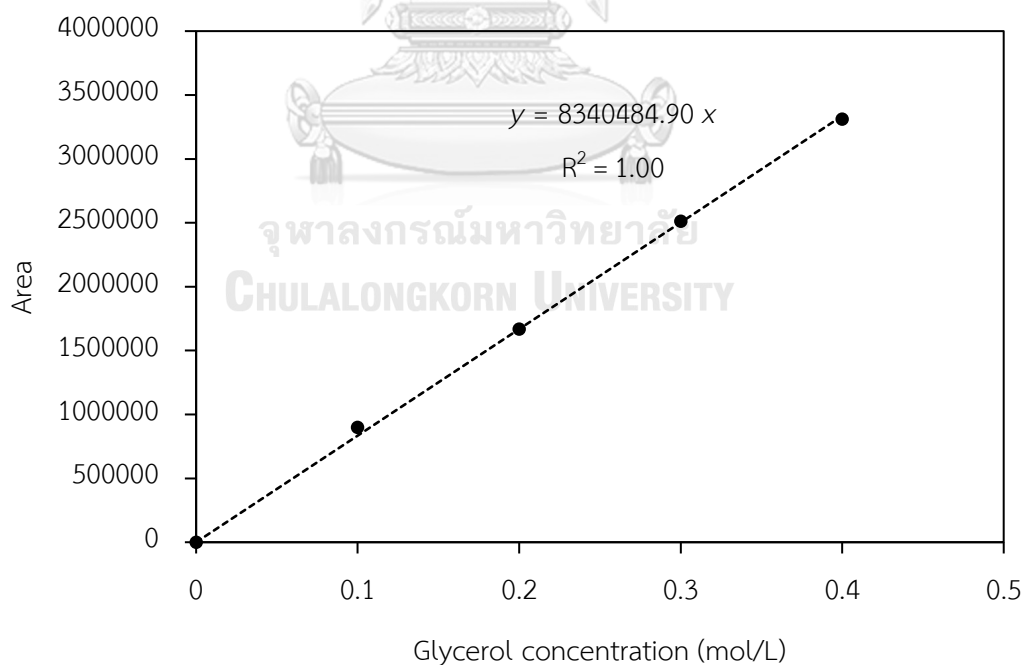


Figure A.1 Calibration curve of glycerol solution.

A.2 Calibration curve of glyceraldehyde solution

Table A.2 Data of different glyceraldehyde concentrations for calibration curve.

| Glyceraldehyde concentration (mol/L) | Peak Area | | |
|--------------------------------------|-----------|--------|---------|
| | 1 | 2 | Average |
| 0.0 | 0 | 0 | 0 |
| 0.0275 | 159738 | 163806 | 161772 |
| 0.0550 | 320846 | 314464 | 317655 |
| 0.1110 | 690537 | 688041 | 689289 |

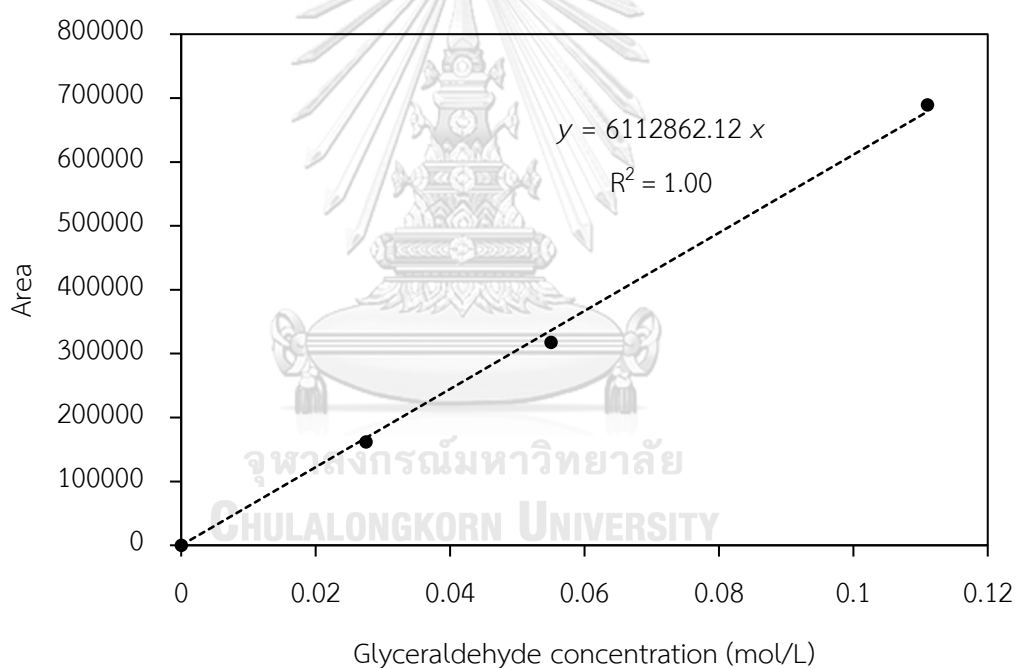


Figure A.2 Calibration curve of glyceraldehyde solution.

A.3 Calibration curve of dihydroxyacetone solution

Table A.3 Data of different dihydroxyacetone concentrations for calibration curve.

| Dihydroxyacetone concentration (mol/L) | Peak Area | | |
|--|-----------|---------|---------|
| | 1 | 2 | Average |
| 0.00 | 0 | 0 | 0 |
| 0.10 | 601219 | 588821 | 595020 |
| 0.15 | 1003142 | 956110 | 979626 |
| 0.30 | 1853706 | 1814052 | 1833879 |

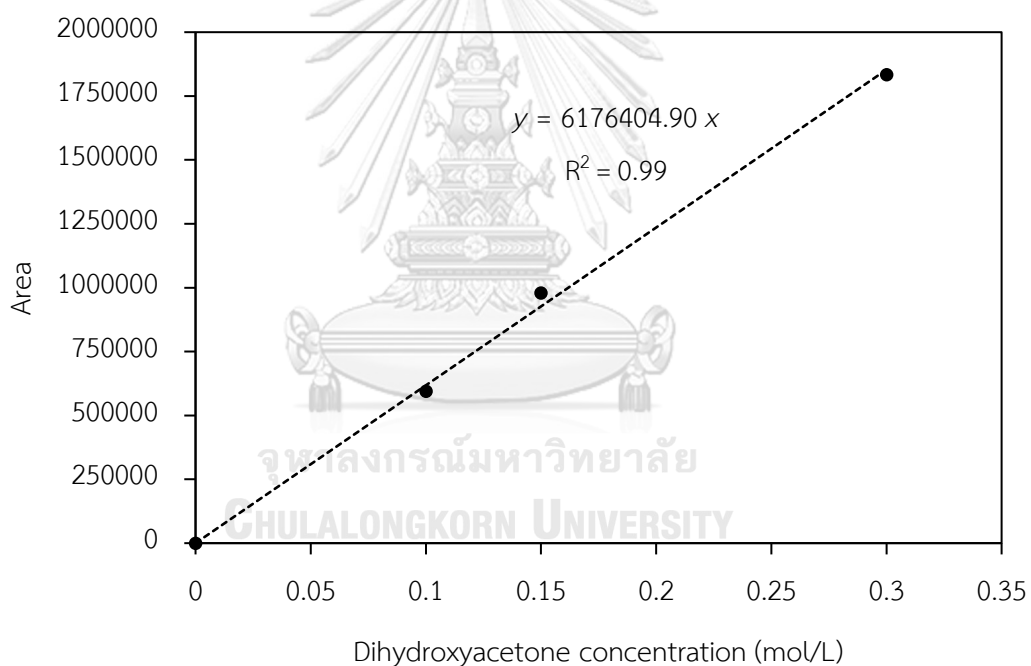


Figure A.3 Calibration curve of dihydroxyacetone solution.

A.4 Calibration curve of hydroxypyruvic acid solution

Table A.4 Data of different hydroxypyruvic acid concentrations for calibration curve.

| Hydroxypyruvic acid concentration (mol/L) | Peak Area | | |
|---|-----------|--------|---------|
| | 1 | 2 | Average |
| 0.00 | 0 | 0 | 0 |
| 0.05 | 99865 | 103299 | 101582 |
| 0.10 | 250173 | 248987 | 246850 |
| 0.30 | 741844 | 755366 | 748605 |

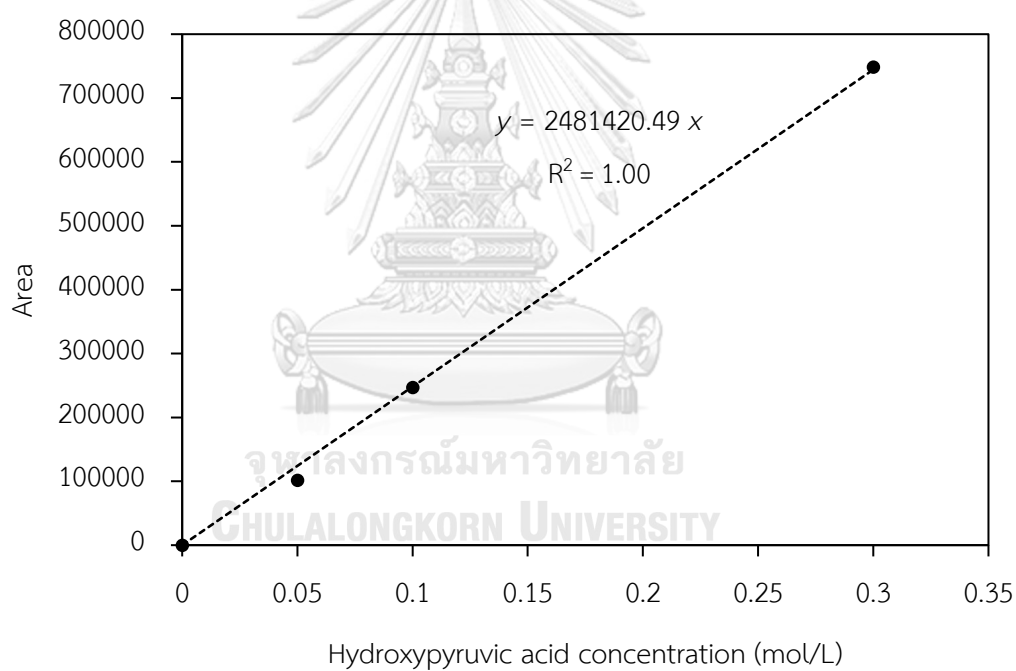


Figure A.4 Calibration curve of hydroxypyruvic acid solution.

A.5 Calibration curve of glycolic acid solution

Table A.5 Data of different glycolic acid concentrations for calibration curve.

| Glycolic acid concentration (mol/L) | Peak Area | | |
|-------------------------------------|-----------|---------|---------|
| | 1 | 2 | Average |
| 0.0 | 0 | 0 | 0 |
| 0.1 | 300521 | 299227 | 299874 |
| 0.2 | 720183 | 699843 | 710013 |
| 0.3 | 919742 | 929172 | 924457 |
| 0.5 | 1611840 | 1585706 | 1598773 |

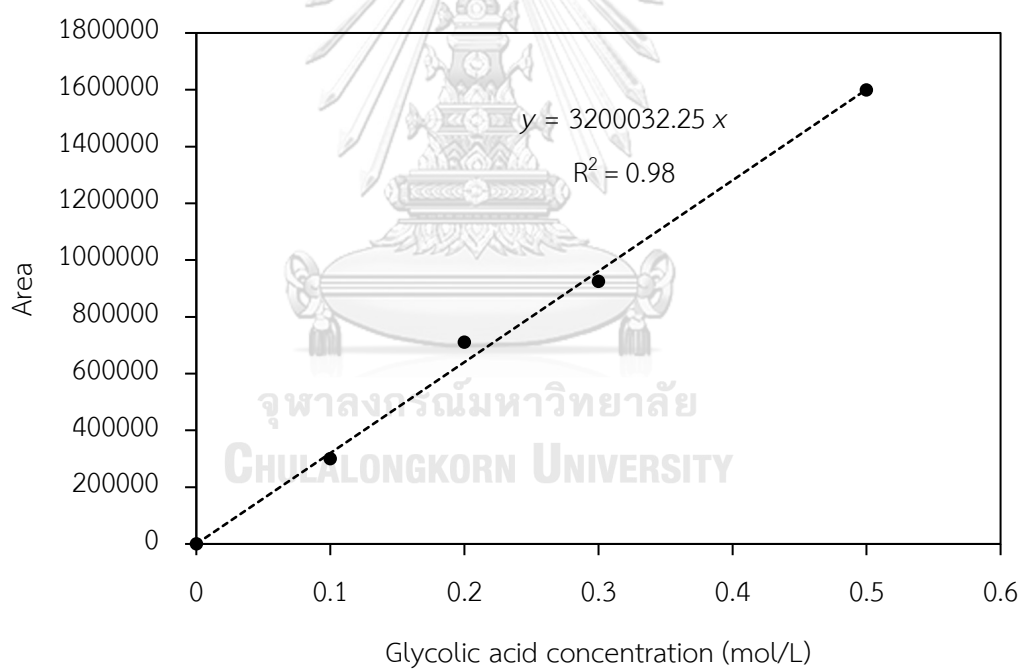


Figure A.5 Calibration curve of glycolic acid solution.

A.6 Calibration curve of formaldehyde solution

Table A.6 Data of different formaldehyde concentrations for calibration curve.

| Formaldehyde concentration (mol/L) | Peak Area | | |
|------------------------------------|-----------|---------|---------|
| | 1 | 2 | Average |
| 0.0 | 0 | 0 | 0 |
| 0.1 | 292331 | 298359 | 295345 |
| 0.2 | 627995 | 622843 | 625419 |
| 0.3 | 1175268 | 1162802 | 1169035 |
| 0.5 | 1746582 | 1792034 | 1769308 |

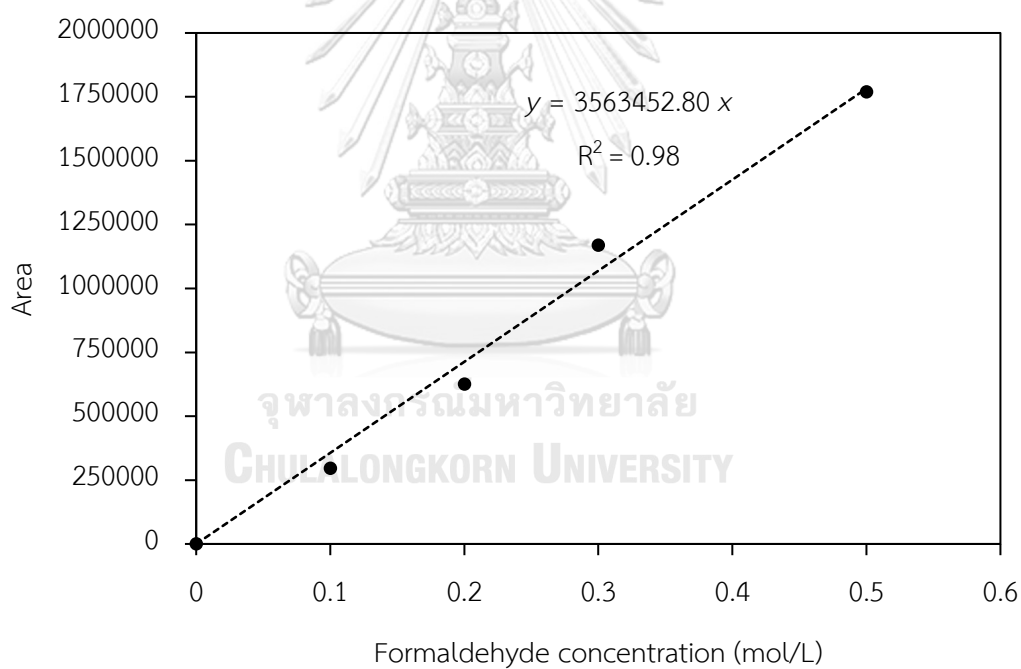


Figure A.6 Calibration curve of formaldehyde solution.

APPENDIX B
EXAMPLES OF CALCULATION

B.1 Calculation of metal loading content

Example : monometallic Au₃/TiO₂ photocatalyst with 3 wt.% Au content

Given; Molecular weight of HAuCl₄·3H₂O 393.83 g/mol

Molecular weight of Au 196.97 g/mol

TiO₂ powder 100 g would have been Au on TiO₂ 3 g

If TiO₂ powder 2.00 g would have been Au on TiO₂ 0.06 g

So, Au metal 0.06 g would have been from HAuCl₄·3H₂O

$$\frac{\text{g HAuCl}_4 \cdot 3\text{H}_2\text{O} \times \text{g Au (TiO}_2\text{)}}{\text{g Au}} = \frac{393.83 \times 0.06}{196.97} = 0.12 \text{ g}$$

And, HAuCl₄·3H₂O 1 g was dissolved as precursor solution 100 mL

So, HAuCl₄·3H₂O 0.12 g would have been from precursor solution 12 mL

Therefore, taking 12 mL of HAuCl₄·3H₂O precursor solution and dissolved with 1.94 g of TiO₂ support.

จุฬาลงกรณ์มหาวิทยาลัย

Example : bimetallic Au₃Pt₃/TiO₂ photocatalyst with each 3 wt.% of Au and Pt

Given; Molecular weight of HAuCl₄·3H₂O 393.83 g/mol

Molecular weight of Au 196.97 g/mol

Molecular weight of H₂PtCl₆·6H₂O 517.90 g/mol

Molecular weight of Pt 195.08 g/mol

TiO₂ powder 100 g would have been Au on TiO₂ 3 g

and would have been Pt on TiO₂ 3 g

If TiO₂ powder 2.00 g would have been Au on TiO₂ 0.06 g

and would have been Pt on TiO₂ 0.06 g

So, Au metal 0.06 g would have been from $\text{HAuCl}_4 \cdot 3\text{H}_2\text{O}$

$$\frac{\text{g HAuCl}_4 \cdot 3\text{H}_2\text{O} \times \text{g Au (TiO}_2\text{)}}{\text{g Au}} = \frac{393.83 \times 0.06}{196.97} = 0.12 \text{ g}$$

And, $\text{HAuCl}_4 \cdot 3\text{H}_2\text{O}$ 1 g was dissolved as precursor solution 100 mL

So, $\text{HAuCl}_4 \cdot 3\text{H}_2\text{O}$ 0.12 g would have been from precursor solution 12 mL

And, Pt metal 0.06 g would have been from $\text{H}_2\text{PtCl}_6 \cdot 6\text{H}_2\text{O}$

$$\frac{\text{g H}_2\text{PtCl}_6 \cdot 6\text{H}_2\text{O} \times \text{g Pt (TiO}_2\text{)}}{\text{g Pt}} = \frac{517.90 \times 0.06}{195.08} = 0.16 \text{ g}$$

And, $\text{H}_2\text{PtCl}_6 \cdot 6\text{H}_2\text{O}$ 1 g was dissolved as precursor solution 100 mL

So, $\text{H}_2\text{PtCl}_6 \cdot 6\text{H}_2\text{O}$ 0.16 g would have been from precursor solution 16 mL

Therefore, taking 12 mL of $\text{HAuCl}_4 \cdot 3\text{H}_2\text{O}$ precursor solution, 16 mL of $\text{H}_2\text{PtCl}_6 \cdot 6\text{H}_2\text{O}$ precursor solution and dissolved with 1.88 g of TiO_2 powder.

B.2 Calculation of glycerol conversion, product selectivity and product yield

The net of glycerol conversion (X), the product yield (Y) and the product selectivity (S) of the selected product was calculated according to Eqs. (B.1), (B.2) and (B.3), respectively;

$$X(\%) = \frac{\text{Amount of glycerol converted (C-based mole)}}{\text{Total amount of glycerol in reactant (C-based mole)}} \times 100 \quad (\text{B.1})$$

$$Y(\%) = \frac{\text{Amount of glycerol converted to product } j \text{ (C-based mole)}}{\text{Total amount of glycerol in reactant (C-based mole)}} \times 100 \quad (\text{B.2})$$

$$S(\%) = \frac{\text{Amount of product } j \text{ generated (C-based mole)}}{\text{Total amount of generated products (C-based mole)}} \times 100 \quad (\text{B.3})$$

Example: Calculation of the glycerol conversion, the product yield and the product selectivity of generated products for glycerol photooxidation over commercial TiO₂ in anatase phase under the condition of catalyst dosage 3 g/L, light intensity 4.79 mW/cm² and 8 h of irradiation time with using O₂ as electron acceptor.

For glycerol conversion (mol/L)

From the Eq. of calibration curve as displayed in Appendix A.1:

$$y = 8340484.90x$$

At the initial time;

Given, $y =$ integrated peak area = 2581903

$x =$ glycerol concentration (mol/L)

$$x = \frac{2581903}{8340484.90} = 0.31 \text{ mol/L}$$

Therefore, the initial glycerol concentration = 0.31 mol/L

At the 8 h of irradiation time;

Given, $y =$ integrated peak area = 2156536

$x =$ glycerol concentration (mol/L)

$$x = \frac{2156536}{8340484.90} = 0.259 \text{ mol/L}$$

Therefore, the glycerol concentration at 8 h of irradiation time = 0.259 mol/L

For glycerol conversion (%) as calculated by Eq.(B.1)

$$X(\%) = \frac{0.310 - 0.259}{0.310} \times 100 = 16.45\%$$

For the product yield of selected product

- Glyceraldehyde concentration (mol/L)

From the Eq. of calibration curve as displayed in Appendix A.2:

$$y = 6112862.12x$$

At the 8 h of irradiation time;

Given, y = integrated peak area = 85814

x = glyceraldehyde concentration (mol/L)

$$x = \frac{85814}{6112862.12} = 0.014 \text{ mol/l}$$

So, the glyceraldehyde concentration at 8 h of irradiation time = 0.014 mol/L

For the glyceraldehyde yield (%) as calculated by Eq.(B.2)

$$X(\%) = \frac{0.014}{0.310} \times 100 = 4.52\%$$

- **Dihydroxyacetone concentration (mol/L)**

From the Eq. of calibration curve as displayed in Appendix A.3:

$$y = 6176404.90x$$

At the 8 h of irradiation time;

Given, y = integrated peak area = 52712

x = dihydroxyacetone concentration (mol/L)

$$x = \frac{52712}{6176404.90} = 0.0085 \text{ mol/l}$$

So, the dihydroxyacetone concentration at 8 h of irradiation time = 0.0085

mol/L

For the dihydroxyacetone yield (%) as calculated by Eq.(B.2)

$$X(\%) = \frac{0.0085}{0.310} \times 100 = 2.74\%$$

- **Hydroxypyruvic acid concentration (mol/L)**

From the Eq. of calibration curve as displayed in Appendix A.4:

$$y = 2481420.49x$$

At the 8 h of irradiation time;

Given, y = integrated peak area = 6695

x = hydroxypyruvic acid concentration (mol/L)

$$x = \frac{6695}{2481420.49} = 0.0027 \text{ mol/l}$$

So, the hydroxypyruvic acid concentration at 8 h of irradiation time = 0.0027 mol/L

For the hydroxypyruvic acid yield (%) as calculated by Eq.(B.2)

$$X(\%) = \frac{0.0027}{0.310} \times 100 = 0.87\%$$

- **Glycolic acid concentration (mol/L)**

From the Eq. of calibration curve as displayed in Appendix A.5:

$$y = 3200032.25x$$

At the 8 h of irradiation time;

Given, y = integrated peak area = 5858

x = glycolic acid concentration (mol/L)

$$x = \frac{5858}{3200032.25} = 0.0018 \text{ mol/l}$$

So, the glycolic acid concentration at 8 h of irradiation time = 0.0018 mol/L

For the glycolic acid yield (%) as calculated by Eq.(B.2)

$$X(\%) = \frac{0.0018}{0.310} \times 100 = 0.58\%$$

- **Formaldehyde concentration (mol/L)**

From the Eq. of calibration curve as displayed in Appendix A.6:

$$y = 3563452.80x$$

At the 8 h of irradiation time;

Given, y = integrated peak area = 5392

x = formaldehyde concentration (mol/L)

$$x = \frac{5392}{3563452.80} = 0.0015 \text{ mol/L}$$

So, the formaldehyde concentration at 8 h of irradiation time = 0.0015 mol/L

For the formaldehyde yield (%) as calculated by Eq.(B.2)

$$X(\%) = \frac{0.0015}{0.310} \times 100 = 0.48\%$$

For the product selectivity (S) of selected product

The all generated products in this condition was

- Glyceraldehyde 0.014 mol/L
- Dihydroxyacetone 0.0085 mol/L
- Hydroxypyruvic acid 0.0027 mol/L
- Glycolic acid 0.0018 mol/L
- Formaldehyde 0.0015 mol/L

Thus, the summation of all generated products concentration is 0.0285 mol/L

- Glyceraldehyde selectivity (%) was calculated by Eq.(B.3)

$$Y(\%) = \frac{0.014}{0.0285} \times 100 = 49.12 \%$$

- Dihydroxyacetone selectivity (%) was calculated by Eq.(B.3)

$$Y(\%) = \frac{0.0085}{0.0285} \times 100 = 29.82 \%$$

- Hydroxypyruvic acid selectivity (%) was calculated by Eq.(B.3)

$$Y(\%) = \frac{0.0027}{0.0285} \times 100 = 9.47 \%$$

- Glycolic acid selectivity (%) was calculated by Eq.(B.3)

$$Y(\%) = \frac{0.0018}{0.0285} \times 100 = 6.32 \%$$

- Formaldehyde selectivity (%) was calculated by Eq.(B.3)

$$Y(\%) = \frac{0.0015}{0.0285} \times 100 = 5.26 \%$$



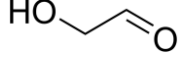
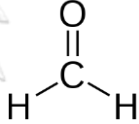
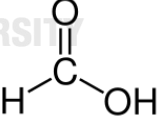
APPENDIX C

LIST OF COMPOUNDS GENERATED FROM GLYCEROL PHOTOOXIDATION
VIA TiO₂-BASED PHOTOCATALYSTS

Table C.1 List of compounds generated from the photooxidation of glycerol over TiO₂-based photocatalysts.

| IUPAC name (Molecular formula) | Other names | Chemical structure | Price (£/kg) (%Purity) [CAS No.] |
|--|--|--------------------|--|
| 2,3-Dihydroxypropanal (C ₃ H ₆ O ₃) | Glyceraldehyde; Glyceric aldehyde; Glyceral | | 100,000 (≥98.0%) ^a [56-82-6] |
| 1,3-Dihydroxypropan-2-one (C ₃ H ₆ O ₃) | 1,3-Dihydroxypropanone; Dihydroxyacetone; Glycerone | | 4,500 (≥98.0%) ^a [96-26-4] |
| 3-Hydroxy-2-oxopropanoic acid (C ₃ H ₄ O ₄) | Hydroxypyruvic acid; Hydroxypyruvate | | 20,040,000 (≥95.0%) ^a [1113-60-6] |
| 2,3-Dihydroxypropanoic acid (C ₃ H ₆ O ₄) | Glyceric acid | | 1,470 (≥20.0%) ^a [473-81-4] |
| 2-Hydroxyethanoic acid (C ₂ H ₄ O ₃) | Dicarbonous acid; Glycolic acid; Hydroxyacetic acid; Hydroacetic acid | | 500 N/A [79-14-1] |

Table C.1 List of compounds generated from the photooxidation of glycerol over TiO₂-based photocatalysts. (Cont.)

| IUPAC name (Molecular formula) | Other names | Chemical structure | Price (£/kg) (%Purity) [CAS No.] |
|--|--|--|--|
| 2-Hydroxyacetaldehyde (C ₂ H ₄ O ₂) | Glycolaldehyde; Hydroxyacetaldehyde; 2-Hydroxyethanal; Hydroxyethanal |  | 84,000 N/A [141-46-8] |
| Methanal (CH ₂ O) | Formaldehyde; Methyl aldehyde; Methylene glycol; Methylene oxide; Formalin; Formol; Carbonyl hydride |  | 35 (≥36.5%) ^a [50-00-0] |
| Methanoic acid (CH ₂ O ₂) | Formic acid; Carbonous acid; Formylic acid; Hydrogen carboxylic acid; Hydroxy(oxo)methane; Metacarbonic acid; Oxocarbinic acid; Oxomethanol |  | 34 (≥95.0%) ^b [64-18-6] |

^a Reagent grade

^b Food grade

VITA

Mr. Trin Jedsukontorn was born on September 28, 1990 in Chonburi, Thailand. He received his B.Sc. (Hons) degree from the Department of Chemical Technology, Chulalongkorn University in 2013. He continued studying for a Doctoral Degree in Chemical Technology, Chulalongkorn University. He has received the Dutsadi Phiphat Scholarship from Chulalongkorn University for his Ph.D. study. Trin also served as a teaching assistant for undergraduate courses “Chemical Engineering Thermodynamic” and “Process Dynamics and Control”. He carried out his Ph.D. research for one year (2016-2017) at Graduate School of Engineering, Nagoya University, Japan.

Journal Publications:

1. T. Jedsukontorn, V. Meeyoo, N. Saito, M. Hunsom, Route of glycerol conversion and product generation via TiO₂-induced photocatalytic oxidation in the presence of H₂O₂. Chem. Eng. J. 281 (2015) 252-264.
2. T. Jedsukontorn, V. Meeyoo, N. Saito, M. Hunsom, Effect of electron acceptors H₂O₂ and O₂ on the generated reactive oxygen species ¹O₂ and OH in TiO₂-catalyzed photocatalytic oxidation of glycerol. Chin. J. Catal. 37 (2016) 1975–1981.
3. T. Jedsukontorn, N. Saito, M. Hunsom, Photocatalytic behavior of metal-decorated TiO₂ and their catalytic activity for transformation of glycerol to value added compounds. Mol. Catal. 432 (2017) 160-171.
4. T. Jedsukontorn, T. Ueno, N. Saito, M. Hunsom, Facile preparation of defective black TiO₂ through the solution plasma process: Effect of parametric changes for plasma discharge on its structural and optical properties. J. Alloys Compd. 726 (2017) 567-577.
5. T. Jedsukontorn, T. Ueno, N. Saito, M. Hunsom, Narrowing band gap energy of defective black TiO₂ fabricated by solution plasma process and its

photocatalytic activity on glycerol transformation. (2018) [Submitted]

6. T. Jedsukontorn, T. Ueno, N. Saito, M. Hunsom, Mechanistic aspect based on the role of reactive oxidizing species (ROSs) in macroscopic level on the glycerol oxidation over defected and defected-free TiO₂. (2018) [Submitted].

7. T. Jedsukontorn, N. Saito, M. Hunsom, Photoinduced glycerol oxidation over plasmonic Au and AuM (M = Pt, Pd and Bi) nanoparticle-decorated TiO₂ photocatalysts. *Nanomaterials* 8 (2018) 269.

Conference Presentation:

1. T. Jedsukontorn, T. Ueno, N. Saito, M. Hunsom, (2017) “Narrowing band gap energy of defective black TiO₂ fabricated by solution plasma process and its application on glycerol conversion”. European Material Research Society Spring Meeting, May 22-26, 2017 at Palais de la Musique et des Congrès, Strasbourg, France.

